Functional Properties and Novel Applications of 1D Supramolecular Nanofibres and Decoupled 2D Graphene Stacks

A Thesis
Submitted for the Degree of

DOCTOR OF PHILOSOPHY

by

Umesha Mogera

Chemistry and Physics of Materials unit

Jawaharlal Nehru Centre for Advanced Scientific Research

(A Deemed University)

Bangalore – 560064 (INDIA)

July-2016

Dedicated to,

My Parents,
My Teachers
and
Professor GUK

DECLARATION

I hereby declare that the thesis entitled **“Functional Properties and Novel Applications of 1D Supramolecular Nanofibres and Decoupled 2D Graphene Stacks”** is an authentic record of research work carried out by me at the Chemistry and Physics of Materials Unit, Jawaharlal Nehru Centre for Advanced Scientific Research, Bangalore, India under the supervision of **Professor G. U. Kulkarni** and that it has not been submitted elsewhere for the award of any degree or diploma.

In keeping with the general practice in reporting scientific observations, due acknowledgment has been made whenever the work described is based on the findings of other investigators. Any omission that might have occurred due to oversight or error in judgment is regretted.

Umesha Mogera

CERTIFICATE

Certified that the work described in this thesis titled **"Functional Properties and Novel Applications of 1D Supramolecular Nanofibres and Decoupled 2D Graphene Stacks"** has been carried out by **Umesha Mogera** at the Chemistry and Physics of Materials Unit, Jawaharlal Nehru Centre for Advanced Scientific Research, Bangalore, India under my supervision and that it has not been submitted elsewhere for the award of any degree or diploma.

Professor G. U. Kulkarni

(Research Supervisor)

Acknowledgements

First and foremost, I would like to thank my research supervisor **Professor Giridhar U. Kulkarni** for his constant guidance throughout this research journey. As a guide, he has allowed me to expose to various fields of science and allowed me to undergo vigorous training. As a person, he is a role model to me. Looking at him and his working style, I have improved myself in many aspects of life. I am always grateful to him and feel privileged to have worked under his guidance. He has given me opportunities to explore various interesting projects and learn useful instrumentations. I express my deep sense of gratitude and profound feeling of admiration for him.

'Bharat Ratna' Professor C. N. R. Rao's mere presence is an inspiration. I am fortunate to be in this campus and to listen to his encouraging words about research on several occasions.

I thank past and present presidents of JNCASR for their immense support and making sure that JNCASR is a world-class research centre for young minds. I acknowledge the past and present chairman of CPMU for allowing me to use all departmental facilities.

It is a pleasure to thank all my collaborators; Prof. Subi George, Prof. Chandrabhas Narayan, Prof. Milan K Sanyal (SINP, Kolkata), Dr. Neena, Dr. Arpan, Dr. Dhanya, Dr. Narendra, Dr. Abhay, Mrs. Priya for active collaboration.

I thank all the faculty members of CPMU, TSU and NCU for their cordiality, especially my teachers, Prof. N. Chandrabhas, Prof. Umesh Waghmare, Prof. A. Sundaresan, Prof. M. Eswaramoorthy, Prof. K. S. Narayan, Prof. S. Balasubramanian, Prof. S. M. Shivaprasad, Prof. T. K. Maji, Prof. S. K. Pati, Prof. Navakant Bhat, Prof. K. N. Bhat, Prof. Shiv Shankar (IISc) for their courses.

I acknowledge Prof. S. N. Bhat, POCE coordinator, for his immense encouragements and support all through the studies.

Timely and ready assistance and also friendly attitude from technical staff, Mr. Srinath and Mr. Srinivas is acknowledged. I am very thankful to Mrs. Usha (TEM), Dr. Jay (TEM), Dr. Kannan (TEM), Dr. Karthik (Talos TEM), Mrs. Selvi (FESEM), Dr. S.

Basavaraja (AFM), Mrs. AVN (IPR), Mr. Anil (XRD), Mr. Mahesh (SEM), Dr. Karthik (TEM), Mr. Vasu (UV, IR and PL) Mr. A. Srinivasa Rao for their invaluable technical assistance. Special thanks to Mr. Sanjith for cleanroom related helps. Ms. Vanitha and Mr. Sunil are acknowledged for their help in various lab activities.

I thank Mr. Somnath and Mr. Nagaiagh for magnetic measurements, Dr. Ankith for various help during organic synthesis.

I am grateful to my past and present labmates, Dr. Radha, Dr. Narendra, Dr. Abhay, Dr. Ritu, Dr. Rashmi, Dr. Padma, Dr. Harish, Dr. Shubra, Dr. Mallik, Dr. Gangaiah, Dr. Ashutosh, Dr. Murali, Dr. Shobin, Kiruthika, Nikita, Ankush, Dipanwita, Sunil, Chaitali, Kartikeya, Bharath, Rajashekhar, Tripurantaka, Suman, Indrajit, Janani, and Navneet for their fruitful discussions and support.

I thank all staffs of academic, administrative, purchase office, library, complab and Hostel for their assistance, especially Dr. Princy and Mrs. Sukanya for their advice and friendly nature. I gratefully acknowledge senior administrative officer, Mr. Jayachandra, who has been friendly, supportive and ready to help in any situation and time.

I thank CSIR for fellowship, DST and CEFIPRA for travel support.

I thank all my friends in JNCASR, especially cricket mates who kept JNC life filled with lots of fun and memorable.

Besides the research life, Prof. G. U. Kulkarni's and his family's personal care and affection is acknowledged. I thank Mrs. Indira Kulkarni, Teju and Poorna for their warmth and hospitality.

All this effort becomes futile without acknowledging my beloved parents, grandparents, my sister, Pavitra and brother, Vinod. At the same time, it is impossible to express my gratitude to them without whose support and wish, I would not have come thus far. They are always ready to share my grief and joy and encourage me to do better than the best

Preface

The thesis work pertains to synthesis, functional properties and novel applications 1D nanofibre and 2D graphene stacks. It is organized into six chapters.

Chapter I introduces the concept of nano, nanoscale materials, and their important properties. Particularly, nanomaterials of different dimensionalities have been discussed in detail by taking a variety of examples from the literature. In the later part, the uniqueness of the present work has been stated contrasting literature results on 1D and 2D nanomaterials. **Chapter II** introduces the characterization techniques used in the thesis work.

Chapter III deals with properties and applications of 1D supramolecular nanofibres made of coronene tetracarboxylate and dodecyl methyl viologen donor-acceptor moieties. This chapter contains four sections. Chapter IIIA describes the design and fabrication of a humidity sensor with the ultrafast response and recovery times. An insight into the possible mechanism for such fast response has been obtained using XRD, AFM and UV-Vis absorption measurements. Chapter IIIB describes the utility of the humidity sensor in breath measuring applications, particularly for simultaneous detection of humidity and flow of exhaled human breath. The novelty of the device has been demonstrated in several dehydration conditions. Chapter IIIC deals with contexts where the sensor is made recall the humidity experienced prior to measurements, essentially serving as a humidity based memory device. Chapter IIID explains the usage of the nanofibre in dry conditions, as an efficient electrolyte medium for micro-supercapacitor with voltage window surpassing that of ionic liquids.

Chapter IV pertains to synthesis and unusual properties of decoupled 2D graphene stacks. This chapter contains four sections. Chapter IVA introduces a rapid, elegant method of producing graphene on Ni substrate without the usage of hydrogen. Thus obtained graphene has been examined as a barrier for corrosion and thermal oxidation of metal surfaces. Chapter IVB describes the process of making a new graphite-like species (called T-SLG), which in spite of being a stack of large number of graphene layers, behaves similar to single layer graphene, due to high degree of decoupling among layers. Several characterization techniques, Raman, SAED, C-AFM etc.,have been employed to ascertain the exact nature of T-SLG. Chapter IVC deals with properties of T-SLG, which resemble greatly properties of a suspended single layer. The observed properties have been related to angular disorder leading to decoupling. Chapter IVD deals with the observed influence of graphene growth on the morphology and orientation of the underlying Ni substrate.

Chapter V describes a method to improve the quality of CVD-grown graphene on copper. In a way, it provides an alternative method for direct transfer of the graphene grown on copper to a targeted substrate without the need of any polymer support. **Chapter VI** presents summary and outlook for the thesis work.

Table of Contents

List of Figures

List of Tables

List of Acronyms

0D	Zero Dimension
1D	One Dimension
2D	Two dimensions
3D	Three dimensions
AB stacked	Bernal stacked
AC	Alternating Current
AFM	Atomic Force Microscope
aq.	aqueous
BAC	Breath Alcohol Concentration
CCD	Charge coupled device
CD	charge-discharge
CNT's	Carbon Nanotubes
C-AFM	Conducting AFM
CS	Coronene tetracorboxylate salt
CV	Cyclic voltammetry
CVD	Chemical Vapour Deposition
CP	Curing RH Pulse
CR	Corrosion Rate
CT	Charge Transfer
D1, D2	Supramolecular Humidity Device 1, Device 2
D-A	Donor-Acceptor
DC	Direct Current
DFT	Density Functional Theory
DI	De-ionised
DLG	Double layer graphene
DMV	Dodecyl methyl viologen
DOS	Density of states
e and I	exhaling and inhaling

E_a	Activation Energy
E_{corr}	Corrosion potential
ED	Electron Diffraction
EDL	Electrical double layer
EDS	Energy dispersive X-ray spectroscopy
EIS	Electrochemical Impedance Spectroscopy
FET	Field-effect transistor
FESEM	Field emission scanning electron microscopy
FIR	Far Infrared
FFT	Fast Fourier transform
FLG	Few layer graphene
FT-IR	Fourier transform infrared spectroscopy
FWHM	Full width at half maximum
G-CNT	Graphene carbon nanotube
GIXRD	Glazing incidence X-ray diffraction
HOPG	Highly oriented pyrolytic graphite
hr	hour
HR-TEM	High-resolution transmission electron micrograph
I_{2D}/I_G	ratio of 2D band intensity with G band intensity
I_{corr}	Corrosion current
I-V	Current-Voltage
iR	(current x resistance) = voltage drop
JH	Joule Heating
J-graphene	Joule heated graphene
LCD	Liquid Crystal Display
LED	Light emitting diode
LEED	Low angle electron diffraction
ln	natural log
LW	Length/Width
MEG	Multilayer epitaxial graphene
MFM	Magnetic force Microscopy

MWNT	Multi wall nanotube
n_c	Charge carrier concentration
NIR	Near field infrared Spectroscopy
NW	Nanowire
OCP	Open Circuit Potential
OLC	Onion like carbon
OP	Optical profiler
PC	Poly carbonate
PDMS	Polydimethylsiloxane
PMMA	Poly-methyl-methacrlyate
PET	Polyethylene terephthalate
Pos	Position
PSI	Phase shifting interferometry
PVA	Poly vinyl alcohol
PVD	Physical vapour Deposition
QD	Quantum Dot
R_{CT}	Charge transfer resistance
rms	root mean square
R_p	Electrochemical polarisation resistance
R_S	Solution Resistance
R2R	Roll-to-roll
RFCVD	Radio frequency magnetic inducting heating
RFID	Radio frequency identification
RH	Relative Humidity
RT	Room temperature
RTCVD	Rapid Thermal Chemical Vapor Deposition
SAED	Selected area electron diffraction
SAXS	Small angle X-ray scattering
SAM's	Self-assembled monolayers
sccm	standard cubic centimetres per minute
SEM	Scanning electron microscopy

SERS	Surface enhanced Raman scattering
SLG	Single layer graphene
SP	Surface Plasmon
SPR	Surface plasmon resonance
STM	Scanning tunnelling microscopy
STEM	Scanning transmission electron microscopy
SWNT	Single walled carbon nanotubes
SXRD	Surface X-ray Diffraction
tBLG	Twisted bilayer graphene
$\mathbf{T_c}$	Bloch-Gruneisen Temperature (crossover temperature)
TEM	Transmission electron microscopy
TMG	Turbostratic multilayer graphene
TP	Testing RH Pulse
TSLG	Turbostratically single layer graphene
TTI	Time –temperature indicator
UHV	Ultra-high vacuum
UV-vis	Ultraviolet-visible
vHS	van-Hove singularities
VSI	Vertical scanning interferometry
VSM	Vibrating sample magnetometer
VW	Voltage window
XRD	X-ray diffraction
$\boldsymbol{\lambda_{ex}}$	Excitation wavelength
μ-SS	micro supramolecular supercapacitor
$\boldsymbol{\sigma_D}$	Dirac point conductivity

Chapter I

Introduction

I.1 Nano

The prefix nano has originated from the Latin word “nanus”, meaning “dwarf” [1]. According to the dictionary definitions, nano refers to “one-billionth” [2] and hence is used to designate “extreme smallness”. It is hard to imagine though just how small a nanometre is! For example, take a human hair, which when cut along its length 1 lakh times gives a diameter of 1 nm which is the diameter of a single walled carbon nanotube. In fact that is how a 10 metre building compares to the hair (see Figure I.1). “Nanoscale” is the length scale where material’s property is size & shape dependent [3]. Nanoscience deals with studying materials having at least one of their dimensions in the range of 1 nm to few 100 nm [4]. Nanoscience is not just physics, chemistry, engineering or biology, it is all of them [5]. The applied stream of nanoscience is nanotechnology which deals with the manipulation, control and integration of nano-objects for designing the nanoscale architectures [4].

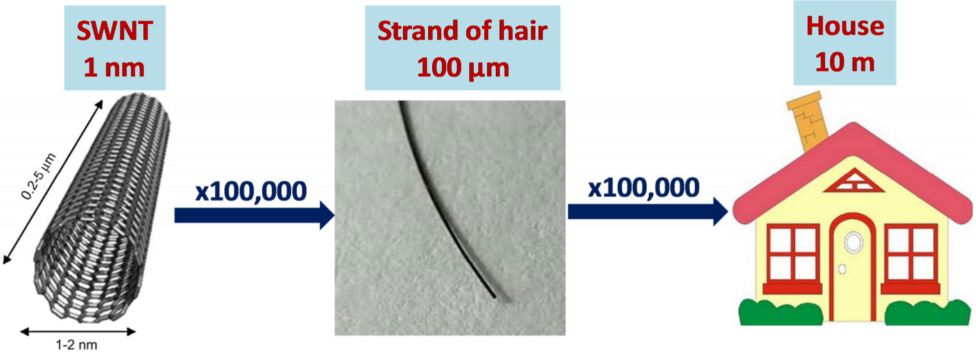

Figure I.1 Size comparison of the objects at nano, micro, and macroscale (adapted from ref. 1).

I.2 History of nanomaterials

Nanoscience has a rich historical background starting from the 4th century A. D. when the Roman glass makers fabricated coloured glasses which essentially consisted of colloidal particles of gold and silver dust dissolved in the glass [6]. Even the creations of the medieval era, the Lycurgus cup, now kept in British museum [7], exhibit beautiful colours such as red and green for the transmitted and reflected light illumination (see Figure I.2a). Coming to the 19th century, Michael Faraday prepared the famous gold sol in the laboratory. Based on his observations, he stated that "the divided state of the metal" was responsible for the various colors of the gold sol such as ruby, green and violet or blue unlike the yellow colour of the bulk gold (see Figure 1.2b) [6]. Thus, the history is abundant with the examples making use of intriguing properties of nanophenomenon in various fields such as fabrication of coloured glasses, photography, catalysis, etc [8].

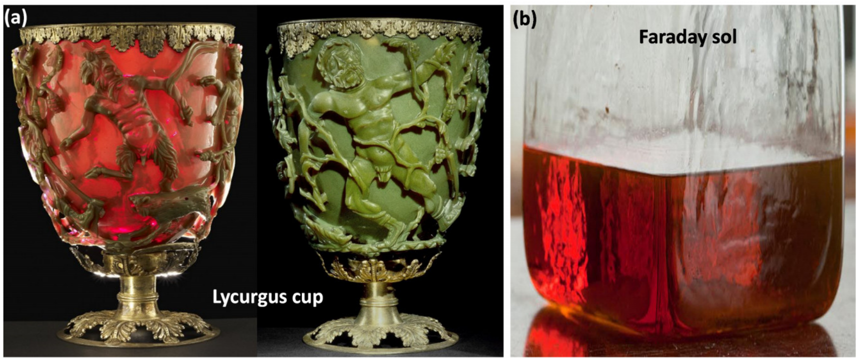

Figure I.2 Early examples of nanomaterials. (a) The apparent dichroism of Lycurgus cup towards the direction of light illumination and (b) gold sol prepared by Michael Faraday (adapted from refs. 6, 7).

The modern spirit of nanotechnology was started through the visionary talk by Richard Feynman when he stated in his lecture, "There's plenty of room at the bottom" [9]. In his pioneering speech, he emphasized on the creation, manipulation and controlling the things on the small scale. He justified his statement by illustrating biosystems which contain many functional elements in the nano regime [10]. He also suggested miniaturization by introducing the concept of nanotechnology in which the fabrication of nano-objects may be possible via top-down and bottom-up approaches.

The subsequent silicon revolution and micro-fabrication technology made a path towards the growth of nanotechnology field. The invention of scanning probe techniques (the 1980s), capable of imaging with atomic resolution besides the precise manipulation of nanostructures, allowed the researchers for understanding the nano processes. In brief, chemical and physical pathways for the synthesis of nanomaterials, the application of quantum mechanics for explaining the phenomenon at the nano and atomic world, detailed understanding of biological functions and developing powerful instrumentation resulted in the explosion of the nanoscience field as we see today [3, 4]. Eric Drexler has elaborated some of these ideas in his technical book of '*Nanosystems*' [11].

1.3 Criterion to be called as a nanomaterial

The first criterion for a material to be called as a nanomaterial is that at least one of its characteristic dimensions should be in the nanometric (1-100 nm) range [3, 4]. Besides having nanometric dimensions, the properties of a nanomaterial should be different when compared to its bulk counterpart. The characteristic dimension is the one that decides the properties of the nanomaterial.

I.4 Why are the properties of nanomaterials different compared to bulk?

As the size of a material goes down to nanometric dimensions and becomes comparable to the mean free path of electrons, the electrons get confined (bound system), and therefore its properties undergo a dramatic change. The confinement critically depends on the number of atoms and electrons, in contrast to the average properties arising from the large-scale periodic arrangement of atoms in the bulk state [12]. The properties of the macromaterials can be successfully explained based on classical laws whereas the properties and the phenomena at the atomic and molecular length scales can be explained only by principles of quantum mechanics. The properties of a material in nanoscale regime become size and shape dependent, primarily due to the large surface area to volume ratio and quantum confinement which are detailed below.

I.4.1 Surface area to volume ratio

As compared to the surface area available with a non-porous bulk cube, nanosized cubes of the same mass from the same material offer surface area which may be few thousand times of the former [13] (see inset of Figure I.3). Similarly, the surface area increases many orders of magnitude after chipping down the bulk material into nanometric dimensions, eventually ending up with a higher surface area to volume ratio as compared to its bulk counterpart. The variation of the fraction of surface atoms with the total number of atoms of a particle is shown in Figure I.3.

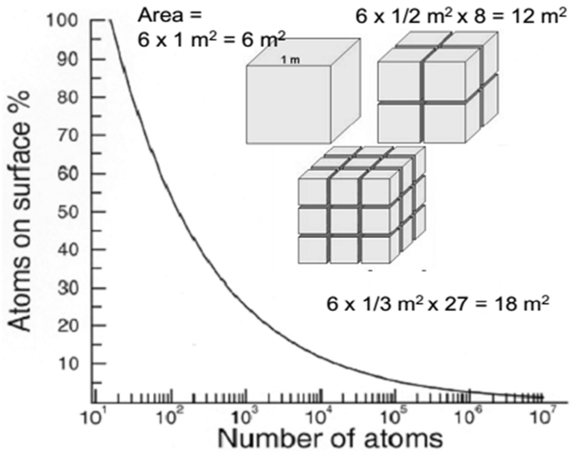

Figure I.3 Plot of variation in the percentage of atoms on the surface with respect to a total number of atoms in a particle (adapted from ref. 13).

The fraction of atoms on the surface of a particle (P_S, %) can be estimated using the following relation,

$$P_S = 4N^{-1/3} \text{x} 100 \ldots\ldots \text{(I.1)}$$

where N is the total number of atoms in the particle. The fraction of surface atoms becomes less than 1% only when the total number of atoms is in the order of 10^7, which for a typical metal would correspond to a particle diameter of 150 nm [14]. For smaller particles, there is a large fraction of atoms at the surface and thus, the average binding energy per atom is relatively high [15]. Moreover, the atoms have lower coordination number and unsatisfied dangling bonds resulting in less stabilized atoms at the surface. Thus, nanosize brings enormous surface area and increased reactivity for a material [16].

I.4.2 Quantum confinement

The bulk materials have extended energy band structures and as the size decreases, gaps start opening up in these bands. The spacing between the energy levels increases as we go further reducing the size, which can be described qualitatively using particle in a box model. The spacing between the energy levels is inversely proportional to the dimensions of the material (see the equation below).

$$\Delta E_n = (2n+1)h^2/8mL^2 \ldots\ldots\ldots\ldots(I.2)$$

where h is Planck's constant, m is the electron mass, L is the dimension of the material and n is the quantum number. For example, for a 1 mm conductor, the spacing is given by 4.5 x 10^{-12} eV while for 5 nm conductor, this corresponds to 0.179 eV. Thus, the energy quantization couldn't be noticed in the case of macroscopic conductors as the thermal energy of the electrons is in the order of 25 meV at room temperature [17].

In the case of atoms and molecules, the energy levels are quantized due to minimized interactions among them (hydrogen atoms and molecules), which is evident from spectroscopic studies. When the interactions are set in, the band structure starts evolving which leads to the extended band structures (as in metals or semiconductors). The contribution of electronic states by the atoms in a solid increases the width of the bands leading to the extended band structures in a solid. As the number of contributing atoms increases, the density of states (DoS) within a band increases proportionally. This evolution of band structure with size is shown in Figure I.4. The typical width of a band would be around a few eVs. The average spacing between consecutive energy levels is specified by the Kubo gap (δ), usually measured in terms of meV [14]. The magnitude of δ varies inversely with nuclearity (the number of atoms) and is given by the following equation

$$\delta = 4E_F/3n_e \ldots\ldots\ldots\ldots(I.3)$$

where, E_F is the Fermi level and n_e is the number of valence electrons.

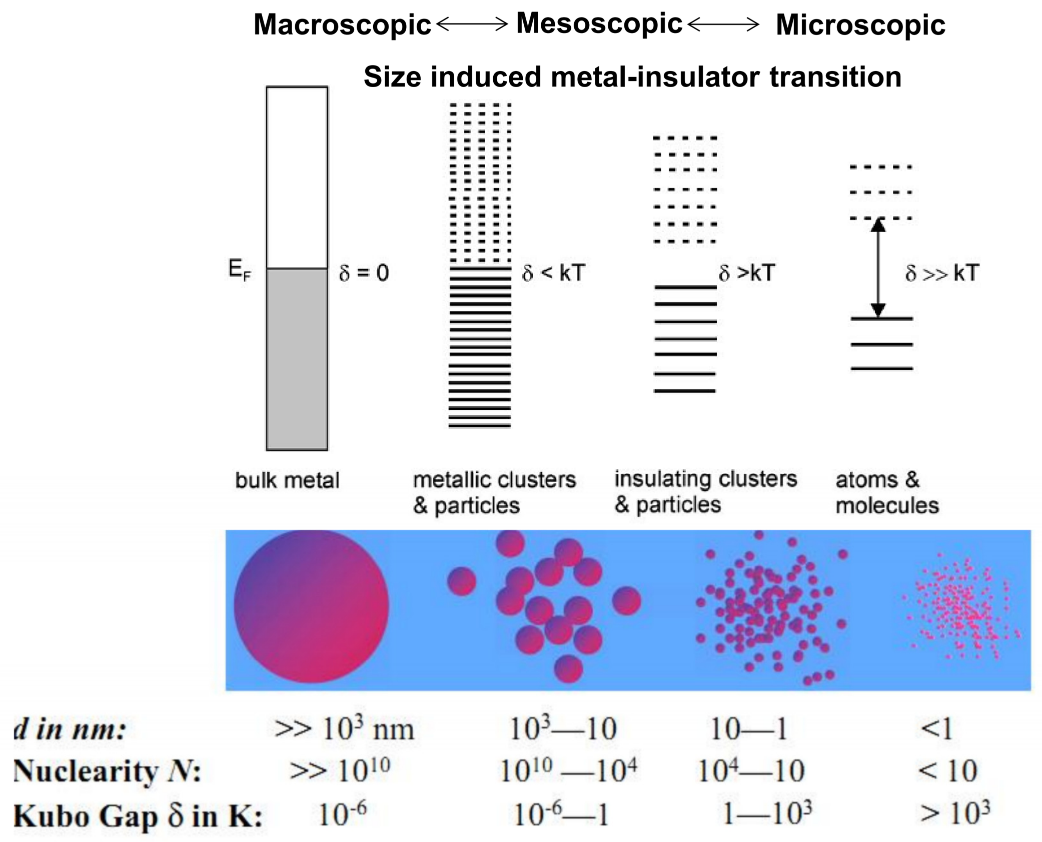

d in nm:	>> 10^3 nm	10^3—10	10—1	<1
Nuclearity *N*:	>> 10^{10}	10^{10} —10^4	10^4—10	< 10
Kubo Gap δ in K:	10^{-6}	10^{-6}—1	1—10^3	> 10^3

Figure I.4 Evolution of the band structure and the density of states with increasing number of atoms (from right to left) (reproduced from ref. 17).

I.5 Size-dependent properties

Due to the quantum confinement and surface effects, nanomaterials exhibit many interesting size-dependent properties. The change in a material property as a function of size is shown schematically in Figure I.5. At larger sizes, dependence on size is smooth and scaling laws can be derived to describe the variation in this regime [18]. At small sizes, however, the properties vary irregularly and are specific to each size. The size dependence [19] can be found in electronic, optical, magnetic, and chemical properties, few of which are mentioned in Table I.1.

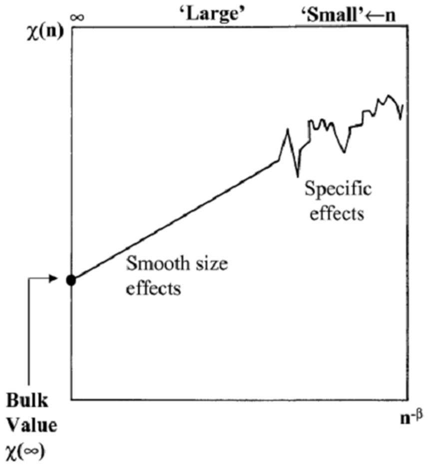

Figure I.5 The size dependence of a property $\chi(n)$ on the number of atoms (n) in a nanoparticle. The data is plotted against n β where $\beta \geq 0$ (reproduced from ref. 18).

Table I.1 List of various size dependent properties in nanomaterials (adapted from ref. 20).

Property	Influence of size reduction on properties of nanoparticle
Chemical	Increase of catalytic activity, kinetics of physicochemical interactions, change in solubility
Optical	Increase of absorption in UV range (blueshift), oscillation of optical absorption, nonlinearity in optical properties
Magnetic	Increase or decrease of coercive force, decrease of Curie temperature, an increase of paramagnetic in ferromagnetics, rise of giant magnetoresistance, rise of magnetic permeability in ferromagnetics
Thermal	Decrease of melting point, decrease of phase transition temperatures, decrease of melting entropy, softening of phonon spectra
Structural	Decrease or increase of lattice parameter, structure transformations
Electrical	Increase of conductivity of nanometals, onset of conductivity for nanodielectric, increase of dielectric inductivity for ferroelectrics
Electronic	Increase of band gap, arise of phonon generation, raising of conductivity under low temperatures
Thermo-dynamical	Increase of heat capacity, increase of thermal expansion, decrease of Debye temperature

I.6 Dimensionality in nanomaterials

According to Siegel (21, 22), nanomaterials can be classified into zero-dimensional (0D), one-dimensional (1D) and two-dimensional (2D) materials based on their characteristic dimensions where dimensions are in the nanometric regime. A 0D material is confined in all three dimensions (width, length, and thickness) with the characteristic dimensions of three. For 1D nanomaterial, confinement is in only two dimensions (width and diameter) with macroscopic third dimension (length). If the confinement is only in one dimension (thickness), the material is treated as 2D material where the length and width are of macroscopic dimensions. If there is no confinement in any one of the dimensions, the material is treated as a 3D material. However, a 3D material with nanometric pores and structures is also called as nanostructured material. For example, zeolites, porous carbons, and molecular sieves are 3D in nature but they have nanoscopic structures and pores. It is not just the overall size of the objects but it is about the internal length scale and associated dimensionality.

1.6.1 Dimensionality dependent properties

Dimensionality of a nanomaterial plays a key role in the control of electronic, optical and catalytic properties of nanostructured materials [23, 24]. The changes in the properties due to different dimensionality are not a result of scaling factors but originate from different causes in different materials.

I.6.2 Density of states (DoS) of nanomaterials

The density of states (DoS) of a system describes the number of states per interval of energy at each energy level that is available to be occupied by electrons [25]. A high DoS at a specific energy level means that there are many states available for occupation. A DoS of zero means that no states can be occupied at that energy level. In general, DoS is an average value of space and time domains occupied by the system. The DoS, $\rho(E)$, of a system varies with the dimensionality by the relationship

$$\rho(E) \approx E^{D/2-1} \text{........ (I.4)}$$

where, D is dimensionality of a system.

In 3D crystals as in the case of bulk materials, *ρ(E)* is a smooth square-root function at energy, E. The 2D and 1D nanomaterials show staircase and saw-tooth like DoS, respectively, while 0D nanomaterials show a δ-function like DoS (see Figure I.6). This sudden variation of density of states with a change of dimensionality imparts nanomaterials their interesting properties.

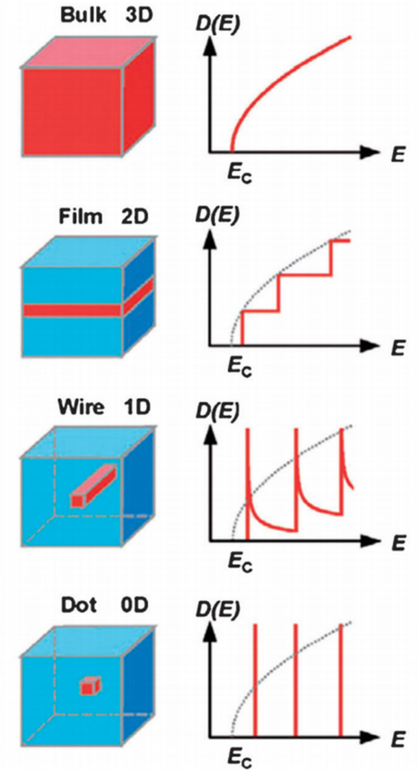

Figure I.6 The electronic density of states for a bulk semiconductor (3D), a quantum well (2D), a quantum wire (1D) and a quantum dot (0D) (adapted from ref. 26).

The relation between the DoS and the energy for 0D, 1D, 2D in comparison with the 3D is given in Table I.2.

Table I.2 DoS for materials of different dimensionalities

Structure	Dimensionality	Degree of confinement	DoS ($\rho(E)$)
Bulk Material	3D	0	$E^{1/2}$
Quantum Well	2D	1	1
Quantum Wire	1D	2	$E^{-1/2}$
Quantum Dot	0D	3	δE

1.6.3 Examples of nanomaterials having different dimensionality

Some important examples of nanomaterials based on dimensionality are given in Figure I.7.

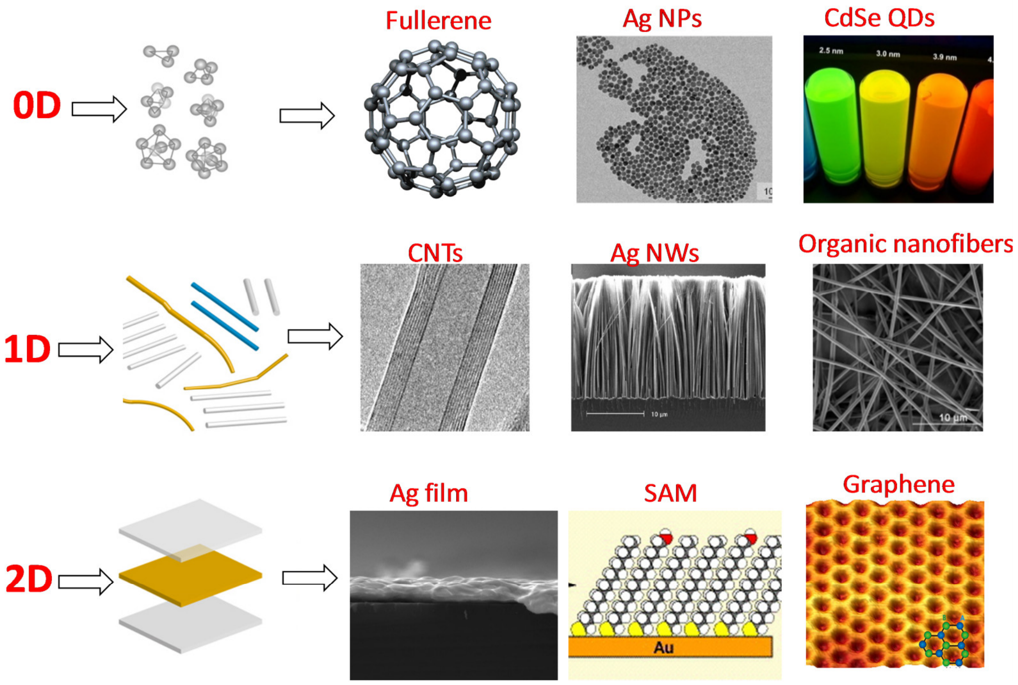

Figure I.7 Examples of nanomaterials with various compositions and dimensionalities (adapted from refs. 27-33).

0D nanomaterials

Fullerene, inorganic metal nanoparticles (NPs) and semiconductor quantum dots (QDs) form three main nanomaterials in 0D nanomaterials where confinement occurs in all three dimensions [27]. A fullerene is a carbon molecule in the form of a hollow sphere, ellipsoid or a tube. Spherical fullerenes are also called buckyballs, and they resemble a football (soccer). The examples of fullerene are C_{60}, C_{70}, C_{50} and C_{28} and their size is typically less than 1 nm. These molecules are known for superconductivity, heat resistance, and ferromagnetism. Ag and Au are typical examples of NPs where the size ranges from 1 to 100 nm and can be synthesized by various wet chemical methods. These NPs have been used extensively as anti-bacterial agents in the health industry, food storage, textile coatings and a number of environmental applications. Semiconducting QDs [28] with sizes below 100 nm exhibit quantum confinement. These have been implemented in a wide range of applications including solar cells, light-emitting diodes and bio-fluorescent tagging.

1D nanomaterials

Among all 1D nanomaterials, carbon nanotubes (CNTs), an allotrope of carbon, are the most studied one [29]. Single-walled nanotubes, double walled nanotubes, and multi-walled nanotubes are three classes of carbon nanotubes which show varied electrical conductivity like semiconducting or metallic. The diameter and length of a CNT can vary from 1to 300 nm and 500 nm to few tens of microns respectively. CNTs have been extensively used in various fields such as electrical circuits and devices, electrical cables and wires, actuators, batteries, solar cells, hydrogen storage, supercapacitor, radar absorption and textile etc. Metallic (Ag) and semiconducting (Si, ZnO) nanowires are another 1D nanomaterial which is extensively studied and used in various applications [30]. Recently, organic based nanowires and nanofibres have been explored which have properties that can be easily modified by chemical functionality. More descriptions of organic nanofibre are explained in later section.

2D nanomaterials

The metal thin films, prepared by vacuum evaporation techniques, were the first studied 2D nanomaterials exhibiting very interesting optical and thermal properties, with increased conductivity compared to bulk [31]. Self-assembled monolayers (SAMs) of organic molecules are another class of 2D nanomaterial which are molecular assemblies formed by spontaneous adsorption on surfaces. SAMs are an inexpensive and versatile surface coating for applications including control of wetting and adhesion, chemical resistance, biocompatibility, sensitization, and molecular recognition for sensors [31]. Last decade has witnessed the exponential rise of 2D layered nanomaterials like graphene, transition metal dichalcogenides like MoS_2, WS_2, $MoSe_2$ etc. with a range of outstanding properties and applications [32, 33]. The unique properties and applications of graphene are explained separately in the section.

In the following sections, some important nanomaterials are described.

I.7 Organic 1D nanostructures

1D organic nanowires (ONWs) prepared from π-conjugated small molecules and polymers have attracted a lot of interest due to their excellent physical and electrical properties [34] with added advantages of easy fabrication, low cost, high throughput, compatibility with flexible substrate etc. [35.] Many interesting possibilities exist in these organic structures such as π–π conjugation [36] and tenability of charge transport according to the molecular packing orientation [34]. In the literature, highly-efficient devices have been reported which include transistors, light-emitting devices, energy harvesting devices, waveguide etc. (see Figure I.8). Methods such as solution-phase self-assembly, template-assisted method, soft lithography, electro-spinning etc. have been successfully employed to have nanowires on the active area of the device.

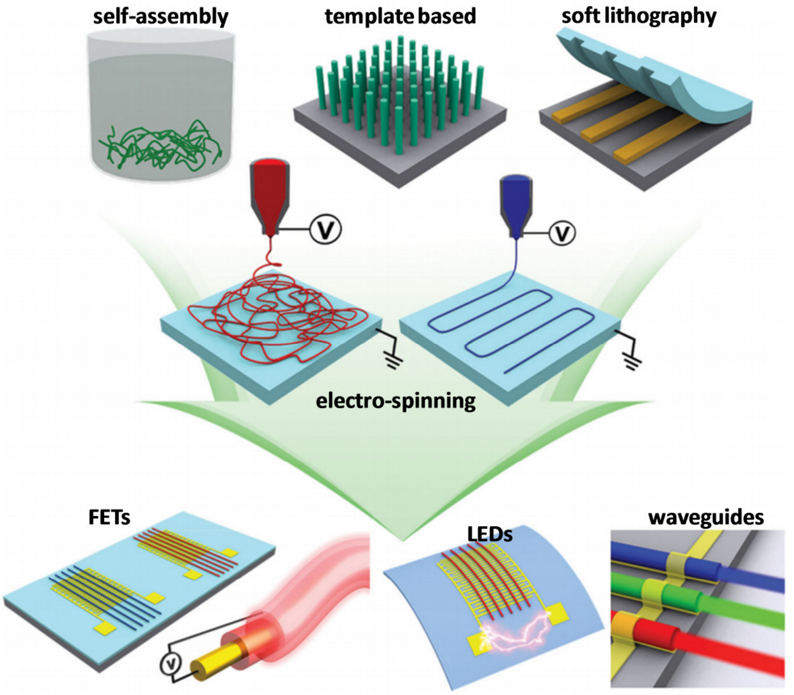

Figure I.8 Methods to prepare ONWs (self-assembly, template based, soft lithography, electro-spinning) and its optoelectronic device applications (FETs, LEDs, energy harvesting devices, waveguide etc.) (adapted from ref. 35).

Supramolecular approach to construct organic 1D nanostructures

Supramolecular chemistry: Supramolecular chemistry is a term introduced by Prof. Jean-Marie Lehn [37]. It is 'chemistry beyond the molecule' i.e. the chemistry of molecular assemblies using non-covalent interactions such as hydrogen bond, dipole-dipole, π-π interactions, van-der-Waals forces, hydrophobic effects etc. whose bond strength is in the order of 5 – 50 kJmol^{-1} (see Table I.3). The strengths of these non-covalent interactions are lower than that of covalent interactions; as a result, supramolecular assemblies are reversible, less stable, more labile, and more flexible than the conventional organic polymers. Supramolecular assemblies result from a spontaneous association of smaller units, possess well-defined microscopic organization and can have various macroscopic morphologies such as films, layers, membranes, micelles, vesicles, etc.

Table I.3 Strength of several non-covalent interactions (green region) compared with other interactions (adapted from refs. 37, 38).

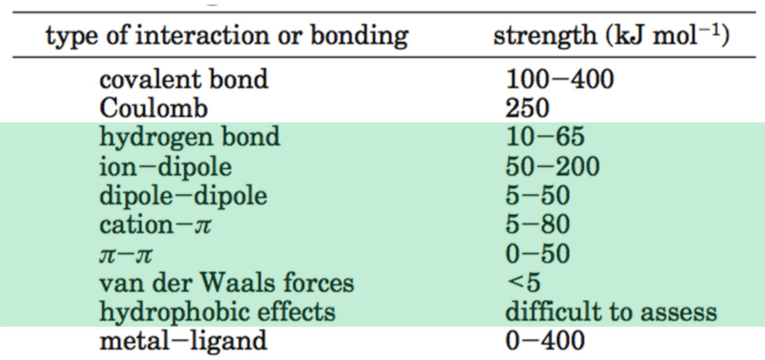

type of interaction or bonding	strength (kJ mol^{-1})
covalent bond	100−400
Coulomb	250
hydrogen bond	10−65
ion−dipole	50−200
dipole−dipole	5−50
cation−π	5−80
$\pi-\pi$	0−50
van der Waals forces	<5
hydrophobic effects	difficult to assess
metal−ligand	0−400

Supramolecular assemblies formed by self-assembly of π-conjugated systems with the length scale 5–100 nm offers an excellent tool to construct wires of electronic components in the nanometric range [39]. This field is called as 'supramolecular electronics' which bridges the gap between 'molecular electronics' and bulk or 'plastic' electronics (see Figure I.9). In the field of molecular electronics, the properties of single molecules are investigated on the Angstrom length scale and simple device structures have been demonstrated. However, realizing its applications in practical devices is hampered by orientational and conformational changes of the molecule with the thermal noise and challenges in making contact between the molecule and electrode.

On the other hand, polymer electronics is a well-established field where properties of polymers in micrometre length scale have been explored. They take advantage of easy preparation and solution processability, flexibility, energy friendly, cheap, and compatible with downscaling with miniaturization. However, these materials show limitations in the precise ordering of their crystalline layers in the bulk, thus impacting the mobilities of charge carriers required for the excellent device performance. Though recrystallization is possible in these polymers giving single crystals, processability for devices becomes impractical. Besides, the ambient stability of these organic polymers is another major issue.

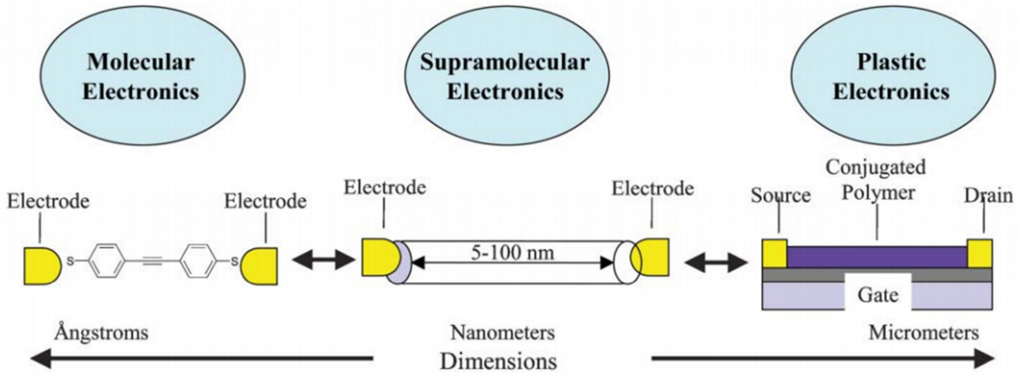

Figure I.9 Schematic representation illustrating the gap between molecular electronics and plastic electronics. Supramolecular electronics bridges the gap between the two with the aim of constructing and investigating supramolecular optoelectronic nanoarchitectures that are hooked up to electrodes (adapted from ref. 39).

Supramolecular assembly is an attractive and efficient bottom-up strategy to build self-assembled nanostructures with the dimensions of 5–100 nm and yields relatively soft functional objects while introducing “pseudo-crystalline” electro-active domains. Essentially, it bridges the gap between single molecular electronics and polymer electronics [39]. Using this approach, supramolecular assemblies such as gels, liquid crystals, soft nanoribbons, nanotubes, nanorods, and nanowires of low dimensionality have been made to have desired electronic functionality.

Supramolecular 1D assembly: Using supramolecular self-assembly, it is possible to design 1D nanowires and nanofibres (bundle of nanowires) for desired electronic functionality. Many supramolecular design rules have been introduced [40] and several synthetic approaches have been explored to fabricate these 1D nanostructures from almost any π-conjugated system. Such conducting self-assemblies used for electronic device applications are mainly made from the following chemical compositions [41, 42] i.e. a) aromatic π-stacks, b) light-responsive triarylamine π-stacks, c) supramolecular charge transfer nanostructures.

a) Conducting self-assemblies made of aromatic π-stacks: Among various methods to construct 1D nanostructures, self-assembled planar π-conjugated organic molecules in solution have proven to be a powerful bottom-up strategy, thanks to the dominance of π–π stacking over hydrophobic forces [41]. For example, an organic nanotube can be constructed using hexa-*peri*-hexabenzocoronene (HBC), similar to a carbon nanotube (see Figure I.10). This nanotube reveals a conducting I/V profile with an ohmic behavior but at the same time, its conductivity decreased as temperature is lowered to 150 K, demonstrating the semiconducting character of the nanotube.

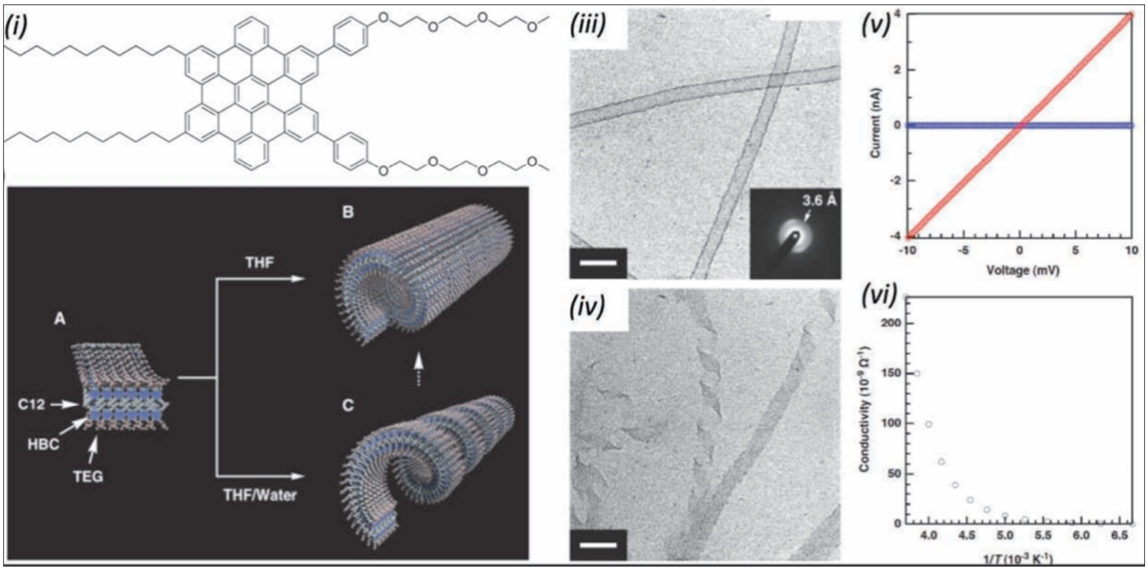

Figure I.10 (i) Schematic molecular structure of amphiphilic HBC, (ii) Schematic illustration of a proposed mechanism for the formation of a supramolecular graphitic nanotube, (iii) TEM image of self-assembled amp-HBC. Scale Bar: 50 nm, (iv) TEM image of self-assembled amp-HBC, obtained as a suspension in water-containing THF. Bar: 50 nm, (v) I/V profiles of unoxidized (blue circles) and oxidized (red circles) single nanotubes at 285 K, (vi) Conductivities of an oxidized single nanotube of amp-HBC at 270–150 K (reproduced from ref. 41).

b) Light-responsive triarylamine π-Stacks: Triarylamine (TAA^{-}) based molecules have been used as active materials in optoelectronic devices such as organic light-emitting diodes, organic solar cells, and organic field-effect transistors [41]. It was demonstrated that a simple irradiation by visible light can generate a non-covalent polymerization leading to supramolecular triarylamine nanowires (STANWs) (Figure I.11). This process occurs by the highly synergetic phenomenon that starts with the formation of a catalytic quantity of triarylammonium radicals (TAA•+) when excited by light, the chlorinated solvent being the electron acceptor. This radical can in turn form a CT complex with its neutral counterpart, and subsequently continue the elongation by combining charge transfer, hydrogen bonding, and π–π stacking for the primary growth, as well as hydrogen bonding and van der Waals interactions for the secondary growth. This leads to the aggregation of several columnar fibrils in larger and stiffer fibers (typically 10 – 50 nm in width and 50 – 1,000 nm in length) (see Figure I.11).

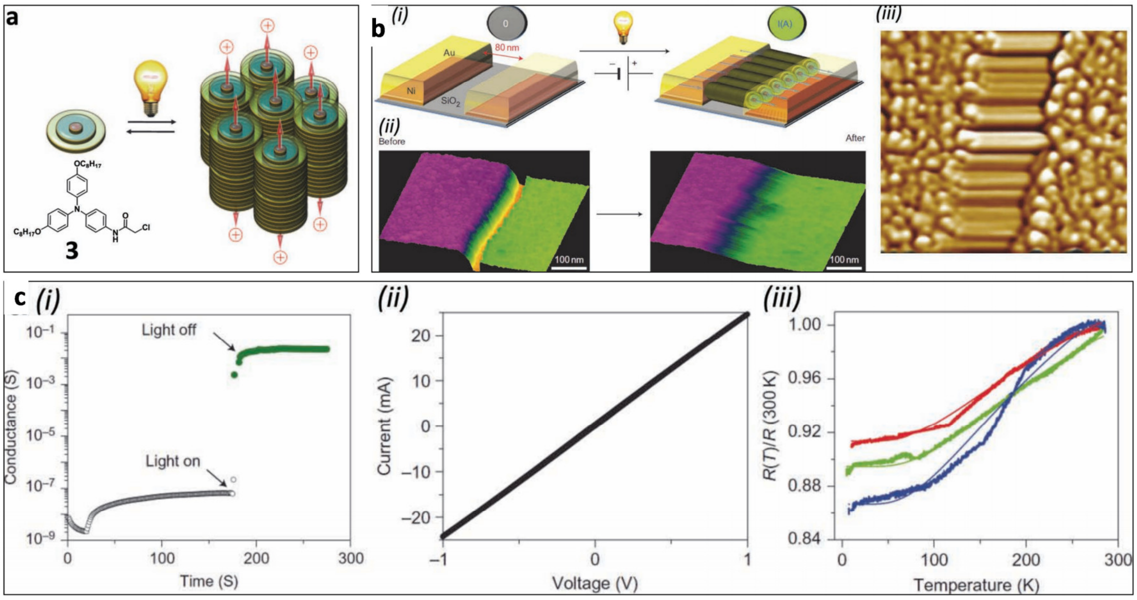

Figure I.11 (a) Hierarchical self-assembly processes that occur upon irradiation of the neutral triarylamine 3; (b) (i) Process of formation of STANWs. (ii) Left: topography of the opened gap seen by AFM before light irradiation. Right: topography of the closed gap filled with STANWs after light irradiation, (iii) AFM zoom into the gap. (c) (i) Conductance measured for the evice as a function of time, (ii) Related *I/V*, (iii) Normalized R(T) measurements of three independently prepared STANWs-functionalized devices (adapted from ref. 41).

c) Supramolecular charge transfer nanostructures: Designing of aromatic π-conjugated donor (D) and acceptor (A) molecules to build conducting 1D nanostructure has gained much attention in the recent past [42]. Particularly, a mixed stack of charge transfer, CT (MS-CT) assemblies, in which D and A molecules are alternately arranged (see Figure I.12a), have emerged as an attractive candidate as an active element in organic electronics. This is mainly due to the presence of (CT) interaction between D and A molecules [42] which generate inherent dipole moment responsible for 1D conduction in the system. The CT assemblies are known since a long time, beginning with the metallic conducting properties in CT crystals of TTF and TCNQ, followed by the discovery of superconductivity in these organic materials. Recently, novel ambipolar charge-transport and room temperature ferroelectricity and multiferroic are reported in this mixed CT donor–acceptor assemblies, which open up new areas of future research (see Figure I.12).

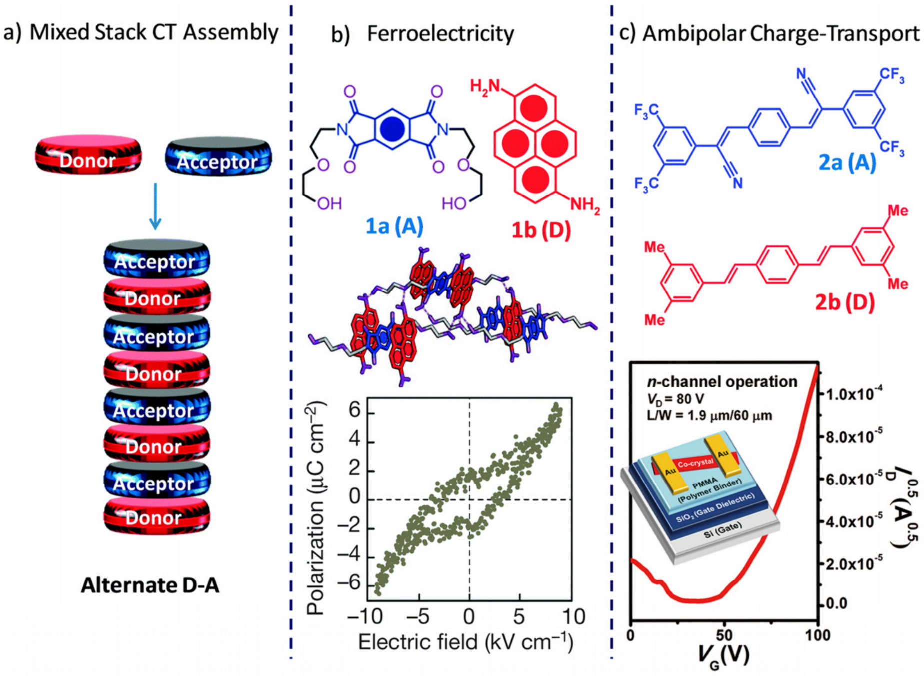

Figure I.12 Prospects of mixed stack charge transfer (MS-CT) assemblies. (a) Schematic representation of alternately stacked donor and acceptor molecules in an MS-CT assembly. (b) Room-temperature organic ferroelectricity exhibited by the 1a–1b co-crystal. (c) Ambipolar charge-transport observed in MS-CT co-crystal of 2a–2b (reproduced from ref. 42).

1.8 Graphene

Graphene is considered as the mother of all graphitic forms. It can be wrapped into a fullerene, rolled into a CNT (1D material) and stacked together to form 3D graphite (see Figure I.13). Initially, it was thought that the 2D materials are unstable due to Peierls instability and cannot be isolated. But in 2004, A. K. Geim and K. Novoselov from Manchester University successfully [43-45] isolated the graphene using scotch tape technique. They won the Nobel Prize in physics in 2010 for their groundbreaking experiments on this wonder 2D material.

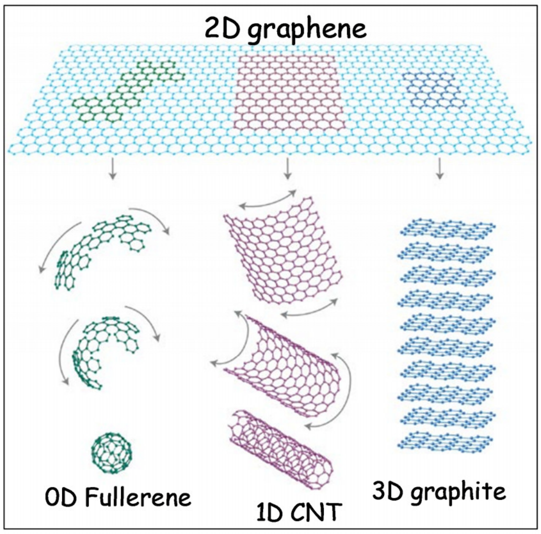

Figure I.13 Mother of all graphitic forms. Graphene is a 2D building block for carbon materials of all other dimensionalities. It can be wrapped up into 0D buckyballs, rolled into 1D nanotubes or stacked into 3D graphite (reproduced from ref. 43).

Unique properties of graphene: Graphene is a semi-metal with zero band gap. It was in 1947, Wallace [46] found that dispersion relation of graphene is linear for low energies near the six corners of the two-dimensional hexagonal Brillouin zone, leading to zero effective mass for electrons and holes (see Figure I.14). Due to this, electrons and holes near these six points, behave like relativistic particles which can clearly be described by the Dirac equation for Fermions. Hence, the electrons and holes are called Dirac Fermions which obey Dirac equation with a Fermi velocity $V_F \sim 10^6$ m/s, and the six corners of the Brillouin zone are called the Dirac points. Graphene exhibits ambipolar electric field effect and absorbs only 2.3% of the incident visible light. Graphene also exhibits the quantum Hall effect. It is mechanically stiff and chemically inert. Thus, due to its intriguing electronic and optoelectronic properties, graphene has become a hot topic of research during the last decade.

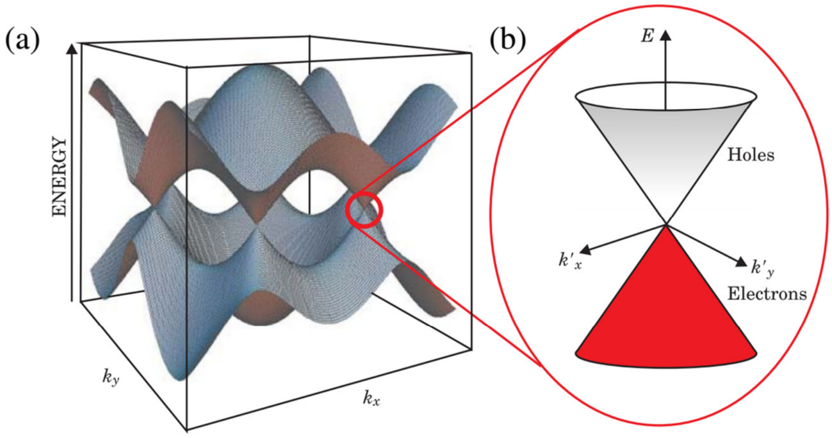

Figure I.14 The band structure of graphene in the honeycomb lattice. The enlarged picture shows the conical band structure close to one of the Dirac points (reproduced from ref .47).

Graphene synthesis: There have been many methods to synthesize single and few/multilayer graphene (see Figure I.15) [48]. These synthetic methods are majorly based on following four types i.e. a) exfoliation of graphite b) chemical methods, c) epitaxial growth of graphene on SiC and d) CVD methods. All these methods are associated with their pros and cons in terms of quality of graphene obtained and cost involved in synthesis. The earliest method, mechanical exfoliation of graphene from highly oriented pyrolytic graphite (HOPG) using Scotch tape, yields good quality, but μm-sized graphene [49]. In addition, it is uncontrollable and not scalable. Other formation techniques, such as epitaxial graphene from a single crystalline SiC substrate [50-54] or transition metals [55-60] can yield good quality graphene domains. However, they encounter difficulty in large-scale production due to high cost of the substrates, the requirement of ultrahigh vacuum, and limited scalability. For applications to utilise the extraordinary properties of graphene, one would require defect-free and uniform graphene on a large scale. Recently, chemical vapour deposition (CVD) technique has been developed by which high-quality [61-65] monolayer and bilayer graphene was obtained via catalytic dehydrogenation of carbon precursors (mostly CH_4 or C_2H_2 gases) in the presence of a metal (like Cu and Ni) heated to ~ 1000 °C in an inert atmosphere. Commercial wafer-scale {66] and 30 inches graphene films [67] have been reported using this method. Currently, CVD technique is widely employed and has great potential for the large-scale production of high-quality films [68-75]. Plenty of modified CVD techniques [76-80] are also in the recent, which majorly vary in the heating techniques with aim to reduce the time consumption in the CVD process.

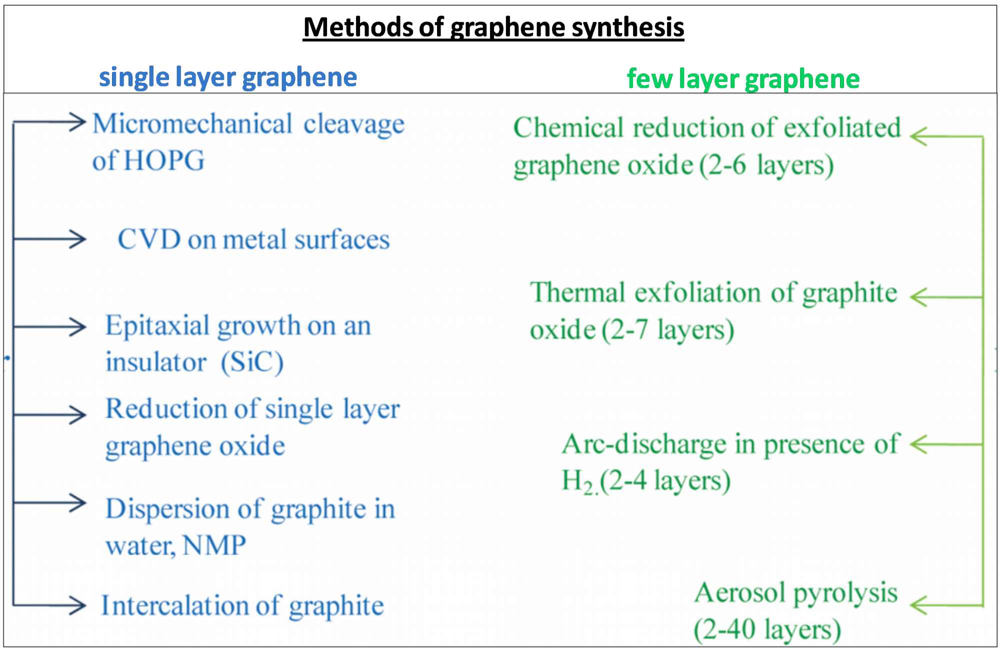

Figure I.15 Different methods of graphene synthesis (reproduced from ref. 48).

Raman spectroscopy of graphene: Raman spectroscopy has become an important structural and electronic characterization tool for various carbon materials, as Raman signal is sensitive to local changes in bonding and molecular morphology [81]. In case of graphene, it can provide information about sp^2 crystallite size, the presence of sp^2-sp^3 hybridization, doping effects, edge structure, strain, the number of graphene layers, and the metallic vs. semiconducting behavior [82]. The π-electrons of the sp^2carbon can easily be polarized by visible photons which make the Raman technique sensitive to sp^2 sites. It is a very sensitive and versatile tool for knowing about defects, stacking and finite sizes of crystallites parallel or perpendicular to the hexagonal axis of graphene. Raman spectroscopy is also sensitive to disorder in *sp*^{2} carbon lattice. In graphene-related materials, Raman spectrum predominantly consists of three peaks which are named as D, G and 2D bands (see Figure I.16) [82].

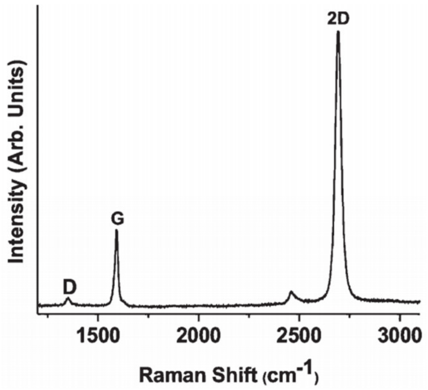

Figure 1.16 Raman spectrum of graphene (obtained from ref. 82)

D band: It is also called as defect band, which arises due to the breathing motion of six atom rings and requires a defect for its activation (see Figure I.17). Any phonon mode satisfying k = q/2 (where k is the wave vector for the electronic transition excited by incident photon and q is the phonon wave vector) condition gives rise to the D peak with A_{1g} symmetry involving phonons near the k zone boundary. This mode is forbidden in perfect graphite and only becomes active in the presence of disorder. Typically, D band position is found to be at 1350 cm^{-1} and it changes with excitation energy. The dispersion of D band is proportional to the order in the *sp*^{2} carbon lattice. The intensity and integrated area of D band reveal the presence of disorders such as defects, grain boundaries, and functional groups in the *sp*^{2} carbon lattice. Hence lower the D band; higher is the electronic quality of the graphene lattice.

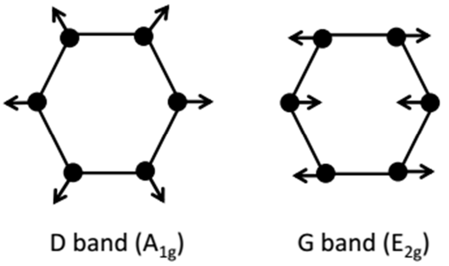

Figure I.17 Schematic representation of D and G bands

G band: It is also called the graphitic band and arises due to in-plane bond stretching motion of pairs of *sp*^{2} carbon atoms (see Figure I.15). G band doesn't require the presence of six-fold rings unlike D band and it occurs at all *sp*^{2} sites. The position of G band is at 1585 cm^{-1} (see Figure I.15), and it is related to the zone center phonons with E_{2g} symmetry. G band doesn't disperse in graphitic samples and disperses in more disordered carbon i.e. dispersion is proportional to the degree of disorder. The position and FWHM of the G band change with increasing number of defects in the graphitic systems.

2D band: It is the overtone of the D band and reveals the stacking order and periodicity along the c-axis. Though D band is absent in some of the locations of graphite sample, 2D band is always seen. The position of the 2D band is at ~ 2700 cm^{-1} (see Figure I.18a), which arises due to the non-centre zone boundary phonons and its origin can be explained by double resonance Raman phenomenon. The position and shape of the 2D band give the information about the number of layers and type of stacking. For a single layer, 2D band is a single, sharp Lorentzian peak with FWHM ~ 30 cm^{-1}. FWHM and number of peaks of 2D band increase with the number of layers (see Figure I.18a). As the disorder in the *sp*^{2} lattice increases, one-phonon assisted D band processes increase more compared to the two-phonon assisted 2D band processes. This competition between Raman allowed and defect induced peaks leads to the decreasing intensity of the 2D band at the cost of increasing D band intensity [83].

I_D/I_G ratio: This ratio is a measure of defects in any graphene. The ratio is also proportional to the abundance of *sp*^{2} carbon cluster area. This ratio gives us the in-plane crystallite size (L_a) of the *sp*^{2} carbon lattice which is given by

$$L_a(\text{nm}) = 560/E^4_{\text{laser}}(I_D/I_G)^{-1}\ldots\ldots\ldots(\text{I.3})$$

where E_{laser} is the laser excitation energy in eV. Typical I_D/I_G ratio for high-quality graphene is in the order of 0-0.05, whereas defected graphene samples have 0.5-2.

I_{2D}/I_G ratio: This ratio provides us the number of graphene layers. For a single layer, the ratio is in the range of 2-4, FWHM of the 2D band is 25-35 cm^{-1} and 2D band position is at ~ 2685 cm^{-1}. For few and multi-layer samples, the ratio is in the range of 0.5-2, with an increase in the FWHM to 50 cm^{-1} and beyond, the position of 2D band will be up shifted to 2700 cm^{-1} as compared to the single layer [84].

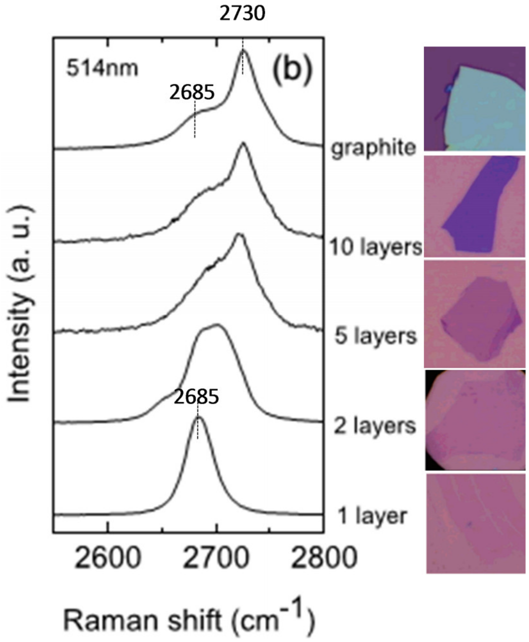

Figure I.18 Shape of 2D band with a number of layers. The right side panel is the optical microscope images of the graphene transferred onto the SiO_2/Si substrate (obtained from ref. 83).

Turbostratic Graphite: The way in which the graphene layers are stacked with each other, the graphite material can be classified broadly into two categories. The Bernal stacked graphite (AB stacking) has the registry of the carbon atoms in the top and bottom graphene layers. In the case of turbostratic graphite, a rotational disorder in the stacking sequence of the graphene layers is observed, which leads to the electronic decoupling among the graphene layers leading to increased interlayer spacing from 3.35 Å to 3.42 Å (see Figure I.19). Raman spectroscopy is a good tool for finding the stacking of the graphitic layers along the c-axis. The shape of the 2D band indicates the stacking order of the graphite layers along the c-axis. It exhibits a single Lorentzian 2D band with typical FWHM of 80-100 cm^{-1}. Typically, in the case of turbostratic stacking, the FWHM of 2D band is at least 20-30 cm^{-1} higher as compared to the Bernal type of stacking for a given number of layers. The 2D band of single layer graphene and turbostratic graphite look similar whereas Bernal stacked graphite exhibits 2D band with left shoulder peak (see Figure I.19b).

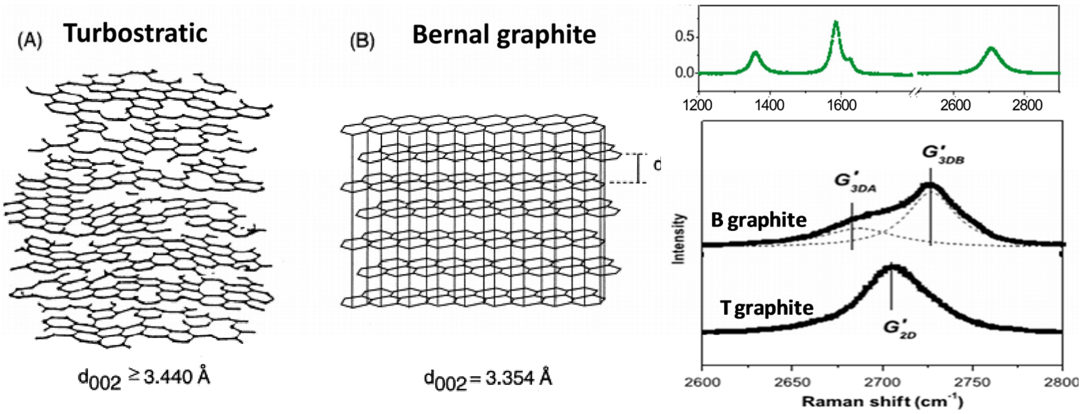

Figure I.19 A schematic representation of the structure of turbostratic graphite as compared to a 3D Bernal-stacked graphite lattice. The right panel is the Raman spectrum of turbostratic graphite (top) and shape of 2D band comparison between two types of graphites (obtained from ref. 85).

1.9 Scope of the thesis

Material properties controlled by dimensionality are increasingly attracting attention in the recent literature [section 1.6]. In the present thesis, two case examples have been chosen for detailed study. As an example of 1D system, supramolecular conducting nanofibres have been considered and for 2D, a graphene related system has been investigated, importantly, both from altogether different standpoints. The first part of the thesis deals with designing of 1D organic nanofibre by the supramolecular self-assembly of π-conjugated organic molecules and exploring their properties and applications. As there are limited results in the literature relating to supramolecular systems in devices (see section IIIA.1), this study is indeed considered worthwhile. While graphene and derivatives have been well studied in the last decade [see section 1.8], a truly intrinsic graphene has been only a theoretical possibility (see section IVC.2.1). The second part of the thesis explores a type of graphene with properties close to the intrinsic one. Specifically, it deals with the preparation of randomly stacked decoupled graphene with high 2D crystallinity and unusual properties. The field of twisted graphene is an upcoming area and this study is considered highly relevant.

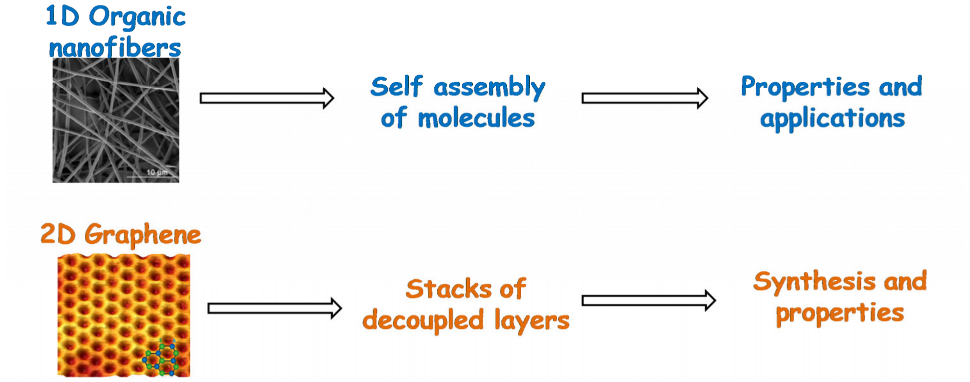

Figure I.20 Scope of the thesis.

References

1. http://www.nano.gov/nanotech-101/what/nano-size

2. Nature Nanotechnology **1**, 8 - 10 (**2006**), doi:10.1038/nnano.2006.77

3. G. L. Hornyak, J. J. Moore, H. F. Tibbals and J. Dutta, Fundamentals of Nanotechnology, CRC Press, Boca Raton, FL, **2008**.

4. Pradeep et al., A textbook of Nanoscience and Nanotechnology, Tata McGraw Hill Education pvt Ltd, New Delhi, **2013**.

5. S.M. Lindsay, Introduction to Nanoscience, Oxford University Press, **2009.**

6. http://www.rigb.org/our-history/iconic-objects/iconic-objects-list/faraday-gold-colloids

7. The British Museum Press, London.

8. M. Haruta, Nature, **2005**, 437, 1098.

9. R. P. Feynman, Caltech Engineering and Science 23, (**1960**) 22.

10. P. Feynman, J. Microelectromechanical Systems, **1992**, 1, 60.

11. K. E. Drexler, Nanosystems: Molecular Machinery, Manufacturing, and Computation, Wiley, New York, **1992**.

12. P. P. Edwards, R. L. Johnston, and C. N. R. Rao, in Metal Clusters in Chemistry (L.A.O. P. Braunstein, P. R. Raithby, ed.) Wiley, Weinheim, **1999**.

13. C. N. R. Rao, and A. K. Cheetham, Science, and technology of nanomaterials: Current status and future prospects, J. Mater. Chem. 11 (**2001**), 2887.

14. D. B. Strukov, G. S. Snider, D. R. Stewart and R. S. Williams, Nature, 453 (**2008**) 80.

15. Emil Roduner, Chem. Soc. Rev. 35 (**2006**), 583.

16. Bond, G. C., Heterogeneous catalysis. **1987**; Pages: 176.

17. Roduner, Emil. "Size matters: why nanomaterials are different." Chemical Society Reviews 35. 7 (**2006**): 583-592.

18 C. N. R. Rao, P. J. Thomas and G. U. Kulkarni, eds., Nanocrystals: synthesis, properties, and applications, Springer, Heidelberg, **2007**.

19. Quantum effect: QED: R. P. Feynman, The Strange Theory of Light and Matter, ISBN: 978069102417.

20. V.V. Pokropivny, V.V. Skorokhod, New dimensionality classifications of nanostructures Physica E 40 (**2008**), 2521–2525.

21. Siegel, R.W. **1994**. Nano phasematerials. In Encyclopedia of applied physics, Vol. 11, G.L. Trigg, ed. Weinheim VCH, 1-27.

22. J. A. García-Calzón and M.E. Díaz-García, TrAC Trends in Analytical Chemistry, **2012**, **35**, 27.

23. Achtstein et al. Electroabsorption by 0D, 1D, and 2D Nanocrystals: A Comparative Study of CdSe Colloidal Quantum Dots, Nanorods, and Nanoplatelets ACS Nano 8, 8, **2014**, 7678–7686.

24. Man-Fai Ng and R. Q. Zhang Dimensionality Dependence of Optical Properties and Quantum Confinement Effects of Hydrogenated Silicon Nanostructures J. Phys. Chem. B **2006**, 110, 21528-21535.

25. Walter Ashley Harrison, Electronic Structure and the Properties of Solid, (**1989**).

26. Bimberg, Dieter, and Udo W. Pohl. "Quantum dots: promises and accomplishments." Materials Today, 14, 9. 2011, 388.

27. Guozhong Cao, Nanostructures & Nanomaterials: Synthesis, Properties & Applications, **2003.**

28. C. B. Murray, D. J. Norris, M. G. Bawendi Synthesis and characterization of nearly monodisperse CdE (E = sulfur, selenium, tellurium) semiconductor nanocrystallites J. Am. Chem. Soc., **1993**, 115, 8706.

29. Iijima, Sumio, and Toshinari Ichihashi. "Single-shell carbon nanotubes of 1-nm diameter." (**1993**): 603-605.

30. Xia, Younan, et al. "One-dimensional nanostructures: synthesis, characterization, and applications." Adv. Mat. **2003,** 15, 353.

31. Novoselov, Kostya S., et al. "Electric field effect in atomically thin carbon films." Science, 2004, 5696, 666.

32. Hua Zhang Ultrathin Two-Dimensional Nanomaterials ACS Nano, **2015**, 9, 9451.
33. Z. Yin, H. Li, H. Li, L. Jiang, Y. Shi, Y. Sun, G. Lu, Q. Zhang, X. Chen and H. Zhang, ACS Nano, **2012**, **6**, 74-80.

34. Ling Zang, Yanke Che, and Jeffrey Moore One-Dimensional Self-Assembly of Planar **π**-Conjugated Molecules: Adaptable Building Blocks for Organic Nanodevices Accounts Of Chemical Research 41, 12, **2008**, 1596-1608

35. Sung-Yong Min , Tae-Sik Kim , Yeongjun Lee , Himchan Cho , Wentao Xu ,and Tae-Woo Lee Organic Nanowire Fabrication and Device Applications small **2015**, 11, No. 1, 45–62

36. Felix Sunjoo Kim, Guoqiang Ren, and Samson A. Jenekhe One-Dimensional Nanostructures of π-Conjugated Molecular Systems: Assembly, Properties, and Applications from Photovoltaics, Sensors, and Nanophotonics to Nanoelectronics Chem. Mater. **2011**, 23, 682–732.

37. Freek J. M. Hoeben, Pascal Jonkheijm, E. W. Meijer, and Albertus P. H. J. Schenning About Supramolecular Assemblies of π-Conjugated Systems Chem. Rev. **2005,** 105, 1491 1546.

38. Lehn, J.-M. Science **2002**, 295, 2400-2403.

39. Albertus P. H. J. Schenning and E. W. Meijer Supramolecular electronics; nanowires from self-assembled p-conjugated systems Chem. Commun., **2005**, 3245–3258.

40. T. Aida, E. W. Meijer, S. I. Stupp Functional Supramolecular Polymers Science 17, **2012**, 335.

41. Emilie Moulin , Juan-José Cid , and Nicolas Giuseppone Advances in Supramolecular Electronics – From Randomly Self-Assembled Nanostructures to Addressable Self-Organized Interconnects Adv. Mater. **2013**, 25, 477–487.

42. Mohit Kumar, K. Venkata Rao, and Subi J. George Supramolecular charge transfer nanostructures Phys. Chem. Chem. Phys., **2014**, 16, 1300—1313.

43. A. K. Geim and K. S. Novoselov, Nat. Mat., **2007**, **6**, 183.

44. K. S. Novoselov, A. K. Geim, S. V. Morozov, D. Jiang, Y. Zhang, S. V. Dubonos, I. V. Grigorieva and A. A. Firsov, Science, **2004**, 306, 666.

45. V. P. Gusynin and S. G. Sharapov, Phys. Rev. Lett., **2005**, 95, 146801.

46. P. R. Wallace, Phys. Rev., **1947**, 71, 622.

47. A. H. Castro Neto et al The electronic properties of graphene, 81, 2009

48. C. N. R. Rao, A. K. Sood, Rakesh Voggu, and K. S. Subrahmanyam Some Novel Attributes of Graphene J. Phys. Chem. Lett. **2010**, 1, 572–580.

49. K. S. Novoselov, A. K. Geim, S. V. Morozov, D. Jiang, Y. Zhang, S. V. Dubonos, I. V. Grigorieva, and A. A. Firsov, Science 306, 666 (**2004**).

50. C. Berger, Z. M. Song, X. B. Li, X. S. Wu, N. Brown, C. Naud, D. Mayou, T. B. Li, J. Hass, A. N. Marchenkov, E. H. Conrad, P. N. First, and W. A. de Heer, Science 312, 1191 (**2006**).

51. J. Kunc, Y. Hu, J. Palmer, C. Berger, and W. A. de Heer, Appl. Phys. Lett. 103, 201911 (**2013**).

52. H. Fukidome, Y. Kawai, F. Fromm, M. Kotsugi, H. Handa, T. Ide, T. Ohkouchi, H. Miyashita, Y. Enta, T. Kinoshita, Th. Seyller, and M. Suemitsu, Appl. Phys. Lett. 101, 041605 (**2012**).

53. K. V. Emtsev, A. Bostwick, K. Horn, J. Jobst, G. L. Kellogg, L. Ley, J. L. McChesney, T. Ohta, S. A. Reshanov, J. Rohrl, E. Rotenberg, K. S. Andreas, W. Daniel, B. W. Heiko, and S. Thomas, Nat. Mater. 8, 203 (**2009**).

54. C. Virojanadara, M. Syv€ ajarvi, R. Yakimova, L. I. Johansson, A. A. Zakharov, and T. Balasubramanian, Phys. Rev. B: Condens. Matter 78, 245403 (**2008**).

55. P. W. Sutter, J. I. Flege, and E. A. Sutter, Nat. Mater. 7, 406 (**2008**).

56. P. Zeller, F. Speck, M. Weinl, M. Ostler, M. Schreck, T. Seyller, and J. Wintterlin, Appl. Phys. Lett. 105, 191612 (**2014**).

57. D. Usachov, A. M. Dobrotvorskii, A. Varykhalov, O. Rader, W. Gudat, A. M. Shikin, and V. K. Adamchuk, Phys. Rev. B: Condens. Matter 78, 085403 (**2008**).

58. A. T. N'Diaye, S. Bleikamp, P. J. Feibelman, and T. Michely, Phys. Rev. Lett. 97, 215501 (2006).
59. J. Coraux, A. T. N'Diaye, C. Busse, and T. Michely, Nano Lett. 8, 565 (**2008**).

60. Y. Pan, H. Zhang, D. Shi, J. Sun, S. Du, F. Liu, and H. J. Gao, Adv. Mater. 21, 2777 (**2009**).

61. X. S. Li, W. W. Cai, J. H. An, S. Kim, J. Nah, D. X. Yang, R. D. Piner, A. Velamakanni, I. Jung, E. Tutuc, S. K. Banerjee, L. Colombo, and R. S. Ruoff, Science 324, 1312 (**2009**).

62. A. Reina, X. T. Jia, J. Ho, D. Nezich, H. Son, V. Bulovic, M. S. Dresselhaus, and J. Kong, Nano Lett. 9, 30 (**2009**).

63. X. S. Li, C. W. Magnuson, A. Venugopal, J. An, J. W. Suk, B. Han, M. Borysiak, W. W. Cai, A. Velamakanni, Y. Zhu, L. F. Fu, E. M. Vogel, E. Voelkl, L. Colombo, and R. S. Ruoff, Nano Lett. 10, 4328 (**2010**).

64. Y. Hao, M. S. Bharathi, L. Wang, Y. Liu, H. Chen, S. Nie, X. Wang, H. Chou, C. Tan, B. Fallahazad, H. Ramanarayan, C. W. Magnuson, E. Tutuc, B. I. Yakobson, K. F. McCarty, Y. W. Zhang, P. Kim, J. Hone, L. Colombo, and R. S. Ruoff, Science 342, 720 (**2013**).

65. X. S. Li, C. W. Magnuson, A. Venugopal, R. M. Tromp, J. B. Hannon, E. M. Vogel, L. Colombo, and R. S. Ruoff, J. Am. Chem. Soc. 133, 2816 (**2011**).

66. A. Zurutuza and C. Marinelli, Nat. Nanotechnol. 9, 730 (**2014**).

67. S. Bae, H. Kim, Y. Lee, X. Xu, J. S. Park, Y. Zheng, J. Balakrishnan, T. Lei, H. R. Kim, Y. I. Song, Y. J. Kim, K. S. Kim, B. Ozyilmaz, J. H. Ahn, € B. H. Hong, and S. Lijima, Nat. Nanotechnol. 5, 574 (**2010**).

68. X. S. Li, Y. W. Zhu, W. W. Cai, M. Borysiak, B. Y. Han, D. Chen, R. D. Piner, L. Colombo, and R. S. Ruoff, Nano Lett. 9, 4359 (**2009**).

69. L. Gao, W. Ren, J. Zhao, L. P. Ma, Z. Chen, and H. M. Cheng, Appl. Phys. Lett. 97, 183109 (**2010**).

70. T. Kobayashi, M. Bando, N. Kimura, K. Shimizu, K. Kadono, N. Umezu, K. Miyahara, S. Hayazaki, S. Nagai, Y. Mizuguchi, Y. Murakami, and D. Hobara, Appl. Phys. Lett. 102, 023112 (**2013**).

71. K. S. Kim, Y. Zhao, H. Jang, S. Y. Lee, J. M. Kim, S. S. Kim, J. H. Ahn, P. Kim, J. Y. Choi, and B. H. Hong, Nature 457, 706 (**2009**).

72. S. H. Lee, K. H. Lee, and Z. H. Zhong, Nano Lett. 10, 4702 (**2010**).

73. H. Ago, Y. Ogawa, M. Tsuji, S. Mizuno, and H. Hibino, J. Phys. Chem. Lett. 3, 2228 (**2012**).

74. Q. Yu, L. A. Jauregui, W. Wu, R. Colby, J. Tian, Z. Su, H. Cao, Z. Liu, D. Pandey, D. Wei, T. F. Chung, P. Peng, N. P. Guisinger, E. A. Stach, J. Bao, S. S. Pei, and Y. P. Chen, Nat. Mater. 10, 443 (**2011**).

75. C. Y. Su, A. Y. Lu, C. Y. Wu, Y. T. Li, K. K. Liu, W. Zhang, S. Y. Lin, Z. Y. Juang, Y. L. Zhong, F. R. Chen, and L. J. Li, Nano Lett. 11, 3612 (**2011**).

76. Ryu J, Kim Y, Won D, Kim N, Park JS, Lee E-K, et al. ACS Nano 013; 8: 950–6.

77. Piner R, Li H, Kong X, Tao L, Kholmanov IN, Ji H, et al. Graphene synthesis via magnetic inductive heating of copper substrates. ACS Nano **2013**, 7, 7495–9.

78. Kim YS, Lee JH, Kim YD, Jerng SK, Joo K, Kim E, et al. Nanoscale **2013**, 5:1221–6.

79. Wan X, Chen K, Liu D, Chen J, Miao Q, Xu J. Chem Mater. **2012**, 24, 3906–15.

80. A Kumar, AA Voevodin, D Zemlyanov, DN Zakharov Carbon 50.4 (**2012**): 1546-1553.

81. M. S. Dresselhaus, A. Jorio, M. Hofmann, G. Dresselhaus and R. Saito, Nanolett., **2010**,10, 751.

82. Gedeng Ruan, Zhengzong Sun, Zhiwei Peng, and James M. Tour, Growth of Graphene from Food, Insects, and Waste ACS Nano 5, **2011**, 9, 7601–7607.

83. A. C. Ferrari et. al, Phys. Rev. Lett., **2006**, 97, 187401.84.

84. A. C. Ferrari and J. Robertson, Phys. Rev. B, **2000**, 61, 14095.

85. Malard, L. M., et al. "Raman spectroscopy in graphene." Physics Reports, 473.5, **2009**), 51.

Chapter II

Experimental Methods

Several spectroscopic and microscopic techniques have been used to characterize the prepared nanomaterials and to study its properties in the thesis. The present chapter details the instruments and the sample characterization methods used in the study.

1. Transmission electron microscopy (TEM) and Electron Diffraction (ED)

The first ever electron microscope was built in the transmission mode by Ruska and Knoll in 1930s. In the modern version, a beam of electrons is transmitted through an ultrathin specimen and an image formed from the interaction of the electrons transmitted through the specimen, is detected by an area sensor such as a CCD camera. The focusing of electron beam can be achieved by using a set of electromagnetic lenses and a resolution of the order of 0.2 nm has been achieved. The diffraction pattern as such helps to identify the local crystal structure of the sample. This requires extensive instrumentation such as electron optics, vacuum system (~10^{-9} Torr) and high accelerating voltages (~300 keV). TEM is routinely used in nanoscience research for imaging nanostructures and to understand local structure and can be integrated with other techniques like electron energy loss spectroscopy and energy dispersive X-ray spectroscopy to get the information on the local chemical composition. The interaction of the primary electron beam with the specimen generates various kinds of signals such as secondary electrons, backscattered electrons, X-rays, etc are shown in Figure II.1. Much information about sample surface, composition and structure can be gained by harnessing the scattered beam.

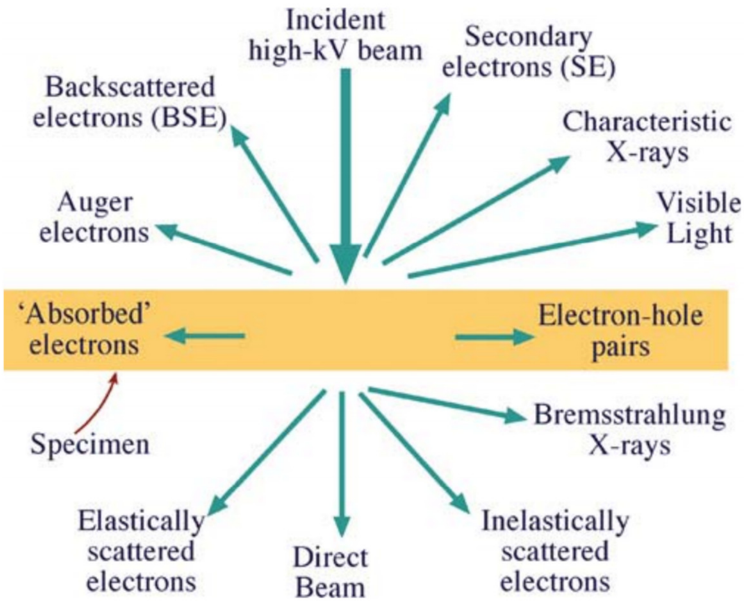

Figure II.1 Signals generated when a high-energy beam of electrons interacts with a thin specimen. Most of these signals can be detected in different types of TEM. The directions shown for each signal do not always represent the physical direction of the signal, but indicate, in a relative manner, where the signal is strongest or where it is detected (Reproduced from Ref 1).

In the present study, TEM measurements were carried out with a JEOL-3010 instrument operating at 300 kV (λ = 0.0196 Å) and selected area electron diffraction (SAED) patterns were collected at a camera length 20 cm (calibrated with respect to the standard polycrystalline Au thin film). Samples for TEM were prepared by depositing a drop of the nanomaterial on a holey carbon copper grid, allowing it to dry in a desiccator overnight. This grid was used for TEM and selected area electron diffraction (SAED) analysis.

2. Scanning electron microscopy (SEM) and Energy-dispersive X-ray spectroscopy (EDS):

In SEM, the focused electron beam scans across the sample surface in a raster fashion, generates the secondary and backscattered electrons, detected by the detectors to generate the topography of the sample surface. The elastic scattering produces backscattered electrons (energy > 50 eV) and inelastic scattering produces secondary electrons (energy < 50 eV), X-rays and also Auger electrons. These signals are obtained from specific emission volumes within the sample and can be used to examine many characteristics of the sample. X-rays emitted are characteristic of the elements present in the sample, hence can be used to study the chemical composition and is called energy dispersive X-ray spectroscopy (EDS) [2]. The Auger electrons can be used to map local chemical composition of nanostructures with good spatial resolution and is called scanning auger microscopy and spectroscopy.

Backscattered and secondary electrons are utilized in imaging surface topography. Topography contrast arises because the number and trajectories of backscattered electrons and the number of secondary electrons depend on the angle of incidence between the beam and specimen surface. The backscattered image can provide a contrast of the chemical composition in terms of variation in atomic number. Due to large depth of focus of electron beams, 3D images can be acquired. Although the probe beam diameter can be made to 1 nm and high currents can be generated using field-emission electron sources, the ultimate resolution depends on the interaction volume of the sample from where the scattered beams are generated. The instrumentation has advanced to such an extent that even biological samples can be imaged without metal coating under low vacuum conditions and also scanning TEM is possible with the present day FESEMs.

In the present study, FESEM measurements were performed using a Nova NanoSEM 600 equipment (FEI Co., The Netherlands). Energy dispersive spectroscopic (EDS) mapping was performed using EDAX Genesis V4.52 (USA) attached to the SEM column. The EDS mapping was performed at 10-15 kV with a beam current of 0.1 - 2 nA. STEM (scanning transmission electron microscopy) and low vacuum imaging were performed on the same instrument using STEM and helix detectors respectively. For working in low vacuum environment, the pole piece was mounted with low vacuum detector (LVD) and the chamber was filled with water vapor at a chamber pressure of ~ 0.4 Torr.

3. Scanning Probe Microscopes (SPMs)

The fundamental principle of all SPMs is based on the interaction between a sharp tip and the sample surface for measuring the topography and the other local physical properties [3].

3a. Scanning tunnelling microscope (STM)

STM is based on measuring the tunnelling current between the sharp conducting tip and the conducting sample (see Figure II.2). The mapping of the tunnelling current at each pixel of the sample surface (xy-palne) according to the z-coordinate produces topography and the contours of the electron density maps. The magnitude of the tunnelling current related to the tip-sample separation is given by the following equation

$$\text{Tunnelling current, } I \propto \exp(-2kd) \ldots\ldots\ldots\ldots\ldots\ldots\ldots\ldots (II.1)$$

where d is the distance between tip and sample surface and $\kappa=(2m\varphi)^{1/2}/\hbar$ φ being the DOS at the Fermi level of the tip (for a small bias applied to the sample). This exponential dependence of tunnel current makes the STM as sensitive probe for atomic information. STM can image the surface of the sample with sub-angstrom precision vertically, and atomic resolution laterally.

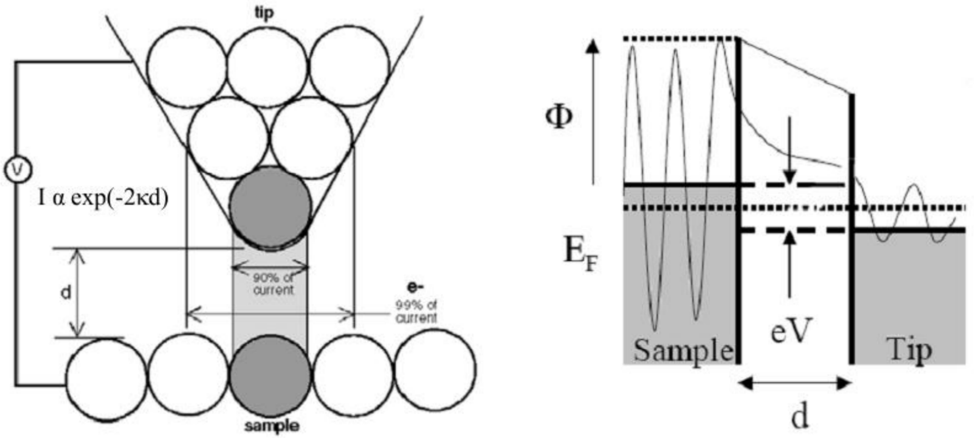

Figure II.b Schematic showing the dependence of the tunnelling current on the tip-sample separation. Tunnelling of the electronic wavefunctions between the tip and the sample [reproduced from ref. 4].

STM can also give information about the local density of states (LDOS) which is also called scanning tunnelling spectroscopy (STS). Reconstructions and the electronic properties of the conducting sample surfaces can be studied. For mapping the electronic density of the atoms of a surface, one needs to minimize the perturbations from the thermal drift and the effects of the ambient environment. For better results, STM is operated in the ultra high vacuum at low temperature conditions. Binnig and Rohrer were honoured with the Nobel prize in Physics in 1986, shared by Knoll for the discovery of electron microscope.

3b. Atomic force microscopy (AFM)

As STM is limited to conducting or semiconducting samples, an alternate technique was proposed based on measuring forces between the cantilever and the sample surface. This technique was developed by Binnig, Quate and Gerber in the year 1986, called as Atomic Force Microscope (AFM). AFM is a mechanical technique and can be used for insulating as well as for conducting samples. The layout for an AFM is shown in Figure II.3a. The cantilever and tip assembly is called the probe, mounted on a piezo scanner with three independent electrodes for controlling the movement of the probe along the X, Y and Z-axes. A laser beam falls on the back side of the cantilever and reflects back to the quadrupole photodetector. The deflection of the cantilever depends

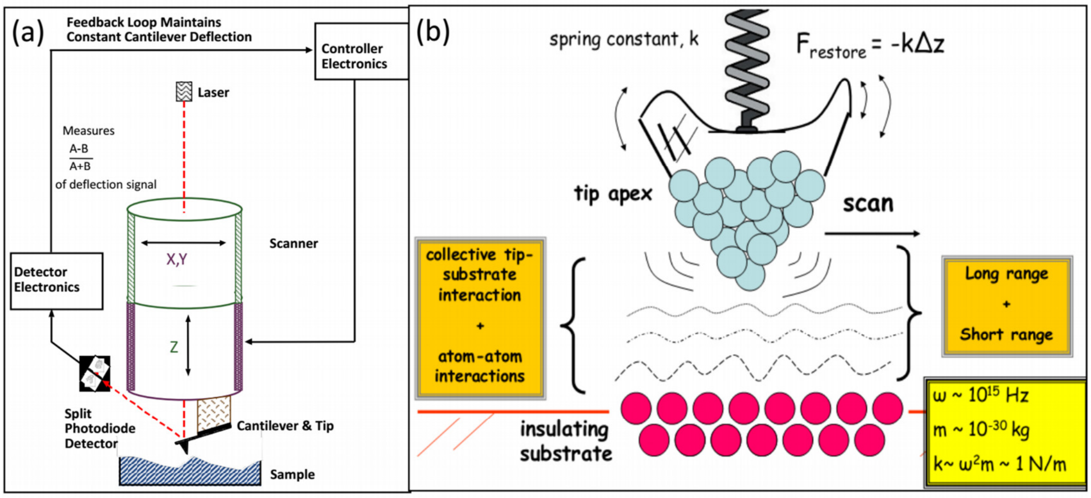

Figure II.3 (a) Schematic for the AFM layout. (b) cantilever restoring force against the tip-sample interaction forces [reproduced from refs. 5, 6].

on the spatial variation of forces on the sample surface, which gets recorded by the photodetector and further this signal gets fed to the feedback circuit which guides the controller to control the tip movement without getting crashed on the sample surface. The cantilevers are designed with specified spring constants according to the mode of operation. Typically, two kinds of forces are encountered during the operation of AFM which include repulsive and attractive van der Waals forces depending on the position of the tip from the sample surface besides the chemical and capillary forces (see Figure II.3b).

The tip-sample interaction forces are given by Lennard-Jones potential (see Figure I.29). AFM can be operated in static (contact) and dynamic modes. In the contact mode, repulsive interactions between the tip and the sample provides the information about the topography. As the tip is always in contact with the sample surface while imaging, there will be a local pressure of the order of GPa (Pressure = Force/area = nN/nm2). To minimize the local deformations of the sample surfaces, dynamic modes were invented such as tapping and noncontact modes. In dynamic modes, the probe vibrates at its resonance frequency and the effective spring constant of the cantilever

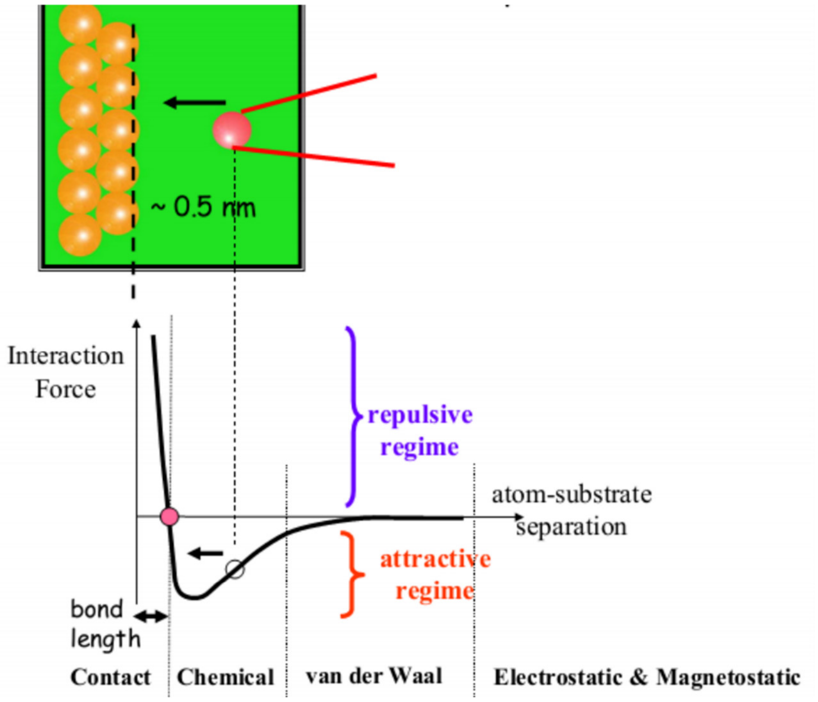

Figure II.4 Lennard-Jones potential to explain the various operating force according to the tipsample separation [reproduced from ref. 6].

dynamic modes are used for imaging the soft samples such as polymers, bio-molecules, etc. Besides imaging, AFM has also been extensively used for probing local mechanical, electrical and magnetic properties, etc. Thus, in general, various kinds of forces can be mapped out from the sample surface to extract various local properties such as mechanical, electrical, magnetic, etc, come under the category of scanning probe force microscopes. AFM has also been employed as a local tool for manipulation, modification of the surfaces locally [6].

In the present study, AFM imaging was carried out using Multimode, Veeco digital instruments, USA with Nanoscope IV controller and Veeco diInnova SPM with Nanodrive controller. Tapping and contact (lateral force) mode imaging was carried out using standard etched Si or Si_3N_4 cantilevers, respectively. The scanner was calibrated using a standard Pt coated Au grid with a pitch of 1 µm. Both height and deflection/amplitude information were recorded at a scan rate of 1 Hz and stored in a 512 x 512 pixel format. Both intermittent contact (dynamic AFM) and direct contact scanning modes were used. Images were processed using the Nanoscope version 7.15 software.

The best images were obtained by tuning the experimental conditions such as mode of operation, tip bias, the amount of the force (Z- position) and relative humidity (RH). Metalized Pt/Ir coated Si cantilevers with a nominal spring constant of 2.2 N/m and the resonance frequency of 75 kHz (Veeco Model, SCM-PIT) were used for tapping mode AFM. For contact mode work, Pt/Ir coated Si cantilevers (Veeco Model SCM-PIC) with a nominal spring constant of 0.2 N/m and resonance frequency of 16 kHz were used. Conducting atomic force microscopy (C-AFM) was performed with Pt/Ir coated Si tips (SCM-PIC) operating in contact mode using diInnova SPM. The conducting tip is brought into contact with the substrate until a preset loading force is reached. The bias voltage on the sample is then varied while the resulting current is measured.

4. Raman spectroscopy

Raman spectroscopy relies on inelastic scattering, or Raman scattering, of monochromatic light, usually from a laser in the visible, near infrared, or near ultraviolet range. The laser light interacts with molecular vibrations, phonons or other excitations in the system, resulting in the energy of the laser photons being shifted up or down. The shift in energy gives information about the vibrational modes in the system. Generally, a laser photon bounces off a molecule and loses a certain amount of energy that allows the molecule to vibrate (Stokes process, see Figure II.5). The scattered photon is therefore less energetic and the associated light exhibits a frequency shift. The various frequency shifts associated with different molecular vibrations give rise to a spectrum that is characteristic of a specific compound. Typically, a sample is illuminated with a laser beam. Electromagnetic radiation from the illuminated spot is collected with a lens and sent through a monochromator. Elastic scattered radiation at the wavelength corresponding to the laser line (Rayleigh scattering) is filtered out by either a notch filter, edge pass filter, or a band pass filter, while the rest of the collected light is dispersed onto a detector.

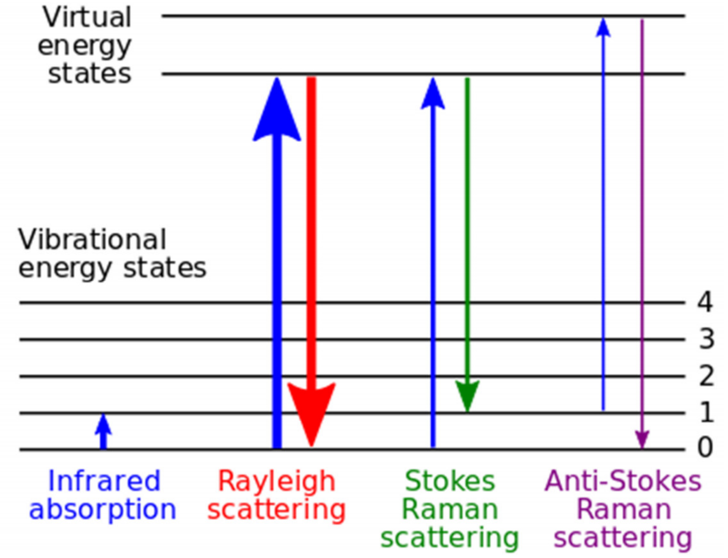

Figure II.4 Energy-level diagram showing the states involved in Raman spectra (reproduced from ref.8)

Raman scattering and Fluorescence emission are two competing phenomena, where A fluorescence process typically requires more than 10^{-9} s. In contrary, a Raman transition is completed within a picosecond or less. Raman scattering is typically very weak (one in 10 million), and as a result the main difficulty of Raman spectroscopy is separating the weak inelastically scattered light from the intense

Rayleigh scattered laser light. Historically, Raman spectrometers used holographic gratings and multiple dispersion stages to achieve a high degree of laser rejection. In the past, photomultipliers were the detectors of choice for dispersive Raman setups, which resulted in long acquisition times. However, modern instrumentation almost universally employs notch or edge filters for laser rejection and use CCD detectors, resulting into fast acquisitions.

In the present study, Raman spectra were recorded in the backscattering geometry using a 532 nm excitation from a diode pumped frequency doubled Nd:YAG solid state laser (model GDLM -5015L, Photop Swutech, China) and a custom-built Raman spectrometer equipped with a SPEX TRIAX 550 monochromator and a liquid nitrogen cooled CCD detector (Spectrum One with CCD3000 controller, ISA Jobin Yvon) [7]. Signal accumulation was performed for 30 s with a spot size of ~ 2 µm. After every acquisition, an optical micrograph was captured with the laser beam incident on the sample, using Moticam-2500 camera.

Raman mapping was performed using Horiba XploRA ONE Raman microscope with a motorized sample stage. The wavelength of the excitation laser used was 532 nm and the laser power was kept at typically on the order of 2 – 5 mW at the sample surface. The laser spot size is ~ 3 µm for the 50X objective used.

5. Optical profiler (OP)

For film thickness measurements, a Wyko NT9100 (Veeco, USA) optical profiler (OP) was used. In OP, the vertical scanning interferometry (VSI) for the samples of roughness more than 160 nm and phase shifting interferometry (PSI) mode for the samples of roughness less than 160 nm were employed with a field of view and objective lens magnifications from 0.5 – 2X and 5 – 50X respectively.

6. UV-Vis and IR spectroscopy

UV-visible spectra were recorded using a Perkin-Elmer Lambda 900 UV/vis/NIR spectrophotometer using 1 mm path length cuvette. Fourier transform infrared (FTIR) measurements were done using a Bruker IFS66 v/s spectrometer.

7. Optical microscopy

The optical images were procured with the Laben microscope, India with a magnification of 50 – 1000X. The images were captured using pixel link software. The upright microscope with transmission and reflective mode and zooming capability of 100X was used for the imaging purpose. An inverted dark-field microscope equipped with a dark-field condensor and a CCD camera (Pixel Link, PL-S621CU) was assembled from the Laben Instruments, India IM-20BD. Dark-field micrographs were obtained at 5X and 10X magnification.

8. X-ray diffraction (XRD)

The structural analysis of the nanomaterials were carried out by X-ray diffraction using Bruker D8 Discover diffractometer attached with temperature and humidity controlled stage. Cu Kα (λ = 1.5419 Å) was used as an X-ray source. Samples were prepared by depositing the materials in the form of films on glass slides and typical scan rate of 1 deg/min was used. The X-ray tube was set at 40 kV and 30 mA. With a receiving slit of 0.3 mm wide and a scintillation counter as a detector, the θ - 2θ scans were performed.

High-purity silicon powder was used as an internal standard. The coherently diffracting crystallographic domain size (D) of the nanoparticles was calculated from X-ray diffraction (XRD) line broadening after subtracting the contribution from the Cu K_{α} component (Rachinger correction) and correcting for the instrumental width. The integral line width was used in the Scherrer formula to calculate XRD of the high-intensity peak.

$$D = 0.9\lambda/\beta\cos\theta$$

where λ is the wavelength of the X-ray beam, β is the angular width at the half-maximum intensity and θ is the Bragg angle.

9. Electrical measurements

Au metal (99.99% pure) was physically deposited either by resistive heating, using 12" vacuum coating unit, (HindHivac system, Bangalore), or by e-beam evaporator (Telemark Inc, USA) under 10^{-6} Torr vacuum. In order to fabricate gap electrodes, 60 nm thick Au film was deposited on desired (glass/PET/SiO_2/Si) substrate while using a carbon fiber (diameter, 6-9 μm) as a shadow mask to define the electrodes (top contacts). Electrical measurements were performed using 'Keithley 236 source measure unit' andK eithley-4200 semiconductor characterization system with a current compliance setting at 100 mA. Temperature dependent resistance measurements were done using a cooling/heating stage (Linkam 600) equipped with a temperature controller (Linkam TMS 94) interfaced with the Keithley 236 source and measure unit. Keithley-4200 semiconductor characterization system was used for measuring the transistor characteristics. Function generator was used to apply different voltage pulses from 10 Hz to 50 MHz at amplitude of 1 V. The input and output signals are monitored using oscilloscope (DPO4104 Digital Phosphor Oscilloscope 1 GHz, Tektronix).

10. Electrochemical measurements

The electrochemical properties were investigated in two electrode configuration. The Cyclic voltammetry, galvanostatic charge/discharge experiments, and the impedance spectra were recorded using CH Instruments 650 Electrochemical Station (Austin, TX, USA).

11. Magnetic measurements

Magnetic measurements were carried out using a vibrating sample magnetometer (VSM 7300, Lakeshore).

References:

1. D. B. Williams& C. B. Carter, Transmission Electron Microscopy, PlenumPress, Newyork (1996).

2. J. Goldstein, D. Newbury, D. Joy, C. Lyman, D. Echlin et al., Scanning Electron Microscopy and X-ray Microanalysis, 3rd Edition, Springer Science and Business Media, Inc., USA (2003).

3. https://nanohub.org/resources/9598

4. S. N. Magonov & M. –H. Whangbo, Surface Analysis with STM and AFM, Wiley VCH, Weinheim (1996).

5. G. Binnig, C.F. Quate and C. Gerber, *Phys. Rev. Lett.*, 1986, **56**, 930.

6. R. Wiesendanger in Handbook of M icroscopy, Methods II, S. Amelinckx, D. Van Dyck, J. Van Landuyt, G. Van Tendeloo, Eds., Wiley VCH, Weinheim (1997).

7. G. V. P. Kumar and C. Narayana, *Curr. Sci.*, 2007, **93**,778.

8. https://en.wikipedia.org/wiki/Raman_spectroscopy

Chapter III

Functional Properties and Novel Applications of Supramolecular 1-D Nanofibres

Supramolecular 1D Nanofibres

III.1 Introduction

Supramolecular charge transfer systems are relatively a new class of organic materials, built via non-covalent interactions among the molecular ingredients [1]. The advantage of a supramolecular assembly is that they belong to an intermediate size regime, few tens of nm to μm, in comparison to single molecules (few nm) and polymer films (~ μm), yet allow easy synthesis and handling [2]. Among various supramolecular systems, conducting 1D nanowires are particularly interesting [3] since they provide low scattering conducting paths [4] and have the benefit of inherent directional dipole moment which drives conduction [5].

III.2 Synthesis of CS and DMV molecules

The detailed synthetic procedure of molecules is studied and reported elsewhere [6]. In brief, CS (coronene tetracarboxylate) was synthesized by a twofold oxidative benzogenic Diels–Alder reaction of perylene with N-ethyl maleimide and subsequent hydrolysis with KOH in methanol. DMV (dodecyl methyl viologen) was synthesized from 4, 4'-bipyridine by the controlled reaction on one nitrogen with dodecylbromide to give mono pyridinium ion and followed by treating it with methyl iodide to give amphiphilic dicationic bipyridine (DMV). The charge-transfer fibers have been assembled from injection of a methanol solution of DMV, in which the viologens are molecularly dissolved, to the aqueous solution containing free CS molecules (10% v/v methanol in water).

III.3 Formation and properties of CS-DMV nanofibres

The charge transfer (CT) nanofibres were prepared by the self-assembly of coronene-viologen based donor and acceptor (D and A) pairs in water [6]. Briefly, the potassium salt of coronene tetracarboxylate (CS) and the dodecyl substituted unsymmetric viologen (DMV) are used as D and A pairs (see Figure III.1a for structure) which interact via ground-state CT interactions (see Figure III.1b). The UV-vis absorption spectra of CS-DMV nanofibres film exhibit strong absorption peaks at 318 and 355 nm along with a broad band centered around 480 nm which originates from the ground state intermolecular charge transfer interaction between donor and acceptor molecules (see Figure III.1c). The peak intensity is highly sensitive to any perturbation to the CT interaction, which in turn influences the electrical transport through the nanofibre. The XRD pattern in Figure III.1d contains a prominent peak with 2θ ~ 25.0388 degrees (d ~ 3.5535 Å) corresponding to the π–π distance between the D and A molecules of the CT pair. Its intensity and sharpness are indicative of the highly ordered nature of the self-assembly or in other words, the D-A stacking and order.

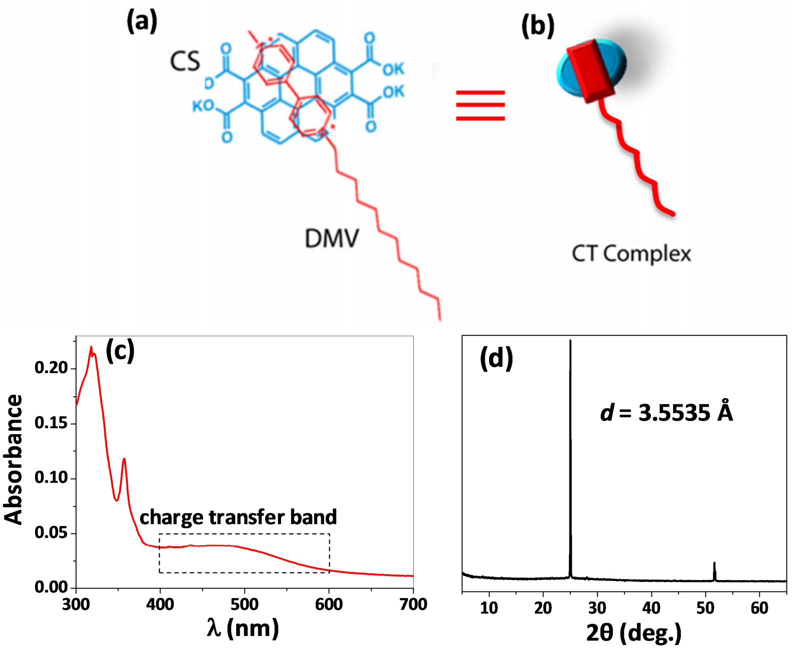

Figure III.1 Structure and characteristics of CS-DMV molecules
a) The molecular structure of aromatic donor, coronene tetracarboxylate (CS) and the acceptor, dodecyl methyl viologen (DMV) molecules. (b) Schematic of the CT complex involving the donor-acceptor pair. (c) The absorption spectra of CS-DMV nanofibres with a band centred around 480 nm. (d) XRD pattern of the film measured at ambient conditions (26 °C, 35% RH).

These CT complex forms hierarchical self-assembly arranged in face to face 1D fashion to form CT complex units (Figure III.2a). In water, these units stack themselves to form cylindrical micelles (diameter, < 6 nm) following a surfactant-like assembly (schematic in Figure III.2b). This forms bilayers of CT-amphiphiles arranged radially with the D and A molecules stacked face-to-face along the length of the nanofibre. Individual micelles further coalesce into higher order structures due to their surface charge to form 1D nanofibres (Figure III.2c). The tapping mode AFM topography image in Figure III.2d shows nanofibres crystallized from 1 mM solution, of varying diameters (100–300 nm) interwoven randomly to form a carpet morphology. We find that the nanofibre size distribution is time and concentration dependent. After initial nucleation of cylindrical micelle, the growth of nanofibre is a slow process; longer fibres can take several days to weeks. The length of the nanofibre of few days dispersion are typically larger than 10 µm. The diameters may vary within 100-300 nm. For aged dispersions, the diameter can be much higher. At higher concentrations (1-4 mM), the as-prepared dispersion contains higher fraction of smaller nanofibres (length~200-300nm) which when coated on a substrate, tend to form a smooth film. At lower concentration (< 1 mM) after many hours, longer nanofibres form with µm lengths, however scarce in number, giving rise to only few nanofibres in the circuit when dropped on a substrate.

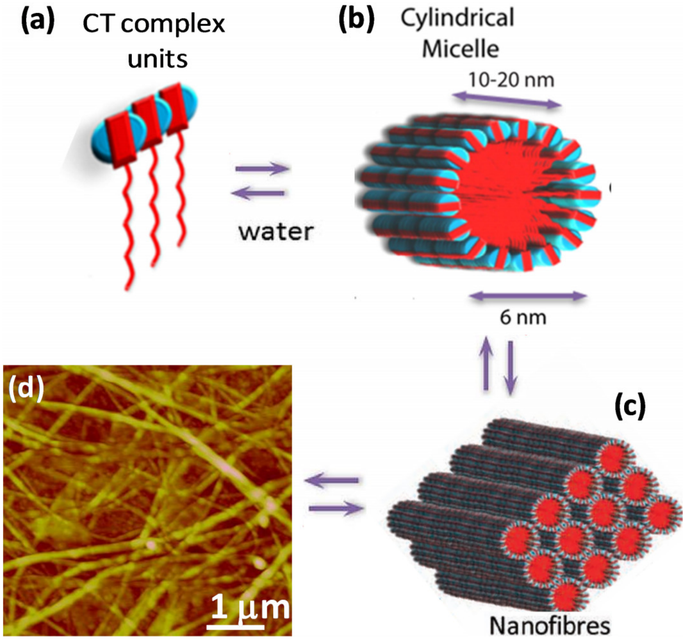

Figure III.2 Self-assembly of CS-DMV to form nanofibres
a) Hierarchical self-assembly of donor and acceptor molecules in co-facial arrangement (b) The stacking of the CT complex units to form a cylindrical micelle in the presence of water. (c) The coalescence of individual cylindrical micelles to from 1D nanofibres. (d) The tapping mode AFM image of a nanofibre carpet film. z scale: 20 nm.

References

1. Hoeben, F. J. M., Jonkheijm, P., Meijer, E. W. & Schenning, A. P. H. J. *Chem. Rev.* **2005,** 105, 1491–1546.

2. Schenning, A. P. H. J. & Meijer, E. W. *Chem. Commun*. **2005,** 26, 3245–3258.

3. Moulin, E., Cid, J.-J. & Giuseppone, N. **2013**, 25, 477–487.

4. Yunlong Guo , Gui Yu, and Yunqi Liu, *Adv. Mater*. **2010**, 22, 4427–4447.

5. L. Zhu, Y. Yi, Y. Li, E. Kim, V. Coropceanu, J. Brédas, *J. Am. Chem. Soc*. **2012**, 134, 2340.

6. Rao, K. V., Jayaramulu, K., Maji, T. K. & George, S. J. *Angew. Chem. Int. Ed.* **2010**, 49, 4218–4222.

Chapter IIIA

Ultrafast Response Humidity Sensor Using Supramolecular Nanofibre

Summary

In this chapter, an ultra-fast, wide range, highly sensitive resistive humidity sensor has been developed based on a coronene-viologen derivative system, self-assembled in the form of nanofibre from water. While a film of nanofibres exhibited high sensitivity ($< 10^4$), devices with few nanofibres showed an extremely fast response (~10 ms). Using UV-vis, XRD, and AFM measurements, the $\pi - \pi$ interaction between the donor and the acceptor molecules found to depend sensitively on the surrounding humidity influencing electrical conduction across the nanofibre. The fabricated devices were found to be stable over 8 months during the study. As is evident, these devices can be used in various contexts. The RH value close to a drop of water was determined by approaching it with a nanofibre film sensor. As the sensing element is a simple organic system from solution processes, these devices are essentially of low cost and also environment-friendly.

IIIA.1 Introduction

Humidity sensing is important in different settings, in chemical industry, hospitals, agricultural fields and so on [1, 2]. A sensor working with fast response and recovery (typically fraction of a second) finds niche applications in situations where the humidity value may change dynamically. Such application areas include industrial process controls, meteorology and various medical diagnostics including monitoring human exhaled breath [3–7]. This explains the need for low-cost humidity sensors with ultra-fast response, high sensitivity and stability. Although the literature is abound with humidity sensors [8], those with fast response form only a small subset (Table IIIA.1). The subset includes those based on inorganic materials in the form of nanowires [9], nanotubes [10, 11], thin films of oxides [12–14] and of few sulfides [15, 16] as well. Similarly, there are examples of organic and composite materials, a notable one being nafion persulphonate [4] with tens of milliseconds of response time.

Table IIIA.1 High-performance humidity sensors reported in the literature

Sr. No.	Active material	Type*	Time (s)		Sensitivity	Flow rate (sccm)	Refs
			R_s	R_r			
	Inorganic Materials						
1	VS_2 ultrathin nanosheets	R	30-40	12-50	30	-	*Adv. Mater.* **2012**, *24*, 1969
2	V_2O_5 nanotubes	R	8-12	20-25	~23	150	*J. Mater. Chem.* **2012**, 22, 5013
3	LiCl Doped TiO_2electrospunnanofibers	I	3	7	~ 6600	-	*J. Am. Chem. Soc.* **2008**, *130*, 5036
4	SnO_2 NW	R	120-170	20-60	35 @ 85%	-	*J. Am. Chem. Soc.* **2007**, *129*, 19, 2007
5	Al doped n- ZnS	R	95-203	209-1185	200 @90%	200	*J. Mater. Chem.* **2012**, *22*, 6856
6	TiO_2/LiCl thin film	SAW	0.75	1	100	-	*ACS AMI* **2011**, *3*, 528
7	Porous TiO_2	I	5	8	1.19 MΩ/%RH	-	*Nanotechnology* **2011**, *22*, 275502
8	CeO_2 nanowires	R	3	3	85@97%	-	*Nanotechnology* **2007**, *18*, 145503
9	Amorphous Al_2O_3 nanotubes	C	10	20	10000	-	*J. Mater. Chem.* **2011**, *21*, 1907
10	Si thin film	R	0.2	-	10000	-	*IEEE Elect. Dev. Lett.*, **2004**, 25, 8
11	Al_2O_3 thin films	C	0.042	-	950	27000	*IEEE Sens.* **2006**, *6*, 1
12	TiO_2 interdigitated	C	0.22	0.4	1000	5000	*IEEE Sens.* **2007**, *7*, 6, 955
13	TiO_2 thin film	C	0.050	3	19nF/%RH	2000	*IEEE Sens.* **2009**, *9*, 12
14	Amorphous TiO_2	C	0.275	0.297	1000 @ 92%	2500	*IEEE Sens.*, **2008**, *8*, 8
15	Amorphous SiO_2	C	0.231	0.229	1000@92%	2500	
16	Amorphous Al_2O_3	C	0.087	0.104	1000@92%	2500	
17	ZnO nanorods	R	3	20	183	-	*Surface Science* **2005**, *242*, 212–217
18	VO_2 (M) nanostructures	R	5-8	2-3	50@97%	-	*Electroanalysis* **2011**, *23*, 7, 1752
19	$MgFe_2O_4$ thin films @ 800 C	R	4	6	20888	-	*Thin Solid Films* **2011**, *519*, 6135
20	ZnO thin film	R	3	12	42,678	-	*Sens. Actuators, A* **2010**, *164* 8
21	TiO_2nanofilms	C	0.064	1.440	1000	2500	*Sens. Actuators, B* **2009**, *140* 610
22	Agarose coated optic fiber	O	0.05	-	5	-	*Sens. Actuators, A* **2012**, *174*, 47

23	Chiral sculptured thin films	O	0.140	1.2	60	-	*Sens. Actuators, B* **2011**, *156*, 593
24	$Na_2TiO_3O_7$ nanowires	I	4	5	10000	-	*Sens. Actuators, B* **2008**, *135*, 317
25	$BaTiO_3$nanofiber	R	20	3	120	-	*Sens. Actuators,* B **2011**, *153*, 460
26	Graphene oxide	I	0.03	0.03	-	450	*ACS Nano* **2013**, *7*, 12, 11166
Organic Materials							
27	Electrospun TiO_2nanofiber	I	1	4	150 MΩ/%RH	-	*Cer. Internal.* **2012**, *38*, 2437
28	Nafion perfluoro sulfonate	R	0.04	0.03	500	200-500	*Anal. Chem.* **2004**, *76*, 2561
29	Nanoporous polymeric gratings	O	0.35	-	43	5	*Nanotechnology* **2007**, *18*, 465501
30	Polyimide columns	C	1	-	3750ppm/%RH		*IEEE Trans. on Electr. Dev.,* **2000**, 47, 4
31	Polymeric photonic crystals	O	1.5	20-30	80	-	*Sens. Actuators B* **2008**, *129*, 391–396
32	Polyimide (interdigitated electrodes)	C	0.5	15	27	-	*IEEE Sens.* **2002**, *2*, 2
33	Benzocyclobutene (interdigitated electrodes)	C	0.65	4.5	0.7	-	
34	Benzocyclobutene (stacked electrodes)	C	0.75	5	8.5	-	
Composite Materials							
35	Electrospun polyamide 6/PEI	M	120-50	-	1000	-	*J. Mater. Chem.* **2011**, *21*, 16231
36	Fe_3O_4@SiO_2/PEG acrylate photonic crystal	O	50-70	26-44	240	-	*J. Mater. Chem.* **2011**, *21*, 3672
37	Carbon-encapsulated superparamagnetic colloidal	O	120	120	160	-	*J. Mater. Chem.* **2012**, *22*, 1021
38	Electrospun composite polymer	M	120	50	1000	-	*J. Mater. Chem.* **2011**, *21*, 16231
39	MWNT - $LiClO_4$	R	420	60	35000	-	*Nanotechnology* **2004**, *15*, 1284
40	Polypyrrole/Ag/TiO_2 nanoparticles	M	12-20	15-18	0.0246 ΔHz/Δppm	-	*Sens. Actuators* B **2008**, 129, 915
Supramolecular Materials							
41	Supramolecular cholesteric liquid crystals	O	120	-	40	-	*J. Am. Chem. Soc. **2012**, 134, 7608*
42	**Present Work**						
	Supramolecular nanofibre film	R	2.2	1.05	~ 45000	200-300	
	Supramolecular nanofibres	R	0.008	0.024	~ 400	~500	

*R: Resistive, C: Capacitive, I: Impedance, O: Optical, M: mass. SAW: Surface Acoustic Wave

Very recently, Borini et al. [17] have reported response time of 30 ms for a graphene oxide based sensor. In addition to this, there are advancements in the fabrication of humidity sensors using optic fibre based sensor technology [18, 19]. There have been reports of humidity sensors using hybrid microcavity [20], AFM micro cantilevers [21], plasmonic materials [22] etc. Fabrication of flexible, printable, chipless and wireless humidity sensors and integrating them with CMOS technology has been recently reported, intended for various humidity related applications [23–25]. The basic mechanism of humidity detection in the above materials is based on the change in proton/ionic conduction (resistive), dielectric constant (capacitive), refractive index (optical), frequency (impedance) or in mass, of the active material with the humidity level [26]. Organic humidity sensors are particularly attractive since the sensing material can be prepared by simple solution processes unlike in inorganic sensors which demand expensive preparation techniques such as chemical vapor deposition, vapor-liquid-solid growth etc.; however, organic sensors usually lack stability in terms of device performance [27–29].

Supramolecular systems are relatively a new class of organic materials, built via non-covalent interactions among the molecular ingredients [30]. Fabricating functional devices such as FETs, solar cells, sensors from the controlled organization of supramolecular components is considered as a promising area of research [31–34]. It takes the advantage of intermediate size regime, few tens of nm to mm, when compared to single molecule (few nm) and polymer films (< mm) [35, 36]. Recently, Herzer et al. [37] reported change in color of supramolecular polymer films upon exposure to humidity. Among various supramolecular systems, 1-D nanowires are of particularly interesting since they provide low scattering conducting paths [38–40] and easy alignment across the electrodes [41].

IIIA.2 Scope of the present investigation

As detailed in the introduction, the physical properties of most of the humidity sensors giving rise to humidity action are based on water adsorption and desorption process which hinders ultrafast response in the sensor. The present investigation pertains to the possibility of using the supramolecular nanofibre as an active material for fast response humidity sensor. The nanofibres are uniquely designed from D-A charge transfer molecules and the electronic conductivity of the nanofibres originates from the face to face charge transfer between each D-A pair. The conductivity of the nanofibre is expected to vary when there is any disturbance in the assembly of the nanofibre. Since nanofibres are assembled in aqueous medium due to prevalent water repellent hydrophobic alkyl chains, giving rise 1D morphology to the nanofibres, the humidity is the best physical parameters to alter the conductivity of the nanofibre. This gives a scope to explore the use of nanofibre as a sensing medium for humidity. The rapid organization of D-A molecules in water is an advantage which may give an ultrafast response.

IIIA.3 Experimental Section

Characterization: The structural analysis was carried out by X-ray diffraction using Bruker D8 Discover diffractometer attached with temperature and humidity controlled stage. Cu Kα (1.5419 Å) was used as an X-ray source. Atomic force microscopy (AFM) was performed using Multimode, Veeco digital instruments, USA with Nanoscope IV controller. The humidity control was achieved by using an environmental hood with the flow of water vapors of different RH 15%, 42% and 62% continuously for 15 minutes. The images were collected in the tapping mode using Si cantilevers. The FE-SEM imaging was done using a Nova NanoSEM 600 (FEI Co., The Netherlands) by drop casting the aqueous solution on Si(100) substrate followed by drying in a vacuum and was operated with an accelerating voltage of 10 kV. Absorption spectra were recorded on a Perkin-Elmer Lambda 900 UV-VIS-NIR Spectrometer using 1 mm path length cuvette. To analyze the intensity variation with increasing RH, a baseline was drawn for each spectrum using Origin 8.0 software in the region of interest, 400 to 600 nm. The raw data was then subtracted from the baseline. For standard calibration, vapors of fixed RH were obtained by controlling the equilibrium vapor pressure of sulphuric acid [15]. A humidity cell was constructed for rapid switching of RH and switching between two RH levels using a Tee with a flow rate of 200–300 sccm. A commercial humidity meter Testo 410-2 was used to measure the obtained RH. For alcohol monitoring, a commercial alcohol meter (BAC$^{\text{TRACK}}$ B70) was used. It is to confirm that the Ethical Committee of the JNCASR approved all the experiments described in this study. Further, informed consent was obtained from all the subjects.

Device fabrication: The glass substrates were cleaned in piranha solution followed by washing with distilled water several times. Metallic contacts were made by physical vapor deposition of Au by shadow masking using a resistive thermal evaporator (HindHivac, India) at a base pressure of 10^{-2} mTorr. A Keithley Semiconductor Characterization System 4200 was used to measure device characteristics. An Oscilloscope Tektronix 4104 was used to measure the voltage drop across resistors.

IIIA.4 Results and discussion

RH sensing by nanofibre film: The performance of the nanofibres as a humidity sensor is described in Figure IIIA.1. A drop (5 μL, 1 mM) of the CS-DMV nanofibre solution was drop coated on gold gap electrodes on glass and allowed to dry for an hour. The device was then placed inside a humidity cell (Figure IIIA.1a) and connected to a Keithley 4200 source unit for electrical characterization. Moisture-nitrogen mixture of varying RH was passed through the humidity cell through the inlet as shown in Figure IIIA.1a. The ON current (when RH was ON) of the nanofibre film device decreases with the time (see Figure IIIA.1b). It exhibits second order exponential decay with typical decay times of 1 - 2 and 20 - 30 seconds. This current decay is due to the electric field induced stress which sets in within the nanofibre, perhaps disturbing the molecular orientation. It appears that this disorder once nucleated, spreads across the nanofibre leading to a gradual decrease in the current (or decay current) with time. Although we do not have any direct spectroscopic and microscopic evidence for voltage dependent molecular orientation leading to current decay, the voltage stress on such molecular assembly is expected [42]. In the present study, the region of stable current (as indicated in squared box) was chosen for humidity sensing and related calibration purposes. The property of current decay by nanofibre film has been explored in Chapter IIIC.

As shown in Figure IIIA.1c, as the RH increased from 5% to 65%, the current in the nanofibres increased from < 0.1 nA to 220 nA (Figure IIIA.1c) and showed a small decay while RH was still on, but dropped down to 0.1 nA sharply when RH switched to 5%. The response and recovery times, measured as the time taken to reach 90% of the peak value are 2.20 and 1.05 s respectively. The sensitivity of the device, which is a direct measure of how well a device detects per unit change of RH, is defined in this case as the change in current normalized with respect to the current at 5% RH [9]. The sensitivity increased rapidly as RH increased to 85% to reach a value of < 45,000 (see Figure IIIA.1d).

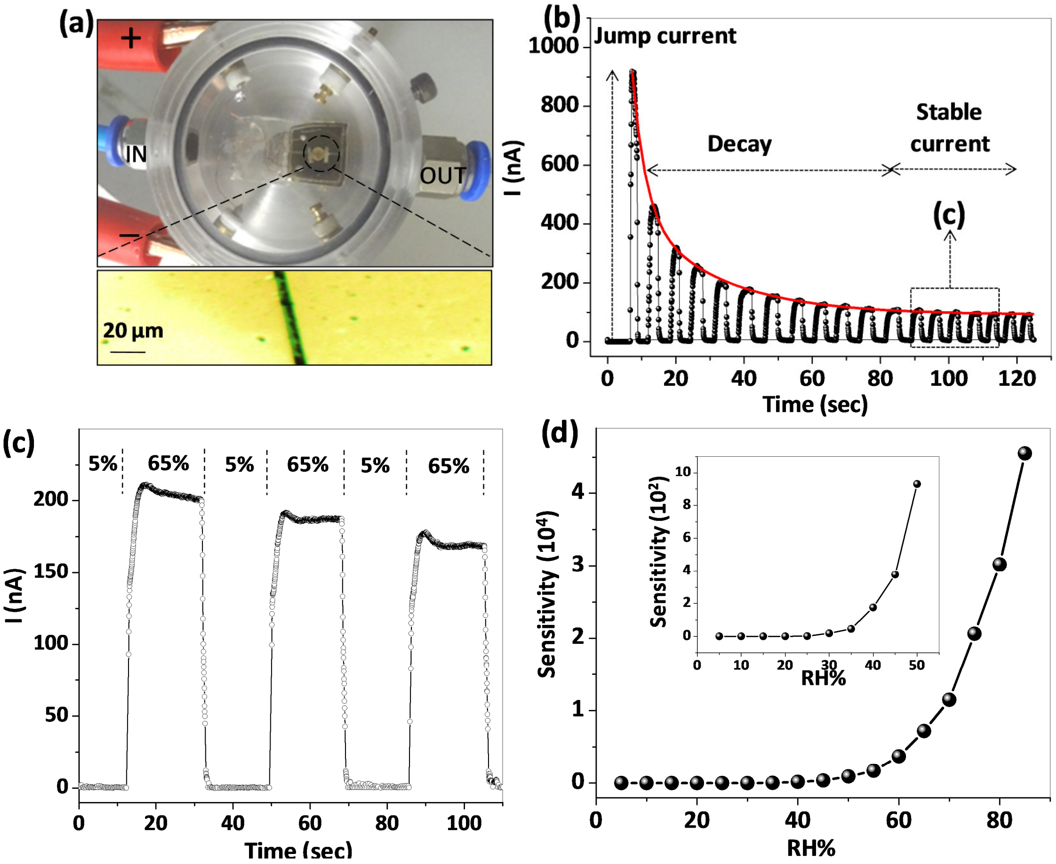

Figure IIIA.1 RH detection by CS-DMV nanofibre film

(a) A photograph of the humidity detection set up used in the study. Inset is the optical microscope image of zoomed in part of the device, which consists of Au gap electrodes drop coated with 5 mL of nanofibre suspension resulting in a nanofibre film laid across the gap. The thin film cannot be delineated due to its transparency. (b) The changes in the measured current from the nanofibre film device when RH was switched between 5% and 65%. The red curve is the second order exponential fit to the ON current of the device. The three current regions are marked. (c) Zoomed in portion of (b) indicated by a square box. (d) The variation in sensitivity for different RH values for a typical device. Inset is the zoomed portion for lower RH.

Conducting Vs capacitive action of nanofibre film: The functionality of the nanofibre film device can be tuned by humidity. It is found that the nanofibre exhibits competing conducting (due to charge transfer interactions) and capacitive (due to ions) behavior, however dominance of each depends on the RH (see Figure IIIA.2b). At higher RH, the current increases drastically with small change in RH, whereas at lower RH the current varies negligibly (see Figure IIIA.2). The higher humidity region was utilized to fabricate humidity sensor, as it is further detailed in the present chapter, whereas the utility as an electrolyte under lower humidity is detailed in the Chapter IIID.

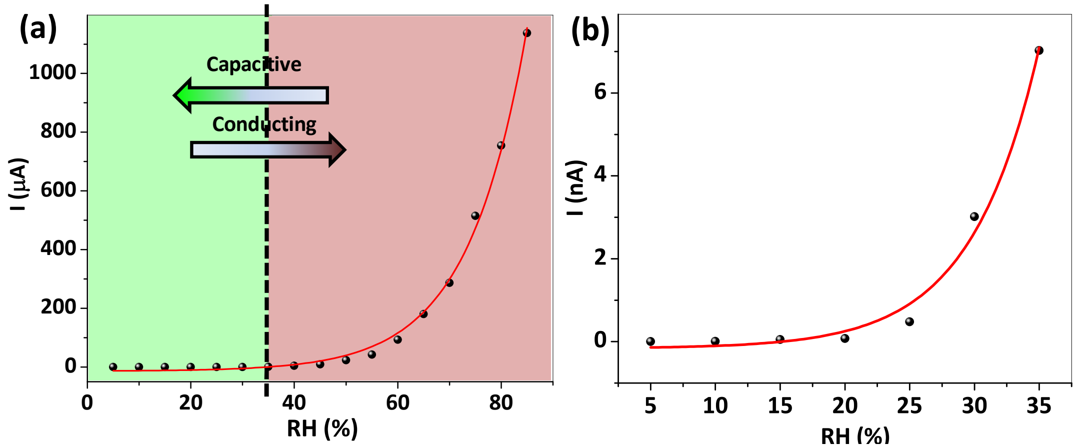

Figure IIIA.2 Different functionality of nanofibres

(a) Capacitive Vs conducting the action of nanofibre film with humidity range. (c) Zoomed in part of (b) at lower RH. Line fitting is to guide the eye.

Mechanism of RH sensing: In order to gain an insight into the observed electrical changes with RH, UV-vis absorption measurements were carried out on a CS-DMV nanofibre carpet film as shown in Figure IIIA.3. Few drops of the nanofibre solution were drop coated on the inner side of a quartz cuvette and allowed to evaporate. The cuvette was then closed with a rubber stopper hosting inlet and outlet for passing a moisture-nitrogen mixture of varying RH. The absorption spectra of CS-DMV nanofibres film exhibit strong absorption peaks at 318 and 355 nm along with a broad band centered around 480 nm which originates from the ground state intermolecular charge transfer interaction between donor and acceptor molecules [43]. The peak intensity is highly sensitive to any perturbation to the charge transfer interaction, which in turn influences the electrical transport through the nanofibre. The intensity of the 480 nm band does show changes with a change in RH (Figure IIIA.3), but accompanying this change, the spectral baseline also shifts due to the varied transmittance of the film (*vide infra*). After baseline correction, the changes in the intensity of the 480 nm band became quite apparent (see inset (a) of Figure IIIA.3). Indeed as shown in inset (b), the intensity was found to increase linearly with increase in RH emphasizing the role of charge transfer in the electrical transport of CS-DMV nanofibre system. The other two peaks (355 and 320 nm) relate to molecular transitions are not affected by humidity.

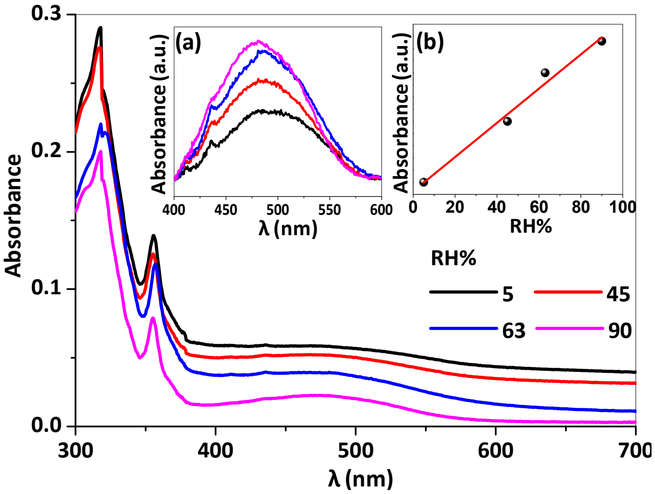

Figure IIIA.3 In-situ optical absorbance measurements of nanofibres film with RH
The change in absorbance of CS-DMV nanofibre film measured on quartz substrate from 300 to 700 nm range at different RH values. Insets are the magnified portion of the charge transfer band in the region, 400 to 600 nm, after baseline correction (a) and the plot of variation in the intensity of the charge transfer band with RH (b).

Further insight into the structural changes comes from in situ X-ray diffraction measurements (Figure IIIA.4). With increase in RH from 5% to 65%, the peak corresponding to the CS and DMV spacing (π-π interaction distance) in the supramolecular assembly is found to shift from a 2θ value of 25.027° (d-spacing, 3.5551 Å) to 25.040° (3.5534 Å), the peak shift of 0.016 Å being well outside of the measurable limit (0.00015 Å). The peak shift is linear (Figure IIIA.4b) and thus follows a similar behavior as the intensity of the charge transfer peak (Figure IIIA.3b). Thus, it appears that an increase in RH brings the CS and DMV units closer, thereby enforcing a tighter packing of the assembly. Since the electrical transport in such systems depends sensitively on the charge transfer interaction and π-π delocalization among the D and A pairs [44], any small perturbation due to change in RH can bring about considerable change in the conductivity. This also clearly indicates that the humidity sensing is not due to surface adsorption and desorption processes, observed in most humidity sensor. The local changes in the nanofibre assembly as discussed above, may have some implications on the morphology of the nanofibres.

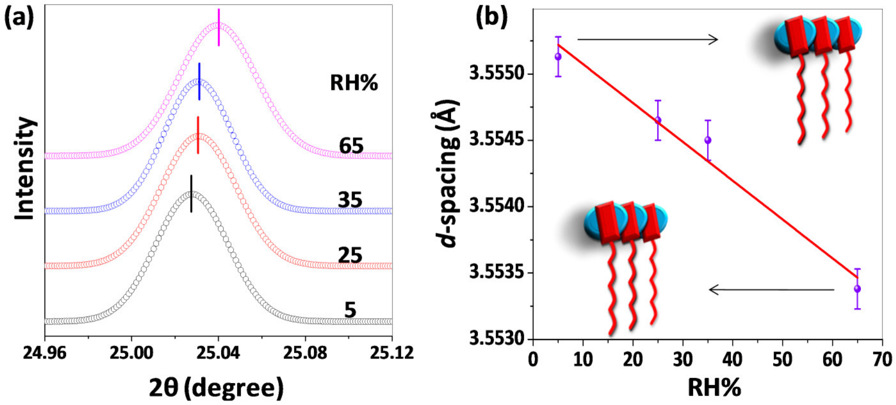

Figure IIIA.4 Humidity-dependent XRD studies of CS-DMV nanofibre film
(a) The XRD patterns of nanofibres film acquired at RH of 5%, 25%, 35%, and 65%. The XRD peak was recorded with step size of 0.001 degree at different RH values. The patterns are shifted vertically for clarity. The peak maxima are marked by vertical bars. (b) The variation in the XRD d-spacing with RH.

Further, AFM measurements were carried out on the nanofibre film at different RH values in an environmental hood (see Figure IIIA.5). At ambient humidity (42% RH), the average width of the nanofibres was 99.6 nm (Figure IIIA.5a) which increased to 118.4 nm when the RH in the hood was changed to 15% (Figure IIIA.5b). The concomitant change in nanofibre height was from 6.25 to 5.26 nm. As the humidity was increased to 62%, the average width decreased to 76.4 nm while the height increased to 8.14 nm (Figure IIIA.5c). The decreasing width can enhance light transmission as seen from the downward shift of the spectral baseline in Figure IIIA.3a. In Figure IIIA.5d are shown the observed morphology changes with respect to a given location on a nanofibre (see arrow marks in Figure IIIA.5a, b and c). Many such individual measurements have been performed (see Figure IIIA.6). The observed morphology changes may be taken to indicate a tighter molecular assembly with higher humidity around the supramolecular fibres. Under very dry conditions, the nanofibres were found to be non-conducting. Indeed, the conduction could be initiated by simply exposing to humid air.

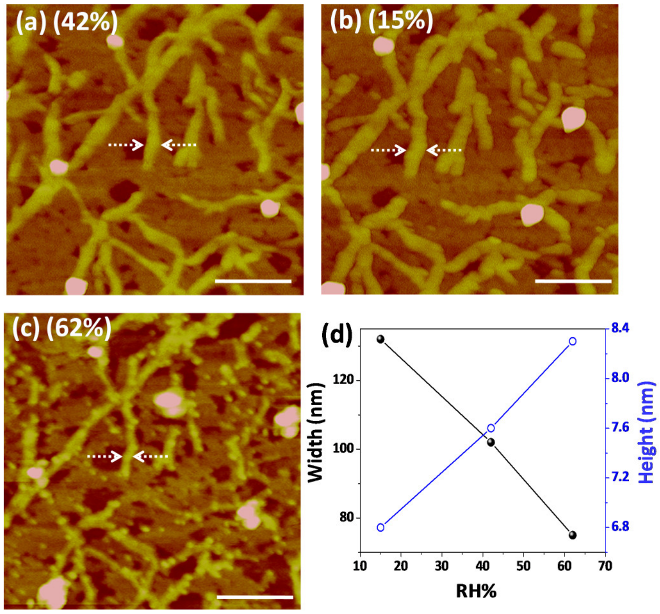

Figure IIIA.5 AFM analysis of nanofibres under different RH conditions
AFM images of CS-DMV nanofibres acquired at ambient RH of 42% (a) followed by at 15% (b) and 62% (c), the last two measurements being carried out in atmospheric hood. Scale bar: 500 nm, z scale: 20 nm. (d). The variations in width (left) and height (right) of nanofibre marked in dotted lines with different RH conditions.

Determination of RH near a water drop: As it is clear from the above observations, the CS-DMV nanofibres can be potentially used for monitoring small variations in humidity levels near a surface, for example; such ideas could be relevant in the context of next generation intelligent device components such as artificial skin or touchless screen, where the 'sensation' of an approaching finger or alive cell would depend on its distance from the skin [15]. An experiment was designed wherein the change in current through a nanofibre film was monitored while a micro tip carrying a tiny water droplet made a controlled approach (see Figure IIIA.7a), from a distance of

2.5 to 0.2 mm in steps of 0.1 mm. As seen from the plot in Figure IIIA.7b, the current in the circuit increased from < 0.45 to 2.3 mA and the increase was nearly linear with distance. On retracting the tip, it followed a similar trend with slightly less current.

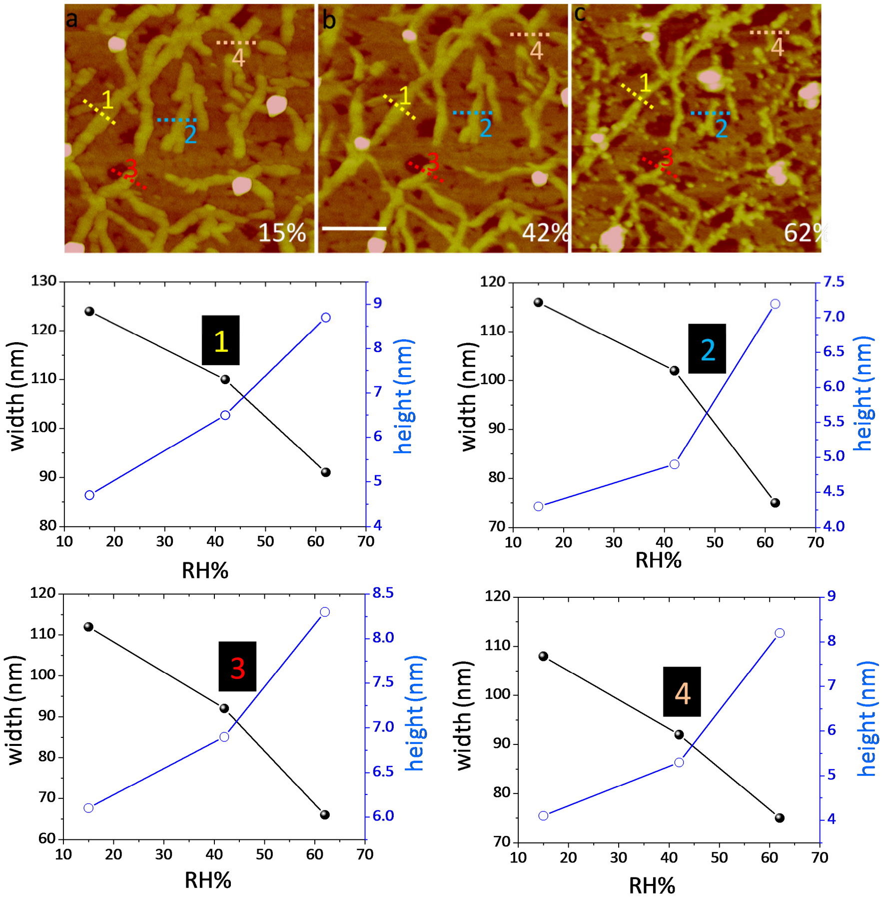

Figure IIIA.6 AFM analysis of additional regions
The variations in the width and height of nanofibres numbered 1, 2, 3, and 4 in AFM image with change in the RH. Scale bar: 500 nm, z scale: 20 nm.

Based on the calibration data collected for this film (Figure IIIA.7c), RH at different tip separation distances (Figure IIIA.7d) was estimated. It is interesting to see that the RH value reaches as high as 60% close to the drop and decreases gradually till 1.5 mm above which it merges with the ambient background. This trend is similar to the one reported by Feng et.al. [15], although this study aims at measurements much closer to the humid surface. This experiment clearly demonstrates the 'action at a distance' possibility in real applications with high degree of sensitivity.

Ultrafast RH sensing using few nanofibres: It may be noted that the nanofibre carpet device developed in this study exhibits quite fast response (< 1–2 s) comparing well with many literature examples (see Table IIIA.1). It is known from the literature that conducting paths in carpet-like morphology come across innumerable scattering junctions, which can adversely influence the device response [25–27]. In our study, the longer and few nanofibres formed at lower concentration are found to give very good response and recovery times (down to 10 ms) but lower sensitivity whereas smaller and dense nanofibre film are found to yield increased response and recovery times (1-10 s) and higher sensitivity. We have explored improving the response by fabricating a device with only a few nanofibres across the gap electrodes instead of a carpet film. This was achieved by placing a 5 mL drop of 0.1 mM CS-DMV dispersion (Figure IIIA.8a). As can clearly seen in Figure IIIA.8, the current decay is minimal. Hence, for humidity sensing by few nanofibre and its related applications (Chapter IIIB), jump current is chosen for the calibration purposes.

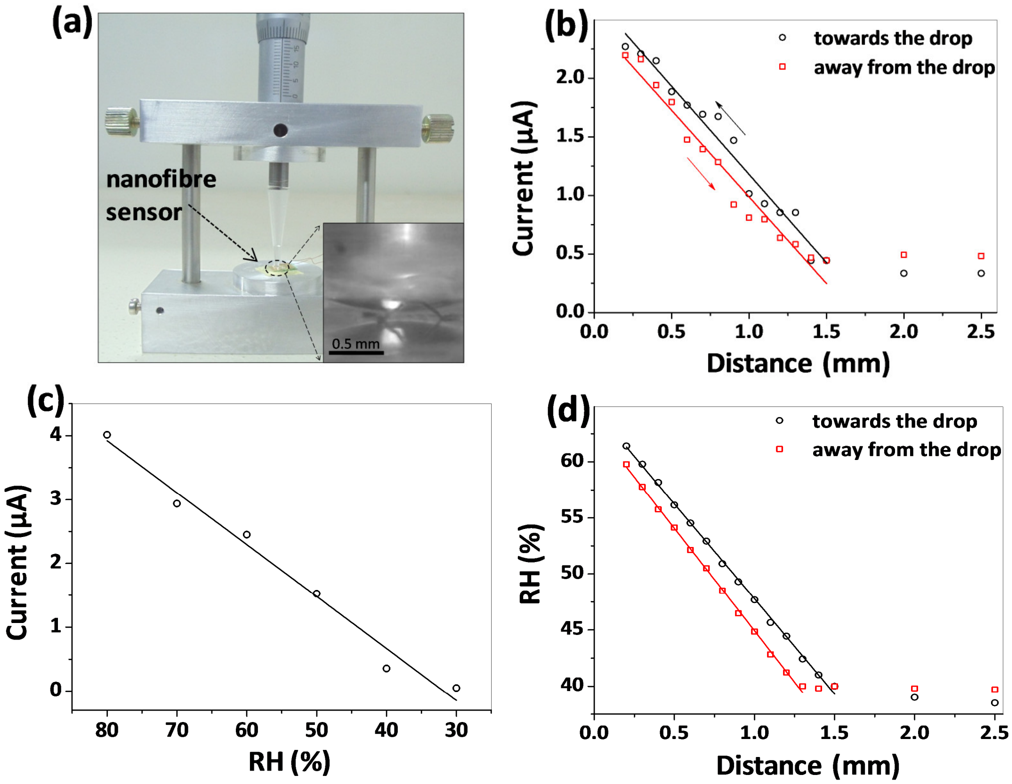

Figure IIIA.7 RH around a water drop

a) A photograph of the setup used for the study. It consists of a plastic tip carrying the tiny water drop which can be moved in vertical direction using a screw gauge arm. Inset is the magnified image when the water drop is very close to the sensor. Reflection of the drop is seen from the device surface. (b) Variation in the current (at 1 V), as the water drop is brought towards and taken away from the nanofibre sensor. (c) Variation of current through the nanofibres at different RH measured at 1 V. (d) Derived plot of the variation of RH of water drop with distance.

The change in the voltage across a standard resistor (20 MV) as measured using an oscilloscope was quite rapid (Figure IIIA.8c) as the humidity over the device was switched between 5% and 80% in cycles. In this case, the response and recovery times turned out to be 8 and 24 ms respectively (Figure IIIA.8d). To our knowledge, this is the fastest humidity sensor made so far; nafion persulphonate [4] and graphene oxide [17] based sensors come close to its performance with 30–40 ms response time (see Table IIIA.1). Further, as the nanofibre are self-repairable with water drop, the prolonged exposure to humidity does not result in any irreversible losses. If any damage does take place, it can be easily recovered by placing a drop of water onto during which nanofibre self-repair and regain original conducting behavior. The nanofibres seem to withstand as many cycles of humidity. If the device fails to sense, it can be simply repaired by putting drop of water onto the nanofibre and allow it to self-repair while drying.

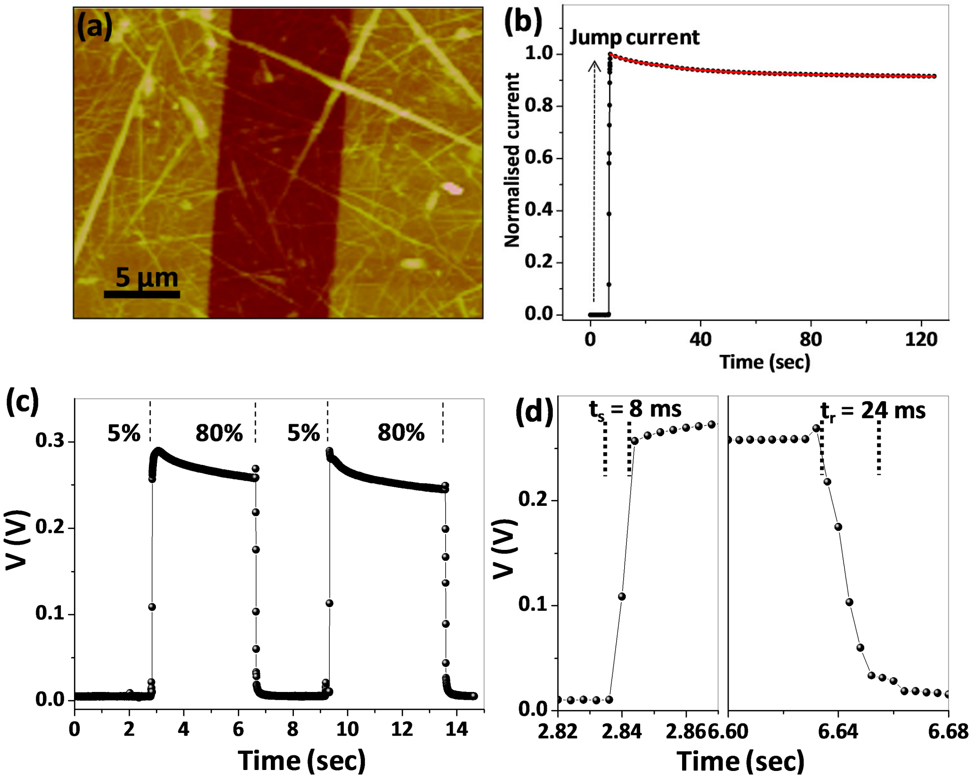

Figure IIIA.8 An ultrafast RH sensor

(a) Tapping mode AFM images of few nanofibres across gold electrodes (< 8 mm). The z scale in the image is 20 nm. (b) The decay characteristics of few nanofibre device for RH. Line line is second order exponential fit. (c)The changes in output voltage measured using an oscilloscope, from a few nanofibre sensor as RH is switched between 5% and 80%. (d) Estimation of response and recovery times of the sensor.

IIIA.5 Conclusions

An ultra-fast, wide range, highly sensitive resistive humidity sensor was developed based self-assembled nanofibre. While a film of nanofibres exhibited high sensitivity (< 10^4), devices with few nanofibres showed an extremely fast response (< 10 ms). Using UV-vis, XRD and AFM measurements, it was found that the π – π interaction between the donor and the acceptor molecules depends sensitively on the surrounding humidity influencing electrical conduction across the nanofibre. The fabricated devices were stable over 8 months during the study. The RH value close to a drop of water was determined by approaching it with a nanofibre film sensor. As the sensing element is a simple organic system from solution processes, these devices are essentially of low cost and also environment-friendly. Potential applications in personal healthcare as use-and-dispose devices, is evident.

References

1. Traversa, E. Ceramic sensors for humidity detection: the state-of-the-art and future developments. *Sens. Actuators*, B 23, 135–156 (**1995**).

2. Wang, Y., Besant, R. W., Simonson, C. J. & Shang, W. Application of humidity sensors and an interactive device. *Sens. Actuators*, B 115, 93–101 (**2006**).

3. Kebabian, P. L., Kolb, C. E. & Freedman, A. Spectroscopic water vapor sensor for rapid response measurements of humidity in the troposphere. J*. Geophys. Res.,[Atmos.]* 107, 4670 (**2002**).

4. Kuban, P., Berg, J. M. &Dasgupta, P. K. Durable microfabricated high speed humidity sensors. *Anal.Chem*. 76, 2561–2567 (**2004**).

5. Laville, C. & Pellet, C. Comparison of three humidity sensors for a pulmonary function diagnosis microsystem. *IEEE Sens*. J. 2, 96–101 (**2002**).

6. Laville, C. & Pellet, C. Interdigitated humidity sensors for a portable clinical microsystem. *IEEE Trans. Biomed.Eng*. 49, 1162–1167 (**2002**).

7. Niesters, M. et al. Validation of a novel respiratory rate monitor based on exhaled humidity. *Br. J. Anaesth.* 109, 981–989 (**2012**).

8. Chen, Z. & Lu, C. Humidity sensors: A review of materials and mechanisms. *Sensor Lett.* 3, 274–295 (**2005**).

9. Kuang, Q., Lao, C., Wang, Z. L., Xie, Z. &Zheng, L. High sensitivity humidity sensor based on a single SnO2 nanowire. *J. Am. Chem. Soc.* 129, 6070–6071(**2007**).

10. Cheng, B., Tian, B., Xie, C., Xiao, Y. & Lei, S. Highly sensitive humidity sensor based on amorphous Al2O3 nanotubes. *J. Mater. Chem.* 21, 1907–1912 (**2012**).

11. Yin, H. et al. Porous V2O5 micro/nano-tubes: Synthesis via a CVD route, single tube-based humidity sensor and improved Li-ion storage properties. *J. Mater.Chem.* 22, 5013–5019 (**2011**).

12. Buvailo, A. I., Xing, Y., Hines, J., Dollahon, N. &Borguet, E. TiO2/LiCl based nanostructured thin film for humidity sensor applications. *ACS Appl. Mater. Interfaces* 3, 528–533 (**2011**).

13. Li, Z. et al. Highly sensitive and stable humidity nanosensors based on LiCl dopedTiO2 electrospun nanofibers. *J. Am. Chem. Soc*. 130, 5036–5037 (**2008**).

14. Steele, J. J., Taschuk, M. T. & Brett, M. J. Nanostructured metal oxide thin films for humidity sensors. *IEEE Sens. J.* 8, 1422–1429 (**2008**).

15. Feng, J. et al. Giant moisture responsiveness of VS2 ultrathin nanosheets for novel touchless positioning interface. *Adv. Mater.* 24, 1969–1974 (**2012**).

16. Jiang, P. et al. Aluminium doped n-type ZnS nanowires as high-performance UVand humidity sensors. *J. Mater. Chem*. 22, 6856–6861 (**2012**).

17. Borini, S. et al. Ultrafast graphene oxide humidity sensors. *ACS Nano* 7, 11166–11173 (**2013**).

18. Alwis, L., Sun, T. & Grattan, K. T. V. Optical fibre-based sensor technology for humidity and moisture measurement: Review of recent progress. *Measurement* 46, 4052–4074 (**2013**).

19. Yeo, T. L., Sun, T. & Grattan, K. T. V. Fibre-optic sensor technologies for humidity and moisture measurement. *Sens. Actuators, A* 144, 280–295 (**2008**).

20. Mehrabani, S., Kwong, P., Gupta, M. & Armani, A. M. Hybrid microcavity humidity sensor. *Appl. Phys. Lett.* 102, 241101–241104 (**2013**).

21. Steffens, C., Manzoli, A., Leite, F. L., Fatibello, O. & Herrmann, P. S. P. Atomic force microscope microcantilevers used as sensors for monitoring humidity. *Microelectron. Eng.* 113, 80–85 (**2014**).

22. Sharma, A. K. & Gupta, A. Design of a plasmonic optical sensor probe for humidity monitoring. *Sens. Actuators, B* 188, 867–871 (**2013**).

23. Amin, E. M. & Karmakar, N. C. Development of a low cast printable chipless RFID humidity sensor. *IEEE Sens. J.* 14, 1 (**2014**).

24. Mattana, G. et al. Woven temperature and humidity sensors on flexible plastic substrates for e-textile applications. *IEEE Sens. J.* 13, 3901–3909 (**2013**).

25. Saeidi, N., Strutwolf, J., Marechal, A., Demosthenous, A. & Donaldson, N. ACapacitive humidity sensor suitable for CMOS integration. *IEEE Sens. J.* 13, 4487–4495 (**2013**).

26. Kulwicki, B. M. Humidity sensors. J. Am. Ceram. Soc. 74, 697–708 (1991).27. Dimitrakopoulos, C. D. &Malenfant, P. R. L. Organic thin film transistors for large area electronics. *Adv. Mater*. 14, 99–117 (**2002**).

28. Guo, Y., Yu, G. & Liu, Y. Functional organic field-effect transistors. *Adv. Mater*. 22, 4427–4447 (**2010**).

29. Toniolo, R. & Hummelgen, I. A. Simple and fast organic device encapsulation using polyisobutene. *Macromol. Mat. Eng.* 289, 311–314 (**2004**).

30. Hoeben, F. J. M., Jonkheijm, P., Meijer, E. W. &Schenning, A. P. H. J. Aboutsupramolecular assemblies of p-conjugated systems. *Chem. Rev*. 105, 1491–1546 (**2005**).

31. Aida, T., Meijer, E. W. &Stupp, S. I. Functional supramolecular polymers. *Science* 335, 813–817 (**2012**).

32. Fabiano, S. et al. Supramolecular order of solution processed perylene diimide thin films: High performance small-channel n-type organic transistors. *Adv. Funct. Mater*. 21, 4479–4486 (**2011**).

33. Huang, Z. et al. Pulsating tubules from noncovalent macrocycles. *Science* 337, 1521–1526 (**2012**).

34. Operamolla, A. & Farinola, G. M. Molecular and supramolecular architectures of organic semiconductors for field effect transistor devices and sensors: A synthetic chemical perspective. *Eur. J. Org. Chem*. 3, 423–450 (**2011**).

35. Moulin, E., Cid, J.-J. &Giuseppone, N. Advances in supramolecular electronics –from randomly self-assembled nanostructures to addressable self-organized interconnects. *Adv. Mater.* 25, 477–487 (**2013**).
36. Schenning, A. P. H. J. & Meijer, E. W. Supramolecular electronics; nanowires from self-assembled small p-conjugated systems. *Chem. Commun*. 26, 3245–3258 (**2005**).

37. Herzer, N. et al. Printable optical sensors based on H-bonded supramolecular cholesteric liquid crystal networks. *J. Am. Chem. Soc*. 134, 7608–7611 (**2012**).

38. Briseno, A. L., Mannsfeld, S. C. B., Jenekhe, S. A., Bao, Z. & Xia, Y. Introducing organic nanowire transistors. *Mater. Today* 11, 38–47 (**2008**).

39. Zang, L., Che, Y. & Moore, J. S. One-dimensional self-assembly of planar conjugated molecules: Adaptable building blocks for organic nanodevices. *Acc. Chem. Res*. 41, 1596–1608 (**2008**).

40. Zhang, C., Yan, Y., Sheng Zhao, Y. & Yao, J. Synthesis and applications of organic nanorods, nanowires and nanotubes. *Ann. Rep. Prog. Chem. Sect. C* 109, 211–239(**2013**).

41. Min, S.-Y. et al. Large-scale organic nanowire lithography and electronics. *Nat. Commun.* 4, 1773 (**2013**).

42. Sagade, A. A. et al. High mobility field effect transistors based on supramolecular charge transfer nanofibres. *Adv. Mater*. 25, 559–564 (**2013**).

43. Rao, K. V., Jayaramulu, K., Maji, T. K. & George, S. J. Supramolecular hydrogels and high aspect ratio nanofibers through charge transfer induced alternate co-assembly. *Angew. Chem. Int. Ed*. 49, 4218–4222 (**2010**).

44. Sagade, A. A., Venkata Rao, K., George, S. J., Datta, A. & Kulkarni, G. U. A charge transfer single crystal field effect transistor operating at low voltages. *Chem. Commun*. 49, 5847–5849 (**2013**).

Chapter IIIB

Supramolecular Humidity Sensor for Breathing Applications

Summary

In this section of the chapter, as fabricated ultrafast response humidity sensor was demonstrated as a novel breath sensor which can monitor any respiration rate. Using two humidity sensors, a breath flow sensor was made which could simultaneously measure the RH as well as the flow rate of exhaled nasal breath. The integrated device was used for monitoring exhaled breath volunteers undergoing exercise and alcohol-induced dehydration.

IIIB.1 Introduction

Motivated by the fast response and sensitivity of the supramolecular humidity sensor, it is interesting to explore the usefulness of this device in monitoring human breath, particularly during exhalation, as the humidity in the exhaled breath is higher compared to inhaled (ambient) air. Such a device should be of importance in breath analysis. Recently, characterization of exhaled breath has become a simple yet powerful non-invasive method of diagnosing diseases such as asthma, cancer, diabetes etc [1-6]. Any such monitoring of exhaled breath should be an online process which can keep track of changes in every breath cycles [7, 8]; off-line trace gas analysis suffers from inherent problems associated with sample preparation and storage, contamination, chemical transformation of the analytes, etc. [8]. While monitoring analytes for specific diseases is important, monitoring humidity itself can possibly throw some light on an individual's health such as dehydration. Although there are many indices suggested in the literature to indicate body hydration status [9-12], for the first time, an attempt has been made to monitor the dehydration through RH in the breath.

IIIB.2 Scope of the present investigation

Due to the poor response of available humidity sensors, it was not possible to monitor the continuous humidity variation in the nasal breath which is envisaged to give health conditions of a living being. The present investigation is related to exploiting the fast response of the fabricated humidity sensor for breath related applications. High sensitivity, as well as the fast response of the present humidity sensor, make it an ideal candidate for monitoring breath of any rate. Further, simultaneous detection of the flow along with humidity of the breath can possibly give new pathways in the area of non-invasive diagnostic techniques.

IIIB.3 Experimental section

The fabrication of supramolecular humidity sensor is explained in the previous chapter. Briefly, a drop (5 μL, 1 mM) of the already prepared CS-DMV nanofibre solution was drop coated on gold gap electrodes on glass and was allowed to dry for an hour. Every sensor was calibrated using known humidity and calibration equations. The details of live demonstration experiments are described in the respective experiment of the chapter.

IIIB.4 Results and discussion

Continuous monitoring of breath: Working with a healthy adult male, the variations in the RH value were monitored by holding the nanofibre device at a distance of 3.5 cm from the nose while breathing normally. Interestingly, the RH over the device showed sharp rise during exhaling and dropped to ambient value while inhaling, which was nearly repetitive corresponding to the breathing cycles (see Figure IIIB.1a). Further, the device could efficiently follow the breathing, no matter how fast or slow it was (Figure IIIB.1b). In the panel given, the breathing varied from 0.3 to 5 s per cycle. Importantly, the nanofibres in the device were stable throughout. Thus device could continuously monitor every breath cycles of the person. Such continuous monitoring of exhaled breath tracks the changes in every breath cycles and hence overcomes several disadvantages associated with the offline trace gas analysis, such as sample preparation and storage, contamination, chemical transformation of the analytes, etc.

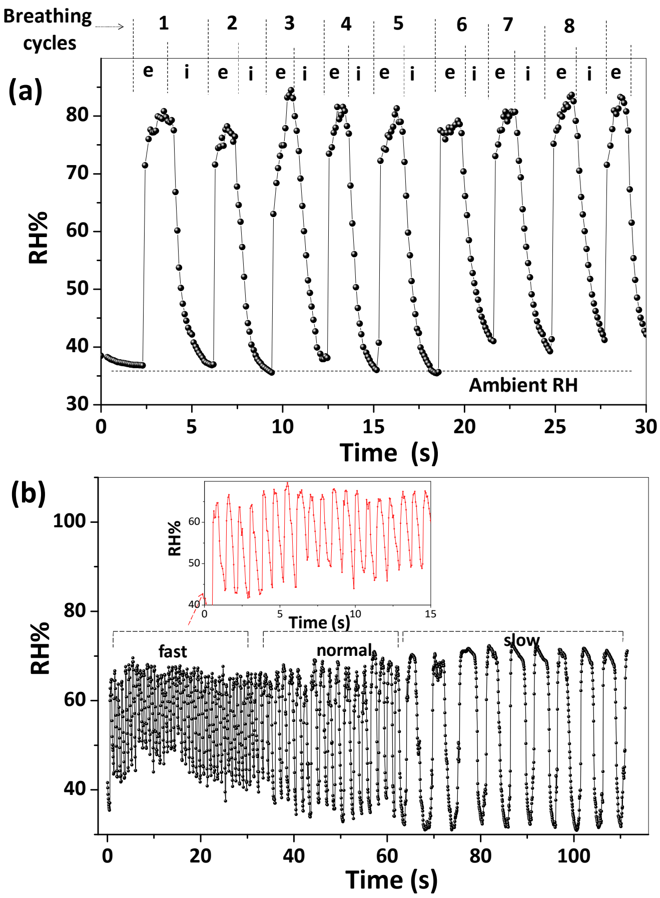

Figure IIIB.1 A breath RHgram

(a) Variations in the RH of the exhaled breath of a healthy person breathing at a distance of 3.5 cm from the sensor. 'e' and 'i' refer to the exhaling and inhaling respectively. (b) Response of the sensor at different breathing rates. Inset shows zoomed in part of the response corresponding to fast breathing.

Portable breath RHgram: To make online monitoring of exhaled breath, a portable (stand-alone) device (RHgram) was fabricated which can be carried to any remote location. The block diagram of the fabricated RHgram is shown in Figure IIIB.2a. It consists of a microcontroller unit where the nanofibre sensor is interfaced through a DC jack with a supply of 1V. The sensor output response (in voltage) is converted into pre-calibrated humidity values and displayed on both the LCD and LED bar graph as shown Figure IIIB.2b. An RS 232 communication port is provided for the transfer of data between RHgram and computer through which individual breath cycles can be obtained, thus making online breath monitoring possible. It is important note that though the nanofibre exhibit the nA range current, it would not pose any challenge in actual practical context.

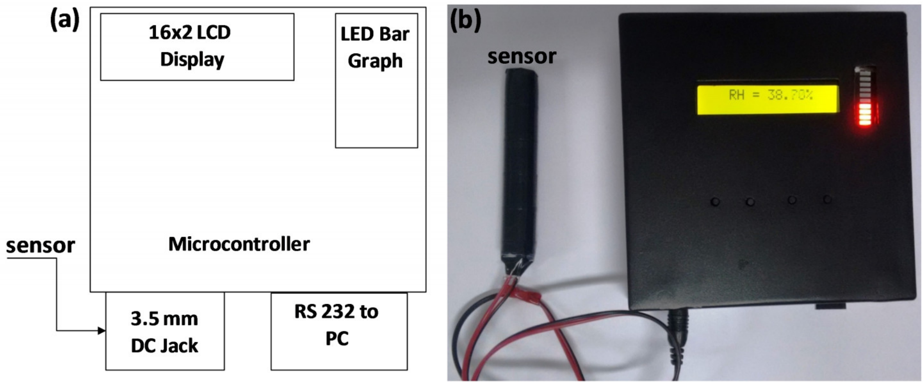

Figure IIIB.2 Fabrication of portable RHgram
(a) The block diagram of the device to fabricate RHgram. (b) Photograph of made RHgram with the connected sensor and both LCD and LED graph displaying humidity values.

Fabrication of flow cum humidity sensor: To increase the confidence in the humidity measurements, it is important to measure the humidity and flow of the exhaled breath, simultaneously. Therefore, a flow cum humidity sensor was fabricated using the CS-DMV nanofibres. The setup consists of two supramolecular humidity devices, D1 and D2, placed in a glass tube 8 cm apart. Two devices were connected in parallel with an applied bias of 1 V. Two resistors (20 MΩ each) were connected in series with the devices to give out voltage signals to an oscilloscope. A commercially available breathing receiving mask (typically used for oxygen supply to patients) was used to carry the exhaled breath over D1 and D2 sensors. After every breath, the stray humidity in the glass tube was driven away by flushing with dry N_2 for a second while the volunteer inhaled. The glass tube is connected to the breath receiving mask, through a flow divider (see Figure IIIB.3a); the latter was required as calibration using typical mass flow controllers proved difficult at realistic breath flow (~ 10 – 50 ksccm [13]). As an individual, breaths out into the mask, the divided flow reaches the sensor D1 at time t1 and D2 at time t2 (at half rising), and the time difference, Δt = t2 – t1 (see Figure

IIIB.3b) was used for calculating the flow. The humidity could be measured from both sensors using the respective calibration curves (see Figure IIIB.4).

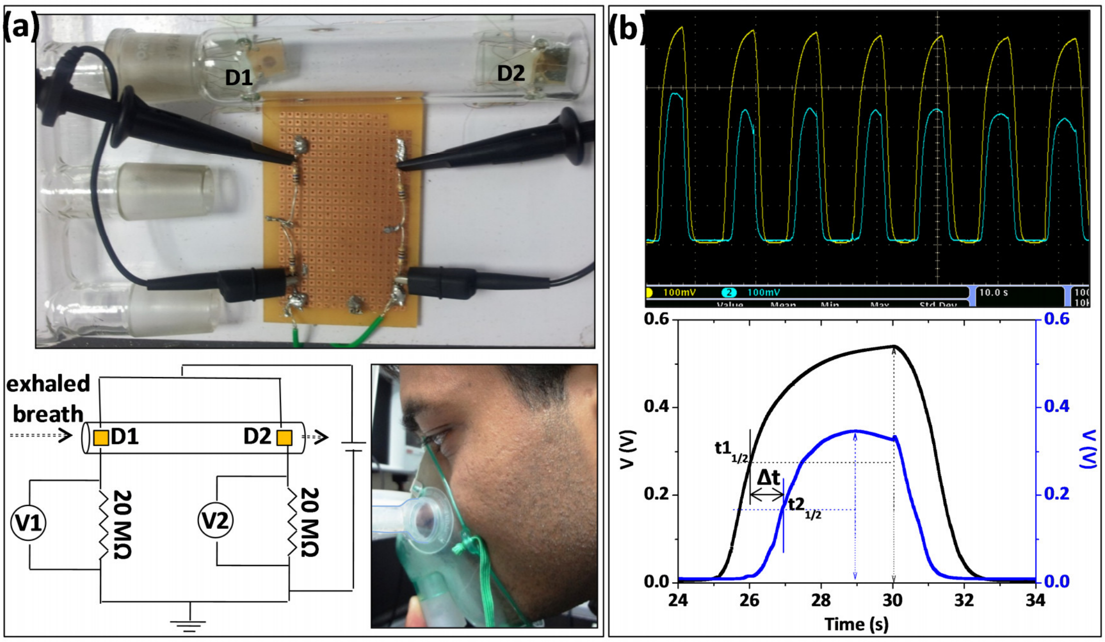

Figure IIIB.3 Integration of two humidity sensors flow cum humidity sensor
(a) A photograph of the humidity cum flow sensor is shown on top. It has two supramolecular humidity sensors, D1 and D2, placed apart at a distance of 8 cm inside a glass tube of inner diameter 21 mm. The circuit diagram of the experimental setup is shown below (left). A photograph of a volunteer performing breathing trial (below, right). (b) Simultaneous humidity and flow sensing from the integrated device. The screen image of oscilloscope output of exhaled breath from a healthy individual (top). Below is a single breathing cycle showing the calculation of 'Δt', the time difference between the two sensors to reach half of the peak value.

For calculation of RH, every peak value, V1, corresponding to every breath was noted down and converted to RH using calibration equation (derived from device D1).

$$\text{RH}\ (\%) = 29.59 \quad \ln\left(\frac{V1+0.0447}{0.0217}\right) \quad \text{.....................} \ \text{IIIB.1}$$

For calculation of flow rate, time difference, 'Δt' was calculated for every breath and converted into flow rate using the equation below:

$$\text{Flow} = \ 237.3 \quad \ln\left(\frac{53.93}{\Delta t - 0.758}\right) \quad 16 \quad \text{.....................} \ \text{IIIB.2}$$

where 16 is the dividing flow factor.

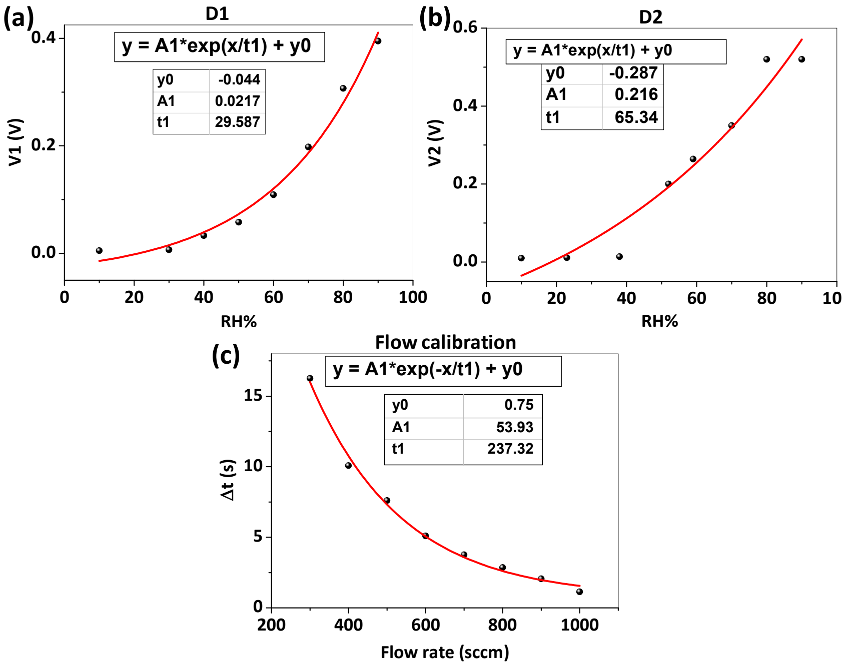

Figure IIIB.4 RH and flow calibration curves

Calibration of voltage measured with varying RH for the devices (a) D1 and (b) D2 respectively. The voltage was measured using an oscilloscope across 20 MΩ resistor connected to each device in series. As the humid air/exhaled breath reaches the devices, the current through the circuit increases and hence voltage drop across the resistor increases. The red curve is 1st order exponential fit and inset shown is equation and constants corresponding to it. (c) Calibration plot of the variation of time delay, Δt, with flow rate. The standard flow rate was obtained using mass flow controller. The red curve is the 1st order exponential fit and corresponding equation and constants are shown in inset.

Exercise-induced dehydration: The above setup was used in varied conditions of volunteers. In the study, the RH present in nasal breath was monitored rather than that from mouth, as the former can be considered as a better representative of the lung hydration levels (with no interference from mouth saliva). The volunteer was made to breath comfortably but consistently such that the flow rate of breath was in a reasonably narrow range (20–30 ksccm). Initially, volunteers in normal condition were asked to breath continuously and readings were recorded for over 30–50 cycles. Average RH and flow rate values obtained for volunteer 1 (male) in normal conditions were 88.8 ± 0.8% and 20.2 ± 0.8 ksccm respectively (see Figure IIIB.5a and e). The volunteer was then made to run around 10 km in nearly 1 hr. After relaxing for few minutes, both the quantities were measured again (see Figure IIIB.5b and e). It is interesting to see a sharp decline in the RH value in the exhaled breath after exercise (80.1 ± 0.3%), which is understandable as the volunteer got dehydrated due to perspiration. The volunteer was indeed feeling thirsty but was restrained from consuming food and water. They were kept in the dehydrated condition without consuming any drink or food including water for a period of next 1 hr and recorded the breathing cycles. When measurements were done, surprisingly, a gradual recovery of RH was found in the breath (84.4 ± 1.6%) (see Figure IIIB.5c and e) . It appears that water from the internal body fluid was diverted towards the respiratory system which reflects in the breath RH level returning to normalcy (90.1 ± 1.1%,). After this, the volunteers were allowed to take normal diet and water. After 4 hrs, once the volunteer attains his normal condition breathing cycles were again recorded (see Figure IIIB.5d and e)

Human lung tissue is known to maintain a high degree of wetness for efficient exchange of gases and when dehydration occurs, it is susceptible to dry out thereby reducing the water content in the exhaled breath. However, in the present study, it was found that the RH in the breath regained even under the dehydrated condition, clearly indicating that the lung tissue, by its nature, regenerated moisture on its (alveolar) surface from various metabolic processes. Upon water intake after the 1 hr measurement, the RH value completely regained (Figure IIIB.5). A similar but mild trend was observed in the case of a female volunteer who undertook to run 3 km in nearly 30 minutes (Figure IIIB.6).

Alcohol-induced dehydration: Another important situation of body dehydration relates to alcohol consumption [14]. Here, the relative humidity in the exhaled breath was examined to see the effect of alcohol consumption (but not as alcohol sensor). In the given two instances (Figure IIIB.7 and Figure IIIB.8), the male volunteers 3 and 4 after consuming alcohol (beer, 8% alcohol, 2 L) were restrained from consuming food and water. A decline in the RH was observed following the alcohol consumption due to dehydration in the body. However, the RH values recovered in spite of not feeding water (Figure IIIB.7 and Figure IIIB.8). The breathing cycles were recorded before and after consumption of alcohol at different time intervals i.e. just after, after1 hr, after 2 hr and after 4 hr. During this period, volunteers were restrained from consuming any food and water to keep the volunteer in dehydrating conditions. After this, they were allowed to drink water and common diet. At the end, after 20 hr of alcohol consumption when the volunteers regain their normal conditions, breathing cycles were again recorded.

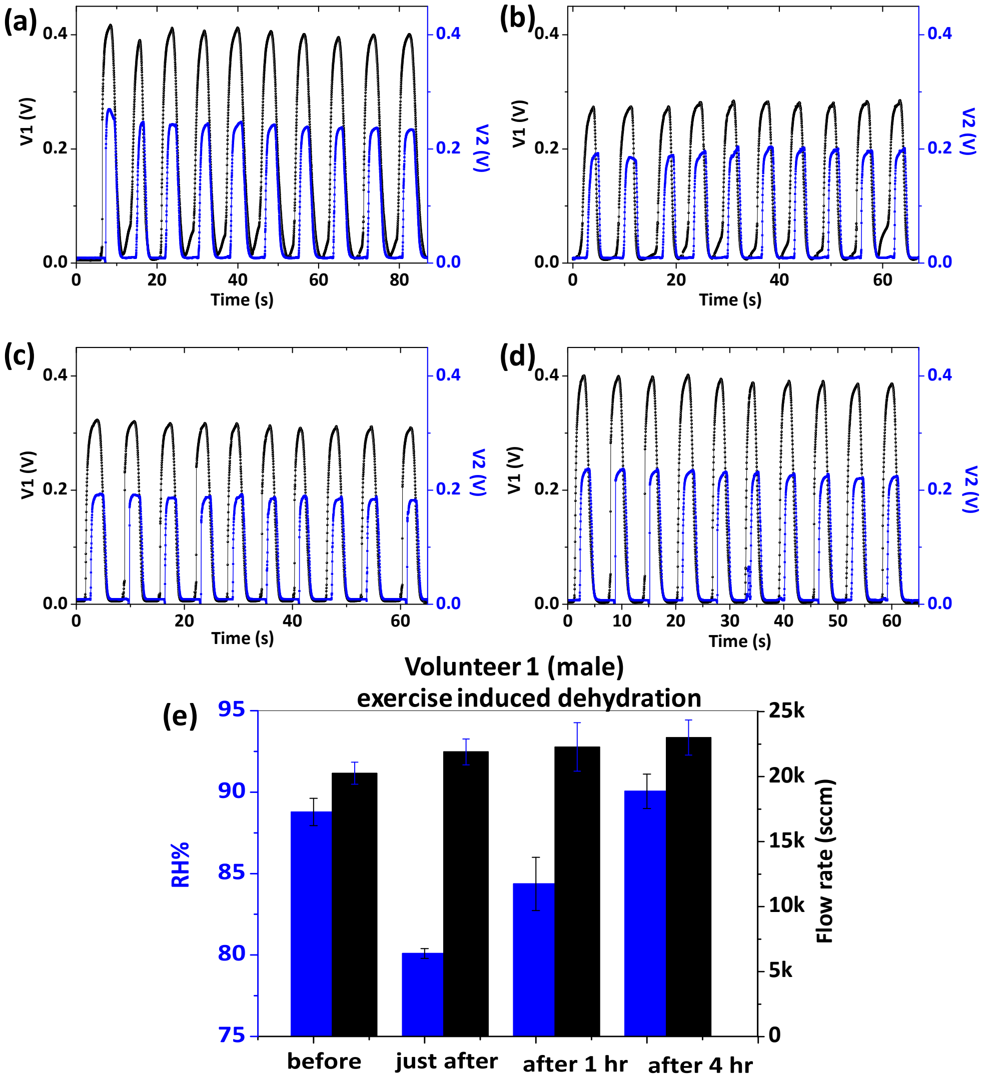

Figure IIIB.5 Demonstration of exercise-induced dehydration (volunteer 1)
A portion of continuous breathing cycles (10 cycles) from the volunteer1 (male) at different stages of exercise. **a**. before exercise. **b**. just after exercise. **c**. after 1 hr of exercise. **d**. after 4 hr of exercise where the person is allowed to take diet and retain back normal conditions. (e) Histogram plots showing the variation of RH and flow in the exhaled breath of volunteer 1 (male) undergoing exercise-induced dehydration.

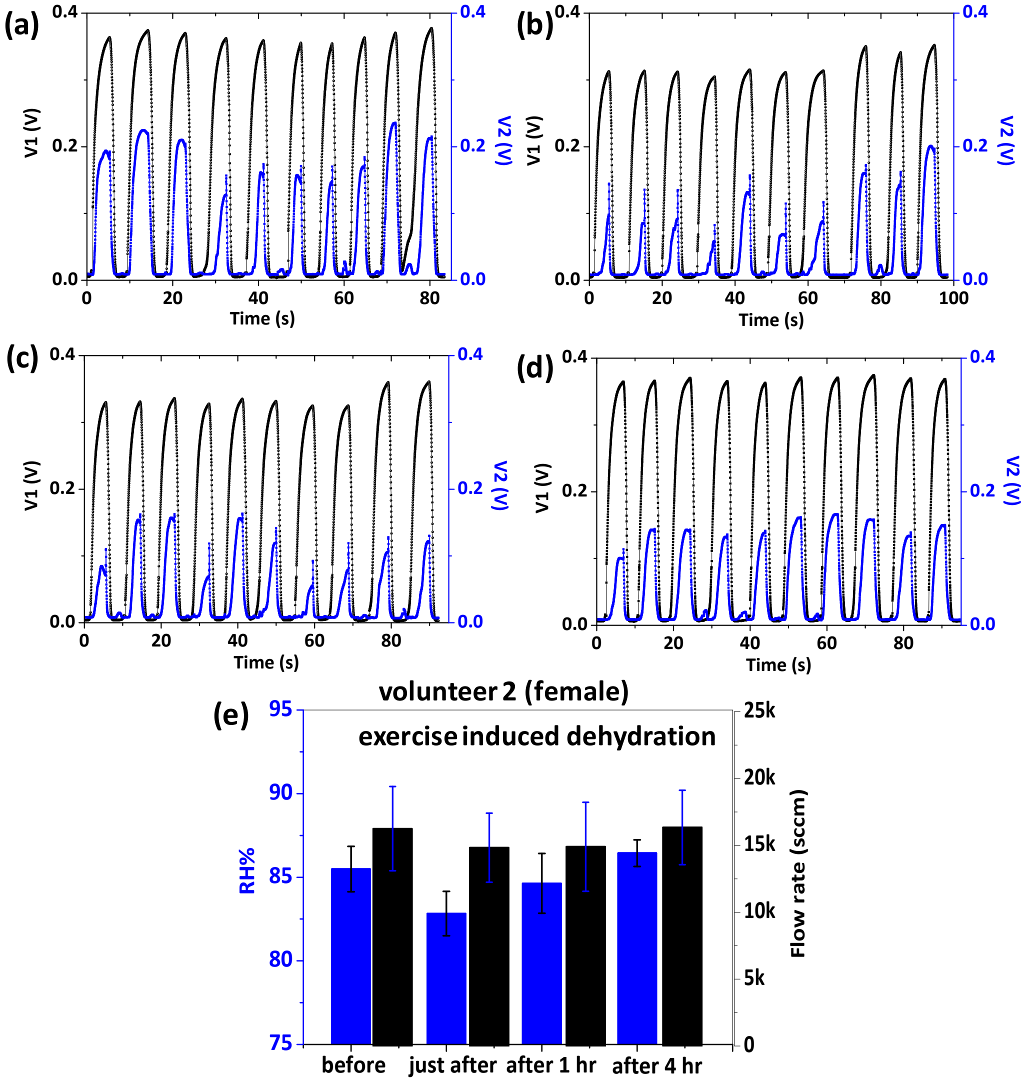

Figure IIIB.6 Demonstration of exercise-induced dehydration (volunteer 2)

A portion of continuous breathing cycles (10 cycles) from the volunteer2 (female) at different stages of exercise. **a**. before exercise. **b**. just after exercise. **c**. after 1 hr of exercise. **d**. after 4 hr of exercise where the volunteer is allowed to take diet and retain back normal conditions. Histogram plots showing the variation of RH and flow in the exhaled breath of volunteer 2 (female) undergoing exercise-induced dehydration.

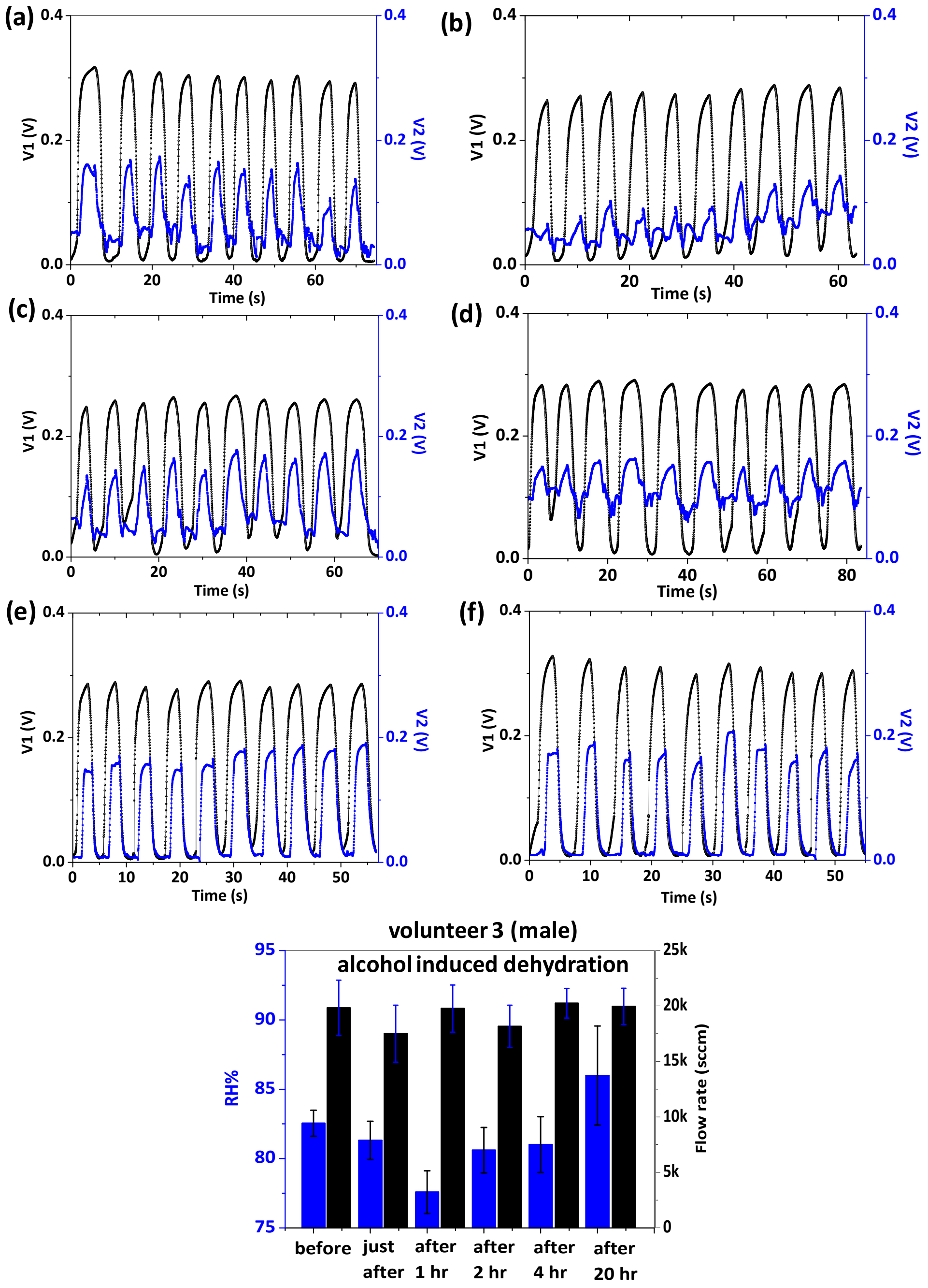

Figure IIIB.7 Demonstration of alcohol-induced dehydration (volunteer 3)

A portion of continuous breathing cycles (10 cycles) from a male volunteer 3 at different stages of alcohol consumption. **a**. before consumption. **b**. just after consumption. **c**. after 1 hr of consumption. **d**. after 2 hr of consumption. **e**. after 4 hr of consumption. **f**. after 20 hr of consumption where the person is allowed to take food and retain back normal conditions.(e) Histogram plots showing the variation of RH and flow in the exhaled breath of volunteer 3 (male) undergoing alcohol-induced dehydration.

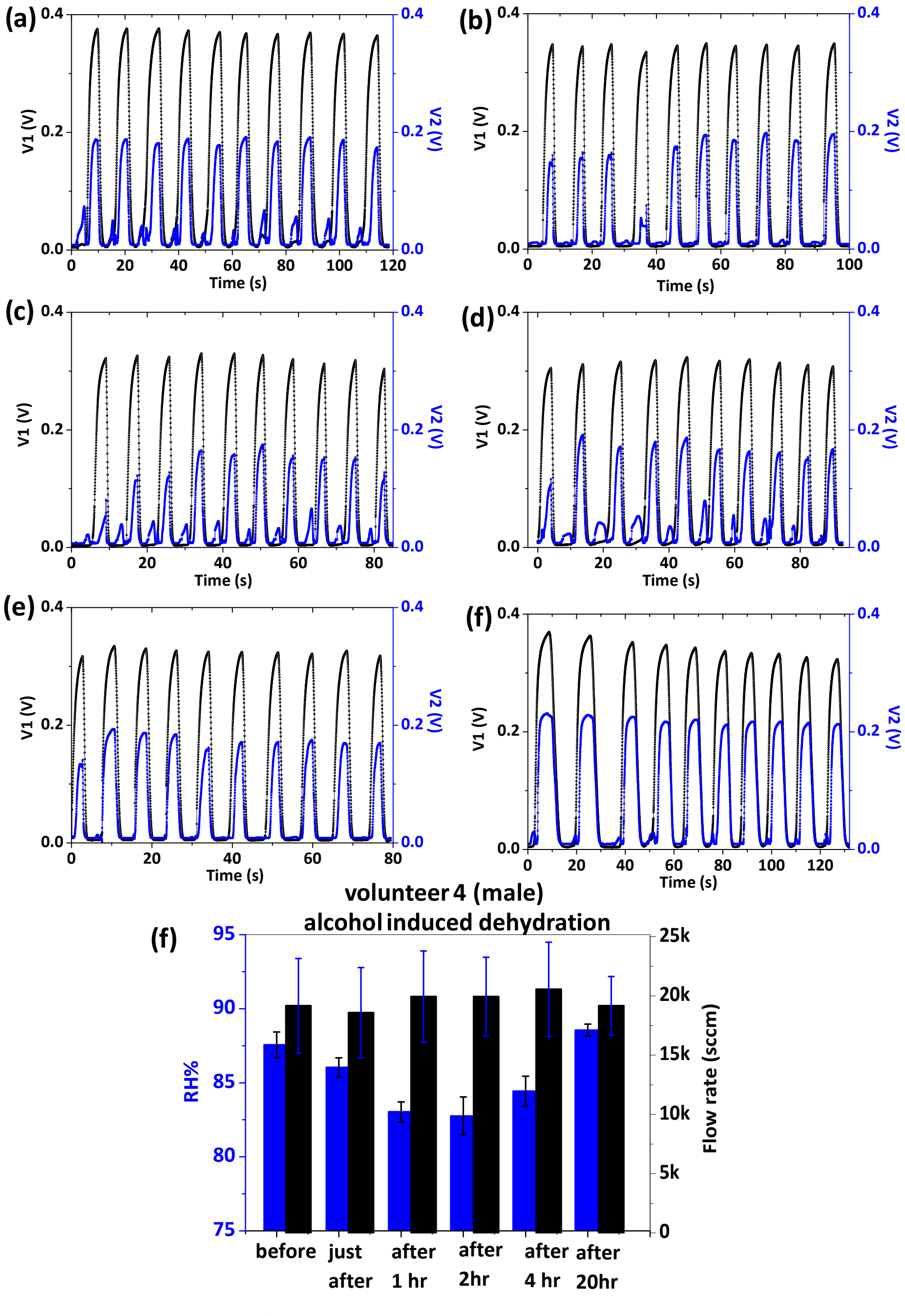

Figure IIIB.8 Demonstration of alcohol-induced dehydration (volunteer 4)
A portion of continuous breathing cycles (10 cycles) from a male volunteer 3 at different stages of alcohol consumption. **a**. before consumption. **b**. just after consumption. **c**. after 1 hr of consumption. **d**. after 2 hr of consumption. **e**. after 4 hr of consumption. **f**. after 20 hr of consumption where the person is allowed to take food and retain back normal conditions.(e) Histogram plots showing the variation of RH and flow in the exhaled breath of volunteer 4 (male) undergoing alcohol-induced dehydration.

Table IIIB.1 BAC (%) of volunteers at different stages of alcohol consumption

	Before alcohol	Just after alcohol	After 1 hr	After 2 hr	After 4 hr	After 20 hr
Volunteer 1	0	0.05	0.12	0.08	0.07	0
Volunteer 2	0	0.04	0.13	0.09	0.07	0

The variation in breath alcohol concentration (BAC) was monitored at every stage; RH declined with increased BAC (Table IIIB.1). The situation is similar to that induced by physical exercise. Among many other control experiments, we have also monitored the RH of exhaled breath when a volunteer was made to drink plenty of plain water to cause excessive hydration; indeed, it was well reflected in the breath RH measurements (Figure IIIB.9). Thus in this study, both flow and RH was measured for every cycle where flow in narrow range ensures good sampling, removing other influences on RH. While this is a preliminary study of body dehydration monitored through RH in the breath, the study should open up new insights into diagnosis through breath analysis.

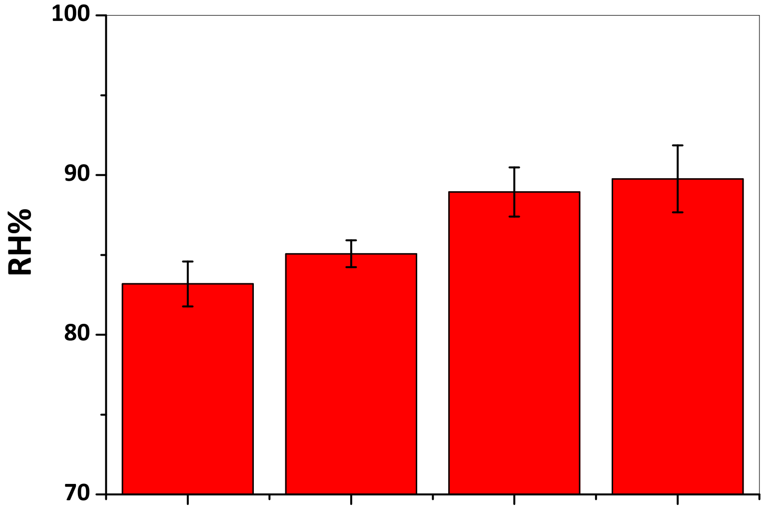

Figure IIIB.9 Histogram of RH in exhaled breath during hyperhydration
After making the volunteer drink half a litre of ORS (Electoral) dissolved in water, further breath cycles were recorded. The improving RH in the breath is evident.

IIIB.5 Conclusions

Fast response devices made of few nanofibres have been effectively employed for dynamic monitoring of human breath. Using two such devices in a circuit, a flow cum humidity sensor has also been fabricated and its application has been demonstrated in analysing dehydrated conditions. As the sensing element is a simple organic system from solution processes, these devices are essentially of low cost and also environment-friendly. Potential applications in personal healthcare as use-and-dispose devices, is evident.

References

1. Niesters, M. et al. Validation of a novel respiratory rate monitor based on exhaled humidity. *Br. J. Anaesth.* 109, 981-989 (**2012**).

2. Hakim, M. et al. Diagnosis of head-and-neck cancer from exhaled breath. *Br. J. Cancer* 104, 1649-1655 (**2011**).

3. Kim, K.H., Jahan, S.A. &Kabir, E. A review of breath analysis for diagnosis of human health.*Trends Anal. Chem.* 33, 1-8 (**2012**).

4. Peng, G. et al. Detection of lung, breast, colorectal, and prostate cancers from exhaled breath using a single array of nanosensors. *Br. J. Cancer* 103, 542-551 (**2010**).

5. Peng, G. et al. Diagnosing lung cancer in exhaled breath using gold nanoparticles. *Nat. Nano.* 4, 669-673 (**2009**).

6. Righettoni, M., Tricoli, A. &Pratsinis, S.E. Si:WO_3 sensors for highly selective detection of acetone for easy diagnosis of diabetes by breath analysis. *Anal.Chem.* 82, 3581-3587 (**2010**).
7. Tisch, U. &Haick, H. *Rev. Chem. Eng.* 26 171 (**2010**).

8. Boshier, P.R. et al. On-line, real-time monitoring of exhaled trace gases by SIFT-MS in the perioperative setting: a feasibility study. *Analyst*136, 3233-3237 (**2011**).

9. Smith, D. &Spanel, P. The challenge of breath analysis for clinical diagnosis and therapeutic monitoring.*Analyst* 132, 390-396 (**2007**).

10. Armstrong, L.E. Hydration assessment techniques. *Nutr. Rev.* **63**, S40-S54 (**2005**).

11. Perrier, E. et al. Hydration biomarkers in free-living adults with different levels of habitual fluid consumption. *Br. J. Nutr.* 109, 1678-1687 (**2013**).

12. Shirreffs, S.M. Markers of hydration status. *Eur. J. Clin. Nutr.* 57, S6-S9 (**2003**).

13. Gupta, J.K., Lin, C.-H. & Chen, Q. Characterizing exhaled airflow from breathing and talking. *Indoor Air* 20, 31-39 (**2010**).

14. Hobson, R.M. &Maughan, R.J. Hydration status and the diuretic action of a small dose of alcohol. *Alcohol Alcohol.* 45, 366-373 (**2010**).

Chapter IIIC

Humidity Based Memory Sensor

Summary

In this section, the fabrication of a humidity based memory sensor has been detailed which has the ability to memorise an unknown humidity it has experienced in the past. Here, the current decay behaviour of supramolecular nanofibre with exposure to humidity was utilised to fabricate the sensor. The device can be switched between two current states which gives memory states to the device. The switching between two states can be performed by interplaying with an external humidity pulse.

IIIC.1 Introduction

Conventionally, memory is stored either digitally [1-3], in the form of 0 and 1, or in the analogue form, for instance, as an electric signal in magnetic tape [4, 5].There are other contexts in which storage of passing event signal becomes important. It may be to do with local changes in temperature, pressure, sound, light, humidity and so on. There have not been many attempts in the literature to design and fabricate devices which memorise past states, perhaps due to lack of availability of relevant active materials which could serve in sensors.

It is only recently that there is an upsurge in this field of recording physical quantities of the past as memory. For example, there are shock and pressure sensors [6-11] which when attached to a package, can sense any shock or tension exerted on the package. New types of labels and indicators have come into the market which monitor the health of vegetables and fruits [12 -14]. Recently, Ham et al, using gold nanoparticles embedded in a polymer matrix, reported a colorimetric sensor which remembers the stress it has undergone [15]. Stimuli-responsive materials, especially shape memory polymers, have been investigated in which shape of the polymer changes when physical quantities such as temperature, light, pH, heat, electricity etc. are varied around [16-19]. These sensors are being increasingly used in industries particularly in smart packaging during transport and distribution. The smart packaging, containing time-temperature indicators (TTIs), ripeness indicators, chemical sensors and radio frequency identification (RFID) as main components, has found widespread attention to assist in ascertaining the authenticity, traceability, tamper evidence, theft protection as well as safety of a good [20].

IIIC.2 Scope of the present investigation

As detailed in the introduction, there have been many sensors for detecting physical quantities like strain, temperature, pressure, chemicals etc. which can memorise the past state these have experienced. However, there is no humidity sensor which can memorise the past humidity it has been taken through. This may find many applications in contexts where ensuring a particular humidity is a must. The present investigation details out the design and fabrication of a humidity based memory sensor.

IIIC.3 Experimental section

The fabrication of humidity sensor is explained in the previous chapter. Briefly, a drop (5 µL, 1 mM) of the already prepared CS-DMV nanofibre solution was drop coated on gold gap electrodes on the glass and allowed to dry for an hour. Every sensor was calibrated using known humidity and calibration equation was obtained to get the unknown humidity values.

IIIC.4 Results and discussion

Figure IIIC.1 is the schematic of the simple two probe device, which consists of two gold electrodes, separated by 10 µm channel length, on a glass substrate. A dispersion of supramolecular nanofibre (1 mM, 10 µL) was placed on it and allowed to vacuum evaporate for an overnight. The details of self-assembly of donor and acceptor molecules to form nanofibre are explained in section IIIA.3.

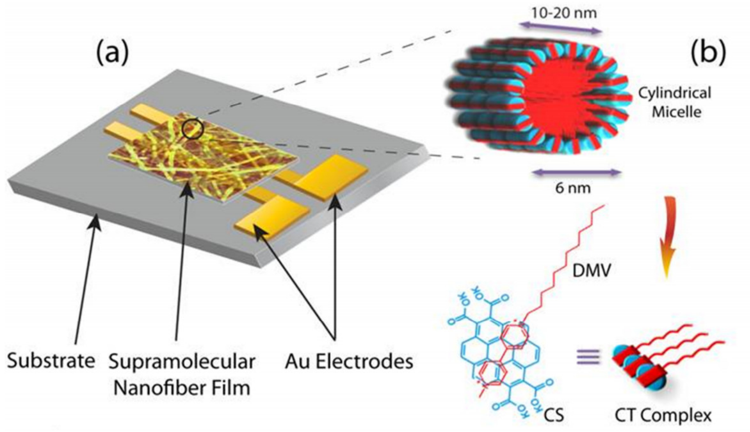

Figure IIIC.1 Schematic of fabrication of the device.
(a) Schematic representation of sensor fabrication and its active elements. AFM image of nanofibre is merged onto electrodes. (b) Schematic of self-assembly of donor-acceptor molecules to form nanofibres.

As described in Figure IIIA.b (Chapter IIIA), the conductivity of the supramolecular nanofibre exhibits a decay behaviour upon exposing to constant RH (70%). The initial jump is termed as state 1 (briefly S1) and the decayed nearly steady current state as S2. Figure IIIC.2 also contains data from RH cycles (5 – 70%). During the first RH cycle, as the RH value increased, the current increased rapidly to S1 and decreased to zero as RH was withdrawn, due to the humidity sensing action. For subsequent RH cycles, the magnitude of current jump upon exposing to RH decreased gradually. Interestingly, the decrease in the jump value was such that it closely mimicked the decay behavior obtained with exposing to constant RH. Thus the nanofibre behaves as though it remembers the jump value in the preceding RH cycle. Importantly, this ‘memory effect’ does not seem to depend on the time period of the RH cycle, the sequence of the time periods as well as the time gap, if any, between the cycles (see Figure IIIC.2). Based on this striking behaviour, a humidity memory device was conceived.

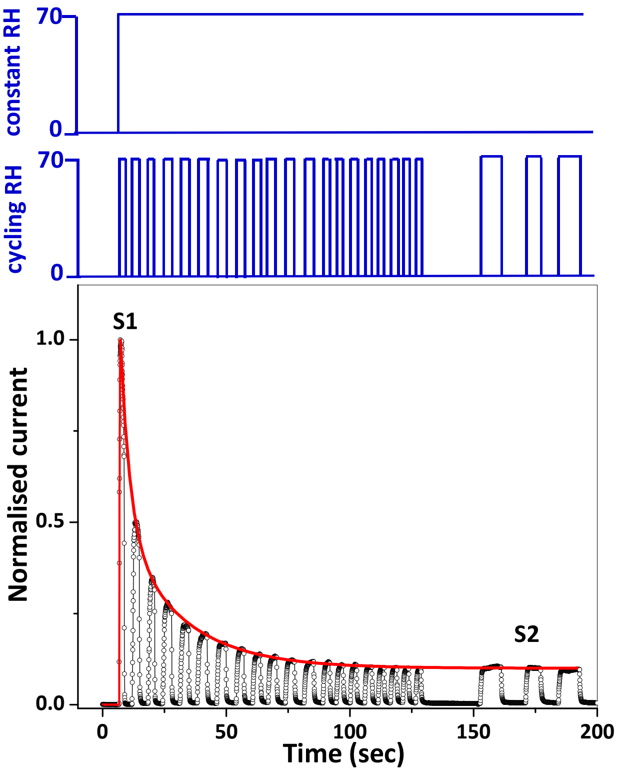

Figure IIIC.2 Decay behavior of nanofibre with humidity

Transient change in conductivity of nanofibre with RH cycles (black curve) and constant RH (red curve). The changes in conductivity with change in RH are color coordinated. The current states S1 and S2 are indicated.

Before taking up discussion on memory action, two RH based terms are to be defined, namely the curing RH pulse (CP) and the testing RH pulse (TP). The CP is defined as the RH pulse, the magnitude of which decides the memory state of the device. The TP is the RH pulse which is used for probing the effect of CP, in other words, it is a reading pulse. Thus, reading with TP is done with a fixed operating voltage. While for CP, the voltage is off. In the study, TP is held at 70% RH, unless otherwise mentioned. The pulse widths are typically few seconds.

The design of the device is as follows (see Figure IIIC.3). In Region 1, corresponding to the reading with two TPs separated by ~ 8 seconds, the memory action followed, which is already described in Figure IIIC.2. The applied voltage (1 V) was turned off at 30 seconds and turned ON again after 10 seconds (Region 2). Subsequent introduction of a TP gave rise to an S2 type signal, reinforcing the memory action from the passive state of the device. However, when a CP was introduced with the voltage off, the subsequent reading with a TP (Region 3) showed an S1 type signal implying the memory effect on the device in its passive state exposed to a different RH value. In other words, the device could remember (Region 2) or forget (Region 3) the S2 type signal, the rewriting being done by CP.

An insight into the memory action of the nanofibre is explained. Humidity restructures the nanofibre to put into a conductive state (see Region 1) depending on the magnitude. More the humidity, the better is the conducting nature of the nanofibre as detailed in Chapter IIIA. This is reflected in the initial current flow (jump) corresponding to an applied voltage. Once having been subjected to a given voltage, an electric field induced stress sets in within the nanofibre, perhaps disturbing the molecular orientation thus increasing the nanofibre resistance. It appears that this disorder once nucleated, spreads across the nanofibre leading to a gradual decrease in the current (or decay current) with time. This spreading of the disorder continues irrespective of the humidity level (see tracing of red dotted curve in Region 1 in Figure IIIC.3 and Figure IIIC.2). Similarly, the spreading continues even after the voltage is withdrawn, as seen between Regions 1 and 2. The above behaviour is reminiscent of a self-assembly process.

It is clear that the disorder can be lifted from the nanofibre only when the voltage is off. Importantly, the extent to which the recovery takes place would depend on the magnitude of the humidity the nanofibre is subsequently exposed to, which is here done through a CP. Accordingly, when a CP of 70% was given with voltage being off between Regions 2 and 3, the device recovered back to the S1 state (Figure IIIC.3), with no memory of the past states.

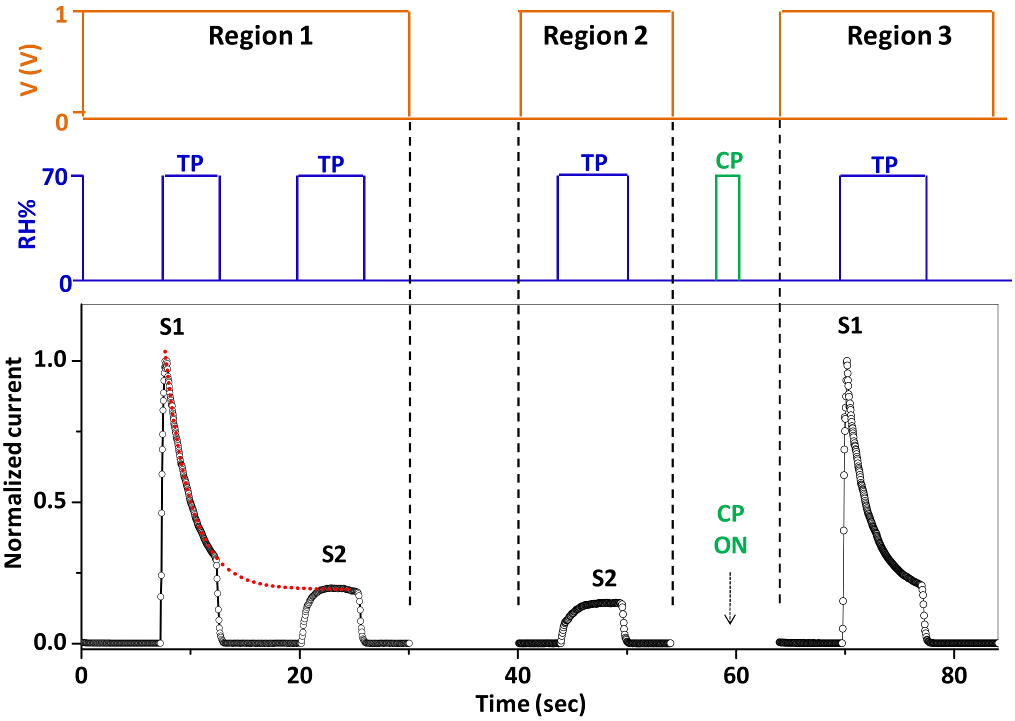

Figure IIIC.3 Memory action of the device

The change in conductive behaviour of the nanofibre with the change in RH in three regions. The sequence of voltage (orange curve) and RH values (blue curve for TP, green curve for CP) are given in three regions.

The influences of the magnitude of CP, the number of CPs and their sequence, and the time of exposure of CP have been studied in detail, which are described below. As explained previously, the extent to which the voltage stress can be recovered depends on the CP values introduced (note that while introducing CP, the voltage is always off) as described in Figure IIIC.4. In order to ensure the reliability of removal of the past memory states, the device was fed with CPs of random values (green curve). One can readily see that the resultant TP-induced current (black curve) varied simply following the magnitude of the CP. These dissimilar responses obtained corresponding to the different CPs, TP value being the same, can give an alternative way to assess whether the measured RH is a true value or it was influenced by other RH (here it is CP) conditions.

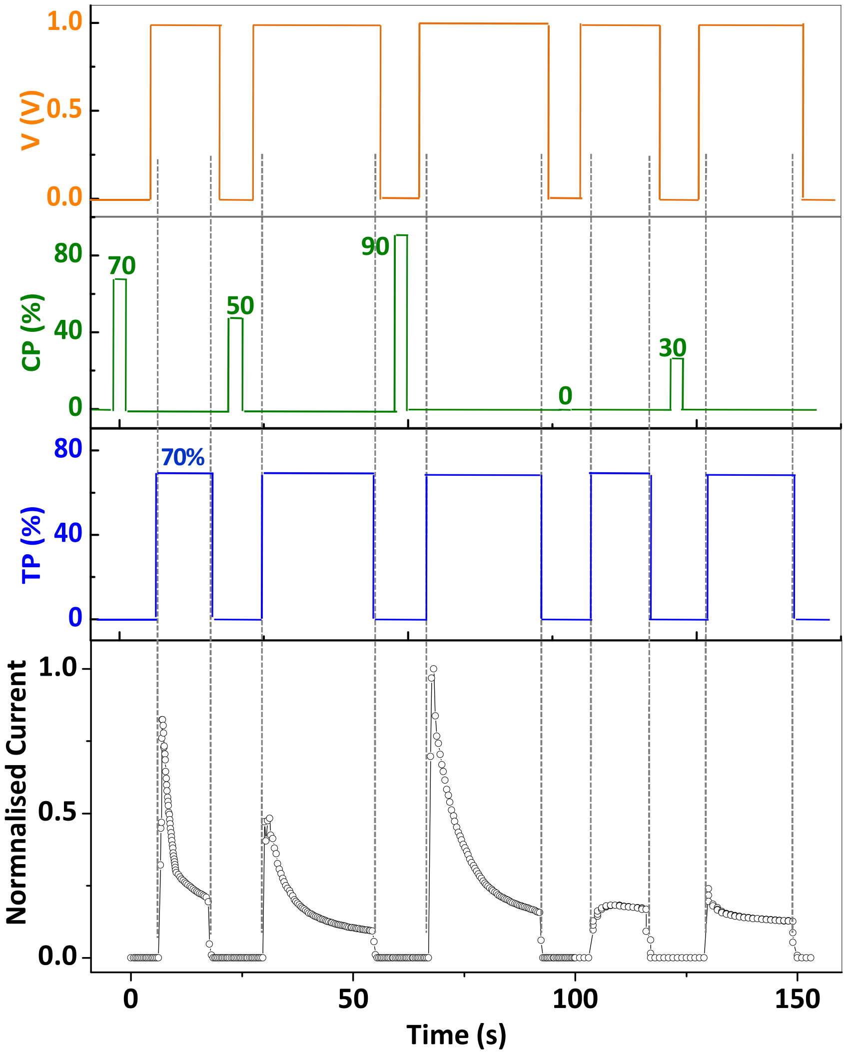

Figure IIIC.4 CP-dependent response of the device

Device response (black curve) measured with TP (blue curve) when different CPs (green curve) was introduced at V_{OFF}. All plots follow same time scale. The vertical lines are drawn for time coordination.

To convert the measured current response to RH values of different CPs, the current responses were measured by feeding the CP at the same value as TP at different values of the latter (Figure IIIC.5). The average jump current values were calculated over many cycles for each TP value and a calibration curve was obtained as shown in Figure IIIC.6a.

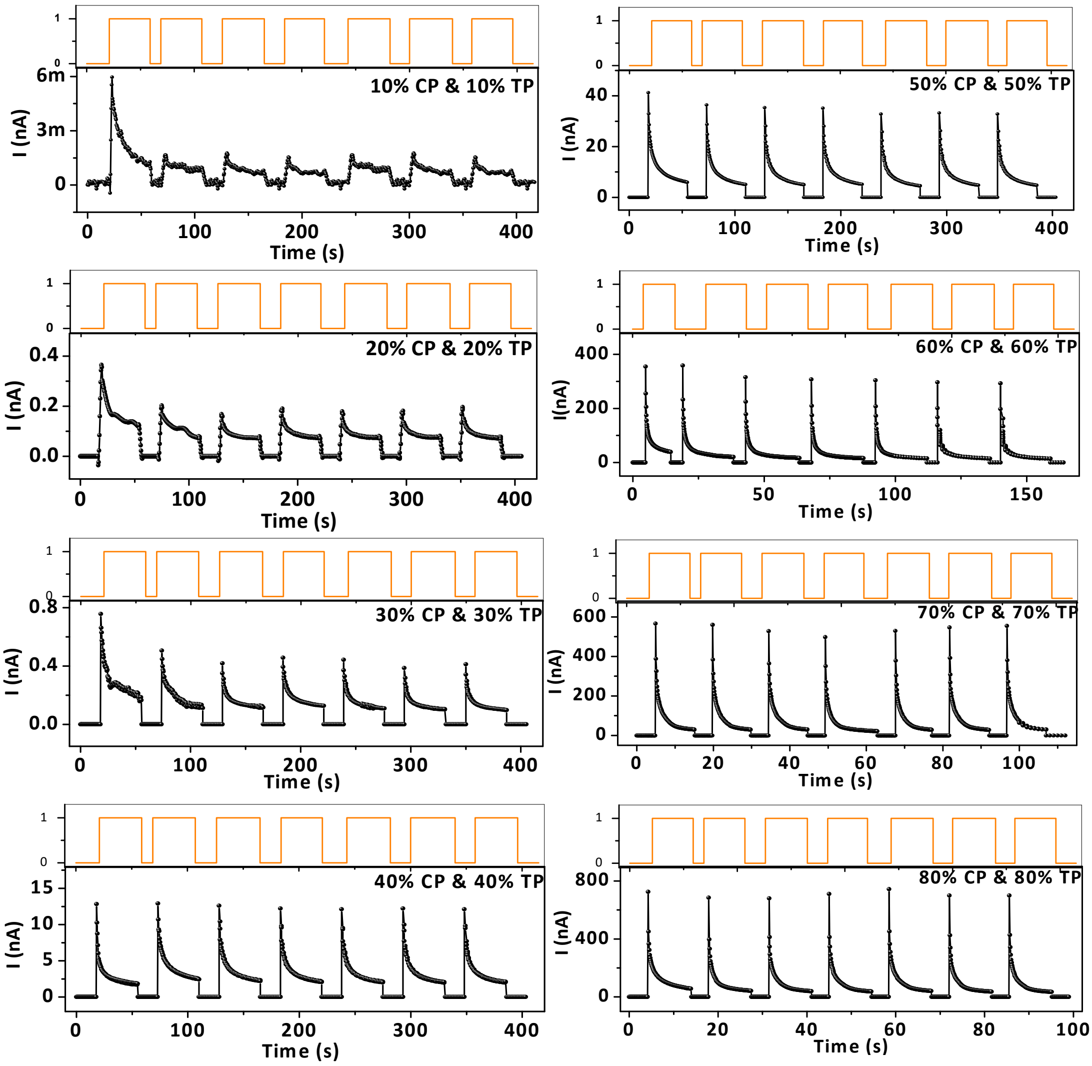

Figure IIIC.5 Responses of the sensor for same CP and TP

The current responses (black curve) of the sensor measured with various CPs and TPs, however with the same magnitude of CP and TPs. CP is applied when voltage (orange curve) was off. The current on/off corresponds to voltage on/off unlike previous cases.

Using the obtained calibration curve, the apparent RH (or measured RH) was extracted against each CP value and given in Figure IIIC.6b. Interestingly, the measured RH value varies linearly with the CPs for a given TP. Now using this curve, an unknown RH, which the device would have undergone in the past, can be traced back and measured.

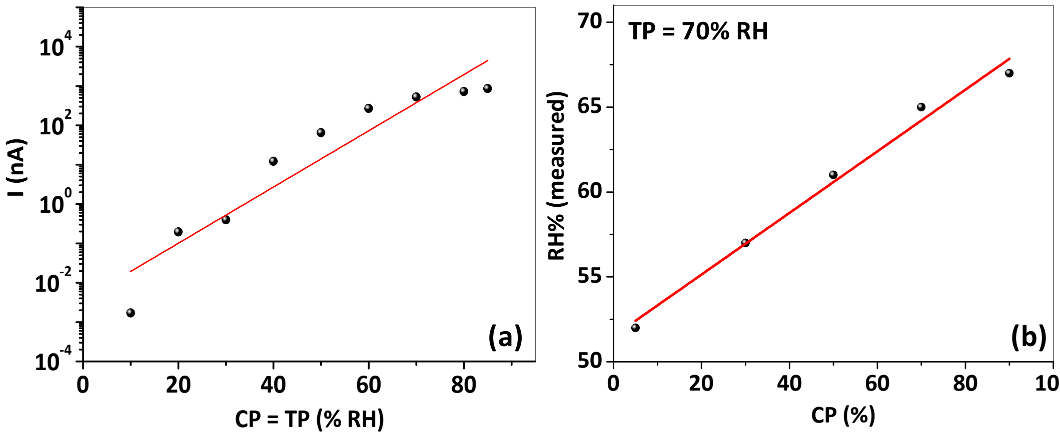

Figure IIIC.6 Variation of measured RH with CP

(a) Calibration of measured current with TP where CP = TP with V_{OFF}. (b) Variation of measured apparent RH with CP.

Further, the ability of the device to memorize multiple RHs in different sequences has been investigated. Three CPs (30%, 50%, and 70%) were exposed and the responses were measured using a TP of 70% RH (see Figure IIIC.7a). The CP sequences used are (30, 50, 70), (50, 30, 70), (50, 70, 30), (30, 70, 50), (70, 50, 30) and (70, 30, 50) and the responses have been compared with the one measured with a single CP of 70% (which is same value as TP). From Figure IIIC.7a, it is observed that the responses for (30, 50, 70) and (50, 30, 70) sequences are indeed comparable to that of single CP of 70% RH (black line in the top panel of Figure IIIC.7a). This implies that the first two CPs (30% and 50%) have no effect on the response of the device. Figure IIIC.7b shows responses for the sequences of (50, 70, and 30) and (30, 70, 50). Noticeably, the response magnitude has decreased in both the cases compared to the one measured with a single CP of 70%. However, the response magnitude for the sequence of (50, 70, 30) was found to be lower than that of (30, 70, 50). In another set of sequence, (70, 50, 30) and (70, 30, 50), the response magnitude has considerably decreased compared to previous cases.

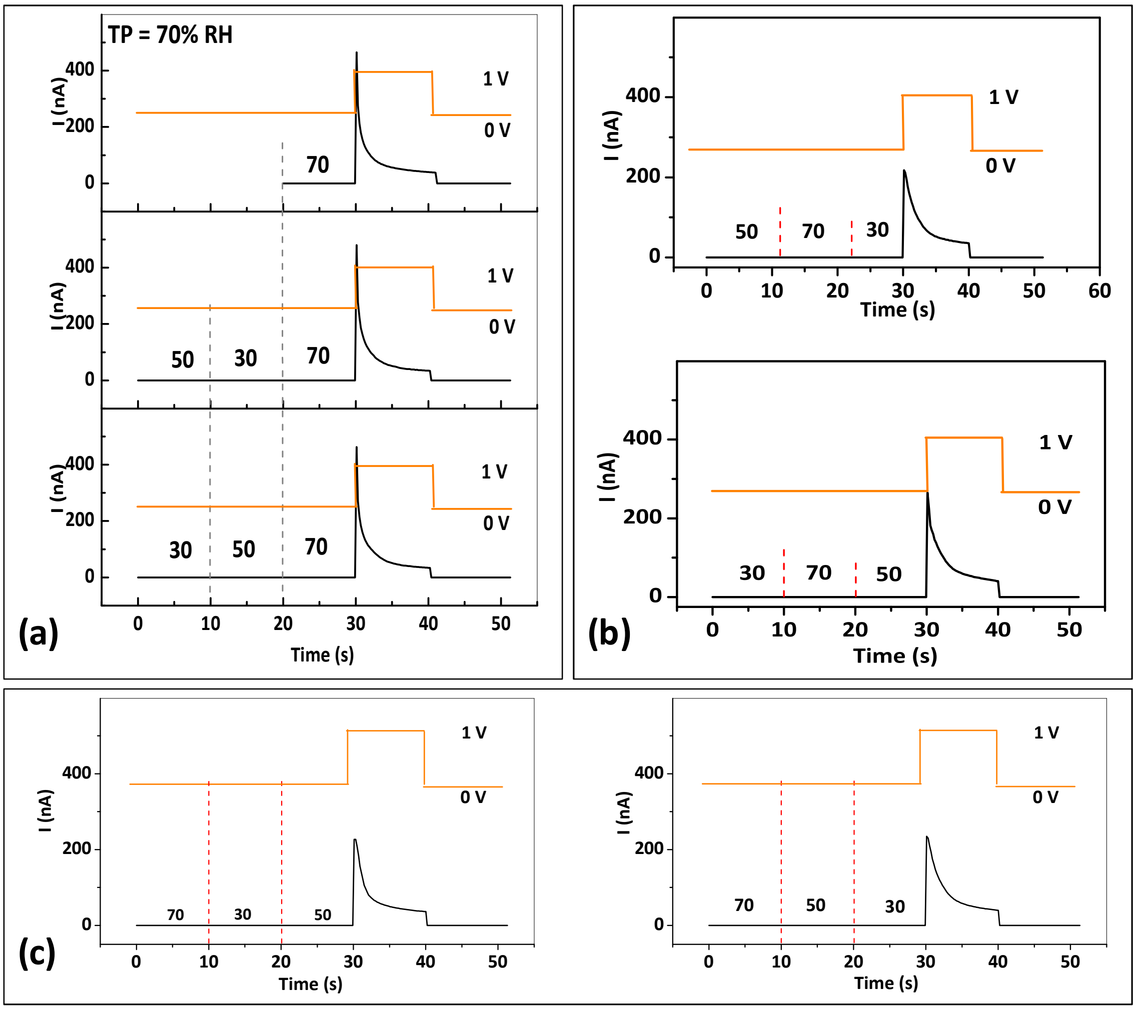

Figure IIIC.7 Influence of sequence of CP of response of the device

The response of the device for different sequences of CP. The three CPs are 30, 50 and 70%, each is introduced at 10 s interval. The TP is kept constant at 70%. The black line is the response of the device where as orange line is voltage variation.

The current responses were converted into RH values using the calibration plot (from Figure IIIC.6a). The measured RH values were plotted in a histogram against each CP sequences (see lined red block in Figure IIIC.8). Additionally, different average values were calculated by considering all possible combinations of the three CPs along with the TP value and such averages have been compared with measured RH values. Interestingly, each measured RH matched with at least one such average. From these observations, it appears that the position of the maximum CP (70% here) in the sequence of CPs influences the response of the device. For example, for the sequence, (70, 50, 30), the measured RH value matched with average value (55%), considering all three CP values whereas for (50, 30, 70), the measured RH value matched with the average value considering only the last CP value. Whereas the responses for the sequences of (50, 70, 30) and (30, 70, 50) shows a dissimilar response, though the position of maximum CP is same.

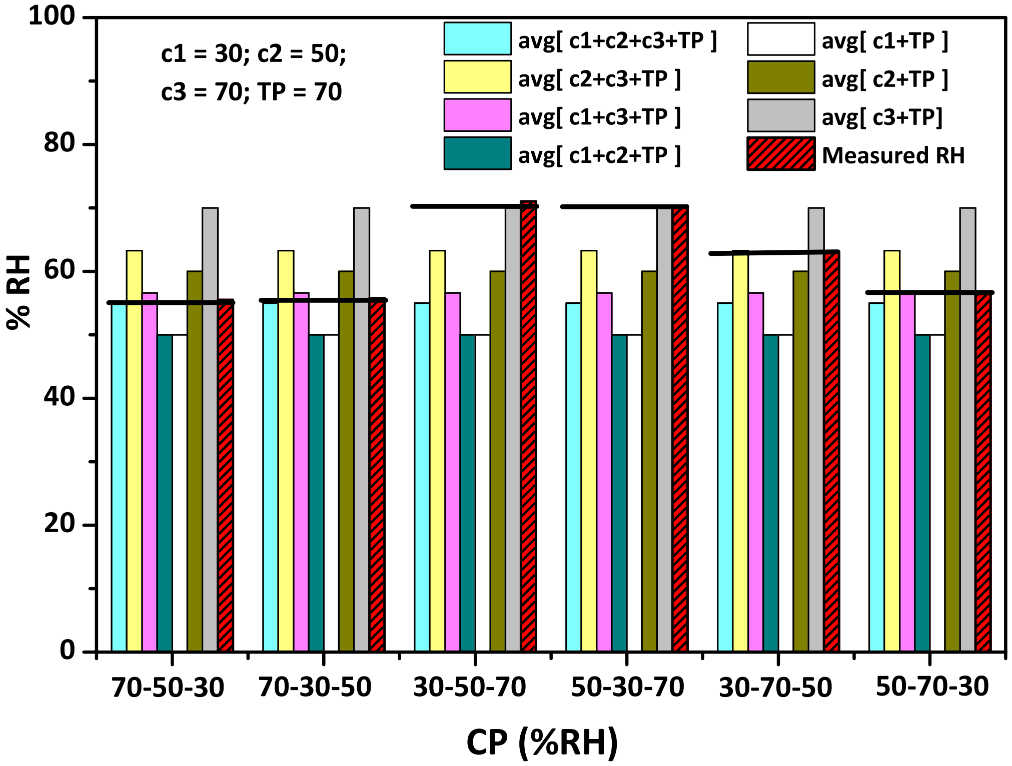

Figure IIIC.8 Correlation of measured RH for different sequences of CPs

Histogram plot of correlation of measured RH (converted from current values) of different sequences of CPs with different average values of CPs. The black horizontal line in each case indicates the best matched average values of CPs. Average values are calculated from the average of CPs and a TP. CPs of magnitude 30, 50 and 70 are represented by c1, c2 and c3 respectively.

IIIC.5 Conclusions

A humidity based memory sensor has been fabricated which memorizes the humidity it experienced in the past. The sensor is also capable of memorizing the range of humidity values it was exposed to. The memory action of the sensor arises from the decay of its ON current when exposed to humidity, whose magnitude varies with the additional humidity pulse (curing pulse). Such device would find many applications in contexts where monitoring a particular humidity for a long time is a must.

References

1. Daniel Gunlycke, Denis A. Areshkin, Junwen Li, John W. Mintmire, and Carter T. White Graphene Nanostrip Digital Memory Device *Nano Lett.*, **2007,** 7, 12.

2. Ricky J. Tseng, Chunglin Tsai, Liping Ma, JianyongOuyang, Cengiz S. Ozkan And Yang Yang Digital memory device based on tobacco mosaic virus conjugated with nanoparticles *Nature Nanotechnol*. **2006**, 1, 72.

3. Sungsik Baek, Dongjin Lee, Jiyoun Kim, Sang-Hyun Hong, Ohyun Kim, and MoonhorRee Novel Digital Nonvolatile Memory Devices Based on Semiconducting Polymer Thin Films *Adv. Funct. Mater.***2007**, 17, 2637–2644.

4. N. Hur, S. Park, P. A. Sharma, J. S. Ahn, S. Guha & S-W. Cheong Electric polarization reversal and memory in a multiferroic material induced by magnetic fields. *Nature*, **2004,** 429, 27.

5. Stuart S. P. Parkin, Masamitsu Hayashi, Luc Thomas Magnetic Domain-Wall Racetrack Memory *Science* **2008**, 11, 320.

6. Martien A. Cohen Stuart, Wilhelm T. S. Huck, Jan Genzer, Marcus Müller, Christopher Ober, Manfred Stamm, Gleb B. Sukhorukov, IgalSzleifer, Vladimir V. Tsukruk, Marek Urban, Françoise Winnik, Stefan Zauscher, Igor Luzinov and Sergiy Minko Emerging applications of stimuli-responsive polymer materials *Nature Mat.* **2010**, 9,101

7. Tao Lu, Shenmin Zhu, Zhixin Chen, Wanlin Wang, Wang Zhanga and Di Zhang Hierarchical photonic structuredstimuliresponsive materials as high-performance colorimetric sensors *Nanoscale*, **2016**, 8, 10316.

8. A Rankin and S McGarry A flexible pressure sensitive colour changing device using plasmonic nanoparticles *Nanotechnology* 26 (**2015**) 075502.

9. Lishun Fu, Yiding Liu, Wenshou Wang, Mingsheng Wang, Yaocai Bai, Eric L. Chronister, Liang Zhen and Yadong Yin A pressure sensor based on the orientational dependence of plasmonic properties of gold nanorods: *Nanoscale*, **2015**, 7, 14483.

10. B. Dong, J. G. Huang, H. Cai, P. Kropelnicki, A. B. Randles, Y. D. Gu and A. Q. Liu An All-Optical Shock Sensor Based On Buckled Doubly-Clamped Silicon Beam *MEMS* **2014**.

11. Benjamin Todd, Mallory Phillips, Stephen M. Schultz, Aaron R. Hawkins, and Brian D. Jensen Low-Cost RFID Threshold Shock Sensors *IEEE Sensors Journal*, **2009**, 9, 4.

12. Birgit Esser, Jan M. Schnorr, and Timothy M. Swager Selective Detection of Ethylene Gas Using Carbon Nanotube-based Devices: Utility in Determination of Fruit Ripeness *Angew.Chem. Int. Ed*. **2012**, 51, 5752 –5756.

13. C. Lang & T. Hübert A, Colour Ripeness Indicator for Apple *Food Bioprocess Technol.* (**2012**) 5:3244–3249.

14. G. Ward and A. Nussinovitch Peel Gloss as a Potential Indicator of Banana Ripeness *Lebensm.-Wiss. u.-Technol.*, 29, 289–294 (**1996**).

15. Xiaogang Han, Yiding Liu, and Yadong Yin Colorimetric Stress Memory Sensor Based on Disassembly of Gold Nanoparticle Chains *Nano Lett*. **2014**, 14, 2466 2470.

16. Debashish Roy, Jennifer N. Cambre, Brent S. Sumerlin Future perspectives and recent advances in stimuli-responsive materials *Progress in Polymer Science* 35 (**2010**) 278–301

17. Carolina de las HerasAlarco´n, Sivanand Pennadam and Cameron Alexander Stimuli responsive polymers for biomedical applications *Chem. Soc. Rev.,***2005**, 34, 276–285

18. Patrick Theatoa, Brent S. Sumerlinb, Rachel K. O'Reillyc and Thomas H. Epps, Stimuli-Responsive Materials *Chem. Soc. Rev*., **2013**, 42, 7055-7056.

19. Etienne Cabane, Xiaoyan Zhang, Karolina Langowska, Cornelia G. Palivan, Wolfgang Meier Stimuli-Responsive Polymers and Their Applications in Nanomedicine *Biointerphases* (**2012**) 7, 9.

20. Bambang Kuswandi, Yudi Wicaksono, Jayus, Aminah Abdullah, Lee Yook Heng, Musa Ahmad Smart packaging: sensors for monitoring of food quality and safety *Sens. & Instrumen. Food Qual*. (**2011**) 5:137–146.

Chapter IIID

Supramolecular Nanofibre based Electrolyte for Micro-Supercapacitors

Summary

This chapter explores the use of supramolecular nanofibres as an electrolyte for the fabrication of in-plane micro-supercapacitors. Here, the 1D face-to-face arrangement of donor and acceptor (D-A) molecules has been utilised to provide an efficient pathway for the diffusion of ions across the electrodes. Though the nanofibres are water-borne, they can operate above 3 V under nearly dry conditions, giving a new approach to design an ambient stable electrolyte with wide operating voltage window (VW). Importantly, since the ions in the naofibres are bound along the 1D chain of molecules, separate fabrication of the high surface area electrode can be completely avoided which gives an additional advantage. These aspects make the present method a very low-cost way of achieving micro-supercapacitor with a high working VW.

IIID.1 Introduction

The supercapacitors have become a promising class of energy storage materials bridging batteries and capacitors with moderate energy and power density values[1, 2]. All focus in supercapacitors research are on achieving energy and power density values equal to that of combustion engines [3, 4]. Earlier efforts to make high energy density supercapacitors were based on volume type supercapacitors [5, 6] (in sandwich geometry) with which considerable success was obtained. However, the integration of such supercapacitors with other active elements for on-chip device fabrication remains a major hurdle for its applications in real life [7, 8].

To make the on-chip integration possible, planar configuration of supercapacitors has been adopted by many [9, 10] which are made of micrometre spaced electrodes. Owing to their several advantages over the sandwich counterparts such as smaller diffusion length of ions, compatibility for on-chip integration, no necessity of separator etc. [11], efforts have been made to achieve high power and energy density values (see Table IIID.1). However, the scarce availability of the electrolytes with compromising benefits restricts the performance of the solid-state micro-supercapacitors. Earlier attempts to make such supercapacitors were based on aqueous based polymer gel electrolytes [12, 13]. However, its VW hardly exceeds 1 V due to eletrolytic breakdown at higher voltages, giving rise to poor energy density values [14]. As the energy density varies as the square of the VW, many new eletrolyte materials were reported wih high VW [14, 15]. For example, the organic based electrolytes provide VW up to 2.8 V [16, 17] but they are liquid in nature rendering them unsuitable for solid-state devices. Recently developed ionic liquid based gel electrolytes provide wide VW up to 3.7 V, good thermal stability and high ionic conductivity [18-20] but these are inherently ambient unstable [21-24]. These issues give rise to two main challenges in using them for solid-state supercapacitor. Firstly, they have to be prepared in an inert atmosphere which intern requires extensive instrumentation and secondly, a device once made has to be encapsulated firmly [25, 26]. Additionally, their long preparation time makes them undesirable for large-scale production [27]. Therefore it is ideal to have an ambient stable electrolyte with wide VW which would bring advantages from both aqueous and ionic electrolytes.

Table IIID.1 Literature of high-performance in-plane micro-supercapacitors

Sr #	material	electrolyte	scan rate (V/s)	C_a (mF/cm^2)	C_v (F/cm^3)	P_v (W/cm^3)	E_v (mWh/cm^3)	Refs.
1	G-CNTs	Na_2SO_4 BMIM-BF_4	400 -	2.16 3.93	1.08	115 135	0.16 2.42	*Nano lett*, 13, 2013, 72
2	OLC	Et_4NBF_4	100	0.9	1.35	1000	1	*Nat Nanotech*, 5, 2010, 651
3	LRGO	Na_2SO_4 $TEABF_4$	0.1 2.5	1 10	-	100 10	1 5	*Nat Nanotech*. 6, 2011, 496
4	Graphene LSG	Ionogel	1	1.78	2.35	141	1.37	*Nat. Commun*. 4, 2013, 2446

5	AC-MnO_2	K_2SO_4	0.5	10-15	-	5	5	*J. Power Sources* 234,2013, 302
6	MnO_2	K_2SO_4	0.5	5	-	1	1	J. *Power Sources* 234,2013, 302
7	MoS2 nanosheets	-	0.2	1	178	-	-	*Small*2013, *9*, 2905
8	LSG/MnO_2	Na_2SO_4		384	1136	10	~5	*PNAS*, 7, 2015, 4233
9	Graphene	H_2SO_4/ PVA	1000	0.1	10	495	0.14	*Nat. Commun*, 4, 2013, 3487
10	Activated carbon	Et_4NBF_4	0.5	11.6	2.7	41	18	*Energy Environ. Sci.*, 2011, 4, 1972
11	rGO-CNTs	3M KCL	1	5.63	4.9	77	2.7	*Adv. Fun. Mat.* 22, 2012, 4501
12	PANI	PVA-H_2SO_4	1	-	588	25	82	*Electroanalysis* 26.1, 2014 30.

IIID.2 Scope of the present investigation

As detailed in the introduction, there are ongoing efforts to increase the energy density of the supercapacitor by increasing the VW of the electrolyte, However, the choice of electrolytes with ambient stability and wide operating voltage is limited. Though ionic liquids are promising materials, their ambient instability limits their usage. Thus having an electrolyte which is ambient stable and operates in wide VW would be worthwhile.

Upon learning that supramolecular nanofibres contain a high number of ion binding molecules (CS and DMV) which are arranged in a compact 1D manner, the potential of these nanofibres as an efficient electrolyte was investigated in this section. Since the nanofibres are self-assembled from water, there were high chances of these being ambient stable, given that the instability in the most of the electrolytes is humidity driven. As the nanofibres have ion channels, they can provide an efficient pathway for the diffusion of ions across electrodes even at higher voltages.

IIID.3 Experimental section

For fabrication of in-plane supercapacitor, the glass substrates were cleaned in piranha solution followed by washing with distilled water several times. Interdigitated patterns having both electrode width and spacings of 50 μm, were made by a maskless photolithography method. Metallic contacts were made by physical vapor deposition of Au using a resistive thermal evaporator at a base pressure of 10^{-2} mTorr. The electrochemical measurements were performed in the two-electrode configuration using CH Instruments 650 (Austin, TX, USA).

IIID.4 Results and discussion

As described in previous chapters, the supramolecular 1D nanofibres were prepared by self-assembly of the potassium salt of coronene tetracarboxylate salt (CS) and dodecyl methyl viologen (DMV) based D-A molecules (see Figure IIID.1) [28]. In water, these two components stack themselves to form cylindrical micelles (diameter, < 6 nm) following a surfactant-like assembly. This forms bilayers of CT-amphiphiles arranged radially with the D and A pairs stacked face-to-face along the length of the nanofibre. The cations (K^+) and anions (Br^-) are bound to carboxylate group of CS and pyridinium group of DMV respectively. Since the D-A molecules of the nanofibre are arranged in 1D, the molecules can efficiently host ions, thus may lead to higher capacitance. Additionally, this avoids the fabrication of high surface area electrodes to store the charges [29-31]. As a result, the entire device consists of only two components, one being the supramolecular nanofibres and the other being gold as a current collector.

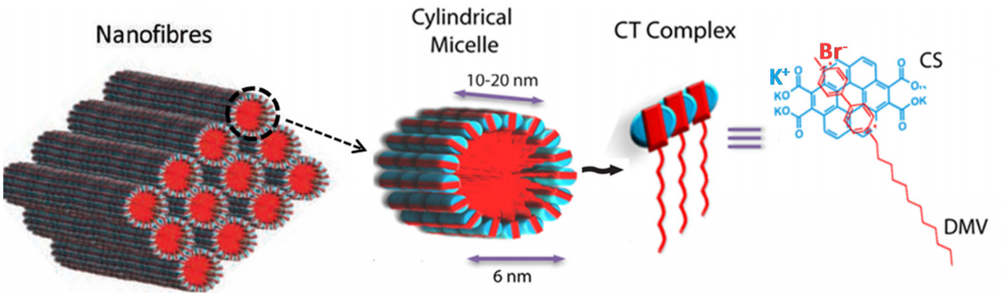

Figure IIID.1 Molecular structure of the nanofibre
Schematic representation of stacking of the CS-DMV based donor-acceptor CT complex involving the co-facial molecular arrangement of the molecules and its molecular structure.

As described in Chapter IIIA (Figure IIA.2), the nanofibre exhibits competing conducting (due to charge transfer interIactions) and capacitive (due to ions) behavior, their relative dominance depends on the humidity. Therefore, in the present study, the performance of the supercapacitor was studied at lower humidities (below 40%).

The major difference between conventional micro-supercapacitor and supramolecular micro-supercapacitor (μ-SS) is schematically shown in Figure IIID.2a and b. The structure of micro-supercapacitors consists of interdigitated microelectrodes designed in a planar configuration where the width and spacing between electrodes are of the order of micrometres. Conventionally, an electrolyte is used as a medium for the movement of ions to have charge storage in the device (see Figure IIID.2a). The physical state of the electrolyte should be highly viscous gel since it has to undergo integration with a solid state device and also act as a medium for the movement of ions. Usually, a pair of porous electrodes is used in which formation of double layer takes place. The surface area of porous electrode is crucial for achieving high energy density. The μ-SS is also a planar micro-supercapacitor device but here the supramolecular1D nanofibre acts as the electrolyte for the device (see Figure IIID.2b).

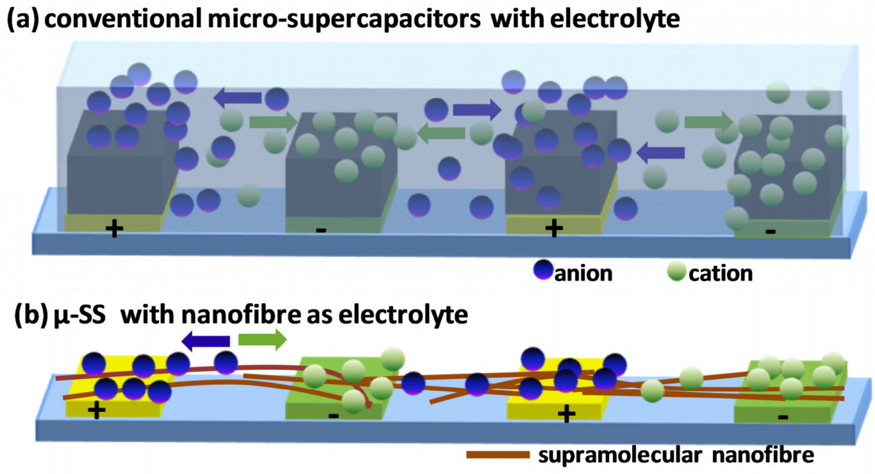

Figure IIID.2 Schematics of device structures

(a) Schematic of conventional micro-supercapacitors where aqueous polymer gel or ionic liquid is used as the electrolyte. (b) Schematic of μ-SS without conventional electrolyte where nanofibre acts as an electrolyte medium for the movement of ions.

The supramolecular micro-supercapacitor (μ-SS) was fabricated by an easy one-step process. A volume of ~ 1 μL of 1 mM aqueous dispersion of nanofibre was drop coated on interdigitated gold electrodes on glass/PET and was allowed to dry for an hour by vacuum evaporation (Figure IIID.3a and b). The volume of the device was calculated by multiplying the surface area (10 mm^2) of the device with its total thickness (~ 100 nm). The surface area includes the area of the microelectrodes and the gaps between them, as reported elsewhere [10]. The total thickness, measured using AFM, accounts for the thickness of nanofibre as well as that of gold electrode [11]. To measure the thickness, a step was created by peeling off one edge of active region using a scotch tape as shown in Figure IIID.3c. Recently, it has been shown that areal and stack (volume) capacitance give an accurate picture of the true performance of micro-supercapacitor [5] than gravimetric values since in these micro devices the mass of the active material is very small.

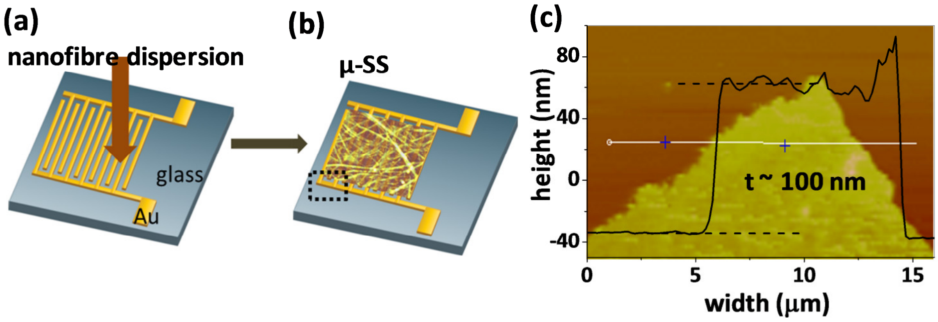

Figure IIID.3 Fabrication of μ-SS

(a) Drop coating of nanofibres dispersion onto premade interdigitated Au electrodes resulting into the μ-SS device, (b). In (e) AFM image of nanofibres is merged onto electrodes. (c) The AFM thickness of nanofibre film along with gold current collector measured in a region shown by the dotted black square in (b). The average thickness of the device was measured to be ~ 100 nm.

To evaluate the performance of the μ-SS device, cyclic voltammetry (CV) curves were measured with wide scan rates ranging from 0.002 to 20 V/s in a VW of 0 – 1 V as shown in Figure IIID.4a and b. The shape of the CV curves shows semi-rectangular behavior till the scan rate of 5 V/s, after which the shape tends to become triangular, possibly due to the resistive loss of the nanofibre [32]. The individual plots of CV curves are given in Figure IIID.5. The stack capacitance of 160 F/cm^3 was observed at a scan rate of 1 mV/s, which decreased to 0.3 F/cm^3 as the scan rate was increased to 20 V/s (see Figure IIID.4c). Importantly, the stack capacitance observed is very high and quite comparable to best-reported values (see Table IIID.1). Such a high stack capacitance was envisaged due to the structure of nanofibre which can host high density of ions bound to the molecules of the nanofibre. The high discharge current of 0.2 – 14 A/cm^3 was obtained with varied scan rates, however, the variation in the discharge current remains linear only at lower scan rates (Figure IIID.4d).

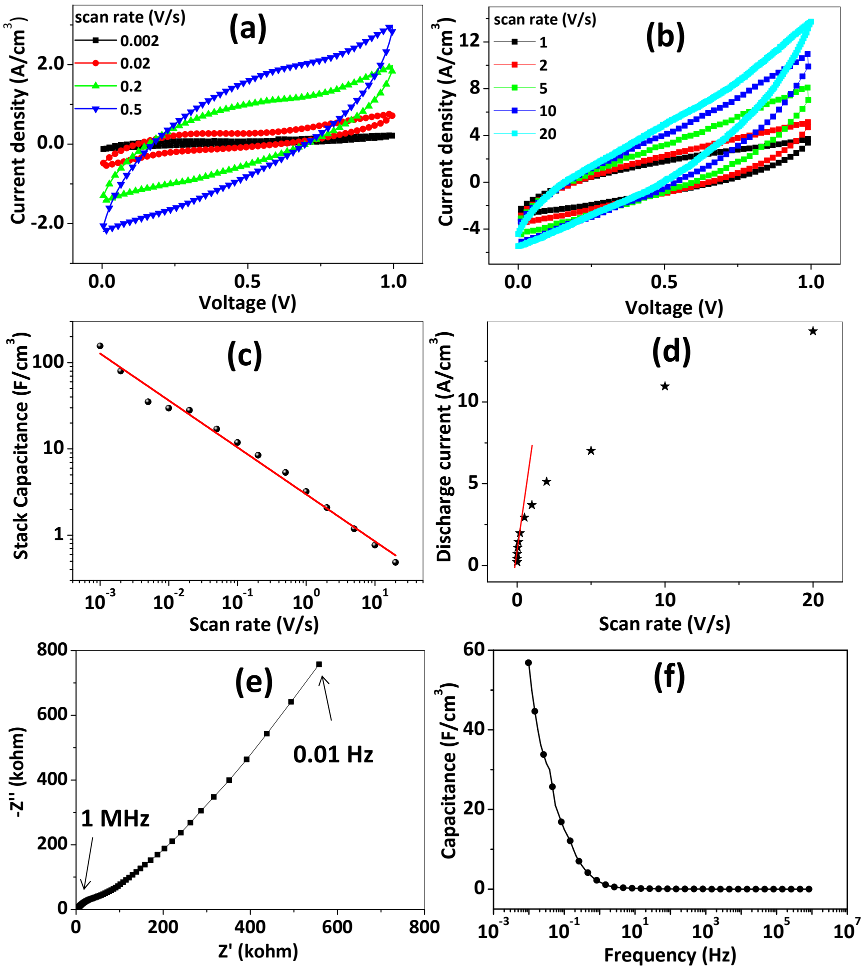

Figure IIID.4 Performance of μ-SS measured at VW of 1 V

Cyclic voltammetry of the device measured at lower (a) and higher (b) scan rates.(c) Plots of stack capacitance versus scan rates. (d) Variation of the discharge current of the device with the scan rate. (e) Electro chemical impedance spectra (Nyquist plot) and measured. frequency resposive capacitance (Bode plot) of of μ-SS measured at 35% RH.

Further electrochemical impedance behavior of the μ-SS was studied as shown in Figure IIID.4. The frequency response of impedance (Nyquist plot) shown in Figure IIID.4e showed a small semi-circle in high frequency region (1 MHz) due to the charge transfer resistance and linear behavior in the low frequency region (0.01 Hz), indicative of capacitive behavior of the device. To work out the transient capacitance more accurately, we have performed the bode measurements which gave capacitance values in the range of 1 - 50 F/cm^3 (see Figure IIID.4f).

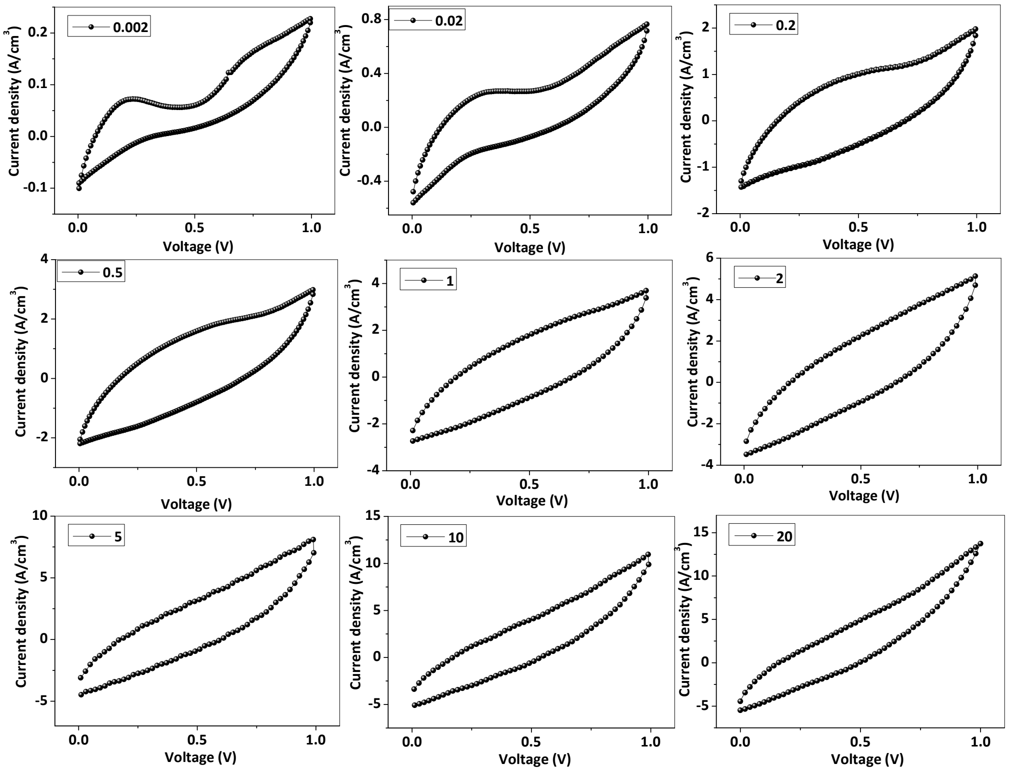

Figure IIID.5 Individual CV curves
Individual CV curves of the μ-SS with scan rates from 0.002 V/s to 20 V/s.

The nanofibres have water and K$^+$ and Br$^-$ ions, as ionic constituents. To check that the CV curves of μ-SS have uniquely appeared due to the nanaofibres and not because of their constituents, control experiemts were performed with drop coating only DI water and 1 mM aq. KBr solution separately on gap electrodes. The DI water showed horizontal and non-cyclic CV with no sign of charging as is expected because DI water is devoid of ions (see Figure IIID.6). A drop of aq. KBr solution showed small cyclic loop with a sudden jump in the current after 0.8 V. This shooting up of current above 0.8 V is an indication of electrolytic breakdown [33]. These two control experiments signify that the observed CV curves of µ-SS is indeed due to the nanofibres and not interfered from presence of water and K^+, Br^- ions. Thus the nanofibre serves as an efficient pathway for the diffusion of ions across electrodes as well as a storage medium for ions leading to high capacitance values.

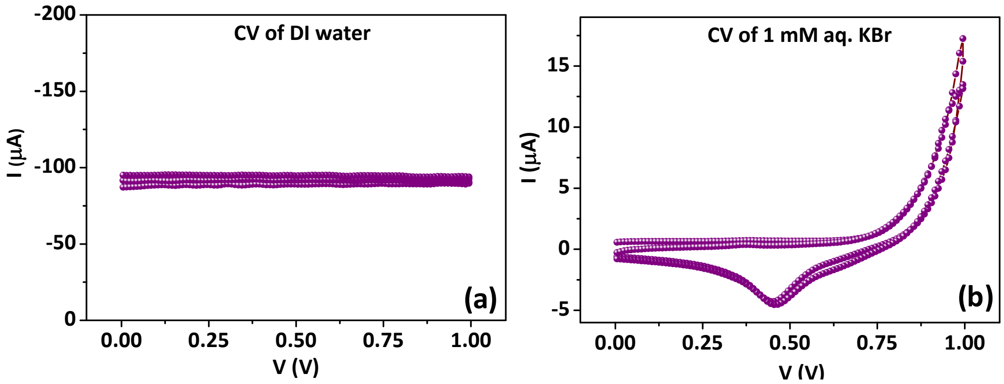

Figure IIID.6 Control experiments

Cyclic voltammetry of (a) DI water (b) aq. 1mM KBr solution after drop coating on the gapped Au electrodes.

Since the supramolecular nanofibres are self-assembled in water, they are expected to become unstable at VW of > 1V due to electrolytic breakdown. Surprisingly, µ-SS did not undergo any breakdown even with VW of up to 3 V (see Figure IIID.7). Clearly, there is no shooting up of current in the CV curves, due to which most of the aqueous electrolytes degrade and is a major issue in developing aqueous based electrolytes with higher operating VW [34]. The non-rectangular shape of CV curve is due to the resistive loss as these nanofibres have considerable electronic conductivity [35]. The high stack capacitance of 2 – 120 F/cm^3 are obtained (see Figure IIID.7c). The discharge current as high as 36 A/cm^3 is obtained, but with non-linear dependency (Figure IIID.7d). The utlity of the wide VW is demonstrated by glowing LED (2.2 V) during discharging of single µ-SS device.

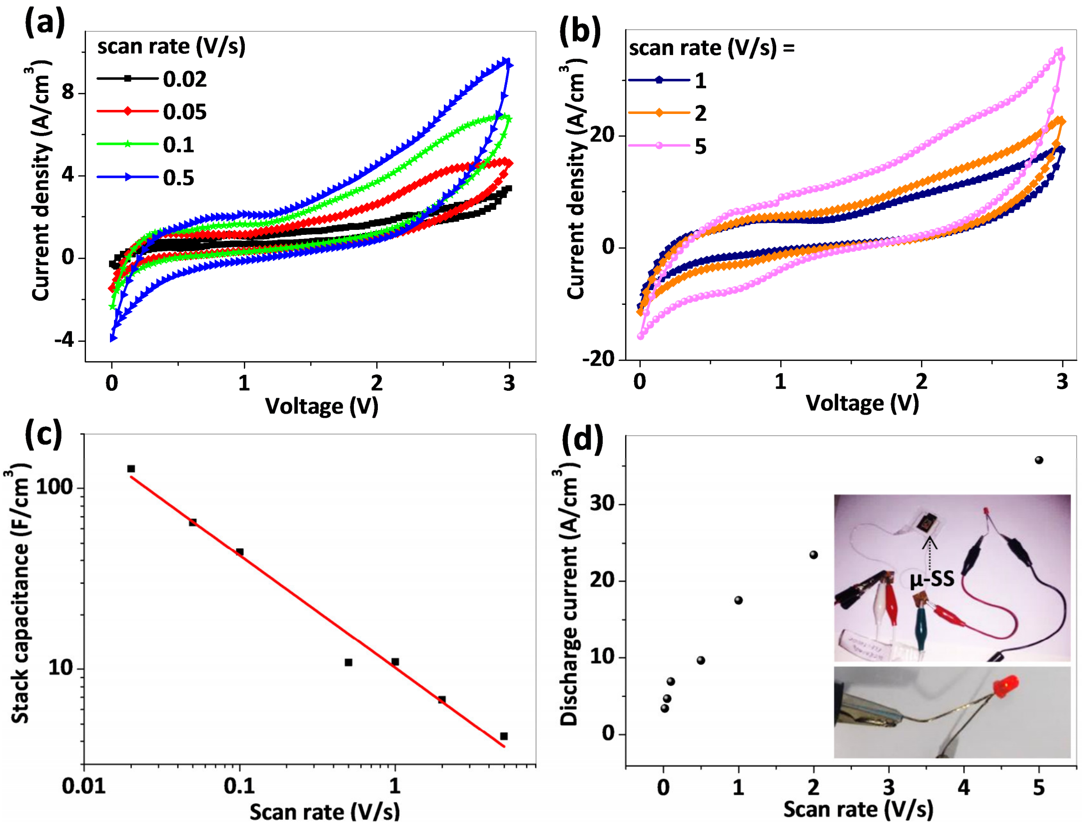

Figure IIID.7 Electrochemical performance of μ-SS at VW of 3 V
Cyclic voltammetry of the device measured at lower (a) and higher (b) scan rates. (c) Plots of stack capacitance of the μ-SS versus scan rates. (d) Variation of the discharge current of the device with the scan rate. In inset demonstrtation of LED glowing is shown using a single μ-SS device.

The stability of the μ-SS device was examined at even higher voltages of > 3 V (see Figure IIID.8). Strikingly, the μ-SS device did not undergo any electrolytic breakdown for voltage of up to 5 V. However, the current decreases for the VW of 5 V, perhaps due to the high electrical stress applied on the nanofibre. It is notable that water oxidation and reduction peaks are completely absent even for VW of 5 V. Thus it is clear that the μ-SS can be comfortably operated up to VW of 4 V. This makes the supramolecular nanofibre as a new class of electrolyte for micro-supercapacitors with highest VW, reported till date.

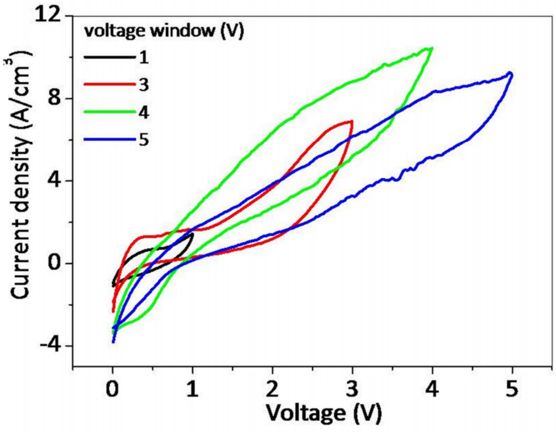

Figure IIID.8 CV curves of μ-SS measured at different VWs
The electrochemical stability of the μ-SS with an increase in VW from 1 to 5 V.

To increase the energy and power density of supercapacitors there have been many efforts to search for new materials with high electrochemical operating VW [11, 36, 37]. The histogram in Figure IIID.9 provides a comparative plot of operating VW of various electrolytes used in the literature along with present supramolecular nanofibre. Clearly, nanofibres used in this study stand better in comparison to the counterparts such as aqueous, organic and ionic liquid based electrolytes. Among the listed parameters, ambient stability and VW are two most important which decides the performance of a micro-supercapacitors. Though aqueous electrolytes have ambient stability, it suffers from narrow VW, whereas ionic liquids have wide VW but suffer from ambient stability. The nanofibre-based electrolyte used in μ-SS is meritorius in both ways i.e., it is ambient stable yet exhibiting wide VW, indeed widest reported till date. Additionally, it can be prepared in few minutes given that the reactant molecules are available readily [28]. Due to easy processing (no glove box required) without the need of encapsulation, the cost of μ-SS reduces by almost 2-3 orders less than that of ionic liquids.

To demonstrate the overall performance of μ-SS, a Ragone plot was derived in Figure IIID.10 at two VWs. Initially, the galvanostatic charge-discharge (CD) curves were measured at various current density values. For 1 V, the discharge time decreased from 25 to 2 seconds as the current density increased from 1 to 6 A/cm^3 (see Figure IIID.10a). The nearly triangular shape of CD curves denotes that the charge storage in μ-SS is based on electrostatic double layer mechanism. The deviation from triangular shape (indicated by two red lines) CD curves is due to the resistive loss, as the nanofibres are electronically conducting too. This is also reflected in the 'iR' drop in the discharge curve of the device.

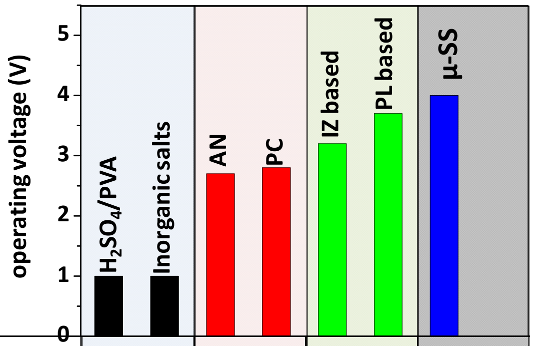

Type	aqueous	organic	ionic liquid	SN
Medium of synthesis	Aqueous	organic	organic	aqueous
Ambient stability	Yes	No	No	Yes
Time of prep.	1 hour	NA	2 days	1 hour
*Cost (Rs)	low	modest	high	negligible

Figure IIID.9 Comparison of advantages of µ-SS with other micro-supercapacitors
The top panel is the histogram of operating voltages of commonly used electrolytes in various supercapacitors. The bottom panel is a table of parameters compared for different electrolytes. AN (acetonitrile), PC (propylene carbonate), IZ (imidazolium), PL (pyrrolidinium), SN (supramolecular nanofibre).

In the Ragone plot (see Figure IIID.10b), the data for commercial high-energy Lithium thin film battery (4 V/500 mAh) [10], high-power aluminium electrolytic capacitor (3 V/300 µF) [11] and Panasonic Li-ion battery (780 mAh) [10] are included for comparison along with the reported range of supercapacitors [41]. Remarkably, µ-SS delivered a volumetric energy density of 0.1 - 20 mWhcm^{-3}, which is an order of magnitude higher than that of typical supercapacitors containing activated carbon (< 1 mWhcm^{-3}) and is comparable to that of lithium thin film batteries (10^{-3} – 10^{-2} Whcm^{-3}) [10, 11]. Additionally, µ-SS shows a power density of 0.5 - 10 Wcm^{-3}, an order higher than that of conventional supercapacitors, higher than that of the state-of-the-art micro-supercapacitors (see Table IIID.1) and comparable to that of high-power electrolytic capacitors (10^1–10^3 Wcm^{-3}) [42]. The energy density values measured at 3 V remain comparable to that measured at 1 V, however, the power density of the device has increased nearly by one order compared to that of 1 V.

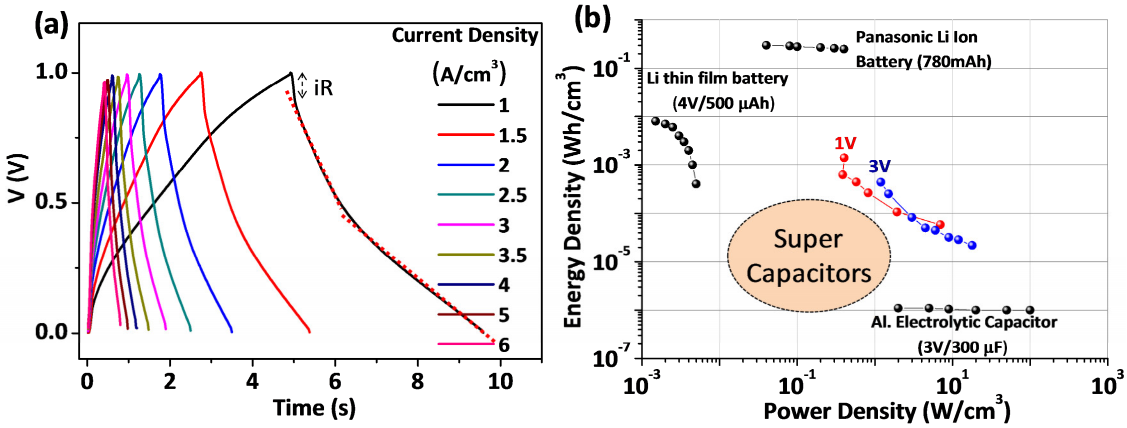

Figure IIID.10 Performance evolution of μ-SS by Ragone plot

(a) CD curves of the supramolecular capacitor at various current densities ranging from 1 A/cm^3 to 6A/cm^3. Red dotted lines are fitted lines for discharge curve measured at 6 A/cm^3. (b) Ragone plots showing the performance of the μ-SS measured two VWs (1 and 3 V).

IIID.5 Conclusions

Using supramolecular nanofibre as an electrolyte medium, a micro-supercapacitor (μ-SS) has been fabricated. The device is not only ambient stable but also exhibits high operating VW up to 4 V surpassing that of ionic liquids. Additionally, it's a simple supercapacitor device made without any additional electrodes. Due to a large number of ion binding molecules present in the nanofibres, very high capacitance of 10-160 F/cm^3 was obtained. The energy density values in as-fabricated device are found to be an order higher than conventional micro-supercapacitors. Though the device suffers from the inherent resistive loss, the present study gives a new approach for designing ambient stable electrolytes for supercapacitor with VW fulfilling the industry standards.

References

1. Chen Kunfeng and Xue Dongfeng An Era of Powerful Supercapacitors: Materials Science and Engineering toward the System-Level Design of Ionic Supercapacitor Electrode and Electrolyte Ann *J Materials Sci Eng* 1, (**2014**), 2.

2. Patrice Simon and Yury Gogotsi Materials for electrochemical capacitors *Nature Mat.* **2008**, 7, 845.

3. Patrice Simon , Yury Gogotsi , Bruce Dunn, Where Do Batteries End and Supercapacitors Begin? *Science* **2014**, 343, 1210.

4. Martin Winter and Ralph J. Brodd What Are Batteries, Fuel Cells, and Supercapacitors? *Chem. Rev.***2004,** 104, 4245 4269

5. Y. Gogotsi and P. Simon True Performance Metrics in Electrochemical Energy Storage *Science*, **2011**, 18, 334,

6. Wang, Q.; Yan, J.; Fan, Z. Carbon materials for high volumetric performance supercapacitors: design, progress, challenges and opportunities *Energy Environ. Sci.* **2016**, 9, 729– 762.

7. Majid Beidaghi and Yury Gogotsi Capacitive energy storage in micro-scale devices: recent advances in design and fabrication of micro-supercapacitors *Energy Environ. Sci.*, **2014**, 7, 867–884.

8. Zhong Lin Wang and Wenzhuo Wu Nanotechnology-Enabled Energy Harvesting for SelfPowered Micro-Nanosystems *Angew. Chem. Int. Ed*. **2012**, 51, 11700 – 11721

9. David Pech, Magali Brunet, Hugo Durou, Peihua Huang, Vadym Mochalin, Yury Gogotsi, Pierre-Louis Taberna And Patrice Simon Ultrahigh-Power Micrometre-Sized Supercapacitors Based On Onion-Like Carbon *Nature Nanotech.***2010**, 5, 651.

10. Zhong–Shuai Wu, Khaled Parvez, Xinliang Feng, Klaus Mullen Graphene-based in-plane micro-supercapacitors with high power and energy densities *Nature Commun.***2013**, 4, 2487.

11. Maher F. El-Kady1,2 & Richard B. Kaner Scalable Fabrication Of High-Power Graphene Micro-Supercapacitors For Flexible And On-Chip Energy Storage *Nature Commun.***2013**, 4, 1475.

12. Wenping Si, Chenglin Yan, Yao Chen,a Steffen Oswald Luyang Hana and Oliver G. Schmidt On-chip, all solid-state and flexible micro-supercapacitors with high performance based on MnOx/Au multilayers *Energy Environ. Sci.*, **2013**, 6, 3218–3223.

13. Hee Y. Lee and J. B. Goodenough Supercapacitor Behavior with KCl Electrolyte *Journal of Solid State Chemistry* **1999,** 144, 220—223.

14. François Béguin, Volker Presser, Andrea Balducci, and Elzbieta Frackowiak Carbons and Electrolytes for Advanced Supercapacitors *Adv. Mater.* **2014**, *26*, 2219–2251

15. Takashi Hibino, Kazuyo Kobayashi, Masahiro Nagao & Shinji Kawasaki High-temperature supercapacitor with a proton-conducting metal pyrophosphate electrolyte *Sci. Rep.* **2015**, 5, 7903.

16. Makoto Use,* Kazuhiko Ida, and ShoichiroMori Electrochemical Properties of Organic Liquid Electrolytes Based on Quaternary Onium Salts for Electrical Double-Layer Capacitors *J. Electrochem. Soc.,* **1994**, 141, 11.

17. Fabrication of a stretchable and patchable array of high-performance micro-supercapacitors using a non-aqueous solvent-based gel electrolyteGrumble Lee, Daeil Kim, Doyeon Kim, Sooyeoun Oh, Junyeong Yun, Jihyun Kim, Sang-Soo Lee and Jeong Sook Ha *Energy Environ. Sci.*, **2015**,8, 1764-1774.

18. Douglas R. MacFarlane, Naoki Tachikawa,a Maria Forsyth, Jennifer M. Pringle, Patrick C. Howlett, Gloria D. Elliott, James H. Davis, Jr, Masayoshi Watanabe, Patrice Simon and C. Austen Angell Energy applications of ionic liquids *Energy Environ. Sci.,* **2014**, 7, 232–250

19. Michel Armand, Frank Endres, Douglas R. Macfarlane, Hiroyuki Ohno And Bruno Scrosati ionic-liquid materials for the electrochemical challenges of the future *Nature Mat.* 8, **2009**, 621

20. Jean Le Bideau, Lydie Viau and Andre Vioux Ionogels, ionic liquid based hybrid materials *Chem. Soc. Rev.,* **2011**, 40, 907–925.

21. Ghandi, Khashayar. "A review of ionic liquids, their limits and applications."*Green and Sustainable Chemistry* **2014**, 4, 44-53

22. Shamsuri, Ahmad Adlie, and Dzulkefly Kuang Abdullah. "Ionic liquids: preparations and limitations." *Makara Sains* 14.2 (**2010**): 101-106.

23. Laus, Gerhard, et al. "Ionic liquids: current developments, potential and drawbacks for industrial applications." *Lenzinger Berichte* 84 (**2005**): 71-85.

24. Švancara, Ivan, Matěj Stočes, and Tomáš Weidlich. "Possibilities and limitations of ionic liquids in electrochemical and electroanalytical measurements (a review)." *Sensing in electroanalysis. K. Vytřas, K. Kalcher, I. Švancara (Eds.).* **2010**, 5.

25. Han, Lijuan, Pengyi Tang, and Li Zhang. "Encapsulation architecture for energy storage." *Materials Today* 18, (**2015**): 352-353.

26. Kim, Hyoungjun, et al. "Encapsulated, High-performance, Stretchable Array of Stacked Planar Micro-supercapacitors as Waterproof Wearable Energy Storage Devices." *ACS applied materials & interfaces* (**2016**) http://dx.doi.org/10.1021/acsami.6b03504

27. Tao, Guo-hong, et al. "Preparation, characterization and application of amino acid-based green ionic liquids." *Green Chemistry* 8.7 (**2006**): 639-646.

28. Rao, K. V., Jayaramulu, K., Maji, T. K. & George, S. J. Supramolecular hydrogels and high aspect ratio nanofibres through charge transfer induced alternate coassembly. Angew. Chem. Int. Ed. 49, 4218–4222 (**2010**).

29. El-Kady, Maher F., et al. "Engineering three-dimensional hybrid supercapacitors and microsupercapacitors for high-performance integrated energy storage." *Proceedings of the National Academy of Sciences* 112.14 (**2015**): 4233-4238.

30. Lin, Jian, et al. "3-dimensional graphene carbon nanotube carpet-based micro-supercapacitors with high electrochemical performance." *Nano letters*13.1 (**2012**): 72-78.

31. Wang, Guoping, Lei Zhang, and Jiujun Zhang. "A review of electrode materials for electrochemical supercapacitors." *Chemical Society Reviews*41.2 (**2012**): 797-828.

32. Kurra, Narendra, S. Kiruthika, and Giridhar U. Kulkarni. "Solution processedsun baked electrode material for flexible supercapacitors." *RSC Advances*4.39 (**2014**): 20281-20289.

33. Szklarczyk, Marek, Ramesh C. Kainthla, and John O'M. Bockris. "On the dielectric breakdown of water: an electrochemical approach." *Journal of The Electrochemical Society* 136.9 (**1989**): 2512-2521.

34. Suo, Liumin, et al. "“Water-in-salt” electrolyte enables high-voltage aqueous lithium-ion chemistries." *Science* 350.6263 (**2015**): 938-943.

35. Mogera, Umesha, et al. "Ultrafast response humidity sensor using supramolecular nanofibre and its application in monitoring breath humidity and flow." *Scientific Reports* 4 (**2014**): 4103.

36. Vu, Anh, et al. "Three-dimensionally ordered mesoporous (3DOm) carbon materials as electrodes for electrochemical double-layer capacitors with ionic liquid electrolytes." *Chemistry of Materials* 25.21 (**2013**): 4137-4148.

37. Kim, Tae Young, et al. "High-performance supercapacitors based on poly (ionic liquid)-modified graphene electrodes." *ACS nano* 5.1 (**2010**): 436-442.

38. Chen, Qiao, et al. "Effect of different gel electrolytes on graphene-based solid-state supercapacitors." *RSC Advances* 4.68 (**2014**): 36253-36256.

39. Senthilkumar, S. T., et al. "High-performance solid-state electric double layer capacitor from redox-mediated gel polymer electrolyte and renewable tamarind fruit shell derived porous carbon." *ACS applied materials & interfaces* 5.21 (**2013**): 10541-10550.

40. Anothumakkool, Bihag, et al. "Design of a high performance thin all-solid-state supercapacitor mimicking the active interface of its liquid-state counterpart." *ACS applied materials & interfaces* 5.24 (**2013**): 13397-13404.

41. Xiong, Guoping, et al. "A review of graphene-based electrochemical micro-supercapacitors." *Electroanalysis* 26.1 (**2014**): 30-51.

42. Rajib Sarkar Rajan, Md. Moshiur Rahman Lifetime Analysis of Super Capacitor for Many Power Electronics Applications IOSR Journal of Electrical and Electronics Engineering (9, 1, **2014**, 55-58.

Chapter IV

Synthesis and Unusual Properties of Decoupled 2D Graphene Stacks

Chapter IVA

A low cost, rapid synthesis of graphene

Summary

Graphene because of its inert and impermeable nature holds a great promise as a protective coating against corrosion and oxidation. It is envisioned that graphene coated metals will be increasingly used in metal and electronic industries. To date, mainly expensive chemical vapor deposition (CVD) methods are being employed for its synthesis over large area involving hydrogen at high reaction temperatures. Here we report, a simple and rapid method of joule heating a Ni foil coated with naphthalene in rotary vacuum to produce graphene without hydrogen gas. The graphene thus grown protects the Ni surface against corrosion and oxidation even at elevated temperatures. This synthetic approach has a great potential for widespread use as it is low cost and adaptable to metal surfaces of complex curvatures.

IVA.1 Introduction

Graphene, a one atom thick sp^2 carbon lattice, is a well celebrated material ever since it was experimentally realized, a decade ago [1]. It exhibits a fascinating range of properties such as high mobilities for charge carriers, high transparency in the visible range as well as high degree of flexibility and mechanical strength [2]. Exploiting these properties, devices such as field effect transistors [3, 4], sensors [5], photodetectors [6-9], supercapacitors [10] as well as transparent conducting electrodes [11] have been fabricated in recent years.

Graphene being a 2D material, its effective usage depends on the ability to synthesize over extended areas, with assured monodispersity in terms of number of layers. The latter is an important parameter in device fabrication as the nature of graphene varies sensitively with the number of layers [12]. There have been several methods for growing graphene employing top-down, bottom-up or hybrid methods. Graphene obtained from micro-mechanical cleavage of graphite crystals [1, 2] does possess high quality but is produced in low yield. To obtain in large quantities, chemical [13, 14] and liquid-phase exfoliation [15] methods have been developed. In practice, CVD over catalytic Ni and Cu substrates has gained importance [16]. As carbon feedstock, solid [17, 18], liquid [19] or gaseous hydrocarbon sources [20] are being used in flowing hydrogen. Natural carbon sources [21] as well as amorphous carbon, [22, 23] have also been used. However, the conventional thermal CVD processes can be energy intensive and time consuming [24]. Recently, there have been reports of modified CVD methods such as radio frequency magnetic inductive heating (RFCVD) which enabled rapid production of high quality graphene over few cm^2 areas [25]. Using halogen lamps as heating unit, a rapid thermal CVD (RTCVD) process has been developed for roll to roll graphene production [24]. As hydrogen is a safety concern, particularly at high process temperatures (~1000 °C), some modified methods [26, 27] have been reported recently without hydrogen usage.

Recently, graphene coating has gained importance as a protective barrier for metal surfaces as it is chemically inert and stable [28-32]. It is perhaps the thinnest coating ever possible. There are several efforts in recent literature for decreasing the corrosion rates of metals such as Cu and Ni using graphene, as graphene can be easily grown on these metals [33-37]. Preventing corrosion and oxidation of metal electrodes is a major challenge in device physics [28, 38] and in spintronic devices for example, involving spin active ferromagnetic metals. Recently, Dlubak et al*.* reported the novelty of graphene passivation for Ni electrodes in spin devices [39]. Graphene is a thermal oxidation barrier as well as it poses a high energy barrier to oxygen diffusion [29] and unlike conventional coating such as that of polymers, it does not alter the intrinsic properties of the metal surface underneath [40].

IVA.2 Scope of the present investigation

The literature methods for graphene rely on heating the mixture of gaseous hydrocarbons, argon and hydrogen at high temperatures with a catalytic substrate. Ideally, one should avoid using hydrogen at elevated temperature. It not only adds to complexity in instrumentation but also brings safety concern associated with its explosive nature. Secondly, the methods employ large volume of heating zone to achieve the desired temperature for the active area, which makes these processes energy intensive. In addition, because hydrogen is used, the active substrate has to be pre-annealed at ultra-high vacuum before introducing the carbon source.

All these steps are necessary in these methods. The quality of graphene produced depends sensitively on the synthetic parameters. What one requires ideally is a method that uses no gaseous species with only necessary heating of the catalytic substrate. This method presented in this section overcomes such limitations in the graphene synthesis methods. A method in which a safe, affordable solid hydrocarbon sources is used and catalytic substrate is locally Joule heated to obtain high quality large area graphene in reasonably less time. This makes the investigated method truly a low cost and rapid method.

IVA.3 Experimental section

Ni foils (4.0 x 0.8 cm^2, thickness ~ 50 μm, Alfa Aesar) were cut to fit into the slots for passing current in a vacuum chamber (~ 4 x 10^{-3} Torr) pumped by rotary pump. Typically, 10 μL of 1 mM chloroform solution of naphthalene was drop casted onto the Ni foil and allowed to dry. AC Currents of 20 - 25 A were passed for 15 minutes. Temperature of the foil was measured using infrared thermometer MIKRON M90-R1. Raman spectra were recorded at different stages in the backscattering geometry using a 532 nm excitation from a diode pumped frequency doubled Nd:YAG solid state laser (model GDLM -5015L, Photop Swutech, China) and a custom-built Raman spectrometer equipped with a SPEX TRIAX 550 monochromator and a liquid nitrogen cooled CCD detector (Spectrum One with CCD3000 controller, ISA Jobin Yvon). The morphology of the grown graphene on Ni was examined using a field emission SEM (Nova Nano SEM 600, FEI Company). AFM imaging was done on a diInnova SPM (Veeco, USA) using Si_3N_4 probes (model, DNP-20, spring constant 0.1 N/m) in contact mode at a scanning force of 5 nN. Transmission electron microscopy (TEM) and selected area electron diffraction (SAED) analysis were performed using a JEOL-3010 instrument operating at 300 kV. Graphene on Ni was transferred onto the holey carbon film of the Cu TEM grid by an electrochemical delamination method [44] followed by lift off of PMMA using acetone.

Electrochemical investigations were performed in order to evaluate the corrosion resistance property of graphene on Ni using CH instruments (Model: CH660E, Austin, USA) in three electrode configuration. In a conventional 3-electrode configuration, Ni or graphene coated Ni (graphene/Ni) was employed as working electrode, Pt as counter electrode and standard Ag/AgCl as reference electrode. The area of the working electrode is 0.64 cm^2 in a 0.1 M NaCl electrolyte at room temperature (25 °C). The open circuit potential (OCP) was monitored continuously till the steady state potential reached. After the OCP measurements, the polarization curves were measured for the samples in 0.1 M NaCl solution. The cathodic and anodic polarization measurements were performed at a scan rate of 10 mV/s. The corrosion potential (E_{corr}) and corrosion current (I_{corr}) were derived through extrapolation from Tafel polarization curve.

The corrosion rate was calculated using equation [41]:

$$CR = (I_{\mathrm{corr}} \times K \times EW)/(\rho A)$$

where, K, corrosion rate constant, = 3272 mm/year, EW (equivalent weight), 29 g for Ni, ρ (material density) = 8.90 g/cm^3 for Ni and the sample area A = 0.8 x 0.8 cm^2.

For thermal oxidation study, Ni and graphene/Ni foils were heated in a heating furnace in O_2 atmosphere. Initially, X-ray diffraction (XRD) (Bruker D8 Discover diffractometer, Cu K_α, (1.5419 Å)) was recorded on bare Ni and graphene/Ni foils. The same foils were heated to 500 °C for 15 min and then again for 30 min in same conditions and XRD were recorded after each process.

IVA.4 Results and discussion

A polycrystalline Ni foil (50 μm, Alfa Aesar, 0.7 Ω) was cut into a 4.0 x 0.8 cm^2 strip to fit into the electrode slot for passing current, (see experimental section IVA.3). Typically, 10 μL of 1 mM chloroform solution of naphthalene was drop casted onto the Ni foil and allowed to dry (Figure IVA.1a). After reaching a rotary vacuum of ~ 4 mTorr, the Ni foil was Joule heated to red hot (~ 1050 °C as read using a pyrometer) by passing ~ 25 A of direct current, in a time span of 2 minutes (Figure IVA.1b) and after 15 minutes, the current was turned off and the foil was allowed to cool for a few minutes before taking out of the vacuum chamber. The formation of graphene is seen from the brown coloration in the middle of the foil (Figure IVA.1c). The nature of graphene obtained varied with the joule heating temperature. A naphthalene coated foil joule heated with 18 A current to reach 700 °C in the given instance, did not show any graphitic features in the Raman spectrum. The foil heated to 770 °C (current, 20 A),

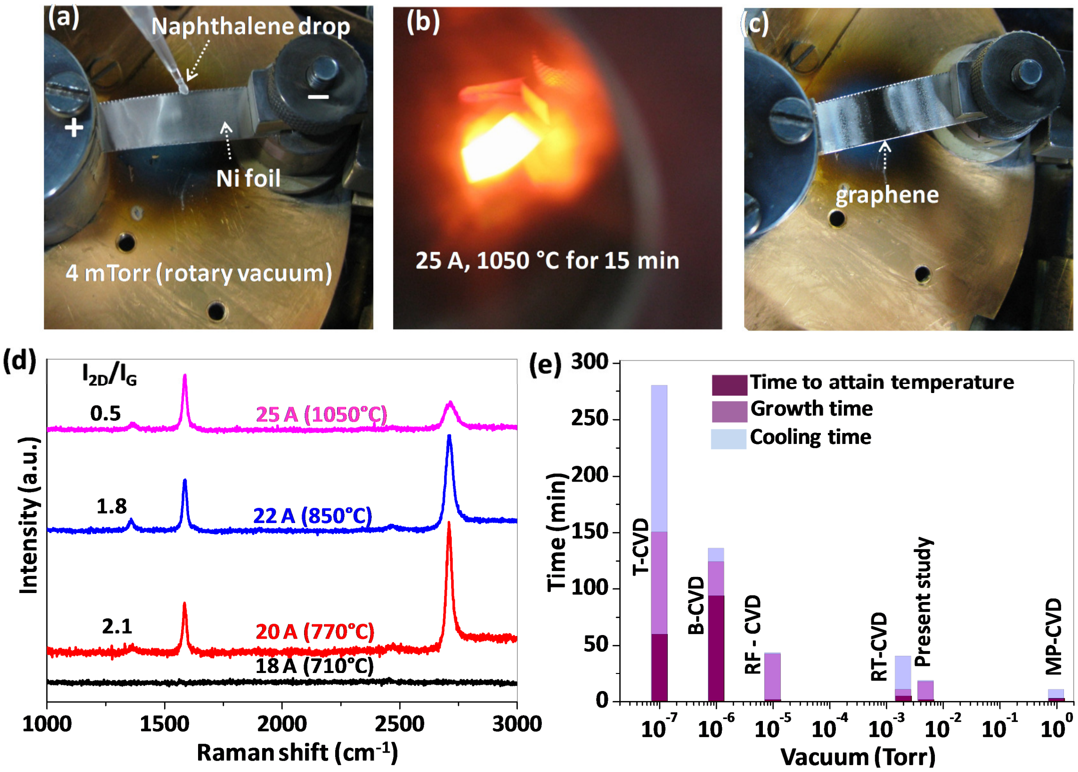

Figure IVA.1Process flow of synthesis and comparison with literature methods

Photographs from different stages of graphene synthesis. (a) Drop casting of naphthalene solution on a Ni foil suspended between two current terminals, (b) the Ni foil joule heated to red hot, (c) after switching off and cooling to room temperature. Relatively darker region in the middle is due to graphene formation. (d) Raman spectra of graphene obtained on Ni foils joule heated using different currents to different temperatures. (e) Histogram showing time span of graphene synthesis with different CVD based synthetic methods reported in the literature (typical examples), in comparison to the present study. The vacuum conditions employed are shown along x-axis and each bar is colored internally to represent the time spent in each sub process (see legend). T-CVD: thermal CVD [43], B-CVD: CVD using boralectric sample heater [27], RF-CVD: Radio frequency CVD using magnetic inductive heating [25], RT-CVD: Rapid thermal CVD using halogen lamps [24].

exhibited the characteristic G (position, 1586 cm^{-1}; FWHM, 21 cm^{-1}) and symmetric 2D (2712 cm^{-1}, 30cm^{-1}) bands with the I_{2D}/I_G ratio of 2.1 which clearly indicates the formation of single layer graphene [42] (Figure IVA.1d, red curve). With the foil temperature of 850 °C (current, 22 A), mostly bilayer graphene (I_{2D}/I_G, 1.8) was produced along with a small intensity defect related D band (1350 cm^{-1}) (d, blue curve). At even higher temperature of 1050 °C (current, 25 A), multilayer graphene (I_{2D}/I_G, 0.5) was obtained on the Ni foil with a prominent D band (Figure IVA.1d, magenta curve), which is a measure of defects. Another observation is that external heating of naphthalene coated Ni to similar temperatures does not seem to aid graphene growth (Figure IVA.2a). This clearly indicates the importance of electric field in the formation of graphene lattice on Ni. It appears that the electric current generates local plasma during joule heating, similar to the situation in plasma assisted CVD [26].

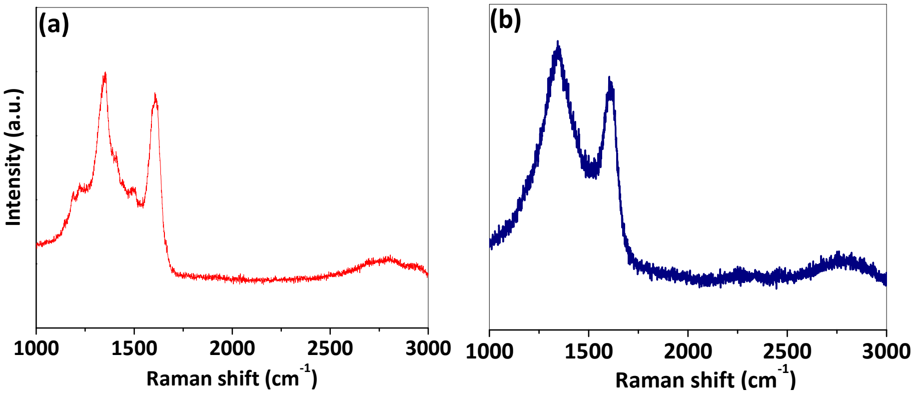

Figure IVA.2 Thermal heating of Ni foil with naphthalene source and Joule heating of plane Ni without any aromatic source

(a) Effect of thermal heating of naphthalene coated Ni placed on molybdenum boat. (b) Joule heating of Ni foil without any aromatic source

The advantages of the present method of graphene synthesis are immediately noticeable. Graphene can be grown in ~ 20 minutes over mm^2 areas which can, in principle, be extended to cm^2 areas. The whole process takes place in rotary vacuum of 4 mTorr which is quick to attain. For comparison, typical CVD based synthetic methods for graphene are shown in Figure IVA.1e in the form of a histogram where the process times are indicated within each bar. Conventional thermal CVD (T-CVD) takes typically 4 - 5 hours to complete the process, while other recently reported methods such as RF-

CVD and RT-CVD take ~ 40 minutes. Importantly in the present method, the use of gaseous sources like methane or hydrogen is avoided; instead, a simple, safe and affordable aromatic solid hydrocarbon source, naphthalene, is used. As a control experiment Joule heating of plane Ni was carried in absence of naphthalene and Raman spectra of which is similar to nanocrystalline graphene obtained from residual hydrocarbons (see Figure IVA.2b). This clearly suggests that there is no influence of local hydrocarbons in the present process of graphene formation. Also other aromatic sources such as coronene and anthracene have also proven useful for this purpose; however they produce low quality graphene with low 2D intensity (see Figure IVA.3). The energy requirement is low as only the Ni foil is heated unlike the thermal CVD, where the whole set up needs to be heated up. This is essentially a cold wall reactor technique where no cooling coils are needed around the vacuum chamber. The above features make it truly a low cost method.

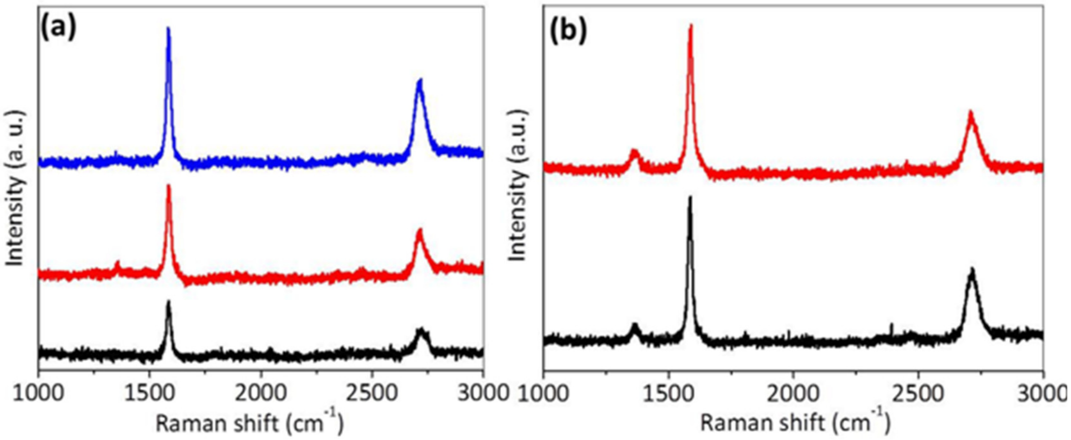

Figure IVA.3 Joule heating of Ni with other aromatic sources

Representative Raman spectra of graphene over different regions of the Ni foil derived from (a) coronene and (b) anthracene.

Graphene grown on Ni at 770 °C is examined in more detail (Figure IVA.4). The representative Raman spectra recorded from different graphene covered regions are shown in Figure IVA.4a along with the photograph of graphene/Ni foil in the inset. The 2D band is seen as single Lorentzian peak, centred at ~ 2712 cm^{-1} is symmetric with FWHM of ~ 30 cm^{-1}, typical signature of single layer graphene [42]. The absence of D band at 1350 cm^{-1}, indicates the high quality of the graphene. The I_{2D}/I_G ratio is found to be ~ 2.0 - 2.7, which is comparable to the values obtained for single layer graphene from CVD method [45]. FESEM image shows the large area uniform growth of the graphene (Figure IVA.4b). Figure IVA.4c is a typical TEM micrograph of graphene freely suspended on a lacey carbon TEM grid. Its highly crystalline nature is evident from the hexagonal electron diffraction pattern (inset of Figure IVA.4c).

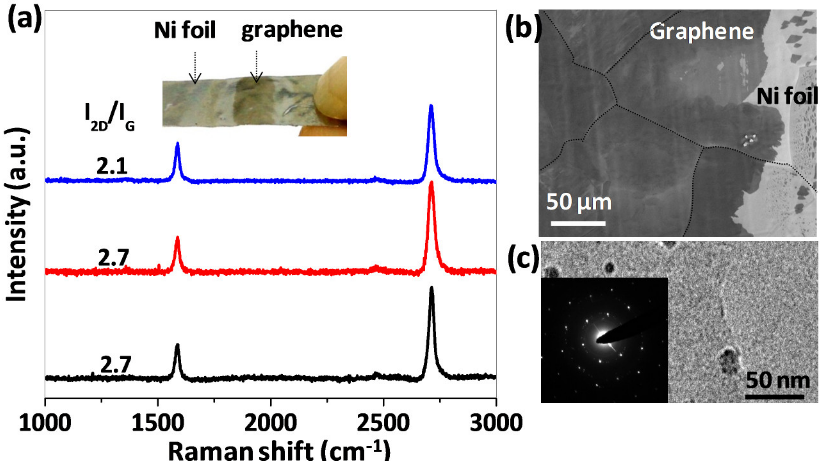

Figure IVA.4 Raman and microscopy analysis

(a) Representative Raman spectra of graphene produced at 770 °C (current, 20 A) from different regions of the Ni foil shown in the photograph in the inset. The estimated I_{2D}/I_G values are also indicated. (b) FESEM image showing uniform growth of graphene on Ni over a large area. Black lines trace the grain boundary of the underlying Ni surface. (c) TEM micrograph of graphene after transferring on lacey carbon grid with electron diffraction pattern in the inset.

Analysis of graphene wrinkles: Graphene produced at high temperatures typically exhibits a network of wrinkles [46, 47] due to thermally induced stress during cooling as the thermal expansion coefficient of graphene (8×10^{-6} K^{-1}) and Ni (13×10^{-6} K^{-1}) differ. Figure IVA.5a shows a network of wrinkles with a depth signifying presence of a grain boundary in Ni. As shown by arrows, the wrinkle lines cross the Ni grain boundaries. Two types of wrinkles were observed where the smaller ones exhibit a height of 13.7 ± 1.7 nm and width, 7.3 ± 1.3 nm while the larger wrinkles are 75.8 ± 6.1 nm high and 57.8 ± 7.9 nm wide (Figure IVA.5b). Recent studies have shown that different types of folding can give rise to different wrinkle dimensions [48, 49]. The wrinkles observed in this study resemble those previously observed in CVD graphene

[47, 50]. The roughness of the graphene within the wrinkle polygon was found to be 0.33 nm indicating its high degree of smoothness compared to plane Ni with roughness value of 2.88 nm (Figure IVA.5c). In present case, the continuous wrinkle formation was found over large area (Figure IVA.5d and e), which is taken to indicate extended nature of the grown graphene.

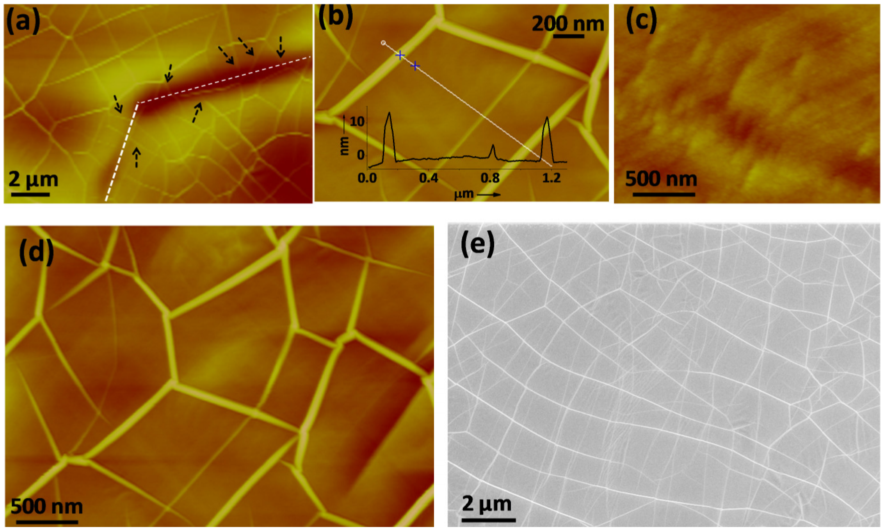

Figure IVA.5 Microscopy of graphene wrinkles

(a) AFM topography of the wrinkle network (z scale, 200 nm). White dashed lines are drawn along the grain boundary of Ni foil. Wrinkles crossing the grain boundary are marked with arrows. (b) A zoomed in image of graphene wrinkles along with a height profile (z scale, 50 nm). (c) AFM topography of Ni without graphene grown on it (z scale: 50 nm). (d) and (e) low magnification AFM (z scale: 50 nm) and FESEM images.

Along with the wrinkles, ripples like structures were also found within the polygons of wrinkles. These ripple like structures possibly might have originated from the wrinkles and thus termed as secondary wrinkles. Figure IVA.6a gives a clear picture of distinction between the wrinkles (or primary wrinkles) and the secondary wrinkles formed on the surface of the graphene sheets. Clearly, primary wrinkles appear brighter and mostly form crossed T-junctions whereas secondary wrinkles are found to be contained within the primary wrinkles. The primary wrinkles are bigger with a height of about 20 - 22 nm while the secondary wrinkles are about 7 - 9 nm (as shown in Figure IVA.6b). It is also observed that the secondary wrinkles are formed in multiplets and exhibits a periodicity with typical wavelength of 200 – 300 nm. Further, the angles formed by meeting of primary wrinkles (see Figure IVA.6c) were analysed and given in histogram plot (see Figure IVA.6d). Among the three categories of the angles measured, the one with angles between 90° to 120° are found to be major (77%) followed by one with the angle > 120° (18%) and one with the angle < 90° (5%).

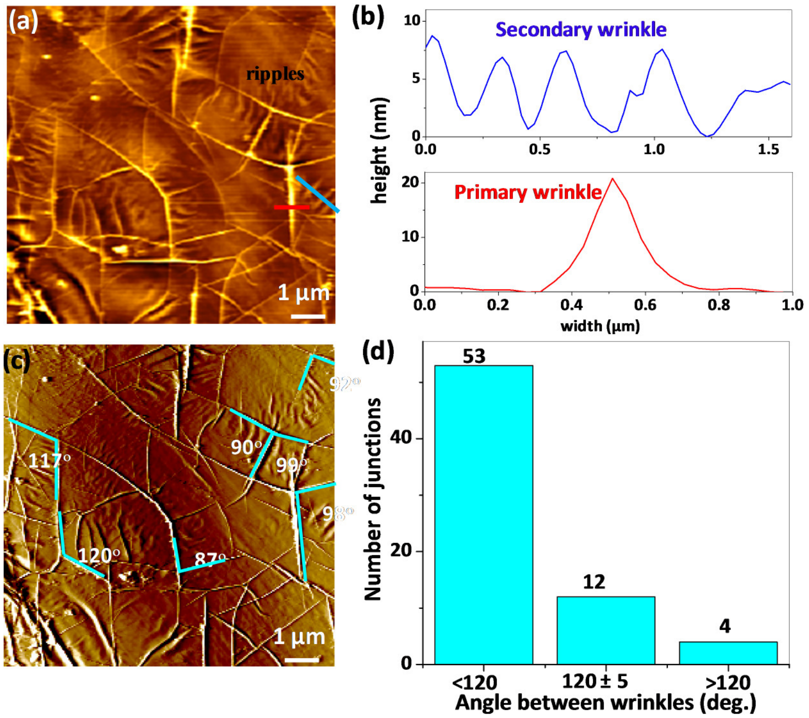

Figure IVA.6 Analysis of graphene wrinkles

(a) AFM image of graphene sheets distinguishing primary and secondary wrinkles formed on its surface. (b) Height profile of primary (red) and secondary (blue) marked in (a). (c) AFM image of graphene surface showing different angles formed at junctions. (b) Histogram collected from the images of multiple regions of the sample showing the different angles formed between primary wrinkles.

The corrosion resistance of graphene to underlying Ni has been studied using electrochemical measurements (Figure IVA.7). First, the OCP curves were measured for bare Ni and graphene/Ni in 0.1 M NaCl solution for over 15 min. As can be seen in Figure IVA.7a, the OCP of graphene/Ni (-82 mV) is shifted higher positive potential compared to that of bare Ni (-145 mV) signifying its high resistance to corrosion. Further, its corrosion resistance was examined using Tafel analysis (see Figure IVA.7b). The Tafel polarisation curve for graphene/Ni shows a positive shift (62 mV) of corrosion potential and a lower corrosion current compared to bare Ni. The corrosion current (I_{corr}) values were found to be 4.13 x 10^{-9} and 2.82 x 10^{-8} Acm^{-2} for graphene/Ni and Ni, respectively. Accordingly, the corrosion rates were estimated [41] to be 1.35 x 10^{-15} and 9.19 x 10^{-15} m/s, respectively. It is significant that the corrosion rate was 7 times lower for graphene/Ni compared to that of bare Ni. These results are comparable to the literature values for graphene/Ni [41] and graphene/Cu [33].

Further, the robustness of graphene coating was examined using electrochemical impedance spectroscopy (EIS). Figure IVA.7c shows the Bode magnitude plot, in which graphene/Ni showed overall higher impedance than bare Ni. From the Nyquist plot in Figure IVA.7d, the electrochemical polarisation resistance (R_p, sum of polarisation and solution resistance) offered by graphene/Ni (R_p = 6.22 x 10^3 Ω cm^2) is three times higher than that of bare Ni (R_p = 2.22 x 10^3 Ω cm^2). In other words, surface resistance offered by graphene coated Ni was higher than that of bare Ni suggesting that graphene forms strong protecting layer for Ni thereby impeding ion diffusion. Further, EIS data was fitted with equivalent circuit using Randles + Warburg circuit model [41]. This network includes the following elements: a resistor, due to solution resistance, Rs, (31.9 Ω cm^2 and 56.9 Ω cm^2 for graphene/Ni and bare Ni respectively), a resistor due to Faradaic charge transfer between metal and the solution (metal corrosion), R_{CT}, (22.1 kΩ-cm^2 and 1.26 kΩ-cm^2 for graphene/Ni and bare Ni respectively), a Warburg element (W), which accounts for diffusion process, and a constant phase element (CPE) to model the capacitance of the electrical double layer (EDL) at the metal/liquid interface.

The excellent adhesion property of graphene on Ni surface was examined by scotch tape test [51] (Figure IVA.8). Only a small portion of graphene was transferred to scotch tape which is direct evidence for its strong adhesion on the Ni surface. Additionally, Raman spectra recorded before and after all the corrosion tests showed that there is no change in the nature of graphene. These observations suggest that the graphene has a strong adhesion with the Ni surface which helps in preventing the corrosion.

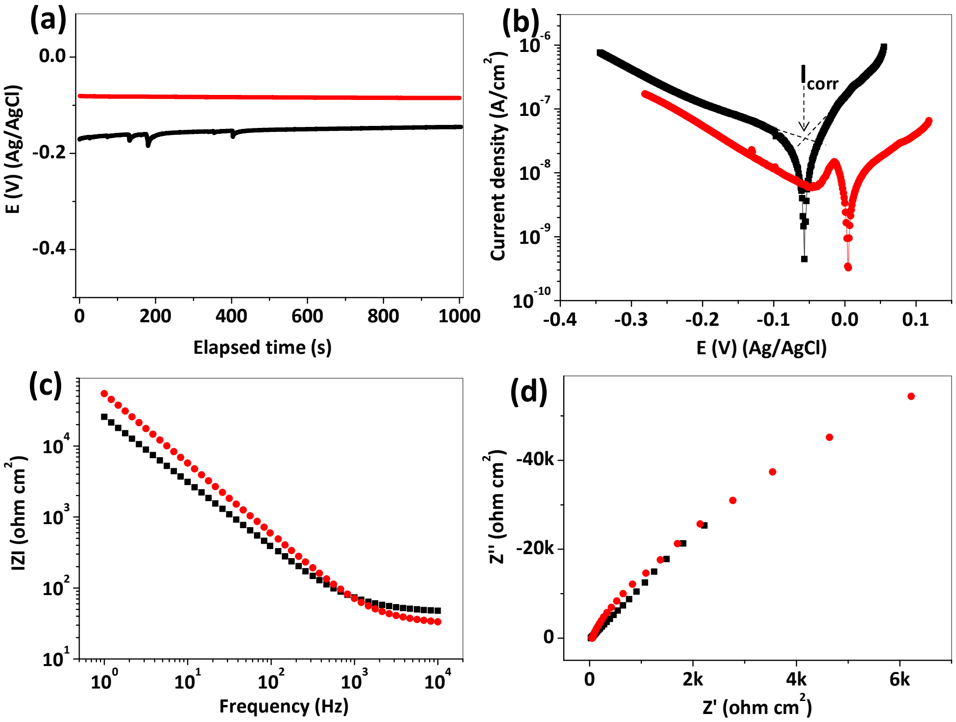

Figure IVA.7 Corrosion resistant studies of graphene coated Ni foil

Corrosion resistant studies of graphene coated Ni foil. (a) Open circuit potential (OCP) curves (b) Tafel plots (sweep rate: 10 mV/s) (c) Bode magnitude plots and (d) Nyquist plots for Ni (black circle) and graphene coated Ni (red squares).

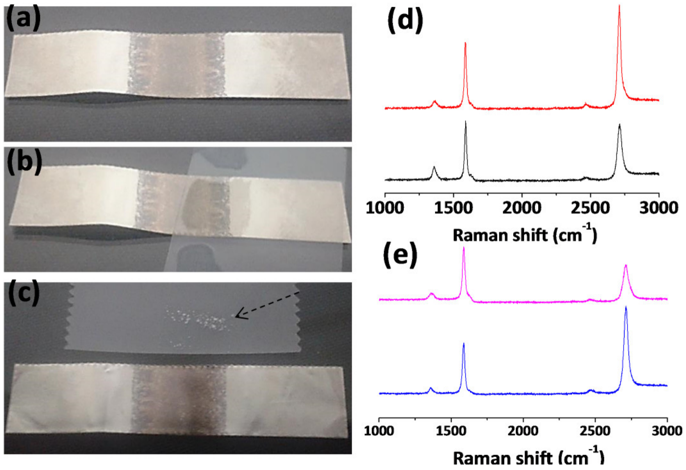

Figure IVA.8 The adhesion quality of graphene on Ni

The photograhs of (a) graphene/Ni, (b) scotch tape pasted on graphene/Ni, (c) after removing scotch tape from graphene/Ni. Raman spectra of graphene/Ni measured before (d) and after all the corrosion tests (e).

We have examined below the efficacy of the grown graphene as thermal oxidation barrier to Ni (Figure VI.9). Prior to heating in oxygen, the bare Ni foil exhibited a prominent Ni(111) peak at 2θ value of 44.5° while graphene/Ni showed, in addition, a peak at 2θ ~ 26.5° corresponding to graphene(002). When the two foils were heated to 500 °C for 15 min in oxygen, a small peak at 2θ value of 37.4° appeared in the case of Ni foil (Figure VI.9a), corresponding to NiO(111). When it was heated for 30 more minutes, the NiO(111) peak grew in intensity and became distinct as expected. Interestingly, there was no intensity in the NiO(111) region in the case of graphene/Ni (Figure VI.9b). Thus, graphene coated Ni was able to withstand oxidation which is also visibly evident from the photographs shown in the middle (Figure VI.9). The graphene coating gave up eventually due to rupturing, after prolonged heating in oxygen (Figure VI.10). This result may be compared with a literature report where graphene covered Cu and Cu/Ni alloy surfaces are shown to withstand oxidation at 200 °C in air [38]. In the present study, the observed high thermal stability may arise from the strong adhesion of graphene on Ni (Figure VI.8).

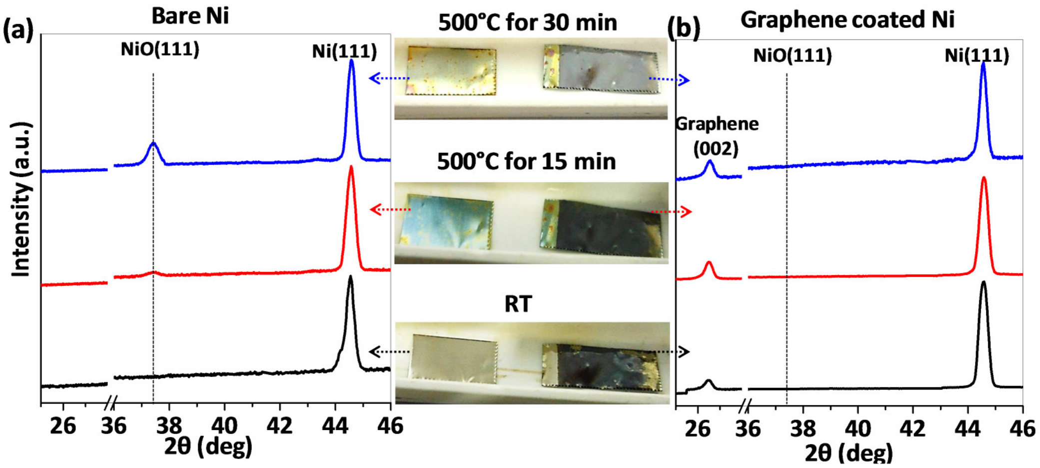

Figure IVA.9 Thermal oxidation resistance

XRD patterns of (a) bare Ni, (b) Graphene coated Ni after a heat treatment in oxygen, pristine foils (black curves), after 15 min treatment at 500°C (red curves), after 30 min treatment at 500°C (blue curves). Photographs of the corresponding Ni foils are shown in the middle panel (see arrows). The position of the NiO(111) peak is shown in both (a) and (b) with a dashed vertical line.

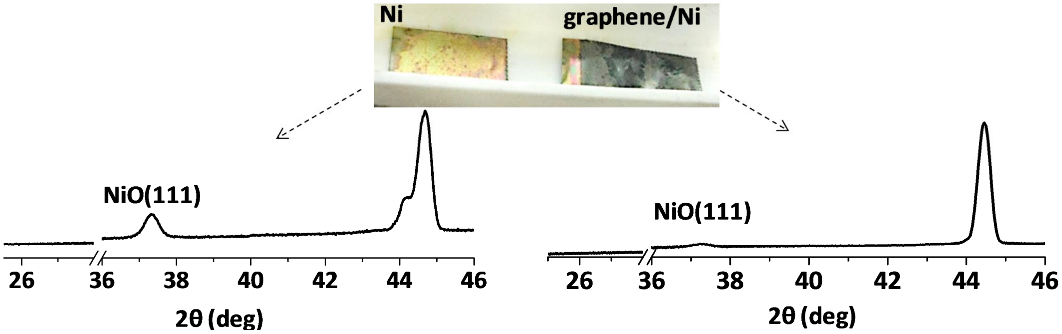

Figure IVA.10 Thermal degradation at prolonged oxidation
The XRD pattern of Ni (left) and graphene/Ni (right) after subjecting to prolonged oxidation in oxygen. The rapture of graphene film can be clearly seen in the photograph (right panel) due to which NiO(111) peak starts to appear at 37.4°.

With the present method, graphene can be obtained not only on flat substrates like foil, but also on curved substrates such as Ni wire, mesh, foam etc., by using them as joule heating substrates. A Ni wire (diameter: 0.5 mm, resistance: 1.3 Ω) required 11 A (current density: 44 A/mm^2) to heat up to 770 °C, while a mesh (thickness: 10 μm, diameter: 30 μm, spacing: 200 μm, resistance: 1.8 Ω) required only 4-5 A (current density: 48 A/mm^2). Figure IVA.11a shows representative Raman spectra of graphene on Ni wire (top four) collected from regions around the wire as shown in arrow mark in FESEM image (Figure IVA.11b). The typical I_{2D}/I_G ratio indicates that it is mostly composed of single and bilayer graphene. The non-uniform coating of naphthalene solution around Ni wire would have resulted in mixture of single and bilayer graphene as the number of graphene layers was found to be varying with the local thickness of naphthalene. Graphene domains were clearly seen in the case of Ni mesh (Figure IVA.11c). Raman spectra in Figure IVA.11a (bottom two) with I_{2D}/I_G of 1-2 indicates the presence of single and bilayer graphene in the regions marked by arrow in FESEM image (Figure IVA.11d).

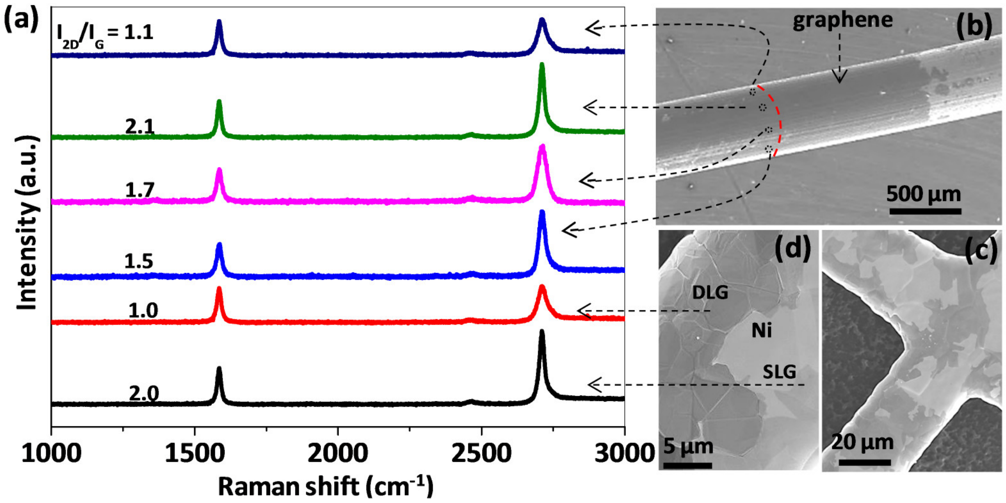

Figure IVA.11 Growth of graphene on other metal geometries

(a) Representative Raman spectra of graphene grown on a Ni wire (top four) and a Ni mesh (bottom two). FESEM images of (b) the Ni wire covered all around with graphene, (c) the Ni mesh covered with graphene domains and (d) single and few layer graphene domains on the Ni mesh.

IVA.5 Conclusions

In conclusion, a rapid method of synthesizing graphene has been developed on Ni under rotary vacuum by simply joule heating the foil after coating it with naphthalene. This is a direct, one step process not requiring any expensive instrumentation nor any gaseous sources including hydrogen. The method can potentially be extended to larger areas with higher throughputs. Besides foils, Ni in the form of wire and mesh have also been explored. Complex geometries may be also be tried. Using other metals such as Cu is another possibility.

References

(1) Novoselov, K. S.; Geim, A. K.; Morozov, S. V.; Jiang, D.; Zhang, Y.; Dubonos, S. V.; et al.. Electric Field Effect in Atomically Thin Carbon Films. Science **2004**, 306, 666-669.

(2) Rao, C. N. R.; Sood, A. K.; Subrahmanyam, K. S.; Govindaraj, A. Graphene: The New Two-Dimensional Nanomaterial. Angew.Chem. Int. Ed. **2009**, 48, 7752-7777.

(3) Schwierz, F. Graphene Transistors. Nat. Nanotechnol. 2010, 5, 487-496.

(4) Lin, Y. M.; Dimitrakopoulos, C.; Jenkins, K. A.; Farmer, D. B.; Chiu, H.-Y.; Grill, A.; et al. 100-GHz Transistors from Wafer-Scale Epitaxial Graphene. Science **2010**, 327, 662.

(5) Yuan, W.; Shi, G. Graphene-Based Gas Sensors. J. Mater. Chem. A **2013**, 1, 10078-10091.

(6) Zhang, W. J.; Chuu, C. P.; Huang, J. K.; Chen, C. H.; Tsai, M. L.; Chang, Y. H.; et al. Ultrahigh-Gain Photodetectors Based on Atomically Thin Graphene-MoS2Heterostructures. Sci. Rep. **2014**, 4, 3826.

(7) Narendra, K.; Venkata Srinu, B.; Chandrabhas, N.; Kulkarni, G. U. Field Effect Transistors and Photodetectors Based on Nanocrystalline Graphene Derived from Electron Beam Induced Carbonaceous Patterns.Nanotechnology **2012**, 23, 425301-8.

(8) Chitara, B.; Panchakarla, L. S.; Krupanidhi, S. B.; Rao, C. N. R. Infrared Photodetectors Based on Reduced Graphene Oxide and Graphene Nanoribbons. Adv. Mater. **2011**, 23, 5419-5424.

(9) Xia, F. N.; Mueller, T.; Lin, Y. M.; Valdes-Garcia, A.; Avouris, P. Ultrafast Graphene Photodetector. Nat. Nanotechnol. **2009**, 4, 839-843.

(10) Chen, T.; Xue, Y.; Roy, A. K.; Dai, L. Transparent and Stretchable High-Performance Supercapacitors Based on Wrinkled Graphene Electrodes. ACS Nano **2013**, 8, 1039-1046.

(11) Eda, G.; Lin, Y.-Y.; Miller, S.; Chen, C.-W.; Su, W.-F.; Chhowalla, M. Transparent and Conducting Electrodes for Organic Electronics from Reduced Graphene Oxide. Appl. Phys. Lett. **2008**, 92, 233305.

(12) Wenjuan, Z.; Dimitrakopoulos, C.; Freitag, M.; Avouris, P. Layer Number Determination and Thickness-Dependent Properties of Graphene Grown on SiC. IEEE Trans. Nanotechnol. **2011**, 10, 1196-1201.

(13) Wei, D.; Liu, Y. Controllable Synthesis of Graphene and Its Applications. Adv. Mater. **2010**, 22, 3225-3241.

(14) Tang, Y. B.; Lee, C. S.; Chen, Z. H.; Yuan, G. D.; Kang, Z. H.; Luo, L. B.; et al. High-Quality Graphenes via a Facile Quenching Method for Field-Effect Transistors. Nano Lett. **2009**, 9, 1374-1377.

(15) Hernandez, Y.; Nicolosi, V.; Lotya, M.; Blighe, F. M.; Sun, Z.; De, S.; et al. High-Yield Production of Graphene by Liquid-Phase Exfoliation of Graphite. Nat. Nanotechnol. **2008**, 3, 563-568.

(16) Li, X.; Cai, W.; An, J.; Kim, S.; Nah, J.; Yang, D.; et al. Large-Area Synthesis of High-Quality and Uniform Graphene Films on Copper Foils. Science **2009**, 324, 1312-1314.

(17) Sun, Z. Z.; Yan, Z.; Yao, J.; Beitler, E.; Zhu, Y.; Tour, J. M. Growth of Graphene from Solid Carbon Sources. Nature **2010**, 468, 549-552.

(18) Ji, H.; Hao, Y.; Ren, Y.; Charlton, M.; Lee, W. H.; Wu, Q.; et al. Graphene Growth Using a Solid Carbon Feedstock and Hydrogen. ACS Nano **2011**, 5, 7656-7661.

(19) Zhang, B.; Lee, W. H.; Piner, R.; Kholmanov, I.; Wu, Y.; Li, H.; et al. Low-Temperature Chemical Vapor Deposition Growth of Graphene from Toluene on Electropolished Copper Foils. ACS Nano **2012**, 6, 2471-2476.

(20) Reina, A.; Jia, X.; Ho, J.; Nezich, D.; Son, H.; Bulovic, V.; et al. Large Area, Few-Layer Graphene Films on Arbitrary Substrates by Chemical Vapor Deposition. Nano Lett. **2008**, 9, 30-35.

(21) Ruan, G.; Sun, Z.; Peng, Z.; Tour, J. M. Growth of Graphene from Food, Insects, and Waste. ACS Nano **2011**, 5, 7601-7607.

(22) Orofeo, C.; Ago, H.; Hu, B.; Tsuji, M. Synthesis of Large Area, Homogeneous, Single Layer Graphene Films by Annealing Amorphous Carbon on Co and Ni. Nano Res. **2011**, 4, 531-540.

(23) Kurra, N.; Bhadram, V. S.; Narayana, C.; Kulkarni, G. U. Few Layer Graphene to Graphitic Films: Infrared Photoconductive versus Bolometric Response.Nanoscale **2013**, 5, 381-389.

(24) Ryu, J.; Kim, Y.; Won, D.; Kim, N.; Park, J. S.; Lee, E.-K.; et al. Fast Synthesis of High-Performance Graphene Films by Hydrogen-Free Rapid Thermal Chemical Vapor Deposition. ACS Nano **2013**, 8, 950-956.

(25) Piner, R.; Li, H.; Kong, X.; Tao, L.; Kholmanov, I. N.; Ji, H.; et al. Graphene Synthesis via Magnetic Inductive Heating of Copper Substrates. ACS Nano **2013**, 7, 7495-7499.

(26) Kim, Y. S.; Lee, J. H.; Kim, Y. D.; Jerng, S.K.; Joo, K.; Kim, E.; et al. Chun, S.-H. Methane As an Effective Hydrogen Source for Single-Layer Graphene Synthesis on Cu Foil by Plasma Enhanced Chemical Vapor Deposition.Nanoscale **2013**, 5, 1221-1226.

(27) Wan, X.; Chen, K.; Liu, D.; Chen, J.; Miao, Q.; Xu, J. High-Quality Large-Area Graphene from Dehydrogenated Polycyclic Aromatic Hydrocarbons. Chem. Mater. **2012**, 24, 3906-3915.

(28) Kang, D.; Kwon, J. Y.; Cho, H.; Sim, J.-H.; Hwang, H. S.; Kim, C. S.; et al. Oxidation Resistance of Iron and Copper Foils Coated with Reduced Graphene Oxide Multilayers. ACS Nano **2012**, 6, 7763-7769.

(29) Topsakal, M.; Şahin, H.; Ciraci, S. Graphene Coatings: An efficient Protection From Oxidation.Phys. Rev. B **2012**, 85, 155445.

(30) Nilsson, L.; Andersen, M.; Balog, R.; Lægsgaard, E.; Hofmann, P.; Besenbacher, F.; et al. Graphene Coatings: Probing the Limits of the One Atom Thick Protection Layer. ACS Nano **2012**, 6, 10258-10266.

(31) Prabakar R. S. J.; Pyo, M, Corrosion Protection of Aluminum in LiPF6 by Poly(3,4-ethylenedioxythiophene) Nanosphere Coated Multiwalled Carbon Nanotube. Corros. Sci. **2012**, 57, 42-48.

(32)Prabakar, R. S. J.; Hwang, Y.-H.; Bae, E. G.; Lee, D. K.; Pyo, M. Graphene Oxide as a Corrosion Inhibitor for the Aluminum Current Collector in Lithium Ion Batteries. Carbon **2013**, 52, 128-136.

(33) Sahu, S. C.; Samantara, A. K.; Seth, M.; Parwaiz, S.; Singh, B. P.; Rath, P. C.; et al. Facile Electrochemical Approach for Development of Highly Corrosion Protective Coatings Using Graphene Nanosheets. Electrochem.Commun. **2013**, 32, 22-26.

(34) Krishnamurthy, A.; Gadhamshetty, V.; Mukherjee, R.; Chen, Z.; Ren, W.; Cheng, H. M.; et al. Passivation of Microbial Corrosion Using a Graphene Coating. Carbon **2013**, 56, 45-49.

(35) Kirkland, N. T.; Schiller, T.; Medhekar, N.; Birbilis, N. Exploring Graphene As a Corrosion Protection Barrier. Corros. Sci. **2012**, 56, 1-4.

(36) Zhou, F.; Li, Z.; Shenoy, G. J.; Li, L.; Liu, H. Enhanced Room-Temperature Corrosion of Copper in the Presence of Graphene.ACS Nano **2013**, 7, 6939-6947.

(37) Hsieh, Y.-P.; Hofmann, M.; Chang, K.-W.; Jhu, J. G.; Li, Y.Y.; Chen, K. Y.; et al. Complete Corrosion Inhibition Through Graphene Defect Passivation. ACS Nano **2013**, 8, 443-448.

(38) Chen, S.; Brown, L.; Levendorf, M.; Cai, W.; Ju, S.Y.; Edgeworth, J.; et al. Oxidation Resistance of Graphene-Coated Cu and Cu/Ni Alloy. ACS Nano **2011**, 5, 1321-1327.

(39) Dlubak, B.; Martin, M.B.; Weatherup, R. S.; Yang, H.; Deranlot, C.; Blume, R.; et al. Graphene-Passivated Nickel As an Oxidation-Resistant Electrode for Spintronics. ACS Nano **2012**, 6, 10930-10934.

(40) Nayak, P. K.; Hsu, C.J.; Wang, S.C.; Sung, J. C.; Huang, J.L. Graphene coated Ni films: A Protective Coating. Thin Solid Films **2013**, 529, 312-316.

(41) Prasai, D.; Tuberquia, J. C.; Harl, R. R.; Jennings, G. K.; Bolotin, K. I. Graphene: Corrosion-Inhibiting Coating. ACS Nano **2012**, 6, 1102-1108.

(42) Malard, L. M.; Pimenta, M. A.; Dresselhaus, G.; Dresselhaus, M. S. Raman Spectroscopy in Graphene. Phys. Rep. **2009**, 473, 51-87.

(43) Mattevi, C.; Kim, H.; Chhowalla, M. A Review of Chemical Vapour Deposition of Graphene on Copper. J. Mater. Chem. **2011**, 21, 3324-3334.

(44) Wang, Y.; Zheng, Y.; Xu, X.; Dubuisson, E.; Bao, Q.; Lu, J.; et al. Electrochemical Delamination of CVD-Grown Graphene Film: Toward the Recyclable Use of Copper Catalyst. ACS Nano **2011**, 5, 9927-9933.

(45) Liao, C.D.; Lu, Y.-Y.; Tamalampudi, S. R.; Cheng, H.-C.; Chen, Y.T. Chemical Vapor Deposition Synthesis and Raman Spectroscopic Characterization of Large-Area Graphene Sheets. J. Phys. Chem. A **2013**, 117, 9454-9461.

(46) Chae, S. J.; Güneş, F.; Kim, K.d K.; Kim, E. S.; Han, G. H.; Kim, S. M.; et al. Synthesis of Large-Area Graphene Layers on Poly-Nickel Substrate by Chemical Vapor Deposition: Wrinkle Formation. Adv. Mater. **2009**, 21, 2328-2333.

(47) Huang, L.; Chang, Q. H.; Guo, G. L.; Liu, Y.; Xie, Y. Q.; Wang, T.; et al. Synthesis of High-Quality Graphene Films on Nickel Foils by Rapid Thermal Chemical Vapor Deposition. Carbon **2012**, 50, 551-556.

(48) Zhu, W.; Low, T.; Perebeinos, V.; Bol, A. A.; Zhu, Y.; Yan, H.; et al. Structure and Electronic Transport in Graphene Wrinkles. Nano Lett. **2012**, 12, 3431-3436.

(49) Pan, Z.; Liu, N.; Fu, L.; Liu, Z. Wrinkle Engineering: A New Approach to Massive Graphene Nanoribbon Arrays. J. Am. Chem. Soc. **2011**, 133, 17578-17581.

(50) Surwade, S. P.; Li, Z.; Liu, H. Thermal Oxidation and Unwrinkling of Chemical Vapor Deposition-Grown Graphene. J. Phys. Chem. C **2012**, 116, 20600.

(51) Beesley, D. J.; Semple, J.; Krishnan Jagadamma, L.; Amassian, A.; McLachlan, M. A.; Anthopoulos, T. D.; et al. Sub-15-nm Patterning of Asymmetric Metal Electrodes and Devices by Adhesion Lithography. Nat. Commun. **2014**, 5, 3933.

Chapter IVB

Highly Decoupled Graphene layers

Summary

The extraordinary properties of graphene are truly observable when it is suspended, being free from any substrate influence. Here, a new type of multilayer graphene is reported wherein each layer is turbostratically decoupled, resembling suspended graphene in nature, while maintaining high degree of 2D crystallinity. Such defect-free graphene multilayers have been made over large areas by Joule heating of a Ni foil coated with a solid hydrocarbon. Raman spectra measured on thick flakes (100 - 250 nm) have shown characteristics similar to suspended graphene with very narrow 2D bands (~ 16 cm^{-1}) and I_{2D}/I_G ratios up to 7.4, importantly with no D band intensity. Electron diffraction patterns showed sets of diffraction spots spread out with definite angular spacings, reminiscent of the angular deviations from the AB packing which are responsible for keeping the layers decoupled. The *d*-spacing derived from X-ray diffraction were larger (by ~ 0.04 Å) compared to that in graphite. Accordingly, the c-axis resistance values were three orders higher suggesting that the layers are indeed electronically decoupled. The high 2D crystallinity observed along with the decoupled nature should accredit the observed graphene species as a close cousin of suspended graphene.

IVB.1 Introduction

Graphene as a two-dimensional carbon material offers wide range of interesting properties such as high charge mobilities [1], superior thermal conductivity [2], high degree of transparency [3], as well as mechanical flexibility [4] among others. Because of such properties, it has attracted great attention in the context of flexible electronics

[5], printable optoelectronics [6], photonics [7], etc. Ideally, graphene has to be perfectly two-dimensional well extended and flat, for it to possess the characteristic electronic band structure and properties associated with it [8]. In reality, the properties of graphene get modified due to the presence of wrinkles [9], edges [10], defects [11] and also due to adsorbed foreign species [12] and dopants [13]. In addition, the substrate hosting the graphene can itself significantly influence its electronic [14], magnetic [15] and chemical properties [16] and such modifications, intentional and otherwise, have been effectively utilised in various contexts [17]. However, if one is serious in exploiting the native properties of graphene, it has to be prepared and handled in such a way that the above influences are minimal. One such case is the suspended graphene which comes close to ideal graphene in nature and therefore has attracted greater attention in recent years due to its extraordinary properties [18] especially in order to achieve near ideal ballistic transport [19] and ultrahigh mobility in field effect transistors [20]. However, synthesis and fabrication of large area suspended graphene reproducibly is a daunting task [21] involving several lithographic processes. The purity of the graphene produced is also under question as such steps leave behind residues from photoresists. In this context, we considered it interesting to explore turbostratic graphite as a form of suspended graphene.

Unlike normal graphite where the layers are perfectly AB stacked [22], in turbostratic graphite, there is no definite stacking order between adjacent layers. The popular form of normal graphite is the highly oriented pyrolytic graphite (HOPG) which is synthetically prepared at elevated temperatures to achieve high degree of crystallinity [23]. In turbostratic graphite, each stacked layer is randomly rotated with respect to its adjacent layers [24] and this angular disorder causes decoupling of the adjacent layers, resulting in increased interlayer spacing (3.35 to 3.42 Å) [25]. Due to the absence of the interlayer interaction, Raman spectrum of turbostratic graphite shows signatures of SLG, namely single Lorentzian 2D peak but FWHM (2D) is almost double that of SLG [26]. Unfortunately, Raman spectra of turbostratic graphite reported in the literature invariably contain noticeable D peak intensity implying non-negligible presence of defects [26]. These defects are present in turbostratic graphite in the form of stacking faults and large number of sp^3 carbon atoms [27]. Despite being a decoupled system, turbostratic graphite is considered ill-defined and not so useful solely due to its defects.

Recently since the graphene era, the turbostratic nature of graphite is being revisited. Ab-initio calculations using DFT has shown that few layered graphitic systems with angular stacking disorder can possess massless fermion behaviour showing Dirac cones in the electronic structure, typical of SLG [28]. Experimentally, Kim et al. studied Raman spectra of double layer graphene with varied rotation between them and found that intensity and FWHM of 2D peak varied sensitively with rotation angles [29]. Among multilayer systems, SLG-like behaviour has been observed only in the case of epitaxially grown graphene (MEG) on C-terminated SiC [30]. Hass et al. have provided evidence based on low angle electron diffraction (LEED), scanning tunnelling microscope (STM) and surface X-ray diffraction (SXRD) that the adjacent graphene layers in MEG are electronically isolated from each other [31] due to angular disorder. Its Raman spectrum contained a single Lorentzian 2D peak with FWHM of 40 cm^{-1} [32]. Using glazing incidence XRD (GIXRD), it was shown that MEG consisted of both Bernal and turbostratic stackings [33]. Orlita et al. reported a mobility of 250 kcm^2/Vs in MEG calculated using far infrared (FIR) transmission experiments [34]. In the above examples unfortunately, significant intensity is seen with the D band. Further, it has been reported that MEG grown on SiC loses its SLG-like behaviour upon transferring onto other substrates [35].

IVB.2 Scope of the present investigation

As detailed out in the introduction, in turbostratic graphite, each stacked layer is randomly rotated with respect to its adjacent layers and this angular disorder causes decoupling of the adjacent layers, resulting in increased interlayer spacing. Unfortunately, turbostratic graphite has very small 2D crystallinity and contains huge number of defects. Due to this, despite being a decoupled system, turbostratic graphite is considered ill-defined and not considered seriously for graphene studies.

Ideally, if one wants to exploit the decoupled nature present in the turbostratic system, it should have high crystallinity with no defects in it. This section explores such a possibility. Indeed, using the recipe described in Chapter IVA, with minor changes, high quality turbostratic graphene could be produced. The aspect that made the study worthwhile is the Raman spectrum from very thick graphene multilayers consisting of 300 - 700 layers showing single Lorentzian 2D peak with FWHM of 16 - 20 cm^{-1} with no D peak in it, resembling suspended graphene characteristics. This multilayer system may be termed as turbostratically single layer graphene (T-SLG), as detailed under Figure IVB.1.

IVB.3 Experimental section

The Raman spectra were recorded in the backscattering geometry using a 532 nm excitation from a diode pumped frequency doubled Nd:YAG solid state laser (model GDLM-5015L, Photop Suwtech, China) and a custom-built Raman spectrometer equipped with a SPEX TRIAX 550 monochromator and a liquid nitrogen cooled CCD detector (Spectrum One with CCD3000 controller, ISA Jobin Yvon). After every acquisition, an optical micrograph was captured with the laser excitation beam Raman beam incident on the sample using Moticam-2500 camera. The morphology of the grown graphene on Ni was examined using a field emission SEM (Nova Nano SEM 600, FEI Company). AFM imaging and I-V measurement were done using a diInnova SPM (Veeco, USA) using Si_3N_4 probes (spring constant 0.1 N/m) in contact mode at a scanning force of 5nN. Transmission electron microscopy (TEM) and selected area electron diffraction (SAED) were performed using a Technai F30 UHR instrument operating at 200 kV. Graphene on Ni was transferred onto the holey carbon film of the Cu TEM grid by an electrochemical delamination method followed by lifting off PMMA using acetone. XRD was carried using Bruker D8 Discover diffractometer, Cu Kα (1.5419 Å).

IVB.4 Results and discussion

Synthesis procedure is similar to our previous work [36] with minor but important modifications (see Figure IVB.2a). Briefly, a polycrystalline Ni foil (7 μm, 99.9%, Advent Research Materials) was taken and cut into a 4.0 x 0.6 cm^2 strip and

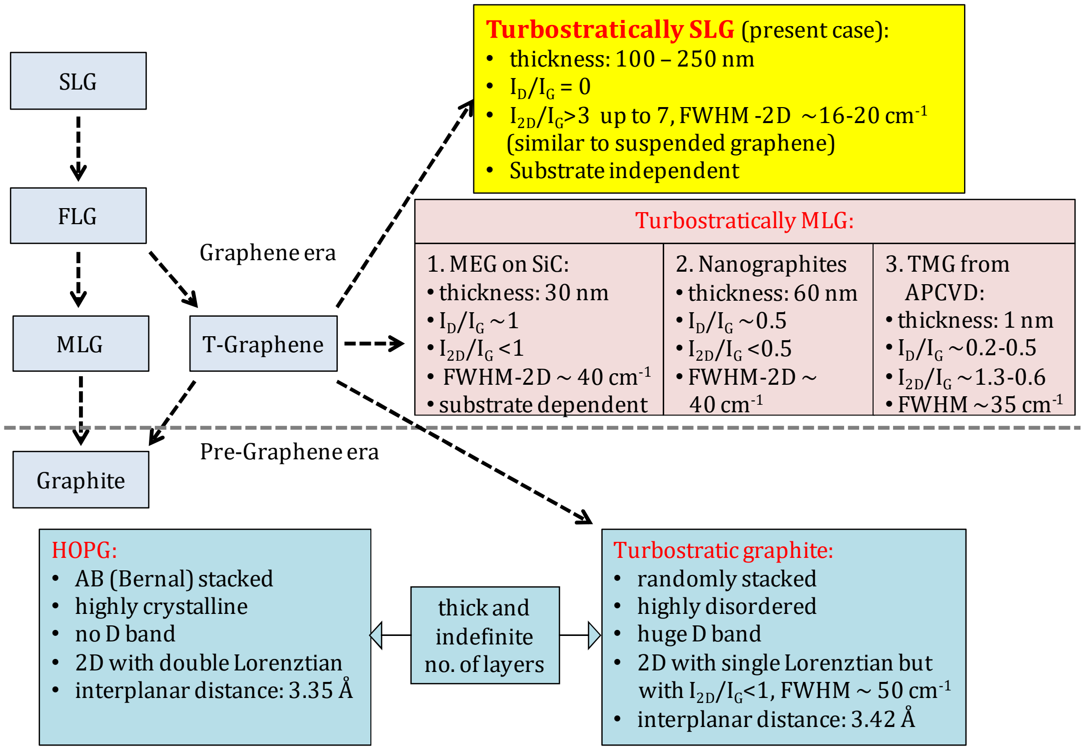

Figure IVB.1 Classification of different types graphitic materials known in the literature
Dotted bar separates the graphene related materials from graphite. SLG: single layer graphene, FLG: few layer graphene, MLG: multilayer graphene, T-graphene: turbostratic graphene, MEG: multilayer epitaxial graphene, SiC: Silicon carbide, T-MLG or TMG: turbostratically multilayer graphene.

connected to the current carrying electrodes. Naphthalene solution (10 µL, 1 mM) in chloroform was drop cast onto the Ni foil and allowed to dry. After reaching a rotary vacuum of ~5 mTorr, the Ni foil was Joule heated to red hot (~800 °C) with a current density of 120 – 150 A/mm^2 using a DC source for 15 min and then immediately cooled. We found that DC source produced higher yield of the desired species (Figure IVB.3). The I_{2D}/I_G ratio is in the range of 3.0 – 7.4 in case of graphene obtained using DC source, in clear contrast to the values from spectra in (b), using AC source. Further, in most regions of graphene obtained using AC source, the 2D band is asymmetric resembling that in HOPG whereas it is highly symmetric in graphene obtained using DC source. Graphene on Ni foil is visibly seen as shown in the photograph in Figure IVB.2b. The optical microscopy image in Figure IVB.2c shows large graphene domains surrounded by graphene wrinkles. Low magnification FESEM image in Figure IVB.2d, where darker regions correspond to graphene, shows uniform large area growth on Ni. The Ni polycrystalline domains are also seen.

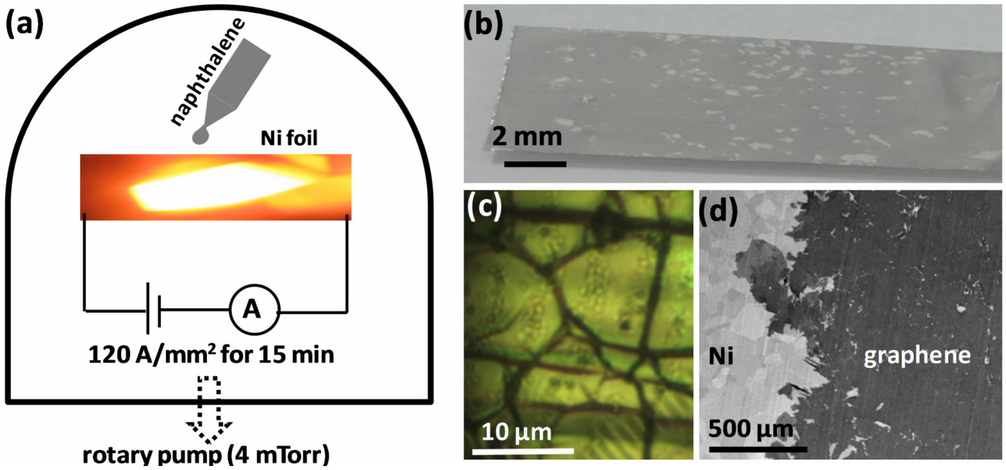

Figure IVB.2 Synthesis and microscopy of graphene

(a) Schematic of synthesis procedure. It involves drop coating of naphthalene solution on a Ni foil followed by Joule heated to red hot and cooling. (b) Digital photograph, (c) optical microscopy and (d) low magnification FESEM image of graphene on Ni. Relatively darker region in (b) is due to graphene formation on Ni.

The graphene obtained on Ni foil was transferred on to gold coated glass substrates by peeling off graphene multilayers using scotch tape. Two such multilayer flakes (flake 1 and flake 2), shown in Figure IVB.4, are random in shape with lateral size larger than 200 μm^2. On flake 1, at different regions 1 (black), 2 (red) and 3 (blue) the thickness, as measured using AFM, was found to be approximately 204, 245 and 205 nm respectively (Figure IVB.4a). Considering typical interplanar distance of graphite of ~ 0.34 nm, the total number of layers may be counted as ~597 ± 10, 717 ± 10 and 600 ± 10 respectively. The variations in the thickness within a flake arise due to the steps as evident from AFM images (Figure IVB.5). Raman spectra recorded on these regions (Figure IVB.4b, optical microscopy image in the inset), surprisingly, exhibit single Lorentzian symmetric 2D band at ~ 2710 cm^{-1} with the FWHM varying between 18 – 20 cm^{-1}, resembling SLG characteristics. The calculated I_{2D}/I_G ratios were found to be 2.75, 3.45 and 2.54 respectively which are typical values observed for SLG (Table IVB.1). AFM topology images show that the surfaces are indeed smooth (Figure IVB.5) with local roughness of the regions being ~ 1.100, 0.607 and 0.774 nm, respectively. These details clearly indicate that the obtained Raman spectra were intrinsically due to the turbostratic nature of graphene layers.

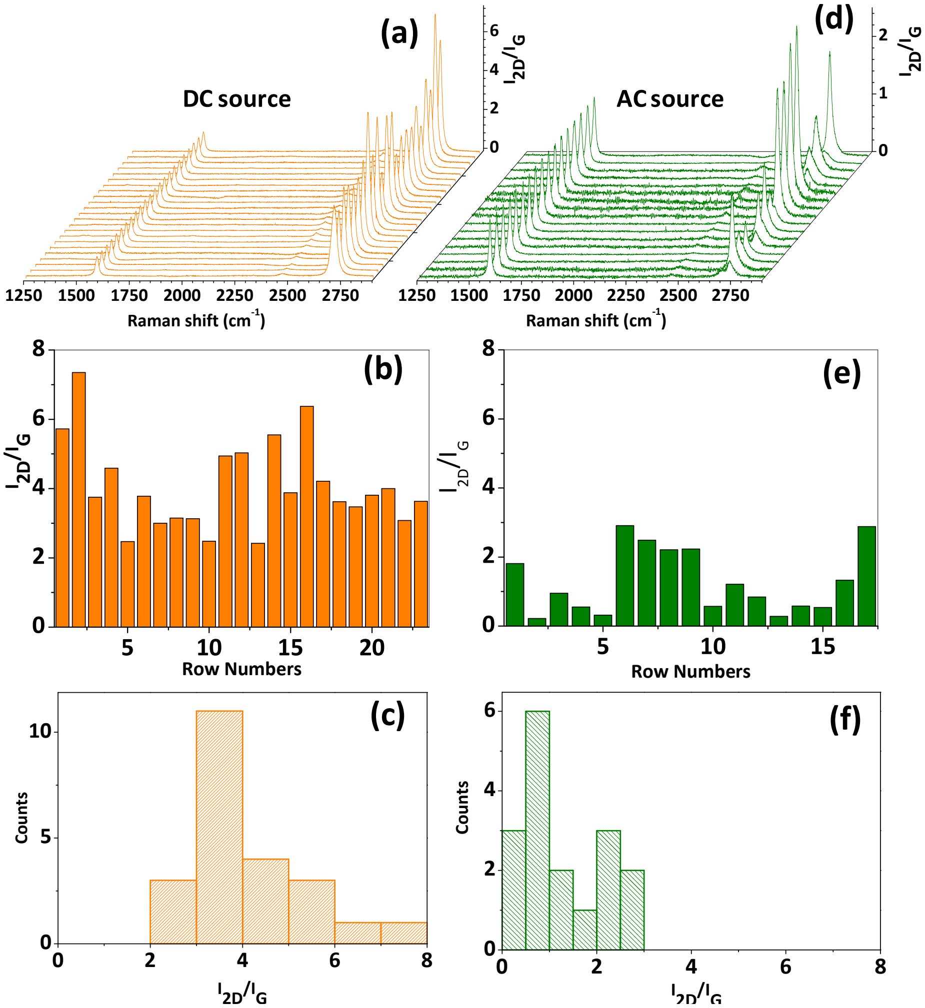

Figure IVB.3 Effect of DC /AC current source on the quality of graphene

Comparison of Raman spectra obtained over randomly chosen regions over 1 cm x 2 cm area of graphene on Ni foil prepared using (a) DC and (d) AC current sources. All spectra were normalized to G band intensity. Histogram and its distribution of I_{2D}/I_G values of Raman spectra of graphene/Ni obtained using (b and c) DC and (e and f) AC current source (for the same Raman spectra presented in (a) and (b)).

To confirm further the turbostratic nature of graphene, its c-axis resistance was measured using conducting AFM (C-AFM) by acquiring I-V curves on the same three regions. All I-V curves were found to be non-linear due to non-ohmic contact between

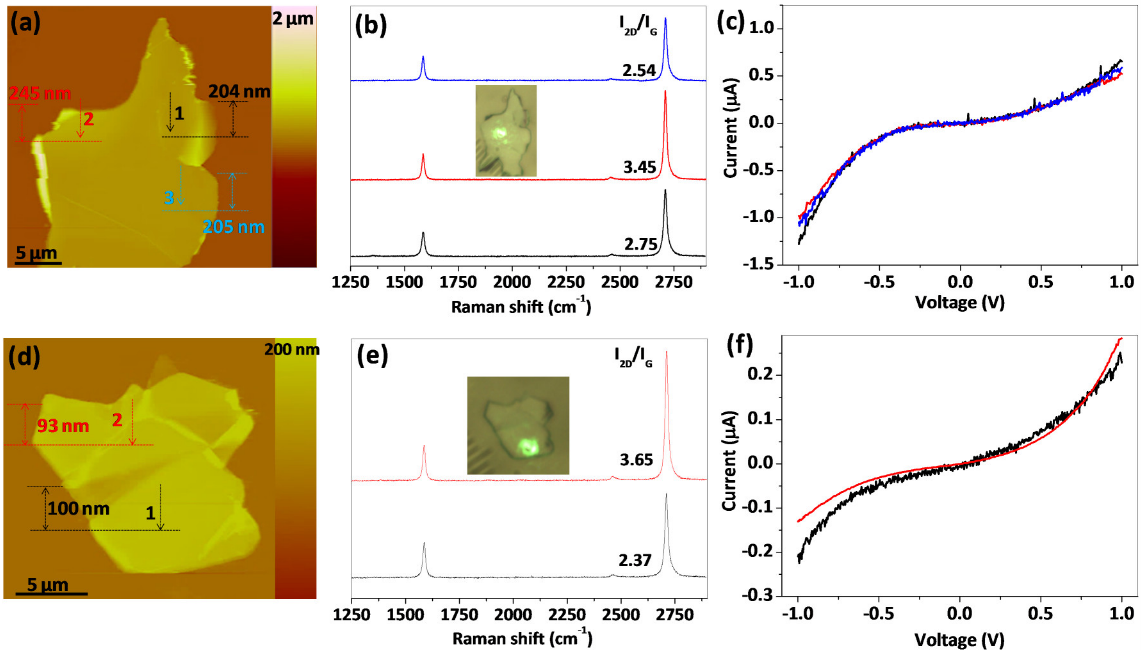

Figure IVB.4 Raman and C-AFM measurements on T-SLG

(a and d) AFM topology of typical T-SLG flakes. Arrows marked 1 (black), 2 (red) and 3 (blue) indicate the spots where Raman and I-V measurements have been made. The flake thicknesses are shown adjacent to the spots. (b and e) Raman spectra from the corresponding regions with its I_{2D}/I_G values. Insets show optical micrographs of the T-SLG flakes with incident Raman beam. (c and f) I-V characteristics of graphene multilayers measured using conducting AFM at the designated spots.

the tip and the sample (see Figure IVB.42c). The c-axis resistance values calculated at -1 V was found to be 1.59, 1.81 and 1.71 MΩ respectively. The small variation of resistance in the flake may be due to the inhomogeneity in the sample in addition due to varied tip contact. However, these values are similar to that reported for graphene sheet measured using C-AFM [37]. As a control, I-V characteristic of HOPG was acquired in similar way and its c–axis resistance value was measured to be merely 1.37 kΩ (Figure IVB.6) which agrees with the literature value [38]. Clearly, there is three orders increase in the c-axis resistance values of flake 1 compared to HOPG. The increase in resistance is solely due to the high degree of interlayer decoupling between graphene layers present in the flake. Here it is important to note that no molecular species like water can be expected between the layers; any impurity if present, would influence the 'D' band in the Raman spectrum. In T-SLG, no D band was observed.

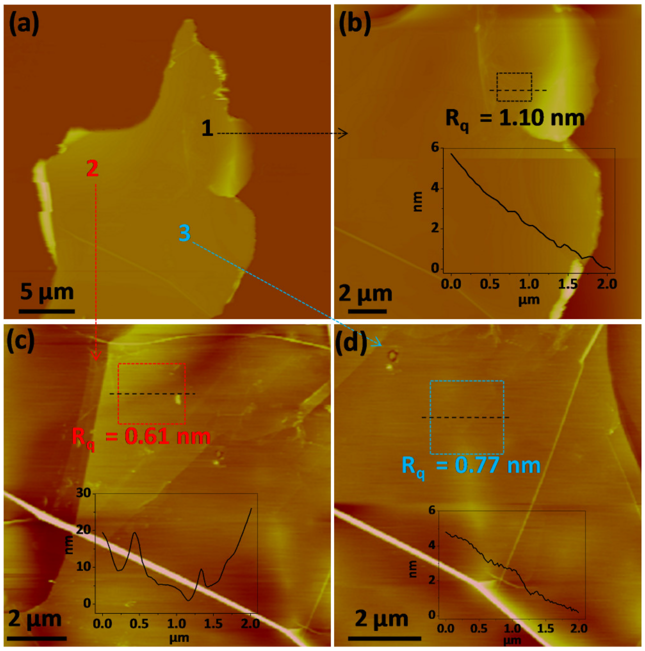

Figure IVB.5 AFM Morphology of graphene on which Raman was done

The zoomed in AFM topology of T-SLG flake 1 where Raman and I-V have been measured. The Raman spectra were measured exactly on the dashed line square box. Local roughnesses of the regions were measured within the square box. The roughness values are written below. z scale: (a) 2 µm, (b) 1 µm. (c) and (d) 50 nm. Black dotted line corresponds to height profile given below it. C-AFM was acquired from center of the square box.

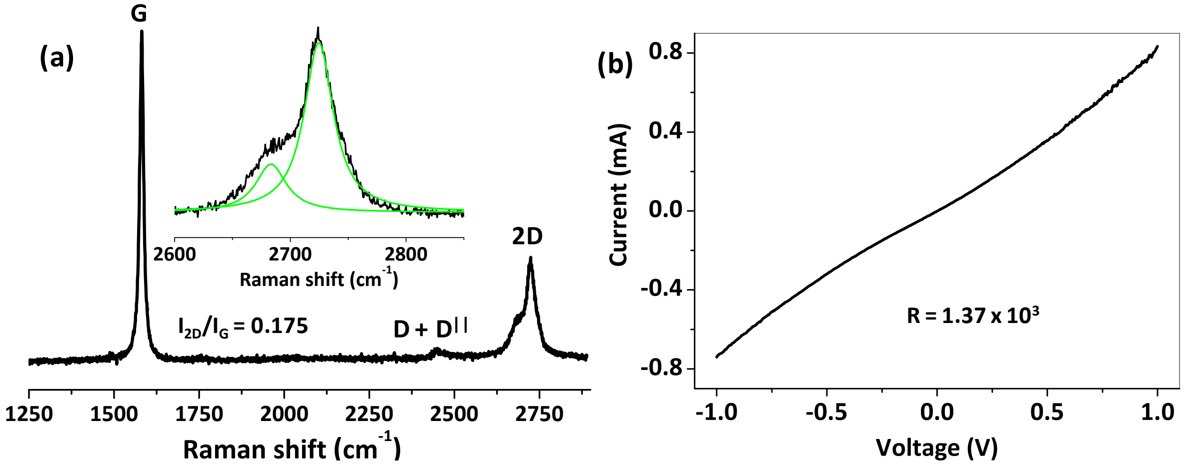

Figure IVB.6 Raman and C-AFM measurements from HOPG

(a) The Raman spectrum measured on HOPG. Inset shows deconvolution of 2D band using Lorentzian function. The peak position of G and 2D and its FWHM are given in Table S1. The peaks G, D + D^{II}, 2D are assigned. (b) I-V characteristic of HOPG measured from conducting AFM.

Similarly, flake 2 was studied in detail by measuring its thickness, I_{2D}/I_G ratio and c-axis resistance values. At two regions 1 (black) and 2 (red), thickness was found to be 100 and 93 nm respectively (Figure IVB.4d) corresponding to 294 ± 10 and 273 ± 10 layers respectively. The local surface roughness values of these two regions were calculated to be 1.17 and 1.42 nm respectively. The Raman spectra (see Figure IVB.4e) from these regions are very similar to those from flake 1with I_{2D}/I_G ratios of 2.37 and 3.65 respectively. Similarly, c-axis resistance values were found to be 6.0 and 6.9 MΩ respectively (see Table IVB.1 for Raman analysis and c-axis resistance values).

In above cases in spite of being thick, the flakes behave as SLG in Raman measurements due to decreased interlayer interaction between graphene layers. We term these flakes as turbostratically SLG (T-SLG). The striking feature of these T-SLG is that the Raman spectra are devoid of any D peak in contrast to conventional turbostratic graphite as well as recently reported turbostratic graphene, which contains noticeable D peak intensity [26]. It is well known that presence of structural defects can strongly influence electronic properties of graphene [39], the current focus on graphene research being defect-free graphene structures. Graphene obtained by other thermal methods is made defect-free by Joule heating post-synthesis, aiding lattice reconstruction and self-repair of defects [40]. Since in our study, graphene synthesis itself involves Joule heating, the defects are naturally absent. Thus, the role of Joule heating for T-SLG formation is evident which also allows rapid thermal cooling of the metal substrate. Experimentally, we found Ni to be the ideal substrate to grow T-SLG due to its higher melting point (1300 °C) and higher carbon solubility, as compared to say, Cu which is commonly used in CVD methods. Cu is known to form mainly single layer graphene unlike Ni. Comparing with the other transition metals like Pd, Pt, the lattice mismatch values between the metal surface and graphene are rather high giving rise to defective turbostratic graphene (as reported elsewhere). The combination of Joule heating and choice of Ni as substrate yields the best quality T-SLG.

To confirm our experimental observations on T-SLG similar analysis have been carried out on conventionally obtained graphitic flakes, namely, flake 3 and flake 4 with typical dimensions of > 200 μm^2 as shown in Figure IVB.7. On flake 3, at two regions 1 and 2, thicknesses were measured to be 152 and 153 nm respectively (Figure IVB.7a).

Raman spectra measured on it showed asymmetric 2D band (see Figure IVB.7b) with I_{2D}/I_G ratios of 0.307 and 0.308 respectively, which typically resembles that of graphite. The 2D band is fitted with Lorentzian function (see inset of Figure IVB.7b) and fit parameters are similar to that of HOPG (see Table IVB.1). The c-axis resistance was calculated to be only of 7.80 and 7.5 kΩ respectively, which are nearly same as that of HOPG but three orders lower than T-SLG. In similar way, another graphitic flake, flake 4, was studied. At two regions, 1 and 2, thicknesses were measured to be 110 and 143 nm respectively (see Figure IVB.7d). Raman spectra recorded showed similar 2D band as that of flake 3 with I_{2D}/I_G ratio of 0.289 and 0.283 respectively. The 2D band is fitted with Lorentzian function and fit parameters are similar to that of HOPG. It showed c-axis resistance of 78 and 120 kΩ respectively, which are 2 orders of magnitude lower than that of T-SLG.

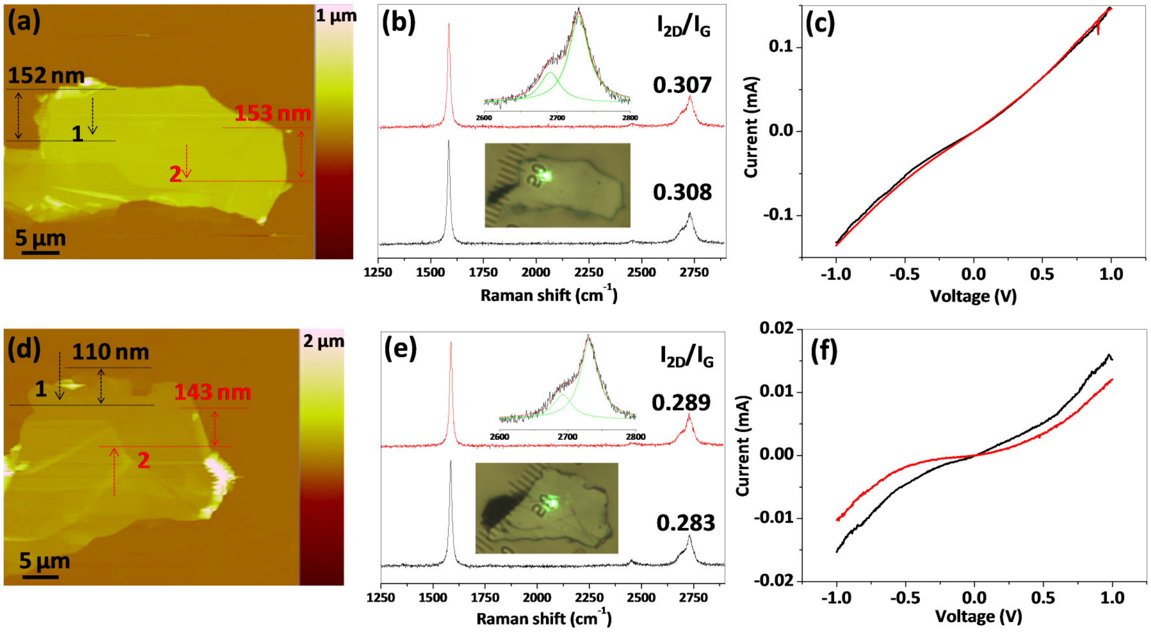

Figure IVB.7 Raman and C-AFM measurements on graphitic flakes

(a and d) AFM topology of two typical graphitic flakes. Arrows marked 1 (black) and 2 (red) indicate the spots where Raman and I-V measurements have been made. The flake thicknesses are shown adjacent to the spots. (b and e) Raman spectra from the corresponding regions with its I_{2D}/I_G values. Insets show optical micrographs of the flakes with the incident Raman beam. (c and f) I-V characteristics of flakes measured using conducting AFM at the designated spots.

For overall comparison, I-V characteristics of all flakes along with that of HOPG are presented in Figure IVB.8. All the c-axis resistance values are plotted in a histogram plot (Figure IVB.8b). It is evident that flake 1 and flake 2, even though consist of more than 300 layers, tend to exhibit SLG-like Raman signatures with the I_{2D}/I_G ratios in the range 2.5 – 4.0. The position of 2D band is observed at ~ 2710 cm^{-1}. The 2D bands are sharp with FWHMs of 18 – 20 cm^{-1} indicating that the graphene obtained (T-SLG) is quite different compared to conventionally obtained SLG [41] (see Table IVB.2) and other forms of turbostratic graphite/graphene known so far (see Figure IVB.1).

Table IVB.1 Table of parameters measured for the flakes

The G and 2D peak position, FWHM and c-axis resistance values for each flake along with that of HOPG are given. Values in bracket correspond to shoulder peaks of 2D bands. 'M' stands for mega and 'k' stands for kilo.

T-SLG flake	Region	G Peak		2D Peak		I_{2D}/I_G	Thickness (nm)	Local roughness (nm)	R (ohm)
		Position (cm^{-1})	FWHM (cm^{-1})	Position (cm^{-1})	FWHM (cm^{-1})				
Flake 1	R1	1586.5	15.6	2710.3	19.3	2.75	204	4.98	1.59 M
	R2	1586.3	13.5	2710.2	18.4	3.45	245	0.607	1.81 M
	R3	1586.1	13.7	2710.8	19.3	2.54	205	0.774	1.71 M
Flake 2	R1	1586.5	14.5	2710.3	18.5	2.37	100	0.665	6.0 M
	R2	1585.9	13.8	2711.4	18.1	3.65	93	0.982	6.9 M
Flake 3	R1	1585.8	15.0	2729.1 (2689.8)	33.4 (32.9)	0.31	152	0.885	7.80 k
	R2	1585.4	15.0	2729.7 (2690.4)	33.49 (32.9)	0.31	153	1.17	7.51 k
Flake 4	R1	1584.8	15.1	2731.2 (2692.2)	31.7 (33.4)	0.29	110	1.38	7.80 k

	R2	1585.9	15.0	2729.4 (2688.5)	35.1 (31.4)	0.28	143	4.88	1.20 k
HOPG		1581.4	13.8	2724.6 (2683.2)	30.59 (32.4)	0.18	-	-	1.37 k

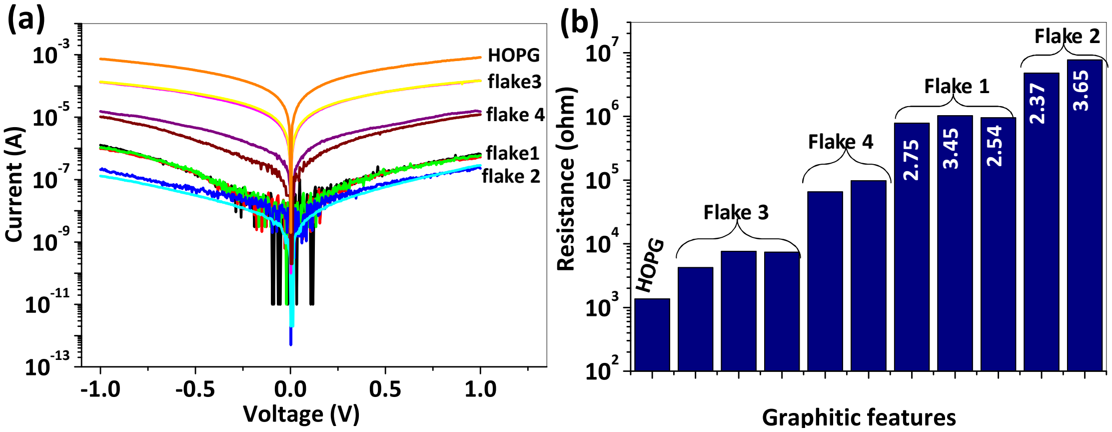

Figure IVB.8 Combined plot of I-V and c-axis resistance

(a) Comparison of I-V curves and (b) histogram of c-axis resistances measured for turbostratic graphene (flake 1 and flake 2) and graphitic graphene (flake 3 and flake 4) along with HOPG. The resistances values were calculated from corresponding I-V curves at V = -1 V. The I_{2D}/I_{G} values are shown for turbostratic graphene on histogram bars.

Table IVB.2 Comparison of position and FWHM of 2D band of graphene/graphite on different substrates

Substrate	Position (cm^{-1})	FWHM (cm^{-1})	References	λ_{ex} (nm)
CVD graphene (on metal substrate)	2685	32.0	*ACS Nano* 2011, *5*, 7601	514.5
MEG	2590	30	*Phys. Rev. Lett.* 2006, *97*, 187401.	
HOPG	~ 2680, ~ 2730	➢ 50	*Carbon* 2008, *46*, 272	
Turbostratic graphene/graphite	~ 2710	50	„	
Suspended SLG	~ 2670	~24	*ACS Nano* 2011, *5*, 6916	
SLG on SiO_2/Si	2676.2	31.8	*J. Phys. Chem. C* 2008, *112*, 10637	532

SLG on Si	2672	28.3	„	
SLG on glass	2672.8	30.8	„	
T-SLG	~2710	16-20	Present work	

Raman spectra were recorded for many such T-SLG samples to carefully analyse the positions and widths of G and 2D bands. Raman spectra obtained from one such is shown in Figure IVB.9, where the sampling area was 1 cm x 2 cm. All spectra are typical of SLG with single Lorentzian 2D band. Clearly, it can be seen that I_{2D}/I_G ratio is greater than 3 in most locations, the maximum value being 7.4. For graphene in general, an I_{2D}/I_G ratio greater than 2 refers to SLG, a value between 1 and 2 to BLG and if it is less than 1, it amounts to FLG. It is noteworthy that for CVD grown SLG lying on any substrate, it is hard to find a region with $I_{2D}/I_G > 4$ [42]. Only suspended graphene routinely shows I_{2D}/I_G values more than 4 [43] rarely up to 9 [44] in the absence of any substrate influence. It is therefore not surprising that the extraordinary transport properties of graphene have been observed only in case of suspended graphene [18-20]. We have observed I_{2D}/I_G values from 3 to 7.4 indicating that T-SLG from this study virtually behaves as suspended defect-free graphene. Here it is to be noted that the variation of I_{2D}/I_G ratios with number of graphene layers is not relevant since the former does not vary with the number of graphene layers, unlike in conventional multilayer graphene. As the thesis states, even with 600 – 700 graphene layers, the I_{2D}/I_G ratios obtained resemble that of best quality single layer graphene.

Similarly, other spectral features fall in line. The position and FWHM of G band are scattered in a narrow range with increasing I_{2D}/I_G ratio, ~1587 to 1583 cm^{-1} and 14.2 to 16 cm^{-1} respectively (Figure IVB.9d and e). Similarly for the 2D band, the position decreases from 2712 to 2707 cm^{-1} and FWHM, from 24 cm^{-1} to 16 cm^{-1} as I_{2D}/I_G varies between 1 and 7.4 (Figure IVB.9f and g). This variation with I_{2D}/I_G is similar to that of suspended graphene [43] with position of 2D band same (~ 2710 cm^{-1}) as that of turbostratic graphite [26]. Indeed, FWHM is lower than the value observed for suspended SLG (24 cm^{-1}) [43], and very low compared to turbostratic graphite values, ~ 50 cm^{-1} [45]. These values are also superior when compared to CVD grown SLG where the FWHM of 2D is ~ 30 cm^{-1} [46]. What is noteworthy is that in case of T-SLG, the FWHM and I_{2D}/I_G are insensitive to the presence of the substrate, as one would expect for thick flakes.

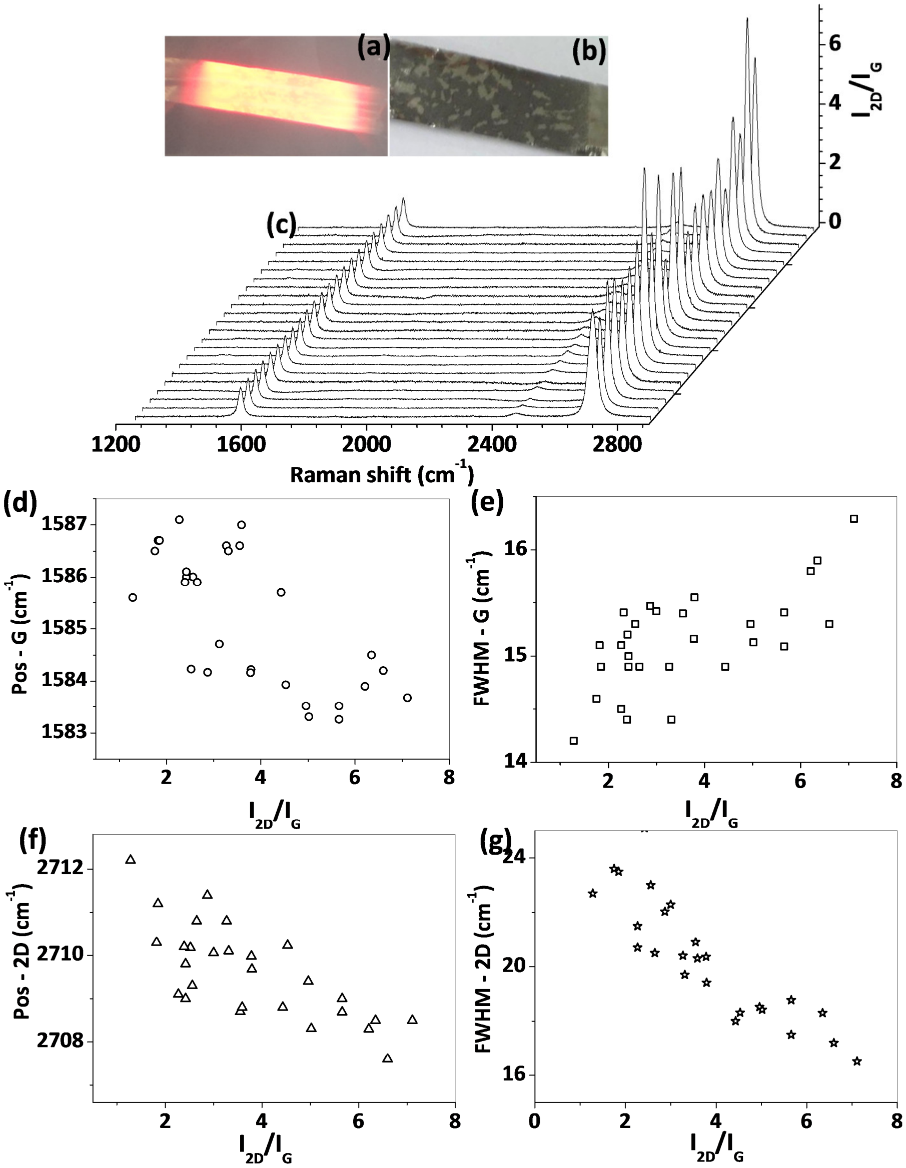

Figure IVB.9 Raman analysis of T-SLG

(a) A photograph of Joule heating of Ni foil using DC current source. The uniform heating of foil can be seen. (b) A photograph of graphene formed on Ni foil on which Raman spectra were recorded at 22 different random regions (c). All the spectra were normalised to G band and hence intensity of 2D band is same as I_{2D}/I_G ratios. Variation of position of (d) G and (e) 2D and FWHM of (f) G and (g) 2D with I_{2D}/I_G ratios for T-SLG obtained from different samples.

Angular disorder in turbostratic graphite/graphene has been a subject of investigation. In the case of MEG grown on SiC, angular mismatch values of 30° have been probed successfully using LEED and STM techniques [31]. Here we used selective area electron diffraction (SAED) technique to investigate the angular relations among T-SLG layers (Figure IVB.10). Unlike SLG which shows hexagonal diffraction spots [47], and bilayer graphene which normally exhibits split spots [48], in the present case surprisingly, each diffraction feature has split into sets of eight distinct spots (see Figure IVB.10b). The sharpness of the spots clearly indicates the 2D crystallinity associated with the graphene layers. The angle between the split spots varies typically from 2°–6° (see Figure IVB.10c) which directly relates to the angular orientation between each graphene layers [49]. These correspond to superlattice reflections with varying weights depending on the number of participating layers with similar angular relation, which in turn decides the spot intensity (Figure IVB.10d). The SAED of graphitic flakes was also acquired which shows that typical of multilayer graphene [50] (Figure IVB.10). Though, The graphene layers in T-SLG are decoupled from one another

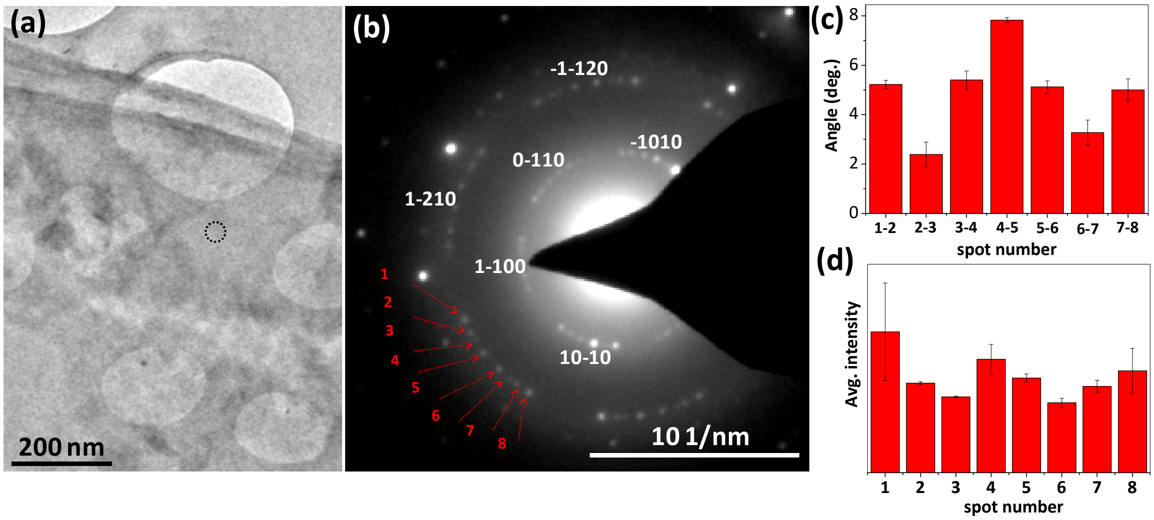

Figure IVB.10 TEM analysis of T-SLG

(a) A bright field TEM image of thin T-SLG flakes (b) SAED pattern of T-SLG acquired on the dotted circle region in (a). (c) and (d) Histogram of angle between diffraction spots and its intensity profile of spots numbered 1 to 8 pointed by arrow mark in (a). A thin region of thickness ~ 15 nm was chosen which is transparent enough to electron beam.

due to interlayer rotations, the interlayer spacing changes slightly from 3.35 Å (graphitic) to 3.39 Å which is lower than that observed in turbostratic graphite (3.42 Å). Based on these comparisons, it is clear that there are no other species between the layers.

Conventional turbostratic graphite is usually defect annealed at high temperature to convert to crystalline graphite [51]. We used the annealing approach to cross-examine the inherent turbostraticity in T-SLG. A T-SLG flake with I_{2D}/I_G ratio of 3.2 (Figure IVB.11a, black curve) was placed in a molybdenum boat and was heated to ~ 1500 °C for an hour at 10^{-5} mTorr. Interestingly, the flake got converted to graphite with 2D band appearing at ~2725 cm^{-1} and a left shoulder at ~2680 cm^{-1} (Figure IVB.11a, red curve). Accordingly, the XRD peak at 26.28° (see Figure IVB.11b, black curve) shifted to 26.49° (blue curve) with the corresponding change in the *d*-spacing (from 3.39 to 3.36 Å). It may be noted that HOPG (red curve) exhibits the XRD peak at 26.56° (*d*-spacing is 3.35 Å). From above observations, it is clear that recrystallization (reorganisation) of T-SLG has led to graphitic form.

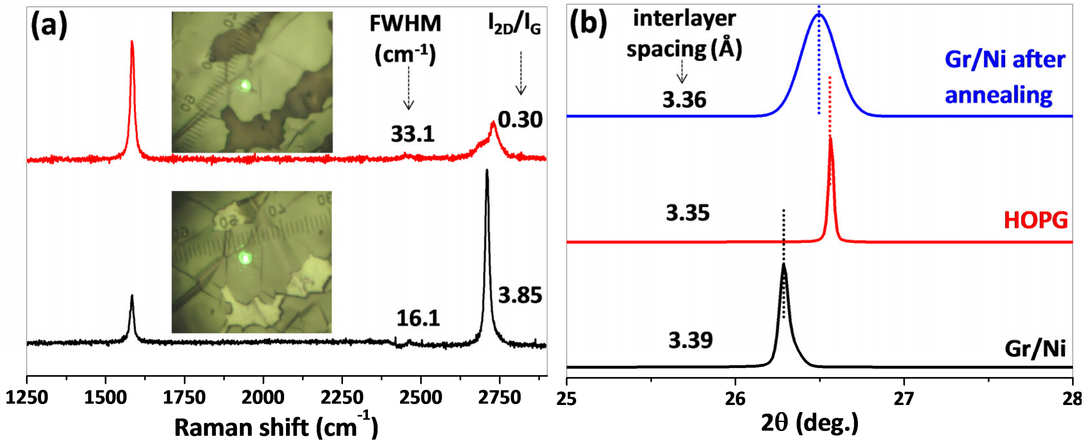

Figure IVB.11 Effect of thermal heating

(a) Raman spectra recorded at same region before (black curve) and after (red curve) heating T-SLG at ~1500 °C. Insets are optical micrograph of same T-SLG flake with incident Raman beam. (b) X-ray diffraction pattern of T-SLG (red curve) measured in bulk compared to that of HOPG (black curve). Blue curve is the XRD of T-SLG after it is subjected to heating at ~ 1100 °C for an hour at ~10^{-5} Torr.

Recently, it has been studied that any twist or fold in graphene can give enhanced 2D band intensity [53]. This puts a question that whether wrinkles present in the graphene are playing any role in the enhanced 2D band observed in the present T-SLG. To verify this, a Raman mapping was performed on the region shown by optical microscope image in Figure IVB.12a where presence of plenty of wrinkles can be seen. Figure IVB.12b is the distribution of I_{2D}/I_G intensity ratio measured in the same region which typically varies from 1 to 9. The distribution of I_{2D}/I_G ratio is a measure of turbostraticity in T-SLG. In Figure IVB.12c, representative Raman spectra are given which are measured on the correspondingly numbered spots in Figure IVB.12b.

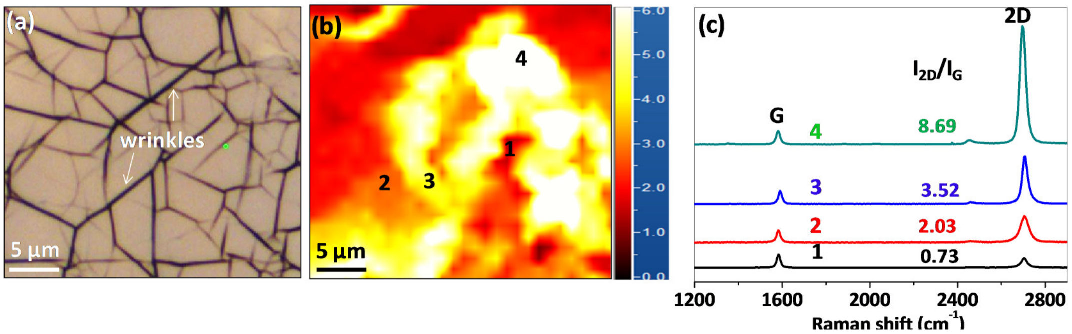

Figure IVB.12 Influence of wrinkles on the turbostraticity of T-SLG.

(a) Optical microscope image of graphene transferred on glass on consisting of network of wrinkles. (b) Raman mapping of I_{2D}/I_G intensity ratio on (a). (c) Raman spectra measured at different of regions indicated by corresponding numbers.

All spectra show single Lorentzian 2D band confirming the T-SLG nature. Notably, when two images are compared, it is very clear that there is no correlation between presence of wrinkles and distribution of I_{2D}/I_G ratios. In other words, the turbostraticity in T-SLG is completely independent of the presence of wrinkles and wrinkles have no influence on observed high I_{2D}/I_G ratios in T-SLG. This further infers that, turbostraticity in T-SLG is indeed due to the angular orientation between the graphene layers causing electronic decoupling in the T-SLG.

IVB.5 Conclusions

A new species of graphene/graphitic material has been obtained by using the concept of turbostraticity in graphene layers and named as Turbostratically-SLG (T-

SLG). It shows Raman characteristics of SLG in spite of hundreds of nanometre thick. From The graphene layers are indeed misoriented and turbostratic in nature. Due to decreased interactions, every graphene layers are highly decoupled from one another to an extent to that of suspended graphene. This places the T-SLG as an as an alternative material for suspended graphene and hence to realise the extraordinary properties observed in suspended graphene for practical applications.

References

(1) Novoselov, K. S.; Geim, A. K.; Morozov, S. V.; Jiang, D.; Zhang, Y.; Dubonos, S. V.; Grigorieva, I. V.; Firsov, A. A., Electric Field Effect in Atomically Thin Carbon Films. *Science* **2004,** *306*, 666-669.

(2) Balandin, A. A.; Ghosh, S.; Bao, W.; Calizo, I.; Teweldebrhan, D.; Miao, F.; Lau, C. N., Superior Thermal Conductivity of Single-Layer Graphene. *Nano Lett.* **2008,** *8*, 902-907.

(3) Nair, R. R.; Blake, P.; Grigorenko, A. N.; Novoselov, K. S.; Booth, T. J.; Stauber, T.; Peres, N. M. R.; Geim, A. K., Fine Structure Constant Defines Visual Transparency of Graphene. *Science* **2008,** *320*, 1308.

(4) Gomez De Arco, L.; Zhang, Y.; Schlenker, C. W.; Ryu, K.; Thompson, M. E.; Zhou, C., Continuous, Highly Flexible, and Transparent Graphene Films by Chemical Vapor Deposition for Organic Photovoltaics. *ACS Nano* **2010,** *4*, 2865-2873.

(5) Torrisi, F.; Hasan, T.; Wu, W.; Sun, Z.; Lombardo, A.; Kulmala, T. S.; Hsieh, G.-W.; Jung, S.; Bonaccorso, F.; Paul, P. J.; Chu, D.; Ferrari, A. C., Inkjet-Printed Graphene Electronics. *ACS Nano* **2012,** *6*, 2992-3006.

(6) Park, H.; Chang, S.; Zhou, X.; Kong, J.; Palacios, T.; Gradečak, S., Flexible Graphene Electrode-Based Organic Photovoltaics with Record-High Efficiency. *Nano Lett.* **2014,** *14*, 5148-5154.

(7) Bonaccorso, F.; Sun, Z.; Hasan, T.; Ferrari, A. C., Graphene Photonics and Optoelectronics. *Nat. Photon.* **2010,** *4*, 611-622.

(8) Meyer, J. C.; Geim, A. K.; Katsnelson, M. I.; Novoselov, K. S.; Booth, T. J.; Roth, S., The Structure of Suspended Graphene Sheets. *Nature* **2007,** *446*, 60-63.

(9) Zhu, W.; Low, T.; Perebeinos, V.; Bol, A. A.; Zhu, Y.; Yan, H.; Tersoff, J.; Avouris, P., Structure and Electronic Transport in Graphene Wrinkles. *Nano Lett* .**2012,** *12*, 3431-3436.

(10) Magda, G. Z.; Jin, X.; Hagymasi, I.; Vancso, P.; Osvath, Z.; Nemes-Incze, P.; Hwang, C.; Biro, L. P.; Tapaszto, L., Room-temperature Magnetic Order on Zigzag Edges of Narrow Graphene Nanoribbons. *Nature* **2014,** *514*, 608-611.

(11) Banhart, F.; Kotakoski, J.; Krasheninnikov, A. V., Structural Defects in Graphene. *ACS Nano* **2011,** *5*, 26-41.

(12) Pirkle, A.; Chan, J.; Venugopal, A.; Hinojos, D.; Magnuson, C. W.; McDonnell, S.; Colombo, L.; Vogel, E. M.; Ruoff, R. S.; Wallace, R. M., The Effect of Chemical Residues on the Physical and Electrical Properties of Chemical Vapor Deposited Graphene Transferred to SiO_2. *Appl. Phys. Lett.* **2011,** *99*, 122108.

(13) Muhammad Farooq, K.; Muhammad Zahir, I.; Muhammad Waqas, I.; Jonghwa, E., Improving the Electrical Properties of Graphene Layers by Chemical Doping. *Sci. Tech. Adv. Mater.* **2014,** *15*, 055004.

(14) Lu, C.-P.; Li, G.; Watanabe, K.; Taniguchi, T.; Andrei, E. Y., Choice Substrate for Accessing and Tuning the Electronic Properties of Graphene. *Phys. Rev. Lett.* **2014,** *113*, 156804.

(15) Wang, Z.; Tang, C.; Sachs, R.; Barlas, Y.; Shi, J., Proximity-Induced Ferromagnetism in Graphene Revealed by the Anomalous Hall Effect. *Phys. Rev. Lett.* **2015,** *114*, 016603.

(16) Wang, Q. H.; Jin, Z.; Kim, K. K.; Hilmer, A. J.; Paulus, G. L. C.; Shih, C.-J.; Ham, M.-H.; Sanchez-Yamagishi, J. D.; Watanabe, K.; Taniguchi, T.; et al. Understanding and Controlling the Substrate Effect on Graphene Electron-Transfer Chemistry via Reactivity Imprint Lithography. *Nat. Chem.***2012,** *4*, 724-732.

(17) Humberto, T.; Ruitao, L.; Mauricio, T.; Mildred, S. D., The Role of Defects and Doping in 2D Graphene Sheets and 1D Nanoribbons. *Rep. Prog. Phys .***2012,** *75*, 062501.

(18) Lau, C. N.; Bao, W.; Velasco Jr, J., Properties of Suspended Graphene Membranes. *Mater. Today* **2012,** *15*, 238-245.

(19) Du, X.; Skachko, I.; Barker, A.; Andrei, E. Y., Approaching Ballistic Transport in Suspended Graphene. *Nat.Nanotechnol.* **2008,** *3*, 491-495.

(20) Bolotin, K. I.; Sikes, K. J.; Jiang, Z.; Klima, M.; Fudenberg, G.; Hone, J.; Kim, P.; Stormer, H. L., Ultrahigh Electron Mobility in Suspended Graphene. *Solid State Commun.* **2008,** *146*, 351-355.

(21) Maurand, R.; Rickhaus, P.; Makk, P.; Hess, S.; Tóvári, E.; Handschin, C.; Weiss, M.; Schönenberger, C., Fabrication of Ballistic Suspended Graphene with Local-Gating. *Carbon* **2014,** *79*, 486-492.

(22) Bernal, J. D., The Structure of Graphite. *Proc. R. Soc. A* **1924,** *106*, 749-773.

(23) Fitzer, E.; Kochling, K. H.; Boehm, H. P.; Marsh, H., Recommended Terminology for the Description of Carbon as a Solid. *Pure Appl. Chem.* **1995**, *67*, 473-506.

(24) Shibuta, Y.; Elliott, J. A., Interaction BetweenTtwo Graphene Sheets With a Turbostratic Orientational Relationship. *Chem. Phys. Lett .***2011,** *512*, 146-150.

(25) Malard, L. M.; Pimenta, M. A.; Dresselhaus, G.; Dresselhaus, M. S., Raman Spectroscopy in Graphene. *Phys. Rep.* **2009,** *473*, 51-87.

(26) Cançado, L. G.; Jorio, A.; Pimenta, M. A., Measuring the Absolute Raman Cross Section of Nanographites as a Function of Laser Energy and Crystallite Size. *Phys. Rev. B* **2007,** *76*, 64304.

(27) Pimenta, M. A.; Dresselhaus, G.; Dresselhaus, M. S.; Cancado, L. G.; Jorio, A.; Saito, R., Studying Disorder in Graphite Based Systems by Raman Spectroscopy. *Phys. Chem. Chem. Phys.***2007,** *9*, 1276-1290.

(28) Latil, S.; Meunier, V.; Henrard, L., Massless Fermions in Multilayer Graphitic Systems With Misoriented Layers: Ab Initio Calculations and Experimental Fingerprints. *Phys. Rev. B* **2007,***76*, 201402.

(29) Kim, K.; Coh, S.; Tan, L. Z.; Regan, W.; Yuk, J. M.; Chatterjee, E.; Crommie, M. F.; Cohen, M. L.; Louie, S. G.; Zettl, A., Raman Spectroscopy Study of Rotated Double-Layer Graphene: Misorientation-Angle Dependence of Electronic Structure. *Phys. Rev. Lett .***2012,***108*, 246103.

(30) Hass, J.; Heer, W. A. d.; Conrad, E. H., The Growth and Morphology of Epitaxial Multilayer Graphene. *J. Phys. Condens. Matter* **2008,** *20*, 323202.

(31) Hass, J.; Varchon, F.; Millán-Otoya, J. E.; Sprinkle, M.; Sharma, N.; de Heer, W. A.; Berger, C.; First, P. N.; Magaud, L.; Conrad, E. H., Why Multilayer Graphene on 4H-SiC(0001) Behaves Like a Single Sheet of Graphene. *Phys. Rev. Lett.* **2008,** *100*, 125504.

(32) Ni, Z. H.; Chen, W.; Fan, X. F.; Kuo, J. L.; Yu, T.; Wee, A. T. S.; Shen, Z. X., Raman Spectroscopy of Epitaxial Graphene on a SiC Substrate. *Phys. Rev. B* **2008,** *77*, 115416.

(33) Mendes-de-Sa, T. G.; Goncalves, A. M. B.; Matos, M. J. S.; Coelho, P. M.; Magalhaes-Paniago, R.; Lacerda, R. G., Correlation Between (In)commensurate Domains of Multilayer Epitaxial Graphene Grown on SiCand Single Layer Electronic Behavior. *Nanotechnology* **2012,** *23*, 475602.

(34) Orlita, M.; Faugeras, C.; Plochocka, P.; Neugebauer, P.; Martinez, G.; Maude, D. K.; Barra, A. L.; Sprinkle, M.; Berger, C.; de Heer, et al. Approaching the Dirac Point in High-Mobility Multilayer Epitaxial Graphene. *Phys. Rev. Lett.* **2008,** *101*, 267601.

(35) Lee, D. S.; Riedl, C.; Krauss, B.; von Klitzing, K.; Starke, U.; Smet, J. H., Raman Spectra of Epitaxial Graphene on SiC and of Epitaxial Graphene Transferred to SiO2. *Nano Lett.* **2008,** *8,* 4320-4325.

(36) Mogera, U.; Kurra, N.; Radhakrishnan, D.; Narayana, C.; Kulkarni, G. U., Low Cost, Rapid Synthesis of Graphene on Ni: An Efficient Barrier for Corrosion and Thermal oxidation. *Carbon* **2014,** *78*, 384-391.

(37) Hauquier, F.; Alamarguy, D.; Viel, P.; Noël, S.; Filoramo, A.; Huc, V.; Houzé, F.; Palacin, S., Conductive-probe AFM Characterization of Graphene Sheets Bonded to Gold Surfaces. *Appl. Surf. Sci.* **2012,** *258*, 2920-2926.

(38) Narendra, K.; Gyan, P.; Basavaraja, S.; Timothy, S. F.; Kulkarni, G. U.; Ronald, G. R., Charge Storage in Mesoscopic Graphitic Islands Fabricated using AFM Bias Lithography. *Nanotechnology* **2011,** *22*, 245302.

(39) Vicarelli, L.; Heerema, S. J.; Dekker, C.; Zandbergen, H. W., Controlling Defects in Graphene for Optimizing the Electrical Properties of Graphene Nanodevices. *ACS Nano* **2015,** *9*, 3428-3435.

(40) Qi, Z. J.; Daniels, C.; Hong, S. J.; Park, Y. W.; Meunier, V.; Drndić, M.; Johnson, A. T. C., Electronic Transport of Recrystallized Freestanding Graphene Nanoribbons. *ACS Nano* **2015,** *9*, 3510-3520.

(41) Ferrari, A. C.; Basko, D. M., Raman Spectroscopy as a Versatile Tool for Studying the Properties of Graphene. *Nat.Nanotechnol.* **2013,** *8*, 235-246.

(42) Zhang, Y.; Zhang, L.; Zhou, C., Review of Chemical Vapor Deposition of Graphene and Related Applications. *Acc. Chem. Res.* **2013,** *46*, 2329-2339.

(43) Berciaud, S.; Ryu, S.; Brus, L. E.; Heinz, T. F., Probing the Intrinsic Properties of Exfoliated Graphene: Raman Spectroscopy of Free-Standing Monolayers. *Nano Lett.* **2009,** *9*, 346-352.

(44) Ni, Z. H.; Yu, T.; Luo, Z. Q.; Wang, Y. Y.; Liu, L.; Wong, C. P.; Miao, J.; Huang, W.; Shen, Z. X., Probing Charged Impurities in Suspended Graphene Using Raman Spectroscopy. *ACS Nano* **2009,** *3*, 569-574.

(45) Ni, Z.; Wang, Y.; Yu, T.; Shen, Z., Raman Spectroscopy and Imaging of Graphene. *Nano Res.* **2008,** *1*, 273-291.

(46) Ferrari, A. C.; Meyer, J. C.; Scardaci, V.; Casiraghi, C.; Lazzeri, M.; Mauri, F.; Piscanec, S.; Jiang, D.; Novoselov, K. S.; Roth, S.; et al. Raman Spectrum of Graphene and Graphene Layers. *Phys. Rev. Lett.* **2006,** *97*, 187401.

(47) Wang, G.; Zhang, M.; Zhu, Y.; Ding, G.; Jiang, D.; Guo, Q.; Liu, S.; Xie, X.; Chu, P. K.; Di, Z.; et al. Direct Growth of Graphene Film on Germanium Substrate. *Sci. Rep.* **2013,** *3*, 2465.

(48) Wilson, N. R.; Pandey, P. A.; Beanland, R.; Young, R. J.; Kinloch, I. A.; Gong, L.; Liu, Z.; Suenaga, K.; Rourke, J. P.; York, et al. Graphene Oxide: Structural Analysis and Application as a Highly Transparent Support for Electron Microscopy. *ACS Nano* **2009,** *3*, 2547-2556.

(49) Wu, Q.; Jung, S. J.; Jang, S. K.; Lee, J.; Jeon, I.; Suh, H.; Kim, Y. H.; Lee, Y. H.; Lee, S.; Song, Y. J., Controllable Poly-crystalline Bilayered and Multilayered Graphene Film Growth by Reciprocal Chemical Vapor Deposition. *Nanoscale* **2015,** *7*, 10357-10361.

(50) He, B.; Ren, Z.; Yan, S.; Wang, Z., Large Area Uniformly Oriented Multilayer Graphene With High Transparency and Conducting Properties Derived From Highly Oriented Polyethylene Films. *J. Mater. Chem. C* **2014,** *2*, 6048-6055.

(51) Cançado, L. G.; Takai, K.; Enoki, T.; Endo, M.; Kim, Y. A.; Mizusaki, H.; Speziali, N. L.; Jorio, A.; Pimenta, M. A., Measuring the Degree of Stacking Order in Graphite by Raman Spectroscopy. *Carbon* **2008,** *46*, 272-275.

(52) Kumar,G. V. P.; Narayana, C., Adapting a Fluorescence Microscope to Perform Surface Enhanced Raman Spectroscopy. *Curr. Sci.* **2007**, *93*, 778-781

(53) Ni, Zhenhua, et al. "Raman spectroscopy and imaging of graphene." *Nano Research* 1.4 **2008,** 273-291.

Chapter IVC

Unusual Properties of T-SLG

Summary

Truly decoupled nature of graphene layers in T-SLG enables one to study a system in which many graphene layers are rotated with each other. Various collective properties of T-SLG are investigated in this chapter. Using randomly rotated stacks of many graphene layers, visible absorption bands were observed with simple UV-vis spectrometer. In another study, SERS activity of T-SLG was examined using Ag nanoparticles wherein it shows unique selective enhancement of Raman bands. Since Raman characteristics of T-SLG are comparable to that of suspended graphene, its temperature dependent behaviour is similar to the pure form of suspended graphene.

IVC.1 Visible Absorption Bands in T-SLG

IVC.1.1 Introduction

The twisted bilayer graphene (tBLG), two graphene layers misoriented with a twist angle θ (0° < θ < 30°), has gained many interests in last few years due to its angle-dependent properties [1-4]. In tBLG, the interlayer coupling between two graphene layers can be tuned with the twist angle and its band structure can be accordingly modified [5]. Here, the twist angle θ, adds a new degree of freedom to the system, generating several θ-dependent properties which are non-existent in SLG [6-8]. For example, SLG has linearly increasing DOS whereas tBLG possesses a logarithmic divergence in DOS giving rise to van Hove singularities (vHS's), one of the most important characteristics of tBLG [9]. The energy difference between the vHSs can be tuned by changing θ, giving rise to various angle dependent optoelectronics properties [10-13]. When the energy difference between the vHS's matches with laser excitation energy (λ_{exc}), it possesses absorption bands in the UV-visible spectral region. Theoretically, the appearance of the absorption bands in tBLG is well studied and the position of absorption maxima found to vary with the twist angle [14]. Experimentally, Robinson et. al., recently have shown the appearance of visible colour in the tBLG using optical colour contrast method [3]. The presence of such absorption bands was further confirmed by experiments of Havener et. al. using a specialised UV vis NIR hyperspectral microscope imaging from which, complex optical conductivity was extracted [15].

IVC.1.2 Scope of the present investigation

Though the appearance of the absorption bands in the UV-vis region have been theoretically detailed, a straightforward observation of absorption band in UV-vis spectrum has not been possible so far, perhaps due to the weak nature of these bands. As the T-SLG represents many sets of tBLG with randomly rotated graphene layers in it, direct observation of visible absorption bands could be possible using a simple UV-vis spectrometer. The present study explores such a possibility.

IVC.1.3 Experimental section

Detailed synthesis procedure of T-SLG is described in the Chapter IVB.3. Briefly, a polycrystalline Ni foil (7 μm thick, 99.9%, Advent Research Materials) was taken and cut into 4.0 x 0.4 cm^2 strip, which was connected to the current carrying electrodes. Naphthalene solution (10 μL, 1 mM) in chloroform was drop cast onto the Ni foil and allowed to dry. After reaching a rotary vacuum of ~5 mTorr, the Ni foil was Joule heated to red hot (~ 800 °C) with a current density of 120 – 150 A/mm^2 using a DC source for 15 min followed by immediate cooling. For TEM measurements, graphene on Ni was transferred onto the holey carbon film of the Cu grid by chemically etching of Ni using 1 M $FeCl_3$ solution. The absorption spectra were recorded in the transmission mode using Perkin Elmer Lambda 900 UV-VIS-NIR spectrometer.

IVC.1.4 Results and discussion

A graphene flake, with an area of ~ 10 mm^2, was obtained by the method described in the Chapter IVB and transferred to a glass substrate (see Figure IVC.1a). To ensure that the obtained graphene is a T-SLG species, Raman spectra were acquired in four different regions numbered 1 to 4 (see Figure IVC.1b). In all the spectra, the 'D' band is completely absent and the 2D band shows single Lorentzian symmetric behaviour with I_{2D}/I_G varying from 3.2 to 5.5 along with FWHM in the range of 18 – 22 cm^{-1}, which are clear characteristics of SLG. The thickness of the graphene flake was measured on these regions (see Figure IVC.1c to f) and found to be approximately 40 - 50 nm. In spite of being so thick (with 120-150 graphene layers), its Raman spectrum show characteristics of SLG, confirming that the graphene flake is indeed a T-SLG graphene species [16].

Using UV-vis spectrometer, the absorption spectrum was recorded in 400 – 800 nm range as shown in Figure IVC.2. The spectrum clearly shows a absorption band at ~ 540 nm. Such an absorption band in the visible region was not observed in any graphene samples using a normal UV-vis spectrometer. Generally, graphitic species including graphene show flat band absorption in the visible spectral range [17, 18]. It is only tBLG which shows the absorption band whose maxima vary with the twist angle [10-13] and λ_{ex}. The absorption band occurs when the energy difference between vHSs induced by the twist angle matches with the λ_{ex}. Here the absorption occurs at 540 nm when λ_{ex} of 532 nm was used. By correlating the position of theoretically reported absorption maxima (from ref. [14]), the twist angle in the T-SLG can be assigned to ~ 13°. Here it is important to note that the observed absorption is not related to number of graphene layers, as in twisted bilayer graphene (tBLG) system also, such absorption band has been observed. However, the intensity of absorption band observed in t-BLG is very weak, and therefore specialised imaging techniques have been used to experimentally observe such bands. In T-SLG case, such absorption was observable in a UV-Vis spectrometer due to large sampling of twisted graphene layers.

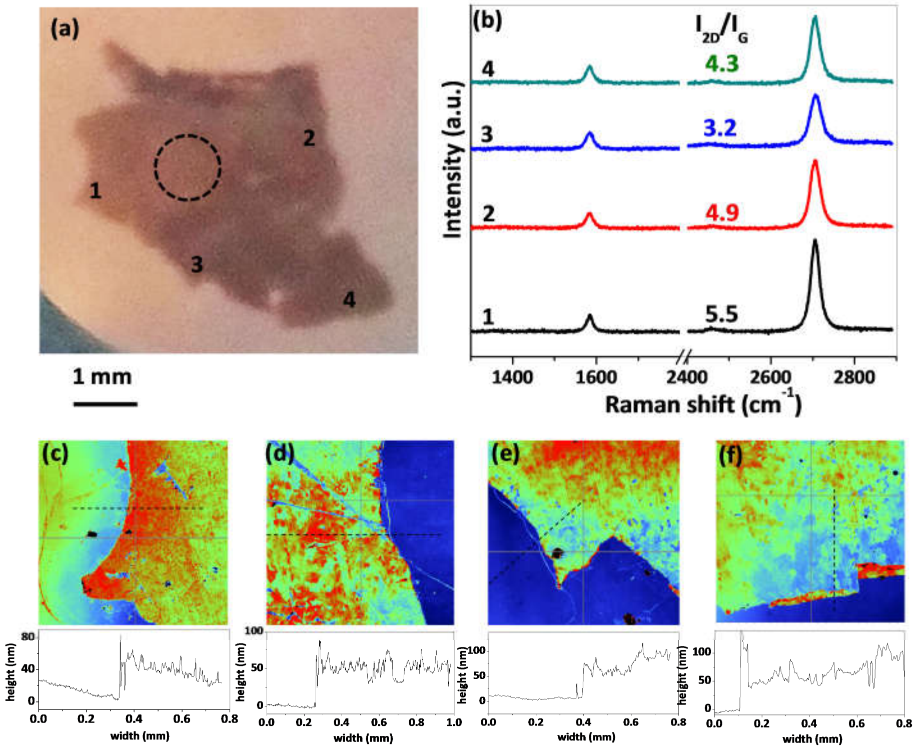

Figure IVC.1 Characterisation of T-SLG flake

(a) A photograph of a T-SLG flake on a glass substrate. The dotted circle indicates the regions on which absorption spectrum was acquired. (b) Representative Raman spectra acquired on the regions indicated by numbers in (a). The I_{2D}/I_G ratios are indicated. (c) to (f) are the thicknesses of T-SLG measured by OP of regions 1 to 4 in (a) respectively. The height profiles of the dotted lines are given below respective OP images.

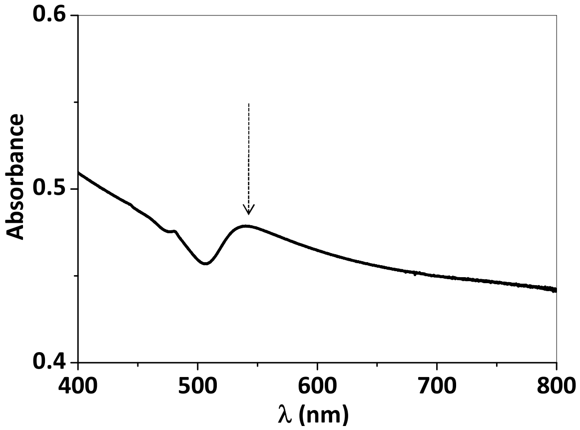

Figure IVC.2 Absorption spectrum of T-SLG

(a) The absorption spectrum of T-SLG measured over visible range. The dotted arrow points to the absorption band.

It is known that the tBLG exhibits G band resonance when the twist angle giving rise to energy difference between vHSs matches with λ_{ex} [11]. For example, tBLG with $\theta = 13°$ shows G band enhancement at λ_{ex} of 532 nm [12]. In the present study, this observation is used to confirm the twist angle of 13° in T-SLG. Three representative Raman spectra, measured on T-SLG, are shown in Figure IVC.3a. Note that all the spectra have single Lorentzian characteristics and thus increased G band is not due to the graphitic behaviour. Clearly, the Raman spectra of T-SLG indeed shows the G band enhancement (see Figure IVC.3a). The intensity of G band has enhanced 2 – 5 times than that of 2D band intensity. Further, the spectra were magnified in the region 1300 – 1550 cm^{-1} which shows appearance of a new band, called as R band, at around ~ 1500 cm^{-1} (Figure IVC.3b). It is known that the position of R band varies with the twist angle too. By correlating the position of the R band with the twist angle [14], the twist angle in T-SLG matches exactly with the twist angle of 13°.

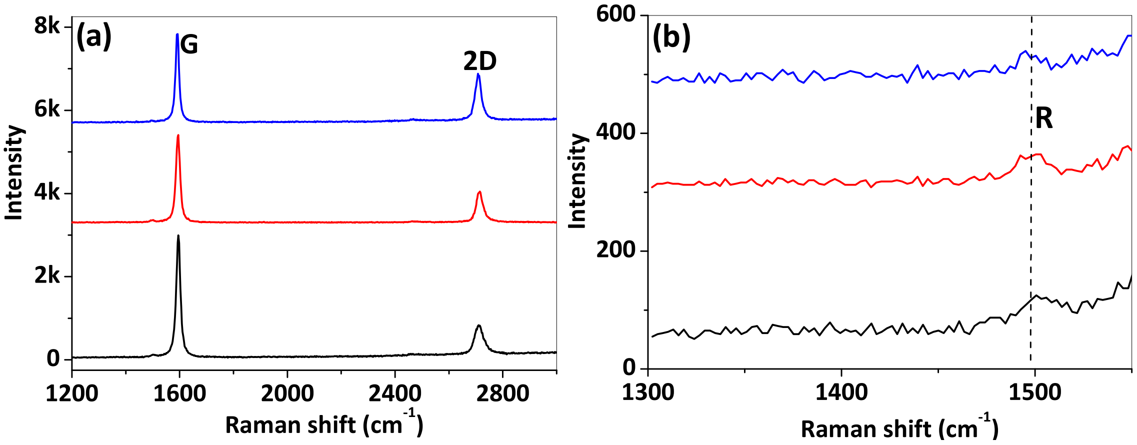

Figure IVC.3 G-band enhancement in T-SLG

(a) Raman spectra acquired over three regions on T-SLG at λ_{ex} = 532 nm. (b) Magnified portion of the Raman spectra over the region of 1300 – 1550 cm^{-1}. Dotted bar indicates the position of R band at ~ 1500 cm^{-1}.

Further, the twist angle between graphene layers was confirmed by TEM analysis (see Figure IVC.4). Figure IVC.4a is the low magnification TEM image of a T-SLG flake. A portion of it is magnified in Figure IVC.4b, which shows parallel stripes like features as marked by the dotted orange lines. Along with the parallel lines, one can also see hexagonal structures in the marked region. The inset of Figure IVC.4b shows the arrangement of carbon atoms along the black colored line. Such arrangement of carbon atoms was observed throughout the TEM image, which implies a high degree of 2D crystallinity of the T-SLG. From TEM image, FFT pattern was generated and as shown in Figure IVC.4c. The main diffraction spots corresponding to hexagonal lattice have split into sharp spots with angular spread of 2 - 3°. In addition to these main spots, many intermediate spots can also be observed but with milder intensity. The spread spots clearly indicate that majority of the graphene layers have angular rotations of 2 - 3° whereas the intermediate spots indicate that there are graphene layers with higher angular rotations.. Interestingly, when two lines are drawn meeting the main and intermediate diffraction spots to measure the angle between them, it exactly turns out to be ~ 13°.

Following FFT pattern, two schematic models are drawn. In the first model (see Figure IVC.4d) three graphene layers are rotated with respect to adjacent layers at an angle of 3° which generates parallel strip-like features with a periodicity of ~ 5 nm. The observed periodicity nearly matches with the periodicity of strip-like structures in TEM (see Figure IVC.4b). In the second model (see Figure IVC.4e), another layer was added with a rotation of 13° with respect to the third layer. This produced hexagonal superlattices with width ~ 1.6 nm, similar to the one observed in TEM in Figure IVC.4b (indicated by yellow colored hexagons). Since TEM is limited by atomic resolution, observation of continuous and uniform moiré patterns was difficult in the present study.

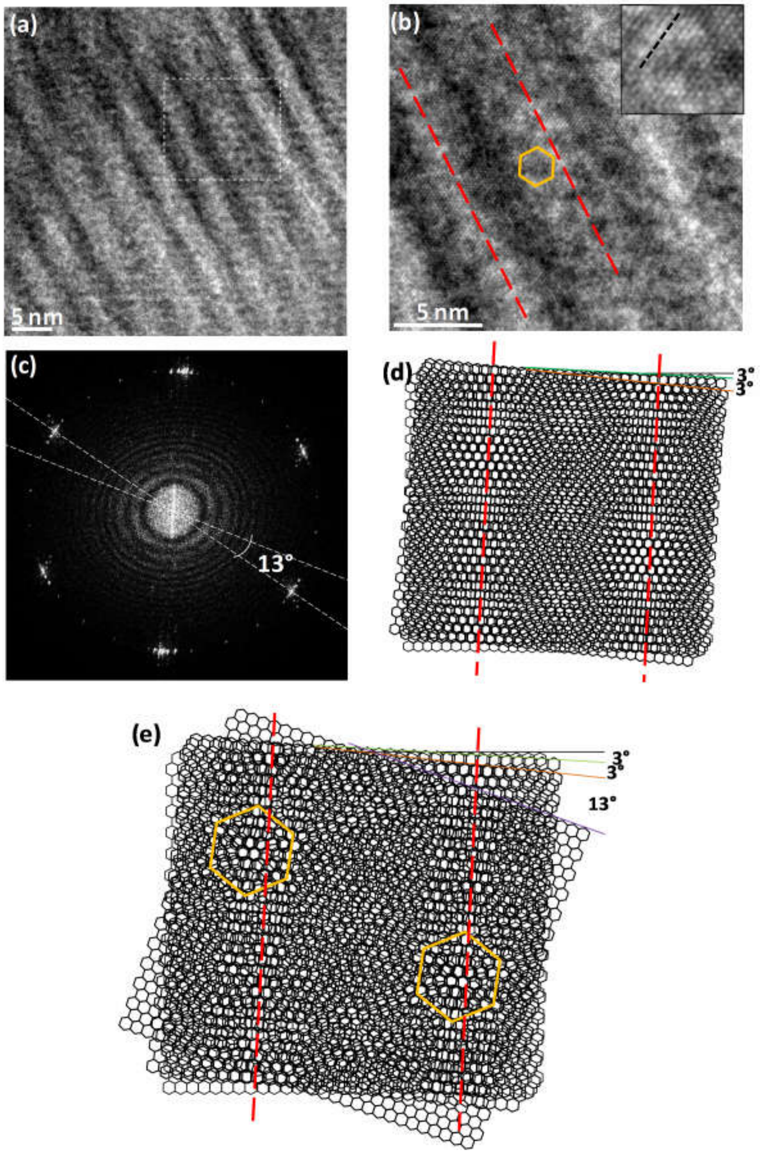

Figure IVC.4 TEM analysis of T-SLG

(a) TEM image of T-SLG flake.(b) High-resolution TEM of magnified portion indicated by the dotted square box in (a). In the inset, a portion of the image is magnified to see the lattice arrangement of atoms along the drawn dashed line. (c) FFT image generated from (a). The lines are drawn at an angle of 13° meeting diffraction points. (d and e) Schematic representation of rotations of graphene layers. Here first three layers are in (d) and (e) rotated at an angle of 3° with respect to adjacent layers (shown by black, red and blue lines) and the fourth layer in (e) is rotated at angle of 13° (shown in brick lines) with respect to 3rd layer. The orange lines are shown along the appearance of strips and golden hexagons are drawn joining hexagonal superlattices.

IVC.1.5 Conclusions

Since T-SLG contains many graphene layers that are rotated with respect to one another, the absorption bands become prominently observable in conventional UV-vis measurements. By correlating the position of absorption bands, the twist angle was assigned to ~ 13 °, which was further confirmed by G-band enhancement and position of R band. The electron diffraction spots in TEM indicates that T-SLG majorly contains graphene layers with angular rotations of 2 - 3 ° and minor number of layers with 13° twist.

References

1. Yan, Wei, et al. "Angle-dependent van Hove singularities and their breakdown in twisted graphene bilayers." *Physical Review B* 90. 11 (**2014**): 115402.

2. Landgraf, W., et al. "Electronic structure of twisted graphene flakes. "*Physical Review B* 87. 7 (**2013**): 075433.

3. Robinson, Jeremy T., et al. "Electronic hybridization of large-area stacked graphene films." *ACS Nano* 7. 1 (**2012**): 637-644.

4 Jorio, Ado, and Luiz Gustavo Cançado. "Raman spectroscopy of twisted bilayer graphene." *Solid State Communications* 175 (**2013**): 3-12.

5. Luican, A., et al. "Single-layer behaviour and its breakdown in twisted graphene layers." *Physical review letters* 106. 12 (**2011**): 126802.

6. Ding, Yao, et al. "Stacking-Mode-Induced Reactivity Enhancement for Twisted Bilayer Graphene." *Chemistry of Materials* 28. 4 (**2016**): 1034-1039.

7. Xian, Lede, Z. F. Wang, and Mei-Yin Chou. "Coupled Dirac fermions and neutrino-like oscillations in twisted bilayer graphene." *Nano letters* 13. 11 (**2013**): 5159-5164.

8. Wang, Z. F., Feng Liu, and M. Y. Chou. "Fractal Landau-level spectra in twisted bilayer graphene." *Nano letters* 12. 7 (**2012**): 3833-3838.

9. Li, Guohong, et al. "Observation of Van Hove singularities in twisted graphene layers." *Nature Physics* 6. 2 (**2010**): 109-113.

10. Liao, Lei, et al. "van Hove singularity enhanced photochemical reactivity of twisted bilayer graphene." Nano letters 15. 8 (**2015**): 5585-5589.

11. Yin, Jianbo, et al. "Selectively enhanced photocurrent generation in twisted bilayer graphene with van Hove singularity." *Nature Commun.* 7 (**2016**).

12. Havener, Robin W., et al. "Angle-resolved Raman imaging of interlayer rotations and interactions in twisted bilayer graphene." *Nano let.* 12 .6 (**2012**): 3162-3167.

13. Ni, Zhenhua, et al. "G-band Raman double resonance in twisted bilayer graphene: Evidence of band splitting and folding." *Physical Review B* 80. 12 (**2009**): 125404.

14. Carozo, V., et al. "Resonance effects on the Raman spectra of graphene superlattices." Physical Review B 88. 8 (**2013**): 085401.

15. Havener, Robin W., et al. "Van hove singularities and excitonic effects in the optical conductivity of twisted bilayer graphene." *Nano letters* 14. 6 (**2014**): 3353-3357.

16. Umesha Mogera, Radhakrishnan Dhanya, Rajashekhar Pujar, Chandrabhas Narayana, and Giridhar U. Kulkarni "Highly Decoupled Graphene Multilayers: Turbostraticity at its Best." The journal of physical chemistry letters 6. 21 (**2015**): 4437-4443.

17. Bae, Sukang, et al. "Roll-to-roll production of 30-inch graphene films for transparent electrodes." *Nature nanotechnology* 5. 8 (**2010**): 574-578.

18. Kim, Hobeom, et al. "Organic solar cells using CVD-grown graphene electrodes." *Nanotechnology* 25. 1 (**2013**): 014012.

IVC.2 Temperature Dependent Transport in T-SLG

IVC.2.1 Introduction

Studying the electronic transport properties of intrinsic graphene (purest form of graphene), especially its temperature dependent conductivity has always been a subject of interest in the recent past [1-3]. However, realising the intrinsic graphene experimentally is a challenging task due to unavoidable presence of scatterers in the graphene devices [4-5]. Many efforts have been made to have ultraclean graphene for this purpose but are met with limited success [6, 7]. Recently, Sarma et al. [8] have developed a theoretical relation between the purity of graphene samples and its temperature dependent conductivity, giving an insight into the influence of impurities on charge carrier density and mobility of the graphene devices.

The three main scattering mechanisms governing temperature dependence of the conductivity in graphene are the short-range disorder, long-range Coulomb disorder and phonon scattering [8]. At lower temperature, it shows semiconducting behaviour (increase in conductivity with temperature), due to dominance of Coulomb disorder and after reaching a conductivity maxima, it exhibits metallic behaviour (decrease in conductivity with temperature) due to the dominance of phonon scattering. The crossover temperature at which transition occurs between semiconducting to metallic behaviour is called as Bloch-Gruneisen temperature (T_c) and conductivity at the metallic region is called as Dirac point conductivity (σ_D). Thus the intrinsic Dirac point physics (or σ_D) for graphene samples can be accessed only after the T_c. However, the position of T_c increases sensitively with increase in amount of disorder in the graphene sample. Sarma et. al. [9] have derived that, $T_c \sim 10^{-3}(n_c)^{1/2}$ where n_c is the carrier concentration. For a graphene supported on a substrate, $n_c \sim 10^{12}$ cm^{-2}[8], and the T_c is ~ 1000 K! In other words, for graphene supported on a substrate, the σ_D can be observed only after 1000 K. Therefore, it was believed for a long time that the graphene always exhibits monotonous temperature dependent transport with semiconducting behaviour at RT. It was only after experiments of

Bolotin et. al. [9], non-monotonic temperature conductivity was observed with metallic behaviour at RT in case of suspended graphene samples, but only after the graphene was current annealed.

IVC.2.2 Scope of the present investigation

In order to observe non-monotonic temperature dependence of conductivity, one needs to have ultraclean graphene devices, which show σ_D at RT. Practically, only suspended graphene free from any substrate influence after current annealing, is known to exhibit such a behaviour. However, the intricacies built around fabricating suspended devices makes it a non-ideal candidate to extract the novel properties associated with its Dirac point physics (or σ_D) for practical applications. This section explores the possibility of having such non-monotonic temperature dependent σ_D in T-SLG, as the graphene layers in T-SLG are highly decoupled with good 2D crystallinity.

IVC.2.3 Experimental section

Detailed synthesis procedure of T-SLG has been described in previous chapter section IVB.3. The graphene grown on Ni was transferred onto glass substrate by etching underlying Ni using 1M aq. $FeCl_3$ solution, followed by scooping away floating graphene flake using the substrate. Metallic contacts were made by physical vapor deposition of Au by shadow masking in the active area.

IVC.2.4 Results and discussion

Before studying the electronic properties of T-SLG, the obtained graphene flake was characterised and confirmed to be a T-SLG flake. After transferring graphene flake onto a glass substrate, gold electrodes were defined by shadow masking with a gap length of ~ 50 μm (see Figure IVC.5a). Its thickness was measured by optical profilometry and found to be ~ 75 nm (Figure IVC.5b). Considering typical interplanar distance of graphite to be ~ 0.34 nm, the total number of layers may be counted as ~ 215 ± 10. Raman mapping was recorded on this graphene flake and mapping of I_{2D}/I_G ratio is given in Figure IVC.5c. The I_{2D}/I_G values found to typically vary from 4 to 10, surpassing the values observed in case of suspended graphene. Representative Raman spectra are shown (Figure IVC.5d) corresponding to the regions marked in Figure IVC.5c. The 'D' band, characteristic of the presence of defects, are completely absent and the 2D band exhibits single Lorentzian symmetric behaviour with FWHM varying between 18 - 20 cm ^{1}, resembling that of SLG. These characteristics clearly certify that the obtained flake was indeed a T-SLG flake [10].

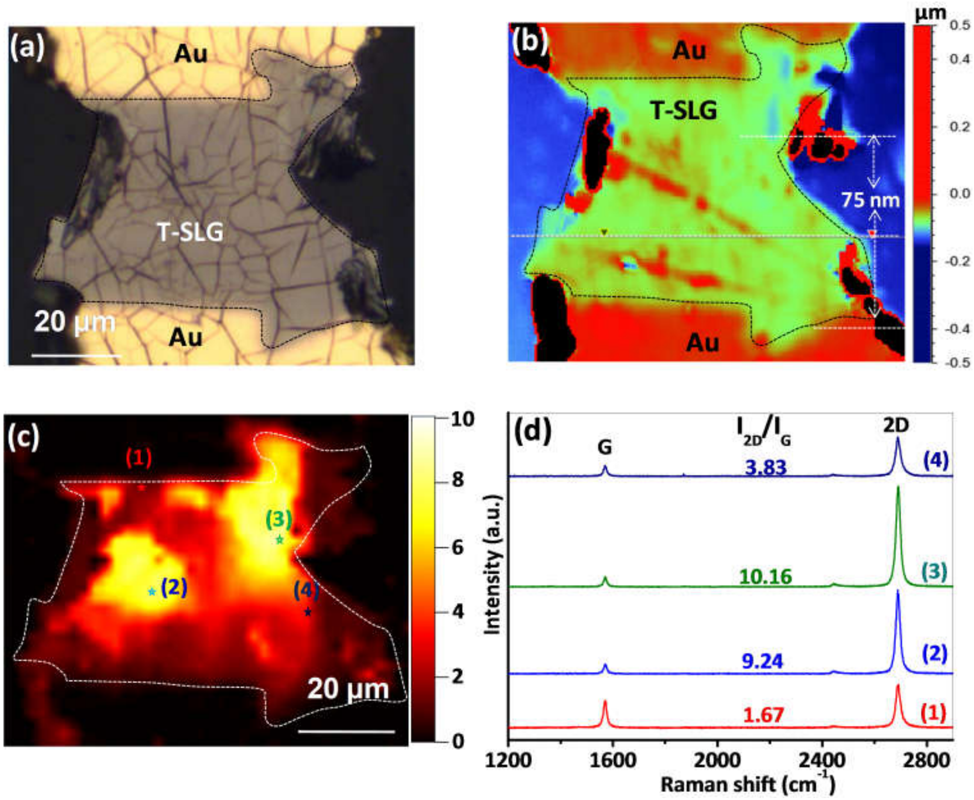

Figure IVC.5 Same area thickness and Raman mapping of T-SLG device
(a) The optical image of T-SLG graphene flake with Au contact pads on it. (b) optical profiler image of (a) from which thickness has been measured to be ~ 75 nm. The black colour is due to colour saturation of the intensity scale, due to graphene folds. A dotted line is drawn along the edges of graphene region. (c) Raman mapping of I_{2D}/I_G ratio acquired on (a). (d) The representative Raman spectra of the regions indicated by numbers in (c) with colour correspondence. The I_{2D}/I_G ratio values are given.

Figure IVC.6 describes the temperature dependent resistance variation of the T-SLG in the range of 93 – 273 K. As the temperature is increased from 93 K, the resistance decreased from 21.25 Ω to 20.1 Ω at ~ 180 K after which it decreased linearly to reach 20.8 Ω at 273 K (see Figure IVC.6a). Clearly, there is a non-monotonic resistance variation with the temperature with semiconducting to metallic transition with T_c appearing at 180 K. The T_c appearing below RT clearly indicates that the T-SLG exhibit metallic behaviour at RT, a characteristics of intrinsic graphene. Even freely suspended graphene also fails to exhibit temperature dependent conductivity, which is well acknowledged in the literature [1]. Only suspended graphene is current annealed, it tends to exhibit such non-monotonous semiconducting to metallic transition [9]. In other words, only when graphene is in its purest form, devoid of any substrate influence and external impurities, such pristine properties may be observed. This infers that the graphene layers in T-SLG are equivalent to high-quality current annealed suspended graphene. This was possible in T-SLG due to decoupled nature of graphene layers in it, to an extent that it virtually behaves as current annealed suspended graphene.

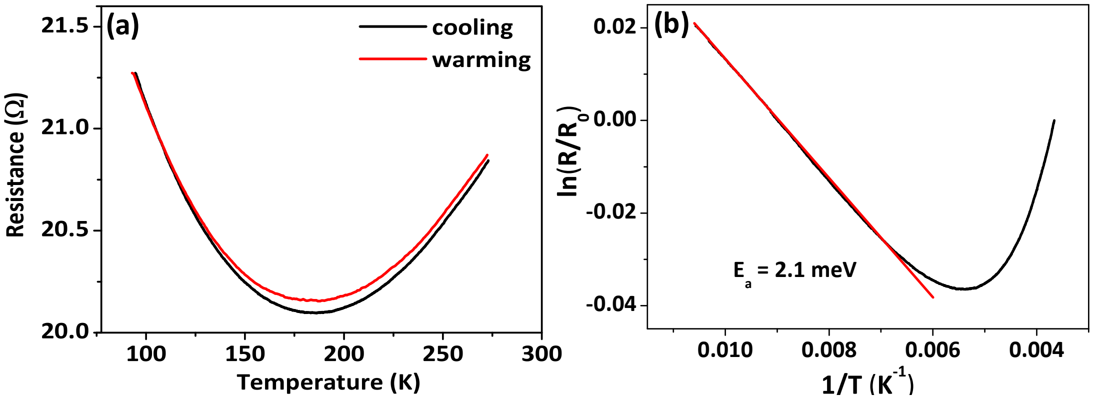

Figure IVC.6 Temperature dependent resistance in T-SLG

a) Variation of resistance of the T-SLG device in the temperature range of 93 – 273 K. (b) Activation energy curve of the device. The red line is fit to the linear region of the curve.

Also, from T_c, one can calculate the carrier density n_c, as $T_c \sim 10^{-3}(n_c)^{1/2}$ [9] which comes out to be 3.2 x 10^{10} cm^{-2}. Knowing n_c, the charge carrier mobility can be calculated using Drude model and was estimated to be ~ 54000 cm^2/Vs at RT. It is important to note that the observation of T_c in T-SLG below room temperature is remarkable and experimentally not observed in any graphene except for high quality suspended graphene. After T_c, the device is meant to exhibit intrinsic Dirac point conductivity. In other words, T-SLG exhibits metallic behaviour at RT without external electric field and hence σ_D. The typical CVD grown graphene shows T_c around 1000 K and so accessing Dirac point physics (or σ_D) for practical applications was not successful so far unless an external gate field is applied to reach Dirac point. On the other hand, σ_D, though observed in current annealed suspended graphene, its integration with other electronic components makes impractical for deriving any applications out of it [11]. Hence, the T-SLG becomes an ideal candidate to study the Dirac point physics, thus bringing it into real life applications. Notably, no hysteresis was observed in the device while cooling and warming cycles, implying the absence of trapped charges in the device. The resistance at $93 < T < 180$ K, varies linearly with 1/T from which activation energy (E_a) was calculated to be 2.1 meV (see Figure IVC.6b).

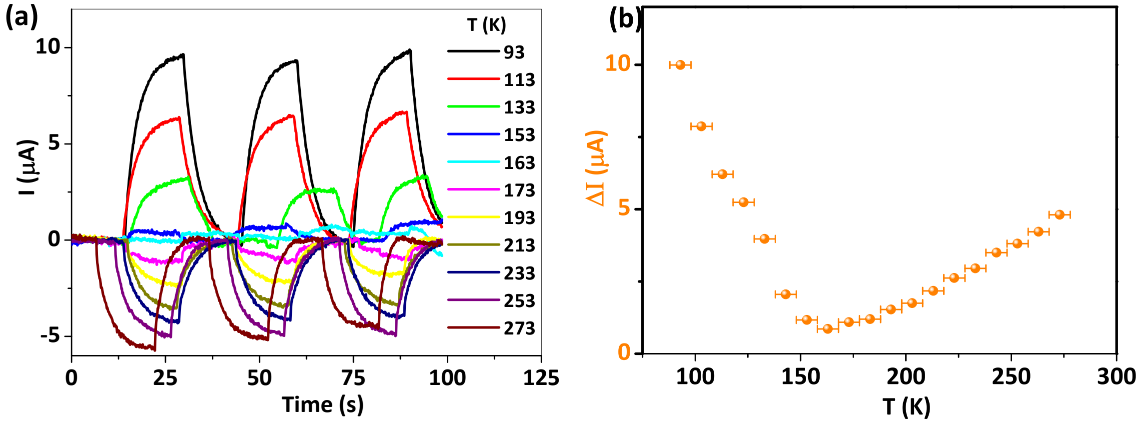

Figure IVC.7 UV photoresponse of T-SLG of varying temperature
(a) Temporal changes in current in T-SLG with the illumination of light source (λ = 365 nm) measured at 50 mV. (b) Variation of change in current of T-SLG measured over the temperature range.

The room temperature metallic behaviour of T-SLG was further confirmed using its light response behaviour. It is well known that graphene with a band gap (semiconducting nature) and pristine graphene exhibit different light response behaviour [12]. The conductivity of semiconducting graphene increases upon exposure to light [13] whereas pristine graphene (or graphene at Dirac point) shows a decrease in current, indicative of its metallic behaviour [14]. This aspect has been utilised in the present study to confirm the observed non-monotonous temperature behaviour i.e. semiconducting to metallic transition in T-SLG. Figure IVC.7a shows the temporal changes in photocurrent exhibited by the device at increasing temperature when a light source was incident on the device. At lower temperature (93 K), the photocurrent increased with incident light (positive photoresponse), but, as the temperature is increased from 93 K, the increase in photocurrent decreased, indicative of its semiconducting behaviour. Interestingly, after 170 K, the photocurrent started decreasing with incident light (negative photocurrent) and decrease in photocurrent increased as the temperature is increased to 273 K, indicative nature of metallic behaviour. Here, though increased photoresponse rate can be expected with the increase in temperature, the observed response rate in T-SLG found to vary slightly with the increase in temperature.

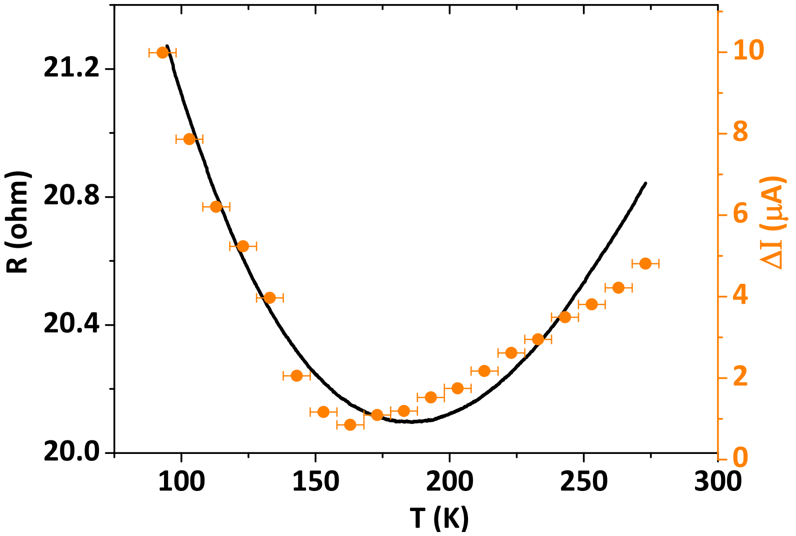

Figure IVC.8 Correlation between temperature dependent resistance and photoresponse The variations in resistance (left, black curve) and change in current (right, orange curve) of the T-SLG device with temperature.

The variations in resistance and photoresponse of the device with temperature were correlated in Figure IVC.8. Interestingly, the change in resistance and photoresponse behaves almost monotonically with the temperature. In other words, when resistance decreased the photoresponse decreased and vice versa. In 93 < T < 170

K, both resistance and positive photorepsonse decreased with increase in temperature, indicative of semiconducting behaviour. Whereas for T > 170 K being in metallic region, the resistance and negative photoresponse increased with temperature. As previously explained [9] in lower temperature at which T-SLG shows a semiconducting behaviour, electron-electron interaction (Coulomb disorder) dominates. The incident photons excite electrons to the system (photoexcitation) and hence photocurrent in the device increases upon exposing to light photons. Whereas in higher temperature range (T > 170 K), the phonon scattering is dominating and hence with the incident photons, the photocurrent decreases for light photons (photo annihilation), typically observed for materials with metallic nature [12].

IVC.2.5 Conclusions

In this study, the highly decoupled nature of T-SLG has been reflected in its temperature dependent conductivity. The semiconducting to metallic transition has been observed with the crossover temperature at ~ 180 K, which otherwise was observed only in case of current annealed suspended graphene. This clearly indicates the high purity of graphene layers in T-SLG, free from any external impurities. The mobility values are calculated from T_c and found to be ~ 54,000 cm^2/Vs which are expected to further increase in three terminal FET measurements. Further, metallic behaviour at RT indicates the T-SLG indeed has Dirac point behaviour without external field, which can be further explored for various applications.

References

1. Mariani, Eros, and Felix von Oppen. "Temperature-dependent resistivity of suspended graphene." *Physical Review B* 82. 19 (**2010**): 195403.

2. Peres, N. M. R. "Colloquium: The transport properties of graphene: An introduction." *Reviews of Modern Physics* 82. 3 (**2010**): 2673.

3. Tan, Y-W., et al. "Temperature dependent electron transport in graphene."*The European Physical Journal Special Topics* 148. 1 (**2007**): 15-18.

4. Chen, Jian-Hao, et al. "Intrinsic and extrinsic performance limits of graphene devices on SiO2." Nature nanotechnology 3. 4 (**2008**): 206-209.

5. Sarkar, Suman, et al. "Role of different scattering mechanisms on the temperature dependence of transport in graphene." Scientific reports 5 (**2015**).

6. Adam, Shaffique, et al. "A self-consistent theory for graphene transport."Proceedings of the National Academy of Sciences 104. 47 (**2007**): 18392-18397.

7. Heo, Jinseong, et al. "Nonmonotonic temperature dependent transport in graphene grown by chemical vapour deposition." *Physical Review B* 84. 3 (**2011**): 035421.

8. Sarma, S. Das, and E. H. Hwang. "Density-dependent electrical conductivity in suspended graphene: Approaching the Dirac point in transport." *Physical Review B* 87. 3 (**2013**): 035415.

9. Bolotin, K. I., et al. "Temperature-dependent transport in suspended graphene." *Physical review letters* 101. 9 (**2008**): 096802.

10. Mogera, Umesha, et al. "Highly Decoupled Graphene Multilayers: Turbostraticity at its Best." The journal of physical chemistry letters 6. 21 (**2015**): 4437-4443.

11. Maurand, Romain, et al. "Fabrication of ballistic suspended graphene with local-gating." *Carbon* 79 (**2014**): 486-492.

12. Kurra, Narendra, et al. "Few-layer graphene to graphitic films: infrared photoconductive versus bolometric response." *Nanoscale* 5. 1 (**2013**): 381-389.

13. Xu, Xiaodong, et al. "Photo-thermoelectric effect at a graphene interface junction." *Nano letters* 10. 2 (**2009**): 562-566.

14. Shi, Yumeng, et al. "Photoelectrical Response in Single-Layer Graphene Transistors." *Small* 5. 17 (**2009**): 2005-2011.

IVC.3 Differential SERS Effects

IVC.3.1 Introduction

Raman spectroscopy has been utilised as a powerful tool for the characterization of graphene, as it allows the monitoring of type of doping, defects, strain, disorder, chemical modifications, edges and to identify the number of layers in graphene [1, 2]. In addition, the interaction between localised surface plasmons of metal nanoparticles and phonons of graphene, has gained a lot of interest in past 6 years due to unique properties associated with the graphene [3, 4]. Surface Enhanced Raman Scattering (SERS) is a well-known method, which offers to study such interaction between them. It involves the enhancement of intensity in Raman spectrum of graphene induced by near-field plasmonic effects of metal nanoparticles [5, 6]. Among various metal nanoparticles, silver (Ag) and gold (Au) nanoparticles are extensively used for studying the SERS of various molecules due to several advantages associated with them [7, 8]. A table of literature survey on graphene-based SERS studies using metal nanostructures is given in Table IVC.1. In all studies, the enhancements of Raman bands, G and 2D, of graphene were studied and enhancement factor up to 200 and 140 respectively were reported from SLG. It is important to note that in all these cases, I_{2D}/I_G of graphene decreases after interacting with metal nanostructures due to the doping effect.

IVC.3.2 Scope of the present investigation

Knowing about SLG's one order of SERS enhancement, it is interesting to study the enhancement of stacks of many non-interacting SLGs. Will it show additive enhancement or a completely different behaviour? This section explores the study of SERS effect of stacks of graphene layers that are electronically decoupled from one another.

IVC.3.3 Experimental section

Detailed synthesis procedure of T-SLG has been described in previous chapter IVB. The graphene grown on Ni was transferred onto SiO_2/Si substrate by etching underlying Ni using 1M aq. $FeCl_3$ solution, followed by scooping out floating graphene flake using the substrate. Ag in the form of grainy nanoparticles was deposited onto T-SLG/SiO_2/Si by thermal evaporation. For the control, smooth and continuous Ag film were deposited using e-beam evaporation on a different T-SLG/SiO_2/Si. In the same region of T-SLG, Raman spectra were recorded before and after the silver deposition and compared with each other.

Table IVC.1 Table of literature examples of SERS of graphene using metal nanoparticles

Ref.	Type of graphene	I_{2D}/I_G		Enhancement factor		Remarks
		before	after	G	2D	
[9]	SLG	5	3.8	71	43	λ_{ex} = 532 nm, Au NP
	MLG	1.6	1.4	17	15	
[8]	SLG	5.1	3.4	23	15	λ_{ex} = 532 nm, Ag NP
	BLG	2.1	1.6	15	12	
	TLG	1.6	1.5	10	8	
[2]	SLG	-	-	5-20	2-30	λ_{ex} = 685 nm, Au NP
[10]	SG	4.1	2.8	200	140	λ_{ex} = 632 nm, Ag

IVC.3.4 Results and discussion

The graphene grown on Ni was first transferred onto SiO_2/Si substrate by etching underlying Ni using 1M aq. $FeCl_3$ solution, followed by scooping out floating flake using the substrate (see schematic in Figure IVC.9a). The thickness of the transferred flake on SiO_2/Si was measured using AFM and was found to be 100 -120 nm (see Figure IVC.9b and c). Considering typical interplanar distance of graphite of ~ 0.34 nm, the total number of layers may be counted as > 300. Representative Raman spectra are shown (Figure IVC.9d-g) corresponding to the regions marked in Figure IVC.9b. It is interesting to note in all the spectra that the 'D' band, characteristic of the presence of defects, is clearly absent. Moreover, the 2D band exhibit single Lorentzian symmetric behaviour centred at ~ 2700 cm^{-1} with the FWHM varying in 15 20 cm ^{1}, resembling SLG characteristics [11]. These characteristics clearly certify that the obtained graphene flake is indeed T-SLG flake [12].

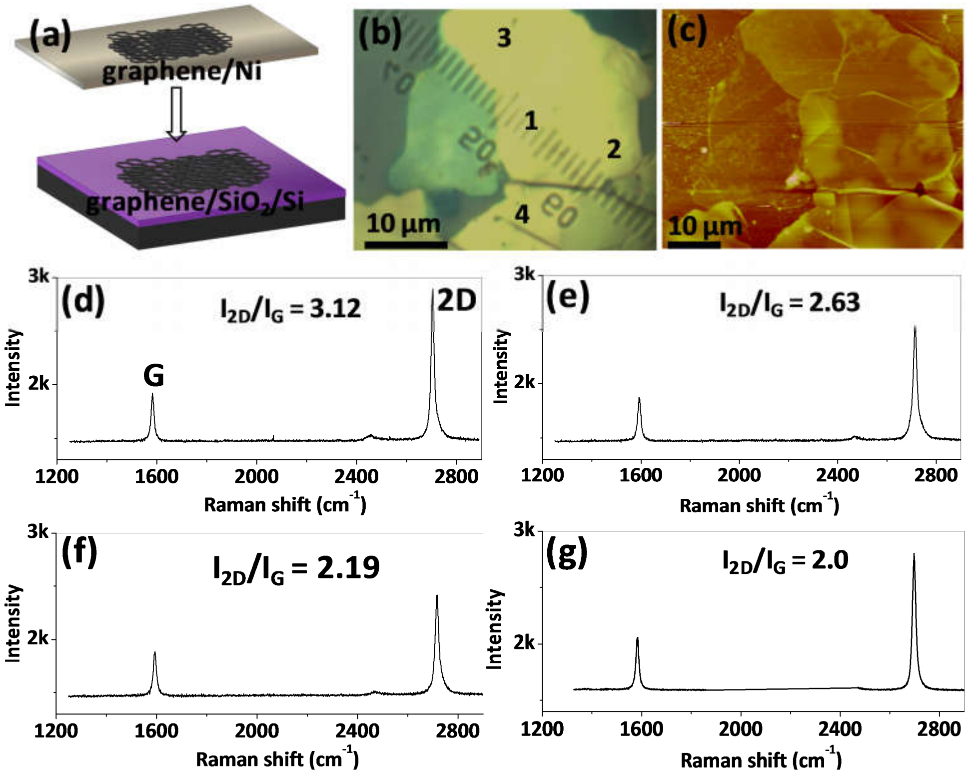

Figure IVC.9 Characterisation of T-SLG before Ag deposition

(a) Schematic of graphene transfer onto SiO_2/Si substrate. (b) An optical microscope image of the T-SLG flake on SiO_2/Si on which Raman spectra were acquired at regions 1-4 indicated by the numbers. (c) AFM topology image of T-SLG flake. z scale: 200 nm. (d-g) Representative Raman spectra of regions indicated by numbers 1-4 respectively. The ratios of 2D to G intensity (I_{2D}/I_G) values are shown.

In order to study the influence of surface plasmons induced by metal nanoparticles on graphene, Ag was coated on T-SLG flake using thermal evaporation (see schematic in Figure IVC.10a). Thermal evaporation of metal film is known to give grainy metal nanoparticles and has been used extensively to study SERS effect [8]. The uniform formation of silver nanoparticulates can be seen in the FESEM image in Figure

IVC.10b whereas high-resolution FESEM image (Figure IVC.10c) shows the formation of grainy Ag silver nanoparticles. The EDS spectrum in Figure IVC.10d further confirms the presence of Ag with a peak at binding energy of 3.0 keV. The thickness of Ag, as measured by AFM, found to be ~ 20 nm (see Figure IVC.10e) which is ideal for inducing near-field plasmonic effects from surface plasmons.

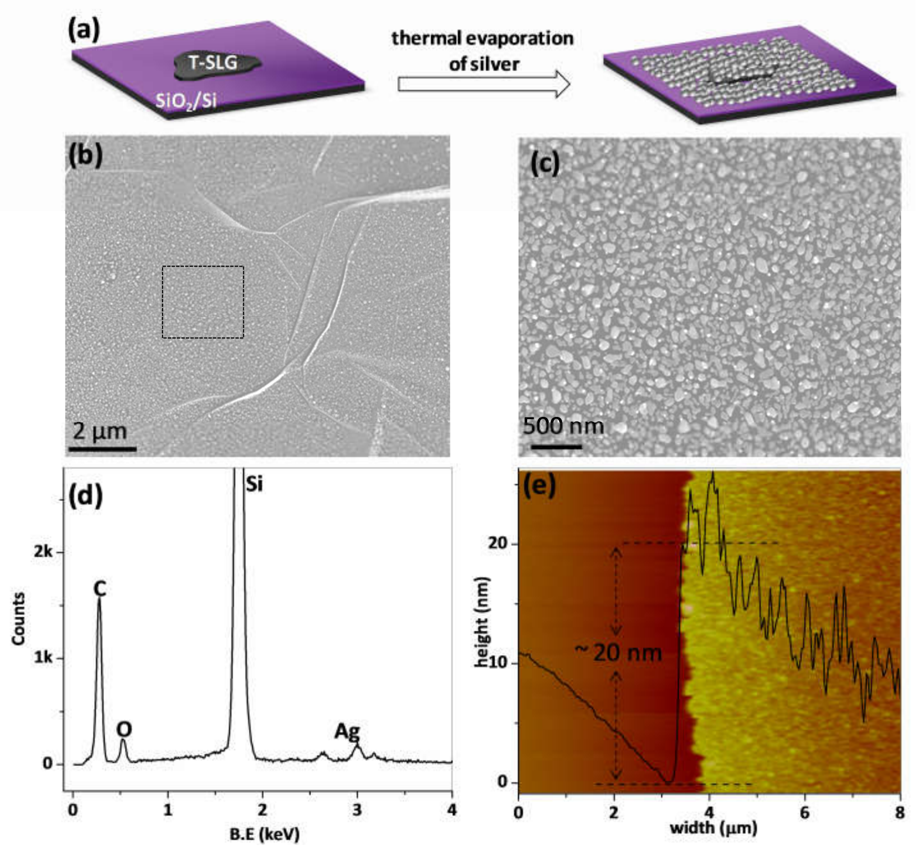

Figure IVC.10 Characterisation of T-SLG after thermal deposition of Ag
(a) Schematic of Ag deposition on T-SLG. (b) Low magnification (c) high magnification FESEM images of T-SLG after Ag deposition. (d) EDS spectrum recorded in a region marked by the dotted box in (b). (e) Thickness measurement of grainy Ag nanoparticles measured on SiO_2/Si.

Figure IVC.11 shows the Raman spectra measured at same regions of T-SLG, before (black curves) and after (red curves) Ag deposition. Interestingly, the intensity of the 'G' band at ~1585 cm^{-1} has not changed, whereas '2D' band has enhanced to different heights. This is seen repeatedly in all the measured four regions (see Figure IVC.11a – d). The I_{2D}/I_G ratios at four different regions increased from 3.12, 2.63, 2.19

and 2.00 to 8.82, 7.25, 4.43 and 3.5 respectively. Accordingly, the 2D enhancements in four measured regions are found to be 3.0, 2.9, 2.3 and 1.75 respectively. This is purely a differential enhancement of Raman bands of T-SLG where only the 2D band is affected by plasmons of metal nanoparticles. However, in all the studies related to SERS of SLG(refer to Table IVC.1) intensities of both G and 2D bands get enhanced, though with slight decrease I_{2D}/I_G by ratio. On the contrary, in T-SLG, the I_{2D}/I_G ratios found to increase after interacting with plasmons. Another intriguing aspect of SERS of nanoparticle coated by T-SLG is that the enhancement of I_{2D}/I_G ratio varies linearly with the initial I_{2D}/I_G ratio (see Figure IVC.11e). The differential enhancement of Raman bands is further analysed and shown in Figure IVC.11. The 2D band enhances with an increase in initial I_{2D}/I_G as shown in Figure IVC.11f (blue sphere), however, G band remains unchanged (orange sphere). Further, from the literature it is known that in case of SLG, BLG to MLG in AB stacking, the interaction between metal nanostructures influences the I_{2D}/I_G ratios along with other parameter. In the present case, the stacking being non-AB, the number of graphene layers does not seem to influence interaction with the metal nanostructures as evidenced by the Raman spectra.

Further, SERS effect of T-SLG was studied with non-localised surface plasmons by depositing Ag film using electron beam (e-beam) evaporation (see schematic in Figure IVC.12a). Due to slow evaporation of metal in e-beam, a smooth and continuous film can be obtained as shown in Figure IVC.12b and c. This smooth film of Ag no longer exhibits local surface plasmons, instead it exhibits non-localised propagating surface plasmons. Interestingly, the Raman spectra measured at regions exhibits no change in their intensity before and after Ag deposition as can be seen Figure IVC.12d and e. The I_{2D}/I_G values remained same (5.4 to 5.4) in one region (see Figure IVC.12c) whereas it slightly decreased (6.3 to 6.1) in another region (see Figure IVC.12d). This is in accordance with the literature where non-localised plasmons fail to enhance Raman signals.

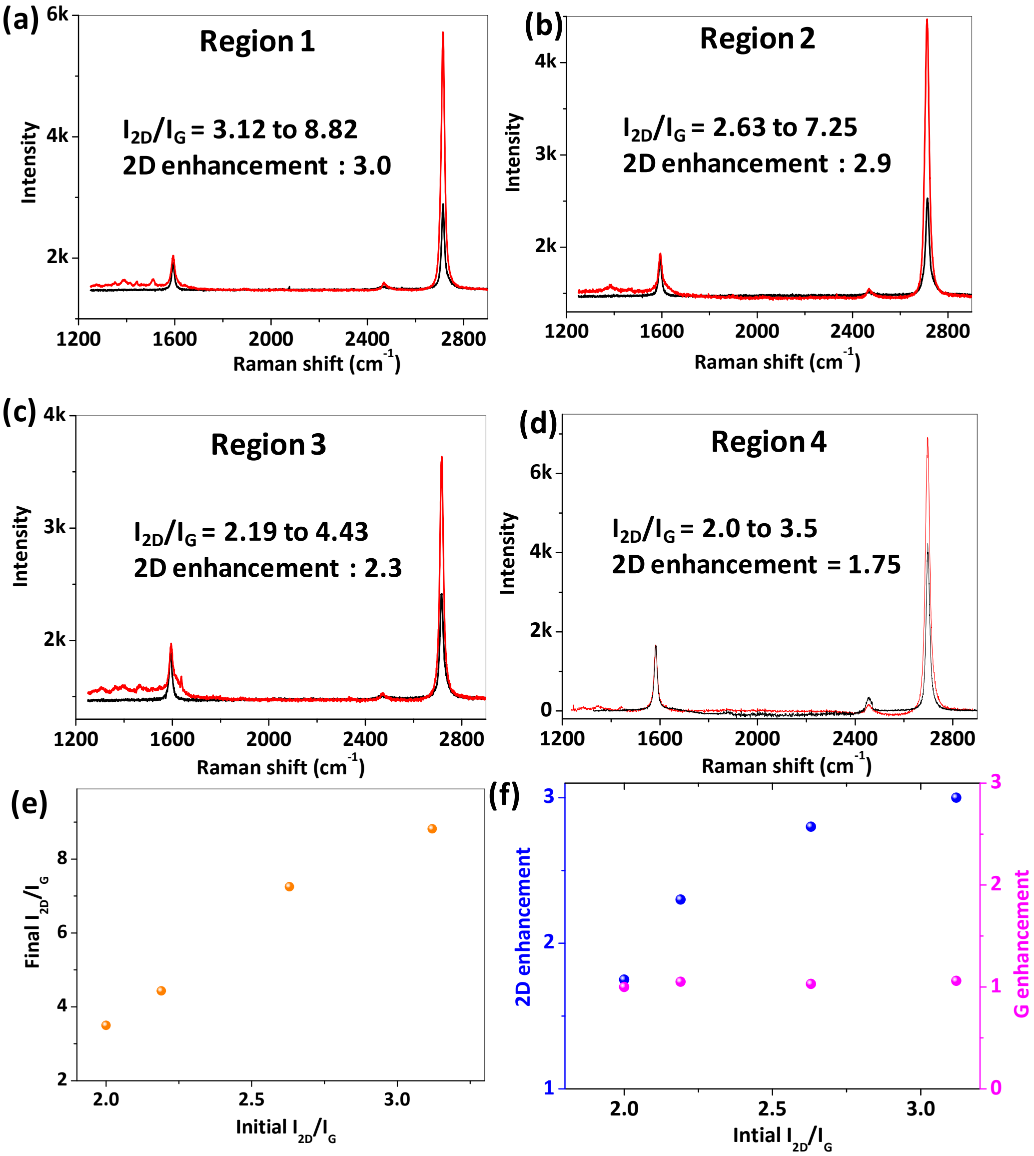

Figure IVC.11 SERS of T-SLG due to localised surface plasmons

(a-d) Raman spectra acquired for T-SLG before (black curve) and after (red curve) Ag deposition on T-SLG measured at four different regions. The increase in I_{2D}/I_G ratio is indicated in each spectrum. The enhancement in 2D band is also shown. (e) The increase of final I_{2D}/I_G with initial I_{2D}/I_G ratios. (f) The change in the enhancement of 2D (left) and G (right) bands with initial I_{2D}/I_G.

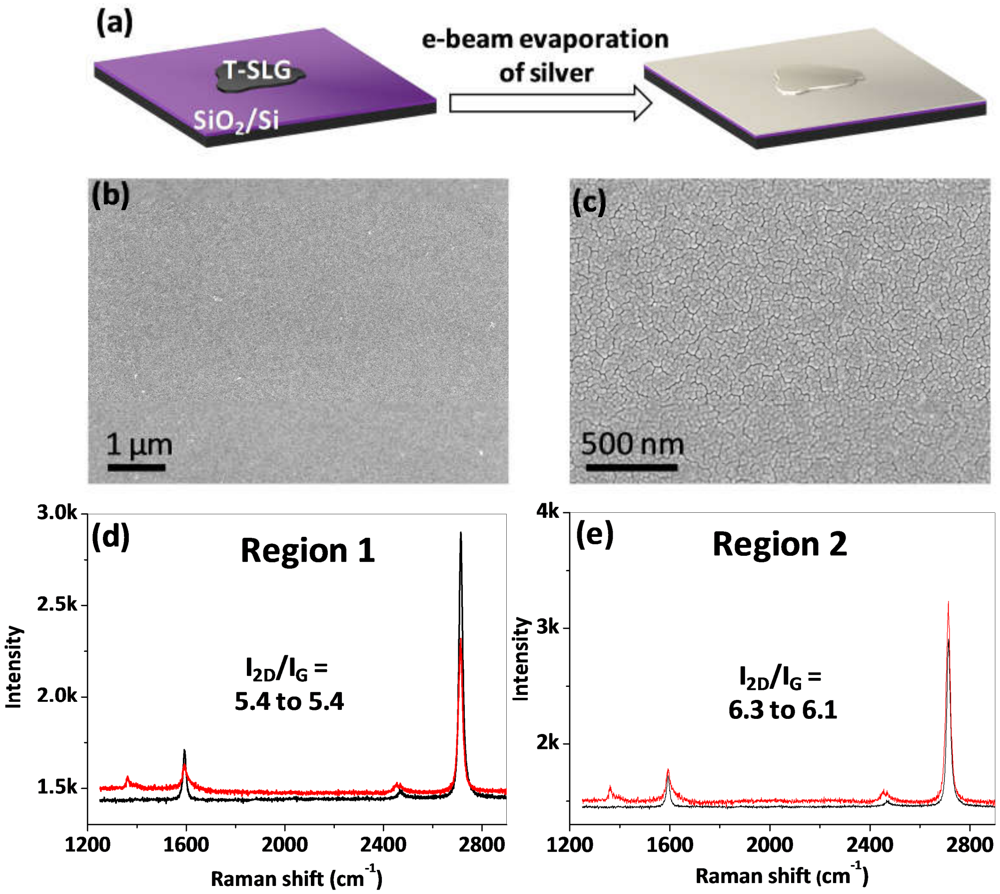

Figure IVC.12 SERS of T-SLG due to non-localised surface plasmons

(a) Low magnification (b) high magnification FESEM images of T-SLG after Ag e-beam deposition. (c and d) The Raman spectra acquired for T-SLG before (black curve) and after (red curve) Ag e-beam deposition on T-SLG measured at two different regions. The change in I_{2D}/I_G ratios is indicated.

IVC.3.5 Conclusions

Influence of silver nanoparticles on T-SLG are investigated using Raman spectroscopy. Astonishingly, Raman spectrum shows selective enhancement of 2D band intensity whereas G band remained intact. This is uniquely observed in T-SLG. Further modelling can be done for better understanding of the phenomenon.

References

1. Ferrari, A. C.; Meyer, J. C.; Scardaci, V.; Casiraghi, C.; Lazzeri,M.; Mauri, F.; Piscanec, S.; Jiang, D.; Novoselov, K. S.; Roth,S.; Geim, A. K. Raman Spectrum of Graphene andGraphene Layers. *Phys. Rev. Lett.* **2006**, *97*, 187401.

2. Ferrari, Andrea C., and Denis M. Basko. "Raman spectroscopy as a versatile tool for studying the properties of graphene." *Nature Nanotech.* 8. 4 (**2013**): 235-246.

3. Tjoa, Verawati, et al. "Hybrid graphene–metal nanoparticle systems: electronic properties and gas interaction." *Journal of Materials Chemistry*21. 39 (**2011**): 15593-15599.

4. Devi, M. Manolata, et al. "Graphene–Metal Nanoparticle Hybrids: Electronic Interaction Between Graphene and Nanoparticles." *Transactions of the Indian Institute of Metals* 69. 4 (**2016**): 839-844.

5. Michaels, Amy M., M. Nirmal, and L. E. Brus. "Surface enhanced Raman spectroscopy of individual rhodamine 6G molecules on large Ag nanocrystals." *Journal of the American Chemical Society* 121. 43 (**1999**): 9932-9939.

6. Xu, Hongxing, et al. "Spectroscopy of single hemoglobin molecules by surface enhanced Raman scattering." *Physical review letters* 83. 21 (**1999**): 4357.

7. Zhang, Zhe, et al. "A facile one-pot method to high-quality Ag-graphene composite nanosheets for efficient surface-enhanced Raman scattering." *Chemical Communications* 47. 22 (**2011**): 6440-6442.

8. Lee, Jisook, Konstantin S. Novoselov, and Hyeon Suk Shin. "Interaction between metal and graphene: dependence on the layer number of graphene." *ACS Nano* 5. 1 (**2010**): 608-612.

9. Lee, Jisook, et al. "Surface-Enhanced Raman Scattering of Single-and Few-Layer Graphene by the Deposition of Gold Nanoparticles." *Chemistry–A European Journal* 17. 8 (**2011**): 2381-2387.

10. Huang, Cheng-Wen, et al. "Surface-enhanced Raman scattering of suspended monolayer graphene." *Nanoscale research letters* 8. 1 (**2013**): 1-5.

11, Ferrari, A. C.; Meyer, J. C.; Scardaci, V.; Casiraghi, C.; Lazzeri,M.; Mauri, F.; Piscanec, S.; Jiang, D.; Novoselov, K. S.; Roth, S.; et al. Raman Spectrum of Graphene and Graphene Layers. Phys. Rev. Lett. **2006**, 97, 187401.

12. Umesha Mogera, Radhakrishnan Dhanya, Rajashekhar Pujar, Chandrabhas Narayana, and Giridhar U. Kulkarni "Highly Decoupled Graphene Multilayers: Turbostraticity at its Best." The journal of physical chemistry letters 6. 21 (**2015**): 4437-4443.

Chapter IVD

Synergy between Graphene and Ni(111)

Summary

In this chapter, the orientation and morphology of polycrystalline Ni foil were studied after graphene growth. It is very well known that Ni(111) is the preferred orientation for the growth of graphene on Ni. Here, the effect of graphene growth on the orientation and morphology of underlying Ni foil are studied. XRD patterns suggest that there exists a synergistic cooperation between the graphene and Ni after graphene growth. Careful microscopy analysis has shown unusual crystal morphology of the underlying Ni following graphene growth.

IVD.1 Introduction

Graphene growth on metal substrates is an interesting subject of research and has been widely studied on various metal substrates [1]. Copper and nickel metal surfaces are well known among them [2-5]. It is known in the case of nickel that graphene preferentially grows on Ni(111) than on other orientations [6, 7] due to very small lattice mismatch (~ 0.3%) between them. Recently, it is shown that graphene layer grows commensurately with Ni(111) [6, 8] and the growth process is most energetically favourable [9-11]. The graphene growth on other Ni orientations such as (110), (755), (771) have also been reported, however, on these Ni orientations, graphene forms distorted structures [12, 13]. Such preferred orientation is also seen in the case of other transition metal catalysts such as Pt(111), Pd(111), Ru(111) and Ir(111) [5]. However, graphene is incommensurate with these metal substrates due to lattice mismatch of > 1%. In case of copper, graphene does not have preferred orientation [14 -16] but this discussion is unclear in the literature.

The typical structure of graphene on Ni(111) is briefly explained as follows. The neighbouring carbon atoms of graphene, as indicated by A and B in Figure IVD.1, occupy non-equivalent sites of Ni(111). The non-neighbouring carbon atoms i.e. sets of A and B, commensurately lies above first and third layer of Ni(111) respectively [17].

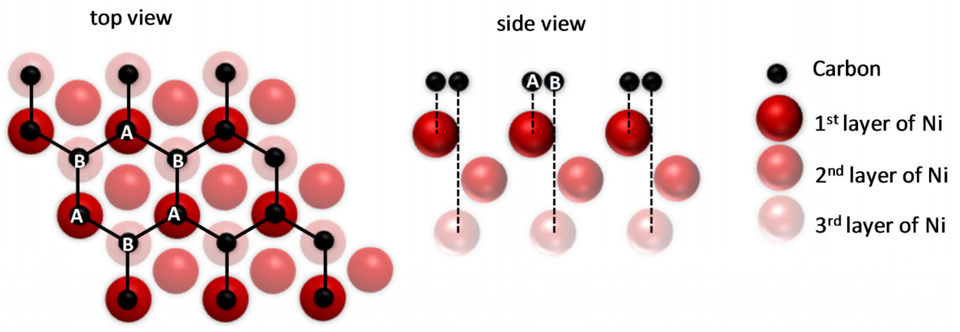

Figure IVD.1 Structure of graphene on Ni(111)
Top and side views of the graphene/Ni structure: Black color indicates carbon, red colors are Ni atoms (more transparent the Ni atoms, further its position from C atoms).

IVD.2 Scope of the present investigation

While it is known that Ni(111) is the most favourable for graphene growth, the effect of graphene growth on underlying Ni has not been studied. As the lattice mismatch is negligible, no significant influence of the growth on the metal substrate can be expected. However, the work presented in this section was taken up to gain an insight into possible re-orientation effects of the metal substrate. Indeed, the observation has been remarkable as detailed below.

IVD.3 Experimental section

Detailed synthesis procedure of graphene has been described in previous chapter IVB.3. Briefly, a polycrystalline Ni foil (7 μm, 99.9%, Advent Research Materials) was taken and cut into a 4.0 x 0.4 cm^2 strip and connected to the current carrying electrodes. Naphthalene solution (10 μL, 1 mM) in chloroform was drop cast onto the Ni foil and allowed to dry. After reaching a rotary vacuum of ~ 5 mTorr, the Ni foil was Joule heated to red hot (~ 800 °C) with a current density of 120 – 150 A/mm^2 using a DC source for 15 min followed by immediate cooling.

IVD.4 Results and discussion

The XRD pattern of graphene/Ni shows prominent graphene peak at 26.3° as expected along with Ni(111) and Ni(200) substrate peaks (see blue curve in Figure IVD.2). The XRD patterns of as-obtained Ni foil (see black curve in Figure IVD.2) shows Ni(111)/Ni(200) ratio of 4.7 whereas annealed Ni foil (see red curve in Figure IVD.2) showed the ratio of 13.8 (clearly no graphene peak is seen). It is known that when a polycrystalline Ni undergoes re-crystallisation by thermal treatment, the intensity of Ni(111) increases as the (111) is stable orientation for Ni. Interestingly, when graphene was grown on Ni, the ratio of Ni(111)/Ni(200) increases to 31.4 (see blue curve in Figure IVD.2, almost twice than annealed Ni. Further, the graphene was subsequently peeled off from Ni foil several times and the XRD pattern is shown in Figure IVD.2 (see magenta curve). As expected no graphene peaks were seen and only Ni peaks were seen. However, Ni(111) intensity decreases from 31.4 to 18.0.

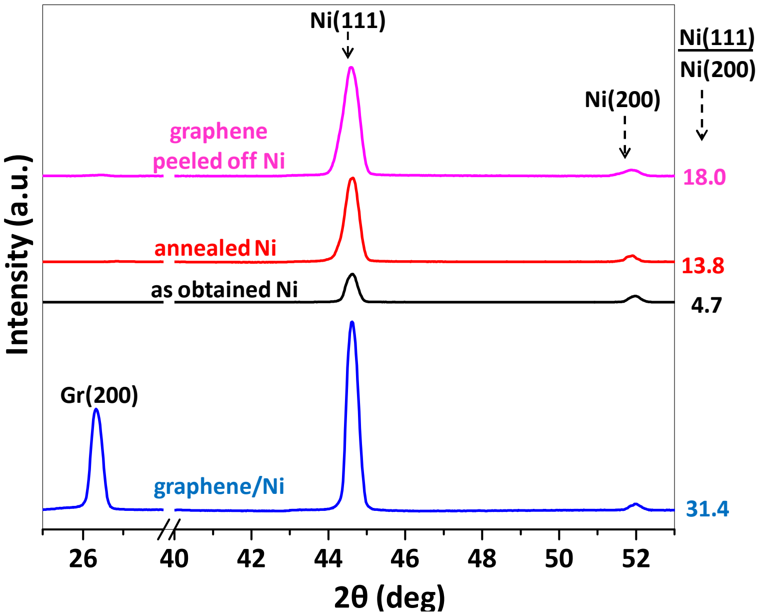

Figure IVD.2 Effect of growth of graphene on Ni orientations

XRD patterns of as-obtained Ni foil (black), annealed Ni foil (red), graphene covered Ni foil (blue) and after graphene is completely peeled off from Ni foil (magenta). The patterns are shifted vertically for an easy guide. Ni(111) to Ni(200) ratios have been indicted on respective patterns. Each pattern has been normalised with respect to the Ni(200) peak.

These observations have been further confirmed by several samples of graphene grown on Ni and presented in Figure IVD.3a. These values are slightly varying but in all the cases, the ratio is significantly higher than the Ni foil which went through similar annealing. Out of six samples (including the one shown in Figure IVD.2), lowest ratio was found to be 29.3. Further, by coating the hydrocarbon source on one side of the Ni foil, graphene was grown on only one side of Ni foil. When the foil was Joule heated, the graphene was formed on one side; another side has simply gone through thermal annealing at same temperature (annealed Ni). The presence and absence of graphene can be seen in photographs of two sides of foil and also can be confirmed from graphene(002) peak of corresponding XRD pattern (see Figure IVD.3b). As expected, the Ni(111)/Ni(200) ratio of graphene covered side was 29.3 whereas graphene uncovered side, it was 13.8. This clearly substantiates the influence of graphene growth

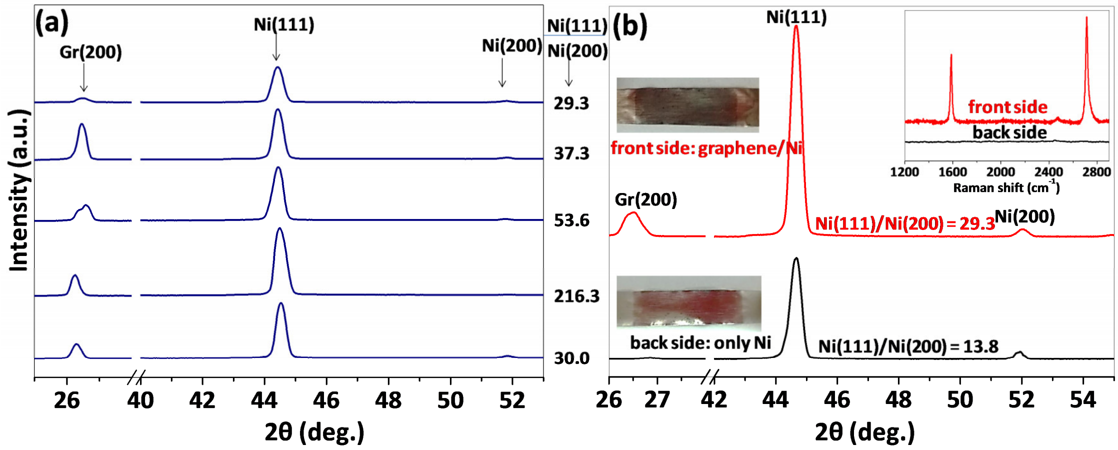

Figure IVD.3 More samples and more analysis

(a) XRD patterns of graphene on Ni recorded over five samples. Ni(111)/Ni(200) ratios are given in right side. (b) The XRD patterns of two sides of same Ni foil. Top red curve is the XRD of front side on which graphene was grown. Bottom black curve is the XRD of back side without graphene (annealed plain Ni). The Ni (111)/Ni(200) ratios are shown. The photographs of two side of the Ni foil are shown along with corresponding XRD patterns. All XRD peaks are normalised with respect to Ni(200) intensity. In insight, Raman spectra of graphene grown Ni(red curve) and graphene uncovered plain Ni (black) are shown.

on Ni orientations. It is known that when a polycrystalline Ni undergoes high-temperature annealing, the Ni(111) intensity increases due to re-crystallisation induced effects. But what is interesting is that graphene growth makes the (111) orientation even more pronounced. In other words, graphene growth turns Ni substrate predominantly into (111).

To study the surface morphology of the graphene covered and uncovered region, AFM analysis was carried out. As can be seen visually (Figure IVD.4a), the local surface roughness of the region where graphene is uncovered, was found to be 71.1 nm, whereas for graphene covered region it was 2.9 nm. As indicated by height profile in Figure IVD.4c a clear transition from smooth to the rough surface can be seen along the graphene covered to uncovered region. The rough nature of the Ni region is due to grainy nature of NiO formed during the growth process. Here primarily two kinds of graphene wrinkles were observed as reported previously [18], one with a height of 20-70 nm and another with a height of > 150 nm (see Figure IVD.4d). The latter one traces along the grain boundary of Ni. This was confirmed by peeling off graphene in the same region from Ni surface. As can be seen along the colored (red and green) dashed lines Figure IVD.4a and b and its height profiles in Figure IVD.4d and e, the wrinkle of smaller height has completely disappeared whereas bigger wrinkle also has disappeared but in its place, clear depth of ~ 120 nm can be seen which emerge from the grain boundary of Ni surface.

In order to have more insight into the effect of graphene growth on Ni, the morphology of Ni was carefully studied in a region before and after peeling off graphene from it. The graphene wrinkles which meet each other randomly form a mostly triangular junction and these junctions are interlocked with respect to one another (see Figure IVD.5c). After removing graphene, interestingly, the underlying Ni grains also are interlocked with respect to each other (see Figure IVD.5d). These grains have sharp edges which are uncommon in normal polycrystalline metals. The highly interlocked structures with sharp edges are characteristics features of highly single crystalline metal and clearly suggest that underlying Ni must be highly crystalline and oriented. Moreover, this kind of interlocked structures are completely absent in Ni which is annealed without any hydrocarbon at a similar temperature (see Figure IVD.5b). This gives a clear evidence for the role of graphene on Ni to turn Ni into highly oriented in (111) direction. In other words, this should validate the predominant formation of Ni(111) over other orientations and hence the high Ni(111)/Ni(200) ratio of > 30.

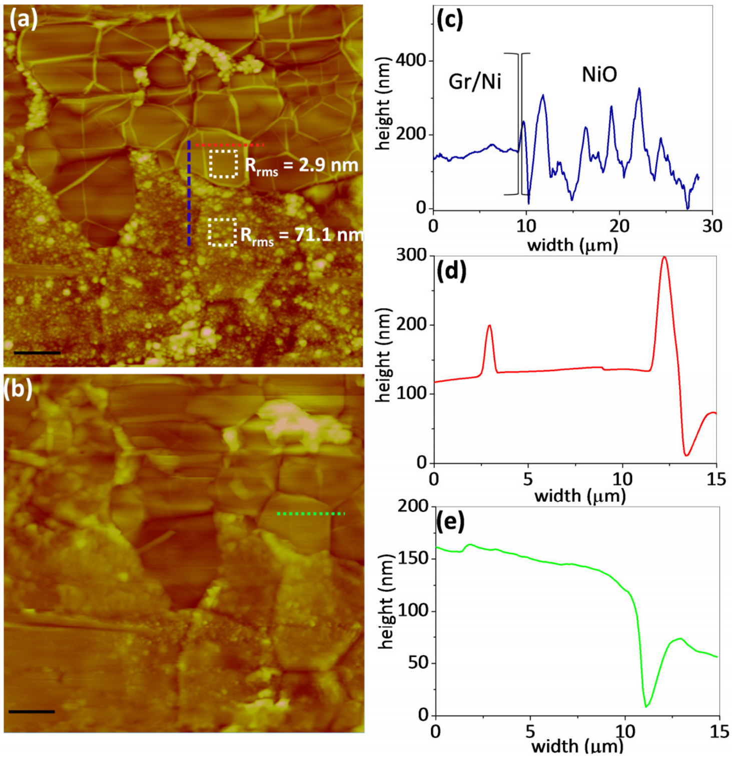

Figure IVD.4 AFM morphology of graphene/Ni before and after peeling off graphene from Ni surface

AFM morphology of graphene/Ni before (a) and after (b) peeling off graphene from Ni surface. Scale bar: 10 μm, z scale: 1μm. (c) a height profile along with dashed line marked in (a) showing a clear transition from smooth to the rough surface as it crosses to graphene/Ni. (d and e) Height profiles along dashed lines marked in (a, red line) and (b, green line) respectively.

Additionally, the intricate structure of junctions formed by wrinkles and its influence on underlying Ni were examined in Figure IVD.6. It mainly forms triangular (R1 in Figure IVD.6b) and quadrangle (R2 in Figure IVD.6) junctions formed by the meeting of three and four wrinkles respectively. It is important to note that when wrinkles meet each other, instead of forming a smooth meeting joint, they clasp each other to form a sharp intertwined structure (see Figure IVD.6a-c). Interestingly, when underlying Ni was examined after peeling off graphene from it, one can see highly interlocked grain boundaries of Ni (see Figure IVD.6d-f). In other words, the clasping nature of graphene wrinkles is directly replicated in Ni grain boundary which forms highly intricate structures with clear crystal facets which are uncommonly observed in Ni metal heated to ~ 1000 °C.

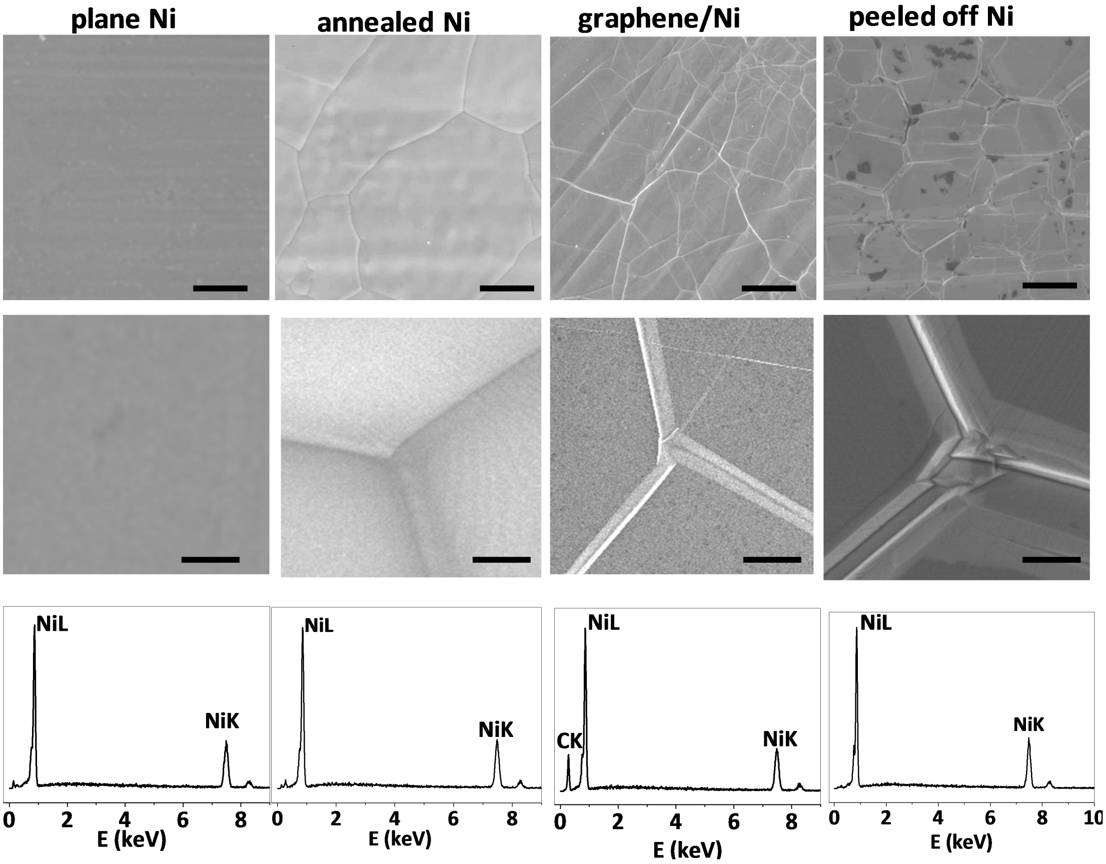

Figure IVD.5 Morphology studies at different magnifications

FESEM images of (a) as obtained Ni foil , (b) annealed Ni foil, (c) graphene covered Ni foil and (d) after graphene is completely peeled off from Ni foil at different magnifications. Scale bar: top row: 10 µm, 2nd row: 1 µm, 3rd row: 300 nm. The bottom row refers to corresponding EDS spectra of respective cases.

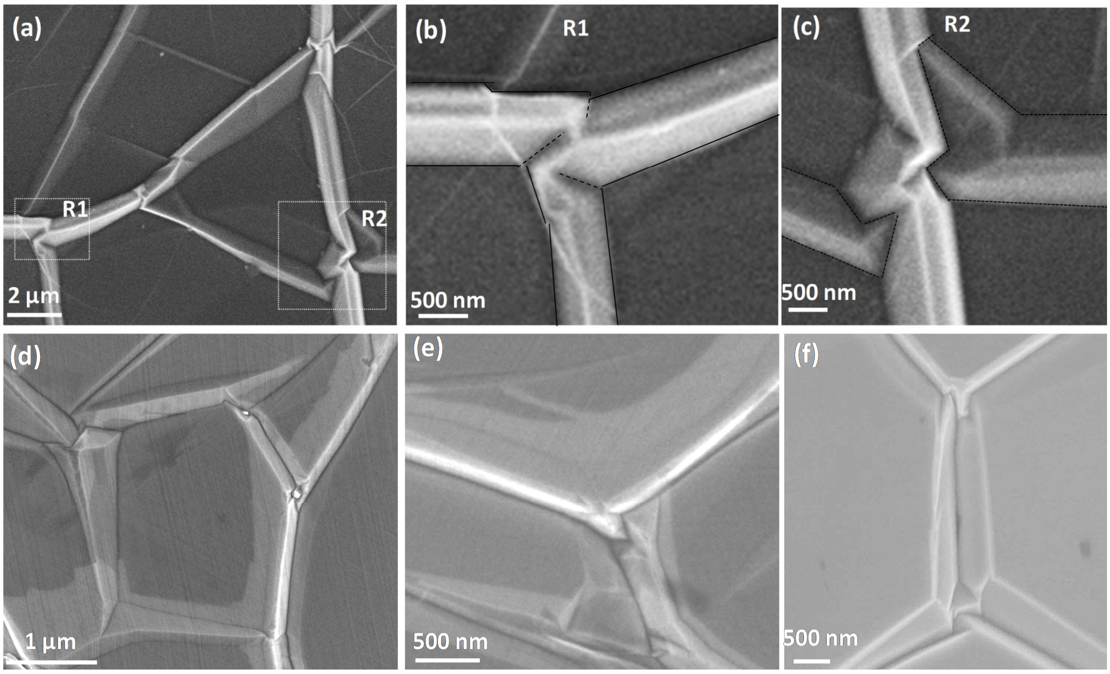

Figure IVD.6 Intricate structure of graphene and underlying Ni

(a-c) FESEM image of graphene wrinkle formed on Ni. The regions R1 and R2 marked in (a) are magnified in (b) and (c) respectively. (d-f) FESEM images of underlying Ni after peeling off graphene from it.

Ni being a ferromagnetic metal, it is interesting to study the influence of graphene growth on magnetic properties of Ni. Figure IVD.7a shows magnetisation curves were obtained for bare Ni (black curve), annealed Ni (red curve), graphene/Ni (blue curve) and graphene peeled off Ni (pink curve). Clearly, the magnitude of magnetisation has decreased in case of graphene/Ni when compared to bare Ni and annealed Ni. The decrease of magnetisation of graphene/Ni is expected since graphene is known to shield magnetic field reaching Ni. The shielding effect can be confirmed by recovery of magnetisation in the case of graphene peeled off Ni. Curie temperature (T_c) was also measured in the four cases by measuring the magnetisation with temperature. The T_c has decreased by 7 K (from 630 to 623 K) in the case of annealed Ni when compared to bare Ni due to re-crystallisation of Ni grains. Notably, T_c in the case of graphene/Ni has decreased considerably by 40 K (from 630 to 590 K). Surprisingly, T_c in case of graphene peeled off Ni increased only by 4 K (590 to 594 K) compared to graphene/Ni, though the magnitude of magnetisation has recovered back to that of bare/annealed Ni. This clearly indicates that decrease in T_c in graphene/Ni is not merely by a decrease in magnetisation but may be also due to the growth of graphene on Ni. Importantly, the variations in T_c in the four cases are similar to variation in Ni(111)/Ni(200) ratios, inferring that role of formation of Ni(111) orientation after graphene was grown on it.

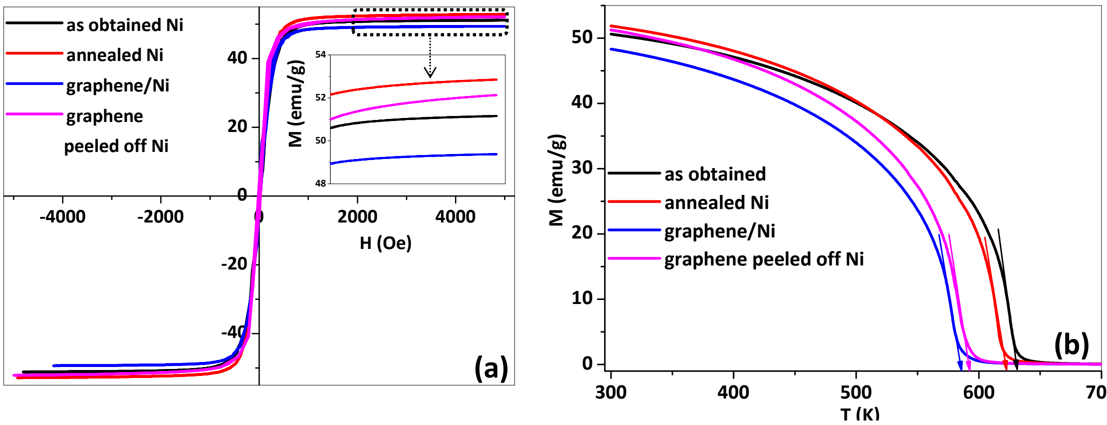

Figure IVD.7 Effect of graphene coating on magnetic properties of Ni

Variation of magnetisation with (a) magnetic field and (b) temperature of as obtained Ni foil (black), annealed Ni foil (red), graphene on Ni (blue) and graphene peeled off Ni (magenta). The dotted square region in (a) is magnified below it. The T_c is indicated by the dotted arrow in (b).

IVD.5 Conclusions

In the present study, a synergistic effect was observed between graphene and Ni(111) orientation. It is known that graphene prefers to grow on Ni(111) due to lowest lattice mismatch between the two. Here it is found that, while growing on Ni, graphene converts Ni more into (111) orientation. This is an experimental observation and we believe that it is purely synergetic (or co-operative effect) between the two. This synergistic action influences the underlying Ni so much that Ni grain boundary exhibits unusual grain interlocking and morphology with sharp facets. Also, the magnetic properties of graphene/Ni show a large shift in T_c of Ni which correlates well with the variation of Ni(111)/Ni(200) ratios. The study provides the new insight in understanding the interaction between graphene and Ni surface.

References

1. Edwards, Rebecca S., and Karl S. Coleman. "Graphene film growth on polycrystalline metals." *Accounts of chemical research* 46. 1 (**2012**): 23-30.

2. Eizenberg, M., and J. M. Blakely. "Carbon interaction with nickel surfaces: Monolayer formation and structural stability." *The Journal of Chemical Physics* 71. 8 (**1979**): 3467-3477.

3. Dedkov, Yu S., M. Fonin, and C. Laubschat. "A possible source of spin-polarized electrons: The inert graphene/Ni (111) system." *Applied Physics Letters* 92. 5 (**2008**): 052506.

4. Jacobberger, Robert M., and Michael S. Arnold. "Graphene growth dynamics on epitaxial copper thin films." *Chemistry of Materials* 25. 6 (**2013**): 871-877.

5. Mattevi, Cecilia, Hokwon Kim, and Manish Chhowalla. "A review of chemical vapour deposition of graphene on copper." *Journal of Materials Chemistry*21. 10 (**2011**): 3324-3334.

6. Bertoni, Giovanni, et al. "First-principles calculation of the electronic structure and EELS spectra at the graphene/Ni (111) interface." *Physical Review B* 71. 7 (**2005**): 075402.

7. Lu, Yujie, and Xiaoning Yang. "Molecular simulation of graphene growth by chemical deposition on nickel using polycyclic aromatic hydrocarbons." *Carbon* 81 (**2015**): 564-573.

8. Xu, Mingsheng, et al. "Single-layer graphene nearly 100% covering an entire substrate." *arXiv preprint arXiv: 1006. 5085* (**2010**).

9. Mittendorfer, Florian, et al. "Graphene on Ni (111): Strong interaction and weak adsorption." *Physical Review B* 84. 20 (**2011**): 201401.

10. Shibuta, Yasushi, and James A. Elliott. "Interaction between graphene and nickel (111) surfaces with commensurate and incommensurate orientational relationships." *Chemical Physics Letters* 538 (**2012**): 112-117.

11. Fogarassy, Zsolt, et al. "Dominantly epitaxial growth of graphene on Ni (111) substrate." *Applied Surface Science* 314 (**2014**): 490-499.

12. Usachov, D., et al. "Experimental and theoretical study of the morphology of commensurate and incommensurate graphene layers on Ni single-crystal surfaces." *Physical Review B* 78. 8 (**2008**): 085403.

13. Rasuli, R., Kh Mostafavi, and J. Davoodi. "Molecular dynamics simulation of graphene growth on Ni (100) facet by chemical vapor deposition." *Journal of Applied Physics* 115. 2 (**2014**): 024311.

14. Rasool, Haider I., et al. "Atomic-scale characterization of graphene grown on copper (100) single crystals." *Journal of the American Chemical Society*133. 32 (**2011**): 12536-12543.

15. Rasool, Haider I., et al. "Continuity of graphene on polycrystalline copper." *Nano letters* 11.1 (**2010**): 251-256.

16. Zhao, Liuyan, et al. "Influence of copper crystal surface on the CVD growth of large area monolayer graphene." *Solid State Communications* 151. 7 (**2011**): 509-513.

17. Dzemiantsova, L. V., et al. "Multiscale magnetic study of Ni (111) and graphene on Ni (111)." *Physical Review B* 84. 20 (**2011**): 205431.

18. Umesha Mogera, Narendra Kurra, Dhanya Radhakrishnan, Chandrabhas Narayana, Giridhar U. Kulkarni "Low cost, rapid synthesis of graphene on Ni: An efficient barrier for corrosion and thermal oxidation." *Carbon* 78 (**2014**): 384-391.

Chapter V

Improving the Quality of Graphene/Cu by Joule Heating

Summary

In this chapter, peculiar properties of Joule heating are utilised to improve the quality of already grown single layer graphene on copper (graphene/Cu) as monitored by Raman spectroscopy. Further, it's effect on the morphology of graphene was found to be so unique that it forms continuous graphene domains over a large area. This leads to an alternative method of polymer-free transferring of graphene on any target substrate. The electronic properties of as-transferred graphene are found to be comparable to that of good quality graphene involving multi-step transferring and post-processing steps.

V.1 Introduction

Graphene has received massive attention as a promising new material due to its extraordinary electronic [1-3], mechanical [4], and optical properties [5]. First successful isolation of graphene was done in 2004 using mechanical exfoliation [6] of graphite, which facilitated exploring its outstanding fundamental properties. However, mechanical exfoliation [7, 8] can only yield relatively small samples with non-controllable sizes and shapes, therefore it is not ideal for the synthesis of large-area and uniform graphene sheets to apply for real-life electronic and optoelectronic devices. Chemical vapour deposition (CVD) [9-14] is currently the most widely adopted technique for the large area scalable production; lengths up to 100 metres have already been shown [15]. However, for device fabrications in electronic and optoelectronic applications, a reliable method is required to transfer the graphene sheets from metallic substrates to various target substrates, such as silicon, glass, PET etc. Till date, the most common method to transfer CVD-grown graphene sheets from Cu to other substrates is the polymer-assisted transfer process, in which a layer of polymers such as polymethyl methacrylate (PMMA) [16-18], polydimethylsiloxane (PDMS) [9], thermal release tape [19], polycarbonate (PC) [20] and special self-release polymers [21] are used as a temporary rigid support to prevent folding or tearing of graphene during the metal-etching step [22]. Though, the polymer-assisted transfer methods have the advantages of easy handling and processing, removing the residual organic contamination on the surface of graphene remains a challenge. Recently, Lin et. al. have shown that it is almost impossible to remove the thin polymer layer from graphene surface, severely affecting the intrinsic properties of graphene [23]. Various solvent treatments and thermal annealing have been used in efforts to remove and decompose the polymer residue after the transfer process. However, these processes can change the band structure of graphene and can induce thermal stress causing damage to the graphene. Recently, several polymer-free graphene transfer methods have been developed [24-27], however, many of these methods involve multiple processing steps and can only transfer graphene in relatively small sizes.

V.2 Scope of the present investigation

As detailed in the introduction, transferring CVD grown graphene/Cu without influencing its electronic properties, is a major challenge. The use of rigid polymer support is inevitable during metal etching step that prevents the folding and tearing of graphene. If somehow the tearing of graphene is prevented, then the graphene can be easily scooped onto any substrate, making it a direct transfer method without the need of polymer support.

The current chapter addresses the transferring large area CVD grown graphene/Cu to a target substrate without using polymer support. The method focuses on preventing the graphene from rapturing during etching step. It involves the Joule heating of as obtained graphene/Cu that forms the continuous graphene domains. Joule heating is used in the present process because it is known for post synthesis defect annealing in the graphene devices.

V.3 Experimental section

Briefly, as obtained commercial (from Graphene Supermarket) and lab prepared graphene/Cu foil were cut into a size of 0.4 x 4.0 cm^2 and were connected to current electrodes, kept in a chamber with a vacuum of ~ 5 mTorr. The Joule heating (JH) was performed by passing AC current through the foil with varying current densities and times. After JH, the foil was cooled to room temperature and disconnected from electrodes. Lab quality graphene/Cu was prepared by homemade CVD set up using known literature methods [9, 10]. To calculate I_{2D}/I_G values, baseline subtracted Raman spectra were used.

V.4 Results and discussion

The process flow of improving the quality of graphene/Cu is described in Figure V.1. Optical microscope image in Figure V.1a is the as obtained commercial graphene that shows the discontinuous graphene domains with its surface contaminated. Figure V.1b is the schematic of JH process where the graphene/Cu foil was connected to current electrodes and AC current of current densities, 50 – 150 A/mm^2 were passed for 5 – 15 minutes. After JH, when the same foil was examined in an optical microscope (see Figure V.1c), it shows continuous graphene domains with a clean surface. The SEM images of the foil before (Figure V.1d) and after (Figure V.1e) JH are shown for comparison. It is clear that, after the JH, all the impurity particles present on the sample completely disappeared and the foil became clear and neat. This clearly infers the effect of JH on the morphology of graphene/Cu to convert into the continuous, smooth and neat surface.

In order to get the optimum Joule heating conditions, the current density and time of Joule heating were varied between 50 – 150 A/mm^2 and 5 – 15 minutes respectively and monitors through Raman spectroscopy. For every sample, Raman spectra were recorded at several regions and average I_{2D}/I_G values were calculated. Table V.1 gives the tabulation of average I_{2D}/I_G values obtained at different JH conditions. When compared with as obtained sample ($I_{2D}/I_G \sim 0.80$), it is clear that with the increase in current density and time, the I_{2D}/I_G has steadily increased. Highest value of I_{2D}/I_G of 2.05 was obtained for current densities of 150 A/mm^2 and 15 minutes. Further JH resulted in rupturing of graphene, as confirmed by the absence of 2D and G bands in the measured Raman spectra. Though JH can be performed for higher time period, the increment in I_{2D}/I_G values was found to be negligible. From these observations, the optimum conditions for Joule heating were obtained to be a current density of 150 A/mm^2 for 15 min.

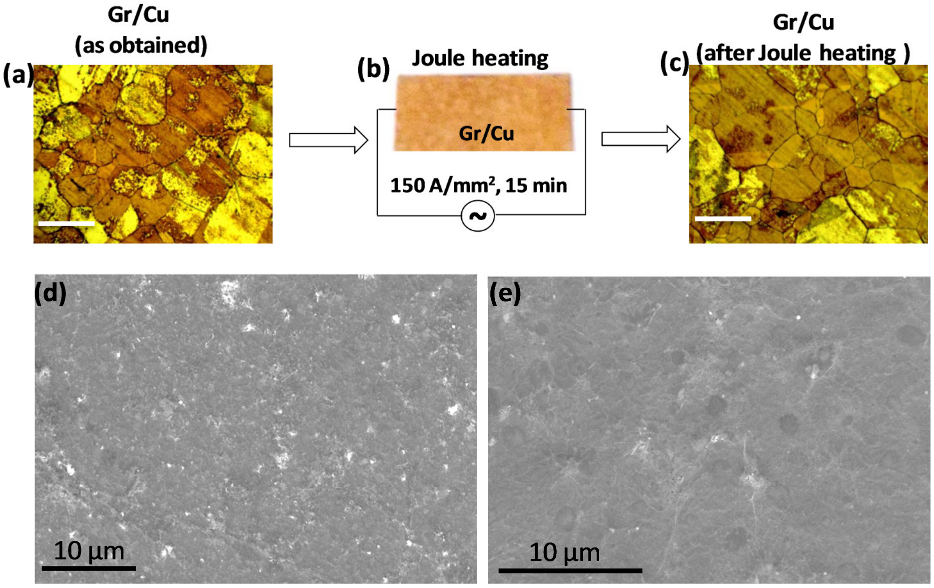

Figure V.1 Process flow of improving the quality of graphene/Cu

(a) Optical microscope image of as-obtained commercial graphene/Cu. (b) Schematic of JH of graphene/Cu. Photograph of graphene/Cu is shown. (c) Optical image of graphene on copper after. SEM image of graphene/Cu (d) before and (c) after JH process.

Table V.1 Table of optimization parameters obtained for commercial graphene/Cu.

Sr. No.	Current density (A/mm^2)	Time (min)	Avg. I_{2D}/I_G ratio
1	As obtained (graphene/Cu)		0.80
2	50	5	1.01
3	100	5	1.31
4	150	5	1.5
5	50	10	0.99
6	100	10	1.52

7	150	10	1.82
8	50	15	0.84
9	100	15	1.63
8	150	15	2.05
9	200	15	Graphene raptured

The effect of JH at these optimum conditions are studied in detail by recording Raman spectra, before and after JH of the graphene/Cu. Figure V.2 shows the Raman spectra obtained from three different regions of commercial graphene/Cu. For clarity, Raman spectra were recorded in the same regions after Joule heating. Interestingly, the average I_{2D}/I_G value of ~ 0.80 (see Figure V.2a), obtained before Joule heating, increased to 2.05 (see Figure V.2b) when the sample was Joule heated for 15 min at current density of 150 A/mm^2. To confirm the JH effect, another batch of graphene/Cu (lab quality) was tested in the same conditions. In this case as well, the average I_{2D}/I_G values of 0.46 (see Figure V.2c), before Joule heating increased to 0.94 (see Figure V.2d), after Joule heating. This clearly indicates the role of Joule heating in improving the quality of graphene. Table V.2 summarizes the variations in I_{2d}/I_g value with JH of the types of graphene/Cu.

As previously observed in the optical microscope images in Figure V.1c, the morphology of graphene/Cu looks apparently continuous and neat when compared to the as obtained sample. Interested by this observation, an attempt was made to transfer the JH treated graphene without bringing polymer support. As mentioned in the introduction, before transferring graphene from Cu surface, it is coated with a thin layer of polymer film. The polymer support gives the backbone support for graphene during etching of the metal substrate. If polymer support is not used during the etching process, graphene simply tears off due to its poor inter-grain bonding. To verify this, as obtained graphene was transferred onto a glass substrate after etching Cu using FeC$_3$ solution without polymer support. During etching it was found that visible graphene on the surface of etchant solution simply tears off making it difficult to be scooped out on a substrate (Figure V.3a). Out of many attempts, a piece of graphene was successfully

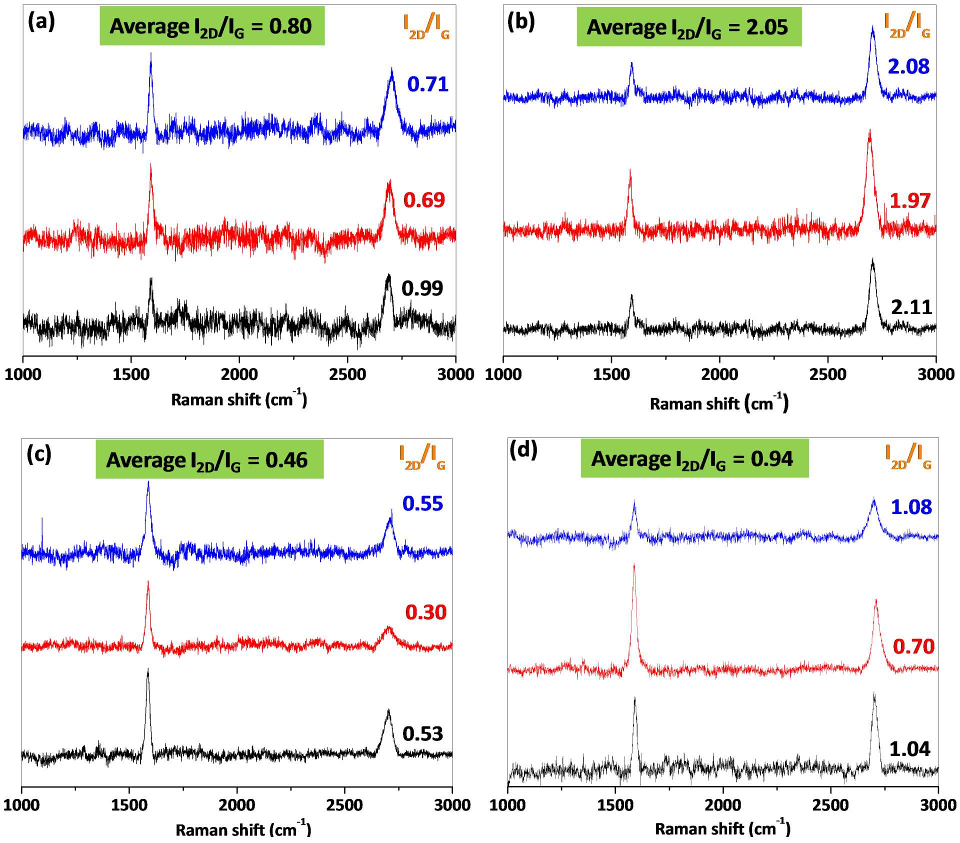

Figure V.2 Effect of Joule heating on Raman spectra of graphene/Cu

The Raman spectra measured at three regions of graphene/Cu (a and c) before and (b and d) after Joule heating. The spectra are color corresponded and measured in the same region. Upper panel (a and b) shows the Raman Spectra of commercial graphene and lower panel (c and d) shows Raman spectra of lab quality graphene.

transferred onto a glass substrate and was examined in the optical microscope. Clearly, the graphene domains are discontinuous as seen in optical microscope image in Figure V.3b. Thus, polymer support is always necessary during transferring of graphene from Cu. But bringing polymer in contact with the graphene gives rise to other issues as described in the introduction. Though it is dissolved several times in hot acetone, a thin layer of residue always remains on the surface. As a result, the electronic properties of graphene, particularly its charge carrier mobility, get severely affected due to the doping of polymer onto graphene. Interestingly, when metal etching was done after JH of graphene/Cu, graphene was seen holding its original shape on the surface of etchant solution without folding and tearing, no matter how large the graphene is (see Figure

V.3c). Further, the metal etched graphene can easily be transferred onto a target substrate by scooping method. Optical microscope image in Figure V.3d shows continuous graphene sheets with very sharp edges. It appears that JH indeed increases the mechanical stability of grown graphene on Copper substrate. However, the influence of crystal structure modification due to JH might not play much role here as the Joule heating increases the temperature only up to 200 – 300 °C at which much crystal modification cannot be expected. This clearly signifies that JH improves the mechanical stability of graphene grown on copper facilitating its support-free transfer onto any target substrate.

Table V.2 Comparison of improvement of two types of graphene

	Graphene type	Condition	Avg. I_{2D}/I_{G} ratio
1	Commercial graphene	As obtained	0.80
		After Joule heating	2.05
2	Lab quality graphene	As obtained	0.46
		After Joule heating	0.94

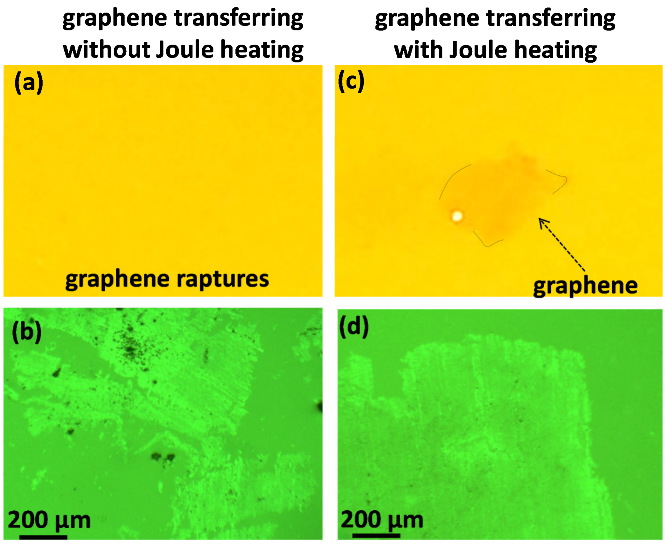

Figure V.3 Morphology changes in transferred graphene

Photographs of graphene, (a) without and (c) with Joule heating, floating on etchant solution during metal etching process. Optical microscope images of transferred graphene, (b) without and (d) with Joule heating, onto a glass substrate.

Clearly, it gives a new way of transferring grown graphene onto target substrates without involving polymer support. The advantages of the present method, Joule heated transfer (or J-transfer) over conventional transfer method is noticeable as shown in Figure V.4. Further, to verify the quality of transferred graphene, its electronic properties were studied by fabricating a field effect transistor out of it. One such J-graphene (Joule heated graphene) was transferred onto SiO_2/Si substrate (Figure V.6a) and its transfer characteristics was measured (Figure V.6b) without doing any annealing process. Interestingly, it shows the field effect mobility of ~ 1700 cm^2/Vs with charge carrier concentration of 1.65×10^{12} cm^{-2}. The mobility values are strikingly comparable with that of good quality graphene. The mobility values can be further improved by current or thermal annealing the device post fabrication, as routinely done on other graphene devices.

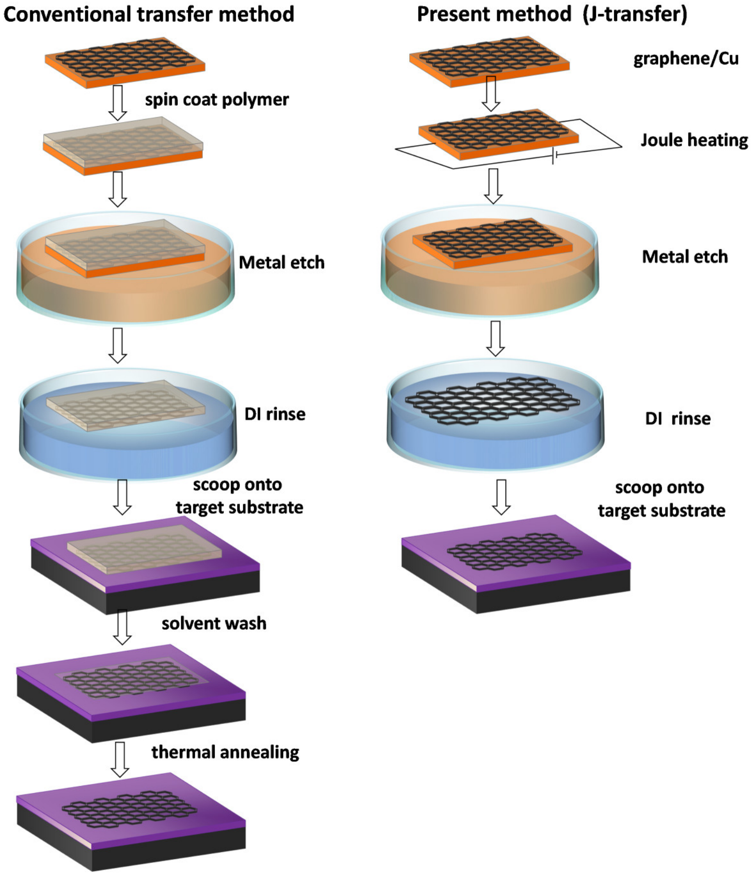

Figure V.4 5 Comparison of transfer methods

Schematics of steps involved in conventional transfer method (left panel) and J-transfer (Joule heated graphene transfer) onto target substrate.

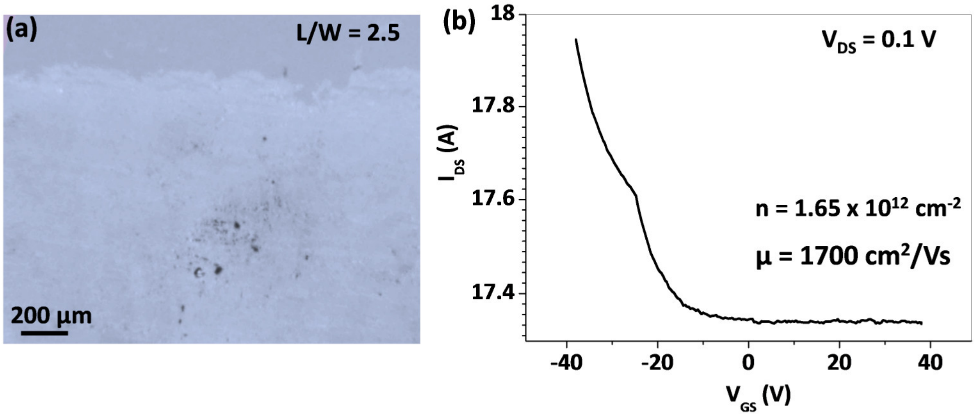

Figure V.6 FET measurements of J- graphene

(a) Optical microscope image of J-graphene on SiO_2/Si substrate with L/W value of 2.5. (b) Transfer characteristics of J-graphene measured at V_{DS} of 0.1 V. Carrier concentration and mobility values are indicated.

V.5 Conclusions

Using Raman spectroscopy, it is shown that Joule heating can be employed to improve the quality of graphene. Joule heating not only makes the graphene surface clean but also makes continuous graphene domains. Joule heated graphene was transferred to target substrate without bringing in polymer support, which makes the J-transfer method, a polymer-free transfer of graphene. Roll-to-Roll compatibility of the Joule heating provides the easy adaptability of the J-transfer in transferring large area graphene sheets.

References

1. Castro Neto, A. H.; Guinea, F.; Peres, N. M. R.; Novoselov, K. S.; Geim, A. K. The Electronic Properties of Graphene. *Rev. Mod. Phys.* **2009**, 81, 109–162.

2. Novoselov, K. S.; Geim, A. K.; Morozov, S. V.; Jiang, D.; Katsnelson, M. I.; Grigorieva, I. V.; Dubonos, S. V.; Firsov, A. A. Two-Dimensional Gas of Massless Dirac Fermions in Graphene. *Nature* **2005**, 438, 197–200.

3. Geim, A. K.; Novoselov, K. S. The Rise of Graphene. *Nat. Mater.* **2007**, 6, 183–191.

4. Lee, C.; Wei, X.; Kysar, J. W.; Hone, J. Measurement of the Elastic Properties and Intrinsic Strength of Monolayer Graphene. *Science* **2008**, 321, 385–388.

5. Nair, R. R.; Blake, P.; Grigorenko, A. N.; Novoselov, K. S.; Booth, T. J.; Stauber, T.; Peres, N. M. R.; Geim, A. K. Fine Structure Constant Defines Visual Transparency of Graphene. *Science* **2008**, 320, 1308.

6. Novoselov, K. S.; Geim, A. K.; Morozov, S. V.; Jiang, D. Zhang, Y.; Dubonos, S. V.; Grigorieva, I. V.; Firsov, A. A. Electric Field Effect in Atomically Thin Carbon Films. *Science* **2004**, 306, 666–669.

7. Lu, X. K.; Huang, H.; Nemchuk, N.; Ruoff, R. S. Patterning of Highly Oriented Pyrolytic Graphite by Oxygen Plasma Etching. Appl. Phys. Lett. **1999**, 75, 193–195.

8. Lu, X. K.; Yu, M. F.; Huang, H.; Ruoff, R. S. Tailoring Graphite with the Goal of Achieving Single Sheets. *Nanotechnology* **1999**, 10, 269–272.

9. Kim K. S., Zhao Y., Jang H., Lee S. .Y, Kim J. M., Kim K. S., Ahn. J H., Kim P, Choi J. Y. and Hong B. H. Large-scale pattern growth of graphene films for stretchable transparent electrodes *Nature* **2009**, 457, 706-10.

10. Li X. S. et al Large-area synthesis of high-quality and uniform graphene films on copper foils *Science* **2009,** 324, 1312–4.

11. Li X. S. et al Graphene films with large domain size by a two-step chemical vapor deposition process *Nano Lett*. **2010**, 10 4328–34

12. Chen S. S., Ji H X, Chou H, Li Q Y, Li H Y, Suk J W, Piner R, Liao L, Cai W W and Ruoff R S. Millimetre-size single crystal graphene by suppressing evaporative loss of Cu during low pressure chemical vapor deposition *Adv. Mater*. **2013,** 25, 2062–5.

13. Yang S Y, Oh J G, Jung D Y, Choi H, Yu C H, Shin J, Choi C G, Cho B J and Choi S Y Metal-etching-free direct delamination and transfer of single-layer graphene with a high degree of freedom *Small* **2015**, 11, 175–81.

14. Na S R, Suk J W, Tao L, Akinwande D, Ruoff R S, Huang R and Liechti K M Selective mechanical transfer of graphene from seed copper foil using rate effects *ACS Nano* **2015,** 9, 1325–35.

15. Kobayashi, Toshiyuki, et al. "Production of a 100-m-long high-quality graphene transparent conductive film by roll-to-roll chemical vapor deposition and transfer process." Applied Physics Letters 102. 2 (**2013**): 023112.

16. Li, X.; Zhu, Y.; Cai, W.; Borysiak, M.; Han, B.; Chen, D.; Piner, R. D.; Colombo, L.; Ruoff, R. S. Transfer of Large-Area Graphene Films for High-Performance Transparent Conductive Electrodes. *Nano Lett*. **2009**, 9, 4359–4363.

17. Suk, J. W.; Kitt, A.; Magnuson, C. W.; Hao, Y.; Ahmed, S.; An, J.; Swan, A. K.; Goldberg, B. B.; Ruoff, R. S. Transfer of CVD Grown Monolayer Graphene onto Arbitrary Substrates. *ACS Nano* **2011**, 5, 6916–6924.

18. Alfonso, R.; Hyungbin, S.; Liying, J.; Ben, F.; Dresselhaus, M. S.; Liu, Z.; Kong, J. Transferring and Identification of Single- and Few-Layer Graphene on Arbitrary Substrates. J. Phys. Chem. C **2008**, 112, 17741–17744.

19. Bae, S.; Kim, H.; Lee, Y.; Xu, X.; Park, J. S.; Zheng, Y.; Balakrishnan, J.; Lei, T.; Kim, H. R.; Song, Y. I.; et al. Roll-toRoll production of 30-in. graphene films for transparent electrodes. *Nat. Nanotechnol*. **2010**, 5, 574–578.

20. Lin, Y.-C.; Jin, C.; Lee, J.-C.; Jen, S.-F.; Suenaga, K.; Chiu, P.-W. Clean Transfer of Graphene for Isolation and Suspension. *ACS Nano* **2011**, 5, 2362–2368.

21. Song, J.; Ksm, F.-Y.; Png, R.-Q.; Seah, W.-L.; Zhuo, J.-M.; Lim, G.-K.; Ho, P. K. H.; Chua, L.-L. A General Method for Transferring Graphene onto Soft Surfaces. *Nat. Nanotechnol*. **2013**, 8, 356–362.

22. Lin, Wei-Hsiang, et al. "A direct and polymer-free method for transferring graphene grown by chemical vapor deposition to any substrate." *ACS nano* 8. 2 (**2014**): 1784-1791.

23. Lin, Yung-Chang, et al. "Graphene annealing: how clean can it be?." *Nano letters* 12. 1 (**2011**): 414-419.

24. Regan, W.; Alem, N.; Alemán, B.; Geng, B.; Girit, C -.; Maserati, L.; Wang, F.; Crommie, M.; Zettl, A. A Direct Transfer of Layer-Area Graphene. *Appl. Phys. Lett*. **2010**, 96, 113102.

25. Zhang, Guohui, et al. "Versatile Polymer-Free Graphene Transfer Method and Applications." *ACS applied materials & interfaces* 8. 12 (**2016**): 8008-8016.

26. Park, Hamin, et al. "Polymer-free graphene transfer for enhanced reliability of graphene field-effect transistors." *2D Materials* 3. 2 (**2016**): 021003.

27. Liu, Shuo, et al. "Triboelectricity-assisted transfer of graphene for flexible optoelectronic applications." *Nano Research* 9. 4 (**2016**): 899-907.

Chapter VI

Summary and Future Outlook

The thesis is essentially about exploring novel properties and functional applications of novel 1D and 2D materials.

In **Chapter III**, the rich properties associated with the organic 1D supramolecular nanofibre have been transformed into multi-functional devices to realise its applications. Using nanofibre as the active channel material, ultrafast response humidity sensor has been realized. Its increase in conductivity with humidity arises from increase in the charge transfer interaction between D-A molecules. The ultrafast sensing has been utilised in monitoring the breath patterns of a human. Using two humidity sensors, humidity cum flow sensor has been fabricated and demonstrated in live dehydration examples. Using the current decay property of the nanofibre, a humidity based memory sensor is made which can memorise the past humidity it has experienced. Finally, nanofibre can also be used in micro-supercapacitors, whose voltage window surpasses that of conventionally used electrolytes.

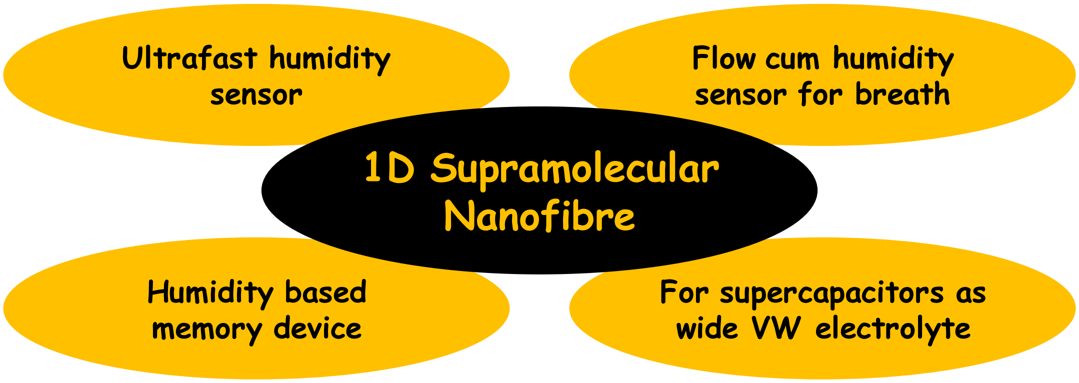

Figure VI.1 Summary of Chapter III

As future prospective, humidity sensor can be used for continuous online monitoring of breath and any perturbation in the breath can be detected. Simultaneous detection of flow and humidity of the breath finds clinical importance for instance, the flow difference from two nasal passages provides health conditions of a person. Humidity based memory device can be explored in contexts where ensuring a particular humidity for long time is necessary. The approach used here, to have ambient stable and wide voltage window electrolyte using nanofibre can be further explored to achieve high energy density values.

Chapter IV describes synthesis and properties of a 2D material, graphene and its stacks. A simple and fast synthesis of graphene was explored without using any gaseous reactants including hydrogen. Stacks of graphene layers are obtained by same method, but by changing precursor concentration and rapid cooling. Such graphene stacks were found to be a new species of graphene/graphitic material which shows single layer graphene behaviour in spite of being hundreds of nanometre thick and named as T-SLG (Turbostratically SLG). The graphene layers in T-SLG are indeed misoriented (turbostratic) and highly decoupled from one another. In the study, Joule heating method was used to make such graphene stacks, which not only allows rapid cooling but also make graphene layers completely defect-free. Since T-SLG is stacks of tBLG containing many rotated graphene layers, its absorption bands become prominent and hence observable in UV-vis spectroscopy. The 2D crystallinity and highly decoupled nature of T-SLG are reflected in its temperature dependent resistance which resembles suspended graphene. Its SERS shows unusual selective enhancement of 2D band. A synergy effect has been observed between graphene and Ni(111) where graphene transforms Ni surface more into (111) orientation. Unusual morphologies and grain interlocking have been observed on Ni surface after the graphene growth which is uncommonly seen **Chapter V** describes a method to improve the quality of CVD grown graphene on copper. In doing so, it provides an alternative method for direct transfer of the graphene grown on copper to targeted substrate without any need of polymer support.

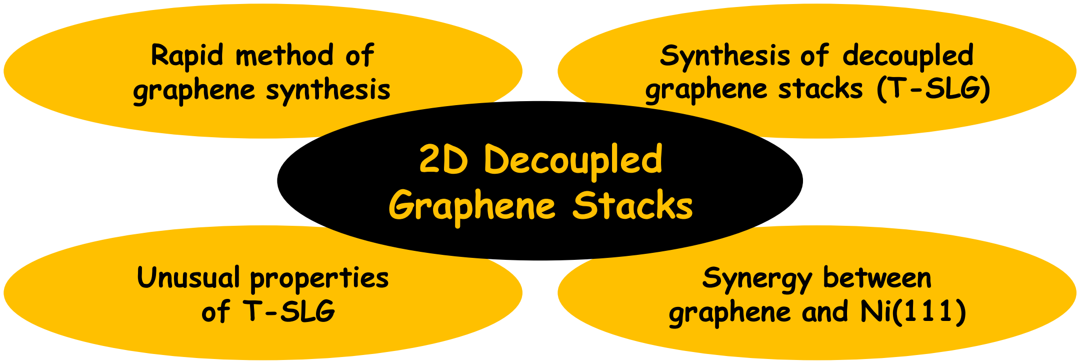

Figure VI.2 Summary of Chapter IV

As future prospective, Joule heating method can be extended to roll to roll process for making large area graphene sheets. The properties of T-SLG are quite comparable to suspended graphene and thus it is an alternative material to suspended graphene whose extraordinary properties can be realized for practical applications. The T-SLG represents many stacks of tBLG, the properties observed in tBLG can be explored in T-SLG. Since graphene layers are decoupled from one another, it can be used for easy exfoliation of large area graphene sheets to make defect-free conducting graphene dispersions.

List of Publications and Patents

Ultrafast Response Humidity Sensor using Supramolecular Nanofibre and Its Application in Monitoring Breath Humidity and Flow

U. Mogera, A. A Sagade, S. J George, G. U Kulkarni

Scientific Reports, 2014, 4, 04103

Supramolecular nanofibre as a novel electrolyte for micro-supercapacitors with high operating voltage window

U. Mogera, M. Gedda, S. J George, G. U. Kulkarni

2016, submitted

Humidity based memory sensing by supramolecular nanofibres

M Gedda, U. Mogera, S. J. George, G. U Kulkarni

2016, submitted

Low Cost, Rapid Synthesis of Graphene on Ni: An Efficient Barrier for Corrosion and Thermal oxidation

U. Mogera, N. Kurra, D. Radhakrishnan, C. Narayana, G. U Kulkarni

Carbon, 2014, 78, 384–391

Analysis of graphene wrinkles and its properties

U. Mogera, M. Priya, N. Gupta. N. Basavaraj, N. John, G. U. Kulkarni

2016, under preparation

Highly Decoupled Graphene Multilayers: Turbostraticity at its Best

U. Mogera, D Radhakrishnan, R, Pujar. C, Narayana, G. U. Kulkarni

Journal of Physical Chemistry Letters, 2015, 6, 4437–4443

Visible absorption bands in T-SLG

U. Mogera, S. Walia, G. U. Kulkarni

2016, under preparation

Temperature dependent transport in T-SLG

U. Mogera, S. Walia, B. Bharath, M. Gedda, G. U. Kulkarni

2016, under preparation

Differential SERS effect in T-SLG

U. Mogera, D. Radhakrishnan, C. Narayana, G. U. Kulkarni

2016, under preparation

Synergy between graphene and Ni(111)

U. Mogera. G. U. Kulkarni

2016, under preparation

Improvisation of CVD graphene on copper by Joule heating

U. Mogera and G. U. Kulkarni

2016, submitted

Nanoscopic Understanding of Ultrafast Humidity Sensing in Supramolecular Nanofibres Through In-Situ GISAXS Measurements

Arpan Bhattacharyya, Milan K. Sanyal, U. Mogera, Subi J George, Mrinmay K. Mukhopadhyay, Giridhar. U. Kulkarni and Santanu Maiti

2016, Submitted

Formation of DMV-CS Charge Transfer Complex in Air-Water Interface

Arpan Bhattacharyya, Milan K. Sanyal**,** U. Mogera, G.U. Kulkarni, Subi George and Philippe Fontaine

2016, under preparation

High-Mobility Field Effect Transistors Based on Supramolecular Charge Transfer Nanofibres

A. A. Sagade, K. V. Rao, U. Mogera, S. J. George, A. Datta, G. U. Kulkarni

Advanced Materials, 2012, 25, 559

Patents filed

A Process for Synthesis of Graphene and a Graphene Thereof

U. Mogera, N. Kurra and G. U Kulkarni

Indian Patent, Application No. 2713/CHE/2014

Date of filing: July 03, 2014

Turbostratic Graphite and Process of Preparing the Same

U. Mogera and G. U Kulkarni

Indian Patent, Application No.: 2967/CHE/2015

Date of filing: June 12, 2015

Supramolecular Nanofiber as Electrolyte

Indian Provisional filed, Application No. 5285/CHE/2015

U. Mogera, M. Gedda, S. J George, G. U. Kulkarni

Date of filing: October 01, 2015